



SAPIENZA
UNIVERSITÀ DI ROMA

FACULTY OF MEDICINE AND PHARMACY

Department of Chemistry and Drug Technologies

PhD School of Pharmaceutical Sciences

XXX cycle

A gas-phase approach to the study of reaction
mechanisms of biological and industrial
sustainable processes

Doctoral dissertation

Candidate:

Chiara Salvitti

Supervisor:

Prof. Federico Pepi

PhD School Coordinator:

Prof. Antonello Mai

Academic year 2016/2017

Table of contents

1. Introduction.....	1
2. Monosaccharide decomposition reactions	8
2.1 Hexose acid-catalysed dehydration	15
2.2 D-fructose base-assisted dehydration	29
2.3 Pentose acid-catalysed dehydration.....	37
2.4 Discussion	53
3. L-Ascorbic acid decomposition reaction	62
3.1 Protonated L-Ascorbic acid structure and ion energetics.....	66
3.2 Protonated L-Ascorbic acid decomposition	77
3.3 Discussion	84
4. Glycosylation reaction	87
4.1 Structural characterization of the oxocarbenium ion intermediate.....	99
5. Ion-molecule reactions.....	108
5.1 Iron promoted C-C bond formation.....	112
5.2 SO ₂ promoted V-O activation	120
5.3 Discussion	128
6. Conclusions.....	133
7. Experimental methods	136
7.1 Electrospray versus chemical ionization	136
7.2 Collisionally activated dissociation.....	139
7.2.1 Energy resolved mass spectrometry	140
7.2.2 Tandem MS ⁿ mass spectrometry.....	143
7.3 Ion-trap kinetic experiments.....	145
7.4 Neutralization-reionization mass spectrometry.....	149

7.5 Ion-mobility mass spectrometry	152
7.6 Superfluid helium nano-droplet infrared spectroscopy	155
7.7 Experimental details	162
8. Bibliography	168

1. Introduction

Chemistry deals with fundamental matter transformations that continuously occur throughout the Universe and deeply influence the human life. All chemical reactions are characterized by a sequence of elementary processes where the product of one reaction is the reactant of the next one, to eventually obtain a thermodynamically stable compound. In the usual synthetic laboratory procedures, the knowledge of the reaction mechanism is crucial to effectively control the reaction outcome, optimize the product yields and reduce the formation of side compounds. This goal can be achieved identifying the intermediates and transition states of the reactions, which can be however a very difficult task.

First of all, most reactions are a series of multistep and multicomponent processes that involve a large number of intermediates. Indeed, many different reactions are frequently used in combination to obtain a designed product and, in some cases, negative synthesis outcomes can be ascribed to the lack for mechanistic information. On the other hand, reaction intermediates are usually high energy and highly-reactive species present at very low concentration in solution and characterized by very short lifetimes. Therefore, only under exceptional circumstances these elusive compounds can be isolated from the reaction mixture and structurally identified. In most cases, the reaction mechanisms and intermediates can only be hypothesized by theoretical conjectures and thermochemical arguments.

According to these considerations, the main focus of the present thesis is the study at the molecular level of important sustainable processes that can contribute to the development of a “green” industry. In particular, the greatest challenge in realizing a sustainable future is the control of the energy consumption and the search for alternative sources of fuels and bulk chemicals.

Energy is essential for all the economic activities aimed at sustaining the quality of life. During the last years, world energetic needs have increased by about 60% and are expected to further grow by 50-60% by 2030.^[1] This trend is

driven by the population growth and the pursuit of improving living standards as well as by a global infrastructure that has expanded to a massive scale.

Nowadays, non-renewable fossil fuels still represent the main global source of energy, and continue to be responsible for pollution and climate change. Considering only the Italian area, it has been estimated that the number of cars amounts to around 37 millions, that means one vehicle for less than two people.^[2] Because of these environmental problems and the progressive depletion of the petroleum supply, the transition from carbon resources to renewable bio-resources has become increasingly urgent. Natural gas such as methane has played a significant role in supporting the energy request, especially after the energy crisis of the 1970s that followed the oil embargo of 1973 proclaimed by the Organization of the Petroleum Exporting Countries (OPEC). In this regard, all the reactions that lead to the activation of C-H, C-C and C-X (X=F, Cl, Br, I) bonds have a great potential in this matter and have been the subject of many studies. Moreover, the selective conversion of hydrocarbon compounds into more user-friendly products are among the most exploited reactions in industrial field.

An alternative solution to the diminishing availability of crude oil is represented by the use of lignocellulosic biomass as a source of energy. Lignocellulosic biomass represents the main carbon source existing on Earth and it is available for a direct use as fuel or fuel precursor.^[3,4] Consequently, over the years, the processes allowing the utilization of carbohydrates from lignocellulosic biomass have received great attention, and some goals have already been reached for biomass utilization. For instance, the use of ethanol from sugarcane has greatly reduced the need for imported oil in Brazil.^[5]

Further to this, another important application field of the lignocellulosic biomass is the chemical industry, where biomass represents a feedstock for organic compounds and platform molecules. For example, ferrulic acid, a precursor of numerous aromatic chemicals, is extracted directly from corn fibres.^[6] Platform chemicals, such as 5-hydroxymethylfuraldehyde (5-HMF) and 2-furaldehyde (2-FA), or simpler molecules such as levulinic acid (LA) and glyceraldehyde, are the products of the thermal acid-catalysed dehydration of hexoses and pentoses.^[3,4;7-9] These compounds are important sustainable

intermediates in the preparation of a large variety of chemicals, pharmaceuticals and furan-based polymers.^[10] In particular, the furan derivatives 5-HMF and 2-FA are included in the “Top 10+4” list of the bio-based chemicals.^[11,12] Interestingly, 50 years ago the world production of 2-FA already ran to the order of 50.000 t per year, ranking it 67th in annual volume among major organic chemicals.^[13] Despite the number of theoretical studies focused on the elucidation of the monosaccharide dehydration mechanisms, the kinetics and thermodynamics of the sugar conversion are still unknown. As anticipated, this is due to the intermediacy of species with a short lifetime that makes difficult to derive a complete and consistent mechanistic picture.

The experimental study of short-lived species in the condensed phase takes advantage of spectroscopic techniques such as nuclear magnetic resonance (NMR), ultraviolet-visible (UV) and infrared (IR) absorption spectroscopies. Despite the efforts made in recent years to improve the high-speed capability of these methods,^[14,15] their use is really advantageous only for the analysis of compounds having light-sensitive chemical groups (chromophores, fluorophores, ect.). Furthermore, these techniques are all characterized by scarce selectivity and sensitivity, which prevents the direct identification of intermediates in the reaction mixture without resorting to time-consuming isolation procedures. The absence of selectivity causes the problem of band overlapping especially when substrates, intermediates and products have similar structures. Hence, they cannot be distinguished and monitored simultaneously. Besides, low sensitive methods require a large amount of pure samples. In this regard, the high thermochemical instability of reaction intermediates does not allow one to meet these mass and purity requirements. Considering the ionic or radical nature of most transient species, a promising approach is reproducing the reactions in the gas phase by means of mass spectrometric techniques.

Gas-phase studies have long been devoted to the behaviour of ions and molecules in the isolated state, providing kinetic, mechanistic and thermochemical information. In particular, they have largely contributed to understand the atmospheric composition of planets, satellites and interstellar medium, through the identification of unknown transient species only observed under particular

conditions of temperature and pressure. Such an approach has also been applied to the study of the reaction pathways occurring in the Earth's atmosphere and responsible for the pollution growth and pollutant formation.

The study of planetary and terrestrial atmospheres is not the only field of application of gas-phase studies, because they are also largely used to support and interpret evidence obtained from solution studies, building a bridge between the gas and condensed phases. The most relevant aspect is the opportunity to study intrinsic characteristics of charged species, such as structure and reactivity, in the absence of solvent molecules and counter-ions. The possibility to exclude any solvent contribution represents a significant achievement, since the reaction medium is known to affect the substrate reactivity. This advantage also gives the unique opportunity to compare experimental to theoretical data concerning structure, reactivity and thermochemistry.

Furthermore, additional efforts made in the gas-phase ion chemistry field have enabled the study of ionic reactions not only in the isolated state, but also within a well-designed micro-solvated environment where charged species are coordinated to a controlled number of solvent molecules (H_2O , CH_3OH etc.). This approach is legitimized by the evidence that, in some cases, the reaction occurrence strictly depends on the presence of the solvent, even if this is represented by a single molecule or a few molecules. For instance, NO^+ ion behaves in the gas phase as a nitrating agent only in the presence of a single molecule of H_2O or CH_3OH , whereas in the absence of solvent molecules it undergoes charge and oxygen atom transfer to arenes.^[16] Finally, the gas phase represents the ideal medium where the effects of the ionic charge on the reaction can be studied.

Mass spectrometry is the instrumental technique most often employed to perform gas-phase studies. As shown in Figure 1, a mass spectrometer can be viewed as a miniaturised laboratory where ionic species are reacted with neutrals and analysed.

Compared to other analytical techniques, mass spectrometry boasts high-sensitivity, selectivity and speed, being a more advisable alternative to NMR and spectroscopy.

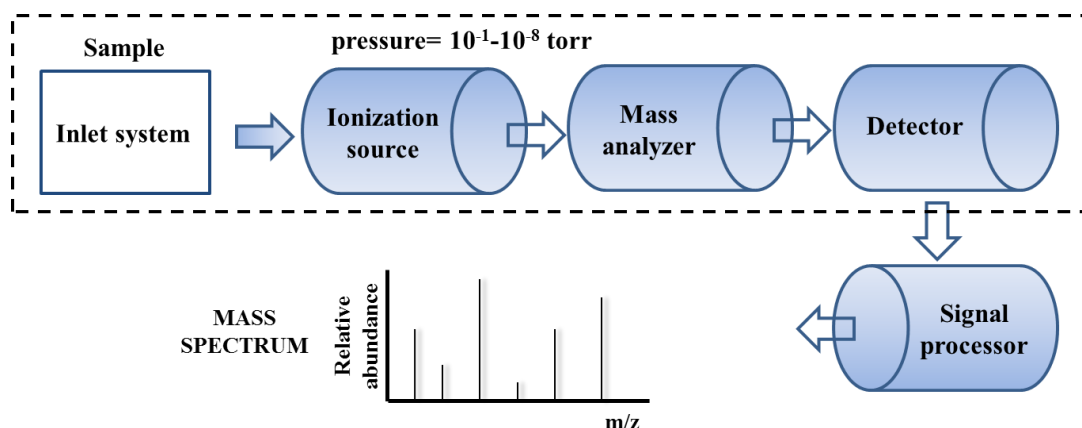


Figure 1: *The main components of a mass spectrometer.*

As regards the study of reaction mechanisms, these technical features are essential to isolate and characterize short-lived intermediates, increasing the throughput and reducing the analysis time. An example of these potentialities is represented by the experimental detection of the HO_3 radical, long suggested as a possible sink for O_2 and $\text{OH}^{[17]}$ and more recently identified as a key intermediate in the antibody-catalysed water-oxidation reaction.^[18] In fact, the $\text{HO}_3\cdot$ formed along this pathway shows an oxidant power that increases the efficiency of bacterial killing. Owing to the short lifetime of this species, its existence has never been experimentally proved until 1999 when the molecule was finally detected by means of mass spectrometry in experiments based on neutralization-reionization and neutralization-reionization/collisionally activated dissociation, starting from protonated ozone (HO_3^+) as the charged precursor.^[19]

The great potential of mass spectrometry has been ultimately accepted with the advent of soft ionization methods, first and foremost the Electrospray Ionization (ESI) technique.^[20] The gentle and efficient manner by which an ESI source can transfer intact ions from the solution directly to the gas phase has opened the way to the study of biological macromolecules (proteins, carbohydrates, lipids and nucleic acids)^[21] expanding mass spectrometry in the biochemical and medical field. An additional application of ESI-mass spectrometry (ESI-MS) is indeed the elucidation of reaction mechanisms occurring in solution. In this respect, Eberlin^[22] and Santos^[23] were among the first to employ ESI-MS in the analysis of the charged compounds at the gas phase/liquid phase interface. The so called

“fishing” technique takes advantage of the ESI capability to rapidly and efficiently fish ionic reactants, intermediates and products directly from the solution medium to the gas-phase environment of the mass spectrometer.^[22] This unique feature allows one to control the reactions following the progress of solution processes as a function of time. Mass and structural variation occurring along the reaction coordinates can be monitored by sampling at regular intervals small portion of the reaction mixture (Figure 2). The ultra-high sensitivity and speed of ESI-MS are essential to detect and characterize even transient intermediates. This approach has been successfully used to study a number of unknown reaction mechanisms (organic, inorganic and organometallic).^[23-29] Several protocols have been recently developed, aimed at the progressive diffusion of this method in the laboratory practice.^[30]

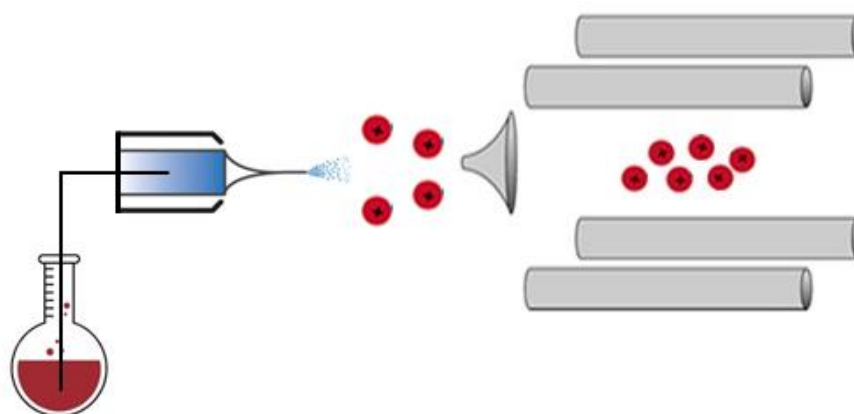


Figure 2: *Continuous reaction monitoring by ESI-MS.*

Due to the undeniable benefits of the gas-phase approach, this was exploited in the present work to highlight the reaction mechanisms of the carbohydrate conversion to platform chemicals. Mass spectrometric techniques were employed to structurally characterize the ionic intermediates and products of the dehydration reactions involving D-hexose (glucose and fructose) and D-pentose (xylose, arabinose and ribose) sugars arising from lignocellulosic biomass decomposition. The knowledge of the sugar degradation pathways on a molecular level is indeed a pivotal step for the development of a sustainable industry, allowing the design of

new reagents and catalysts that can increase the selectivity towards the formation of 5-HMF and 2-FA.

The same experimental method was then utilized to study the mechanism of the reactions involving other sugar substrates and molecules structurally correlated to carbohydrates. In particular, the decomposition reaction of L-Ascorbic acid (Vitamin C) has been investigated in order to identify the mechanisms leading to the formation of furan derivatives in foods. These compounds are supposed to be carcinogenic to humans,^[31] thus the knowledge of the reaction details could help keeping the level of these products under the critical threshold, ensuring the safeguard of the public health. In addition, the carbocationic intermediate formed along the glycosylation pathway has been structurally characterized. This species has never been isolated before and its conformational details may confirm a reaction mechanism only theoretically predicted.

Finally, a part of the work has been devoted to a fundamental issue, the activation of intrinsically inert bonds.^[32] In the gas phase, many elementary reactions of metal-containing ions have been studied as they are good models for catalytic or biochemical processes occurring at the active sites. In this thesis, an unprecedented reactivity has been observed with two metal-centered reactants: the iron-containing cation ($\eta^5\text{-C}_5\text{H}_5\text{Fe}^+$) has been found to undergo an unusual iron-atom transfer and C-C coupling reaction; the doubly-charged vanadium hydroxide anions, $\text{H}_2\text{V}_2\text{O}_7^{2-}$ and $\text{HNaV}_4\text{O}_{12}^{2-}$, have been found to perform unprecedented bond-forming reactions by activation of V-O bonds.

2. Monosaccharide decomposition reactions

Lignocellulosic biomass is generated through a carbon fixation process that converts inorganic carbon (CO₂) to organic compounds. The primary products arising from this assimilation reaction are C₆- and C₅-sugars, D-glucose and D-xylose respectively. Each monosaccharide is the starting reactant unit for condensation reactions that lead to two polymers, cellulose (obtained by the polymerization of D-glucose) and hemicellulose (obtained by the polymerization of D-xylose). Finally, a highly cross-linked polymer composed by substituted phenols, known as lignin, represents the third component of the wood biomass. Cellulose, hemicellulose and lignin are important structural components of the primary cell wall of the green plants, providing the cell with both protection and tensile strength (Figure 3).

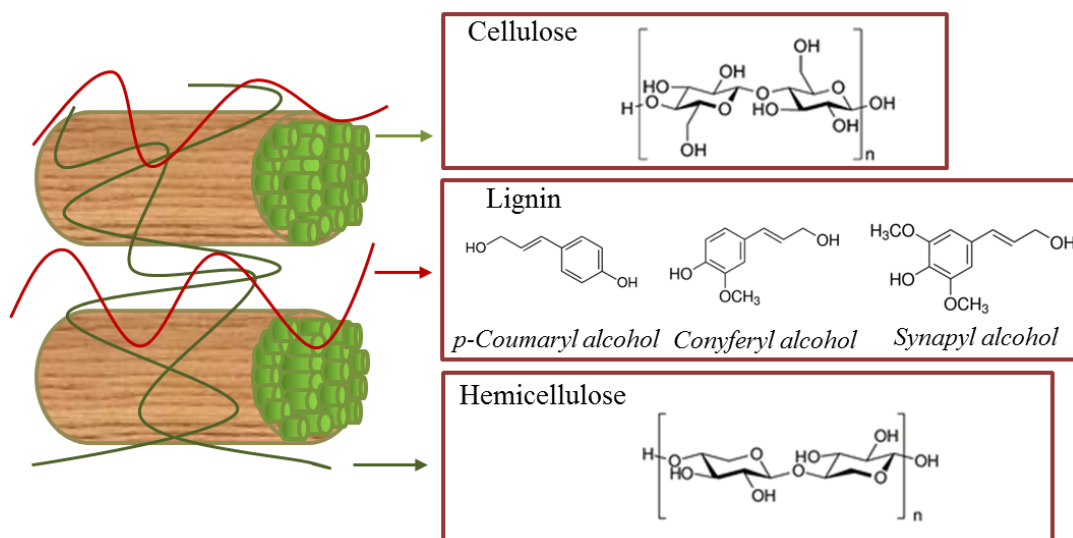


Figure 3: Main components of the lignocellulosic biomass.

Among all biomass constituents, carbohydrates are a promising feedstock since they represent a natural source of carbon. In particular, the removal of water, exemplified by the dehydration of D-glucose (from cellulose) and D-xylose (from hemicellulose) leads to a wide variety of interesting compounds (Figure 4).

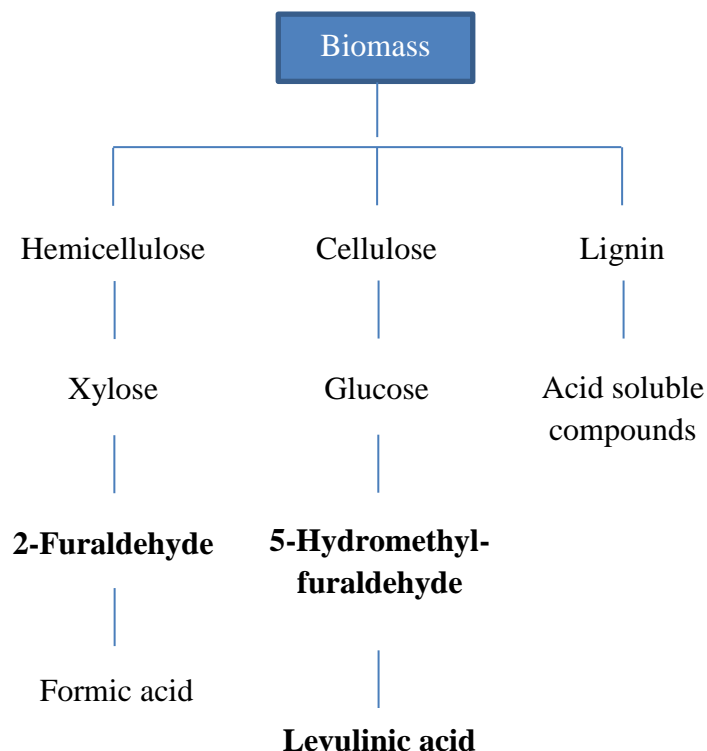
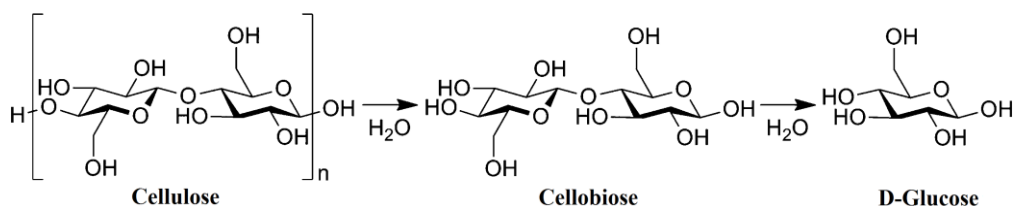


Figure 4: Schematic picture of the acid-catalysed conversion pathways of the lignocellulosic biomass to useful chemicals.

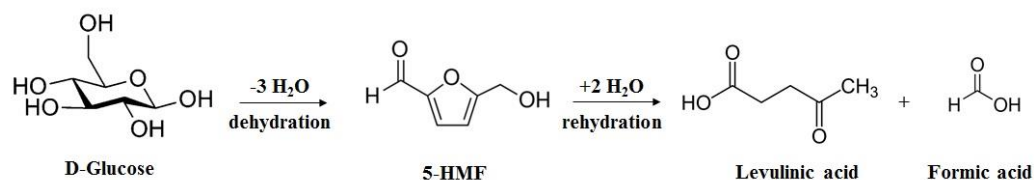
One class of dehydration products, the furan compounds, is considered highly promising for the production of fuels and chemicals. In order to obtain these products, cellulose extracted from wood biomass can be easily hydrolysed to D-glucose units through an acid-catalysed decomposition reaction (Scheme 1).^[33, 34]



Scheme 1: Hydrolysis of cellulose to D-glucose.

Subsequently, the thermal acid-catalysed dehydration of D-glucose leads to 5-hydroxymethylfuraldehyde (5-HMF) that is a reaction intermediate in the synthesis of levulinic acid (LA). This important platform chemical is formed together with formic acid by 5-HMF double hydration (Scheme 2).^[35] The

apparent simplicity of Scheme 2 is complicated by the formation of side products, in particular, insoluble polymeric materials named humins.



Scheme 2: Dehydration pathway of D-glucose leading to 5-HMF and levulinic acid.

Also another monosaccharide, D-fructose, is characterized by the dehydration route reported for D-glucose. It has been demonstrated that in solution the 5-HMF yield from the D-fructose dehydration is about 40 times higher than that obtained from D-glucose (Table 1).^[36] A reasonable explanation for the scarce selectivity found when using D-glucose as starting reactant could be the occurrence of multiple reaction pathways, such as condensation, mutarotation, isomerization and dehydration/degradation, that lead to the formation of many by-products.^[37]

Table 1: D-glucose and D-fructose dehydration to 5-HMF in aqueous system. a) Heating by microwave irradiation.

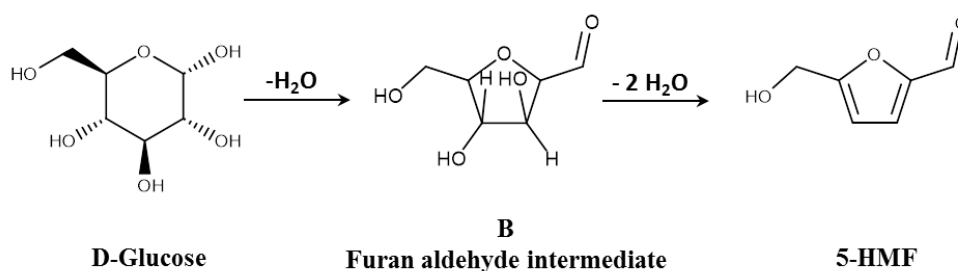
Sugar	Conc. (wt%)	Catalyst	T (C°)	time	Yield (%)	Conversion (%)	Selectivity (%)
Glucose ^[36]	2	H ₂ SO ₄	200 ^a	3-5	2	11	23
				min			
Fructose ^[36]	2	H ₂ SO ₄	200 ^a	3-5	47	97	48
				min			

Hence, the knowledge of the dehydration mechanism is essential to selectively address the D-glucose conversion to 5-HMF and improve the final yields.

In the gas phase, a number of computational studies have provided detailed information on the mechanism, kinetics and thermodynamics of sugar conversion.^[37-49] Conversely, the lack for experimental data in solution is due to the short lifetime of the intermediates, which prevents their isolation and

identification. For this reason the reaction pathways theoretically proposed have never been confirmed by experimental evidence.

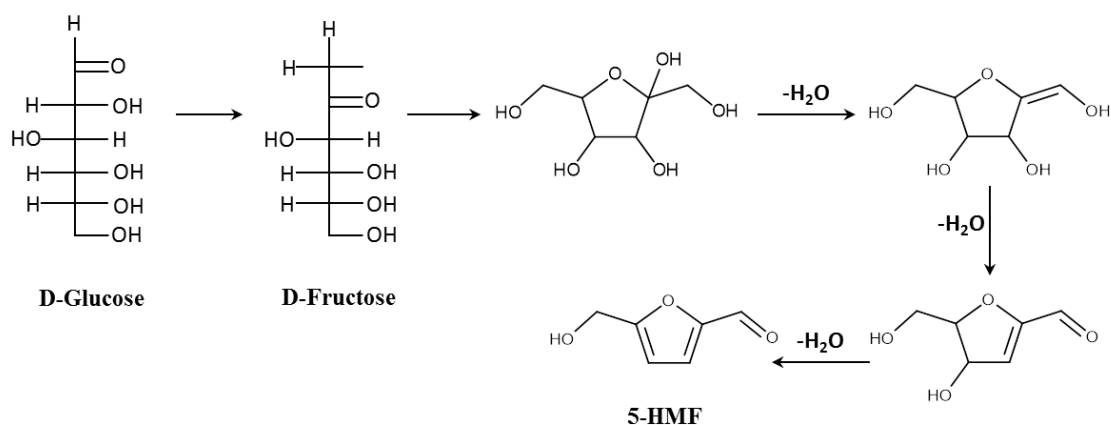
In particular, a debate exists concerning the mechanism of the D-glucose conversion to 5-HMF. Two different routes have been suggested. The former, named the “*cyclic mechanism*”, has been hypothesized by Antal (Scheme 3)^[40,41] and consists in the direct transformation of the D-glucose pyranosic ring to 5-HMF furanose ring, without the intermediacy of open-chain structures.



Scheme 3: The cyclic mechanism for the conversion of D-glucose to 5-HMF.

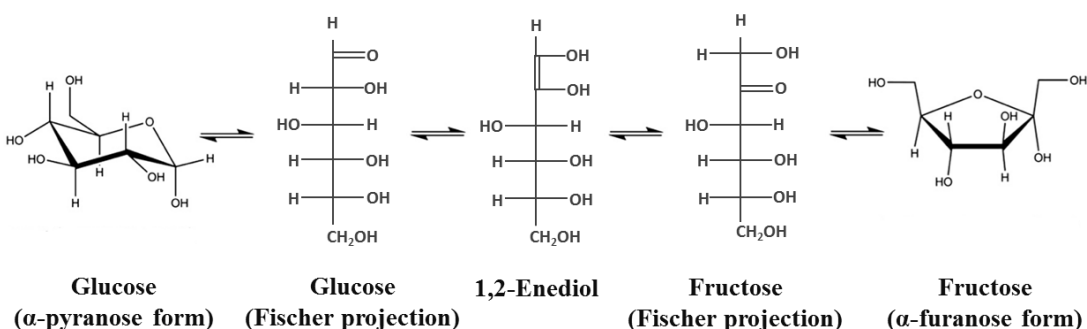
According to this mechanism after the first dehydration step a critical intermediate, the Furanaldehyde (B), is formed. This species evolves into 5-HMF through the subsequent release of two water molecules.

The latter alternative route (Scheme 4) has been proposed by Feather and Harris^[42] and is known as the “*fructose pathway*”.



Scheme 4: The fructose pathway for the conversion of D-glucose to 5-HMF.

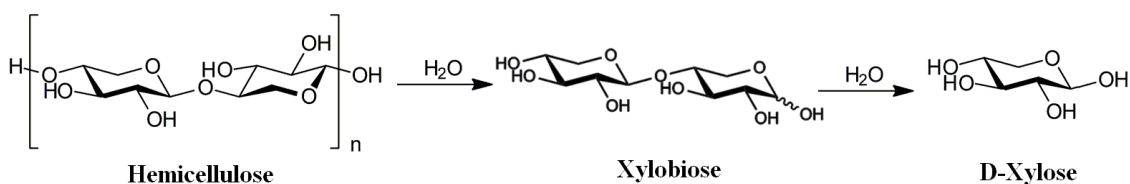
This mechanism involves the acyclic structure of glucose, which isomerizes to fructose through a 1,2-enediol intermediate (Scheme 5) and undergoes cyclization and subsequent dehydration leading to the formation of 5-HMF.



Scheme 5: *glucose/fructose conversion mechanism.*

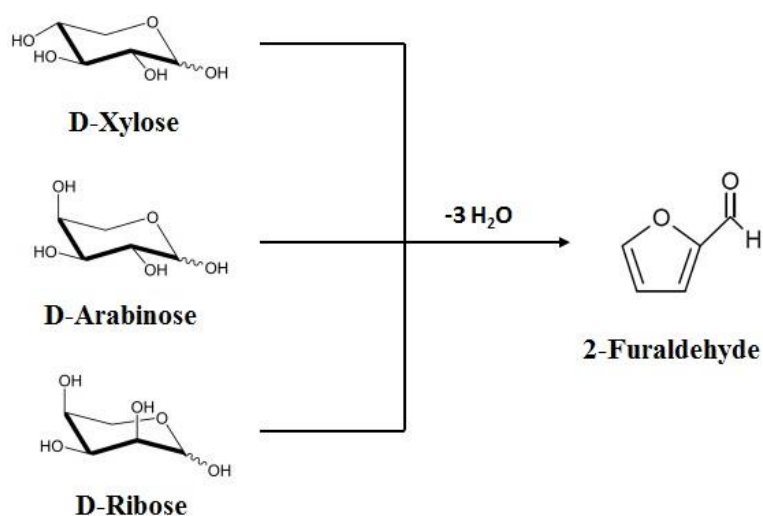
In this regard, the glucose/fructose tautomerization could justify the higher yields of 5-HMF obtained from fructose. Indeed, the acidic conditions required by the glucose dehydration process hinder the glucose conversion into fructose, that is instead promoted by an alkaline pH. The non-occurrence of the tautomerization reaction may drive the glucose along other decomposition routes, increasing the formation of side products.

By analogy with cellulose, the acid-catalysed hydrolysis of hemicellulose from biomass produces the monosaccharide units of D-xylose (Scheme 6).^[34]



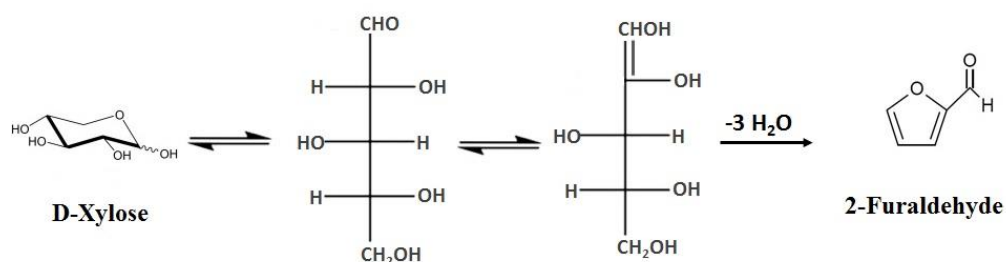
Scheme 6: *Hydrolysis of hemicellulose to D-xylose.*

The subsequent thermal acid-catalysed dehydration of D-xylose and isomeric pentose sugars (D-arabinose and D-ribose) leads to 2-furaldehyde (FA) (Scheme 7).^[9,13]



Scheme 7: *D*-pentose sugars dehydration to 2-FA.

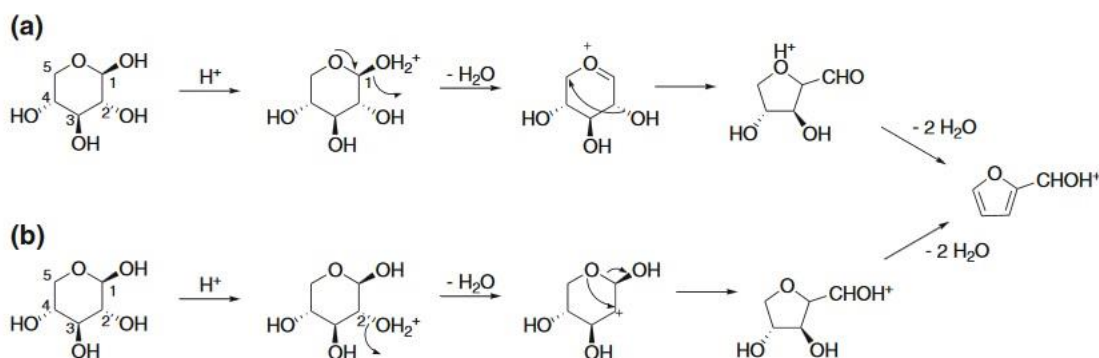
Like in the case of D-glucose, a debate exists in literature concerning the real reaction route. Theoretical calculations also in this case have suggested two main degradation pathways involving acyclic or cyclic forms of D-xylose. The acyclic mechanism consists in an open-chain D-xylose tautomerization leading to 1,2-enediol intermediate that subsequently undergoes three dehydration steps (Scheme 8).^[13,50-52] The alternative acid catalysed reaction sequence starts from the pyranose form of D-xylose and, after protonation and loss of the first water molecule, leads to a structure that rearranges to a furanose ring.



Scheme 8: *The acyclic mechanism for the conversion of D-xylose to 2-FA.*

The intermediate formed is prompt to release the remaining two water molecules (Scheme 9, a and b).^[37-39,41,53-55] Antal et al.^[41] reported that the cyclic mechanism is the most plausible. Theoretical calculations performed by Nimlos^[38]

strongly supported the degradation pathway starting from D-xylose protonated at C2-OH, whereas C1-OH protonation was excluded on the basis of the high energetic barrier for the subsequent ring contraction to the furanose intermediate, estimated to be 39.3 kcal mol⁻¹.



Scheme 9: The cyclic pathways for the conversion of D-xylose to 2-FA starting from C1-OH protonation a) or C2-OH protonation b).

Owing to the strong impact of the lignocellulosic biomass utilization and the absence of experimental evidence on this subject, the aim of this thesis has been the investigation in the gas phase of the thermal dehydration mechanism that starts from protonated D-hexoses (glucose and fructose) and D-pentoses (xylose, arabinose and ribose) and leads to 5-HMF, levulinic acid and 2-FA.

In particular, the gas-phase approach has been utilized (i) to identify the ionic precursors of the reactions, (ii) to structurally characterize the ionic intermediates and products, (iii) to obtain mechanistic information on the monosaccharide dehydration reactions with the aim of identifying preferential catalytic pathways.

In order to validate the mechanistic picture arising from the mass spectrometric results, the collected data were compared with those obtained from quantum mechanical calculations.

2.1 Hexose acid-catalysed dehydration

Figure 5 displays the ESI mass spectra of the D-fructose (panel a) and D-glucose (panel b) H₂O (0.1% HCOOH)/MeOH 1:1 solutions.

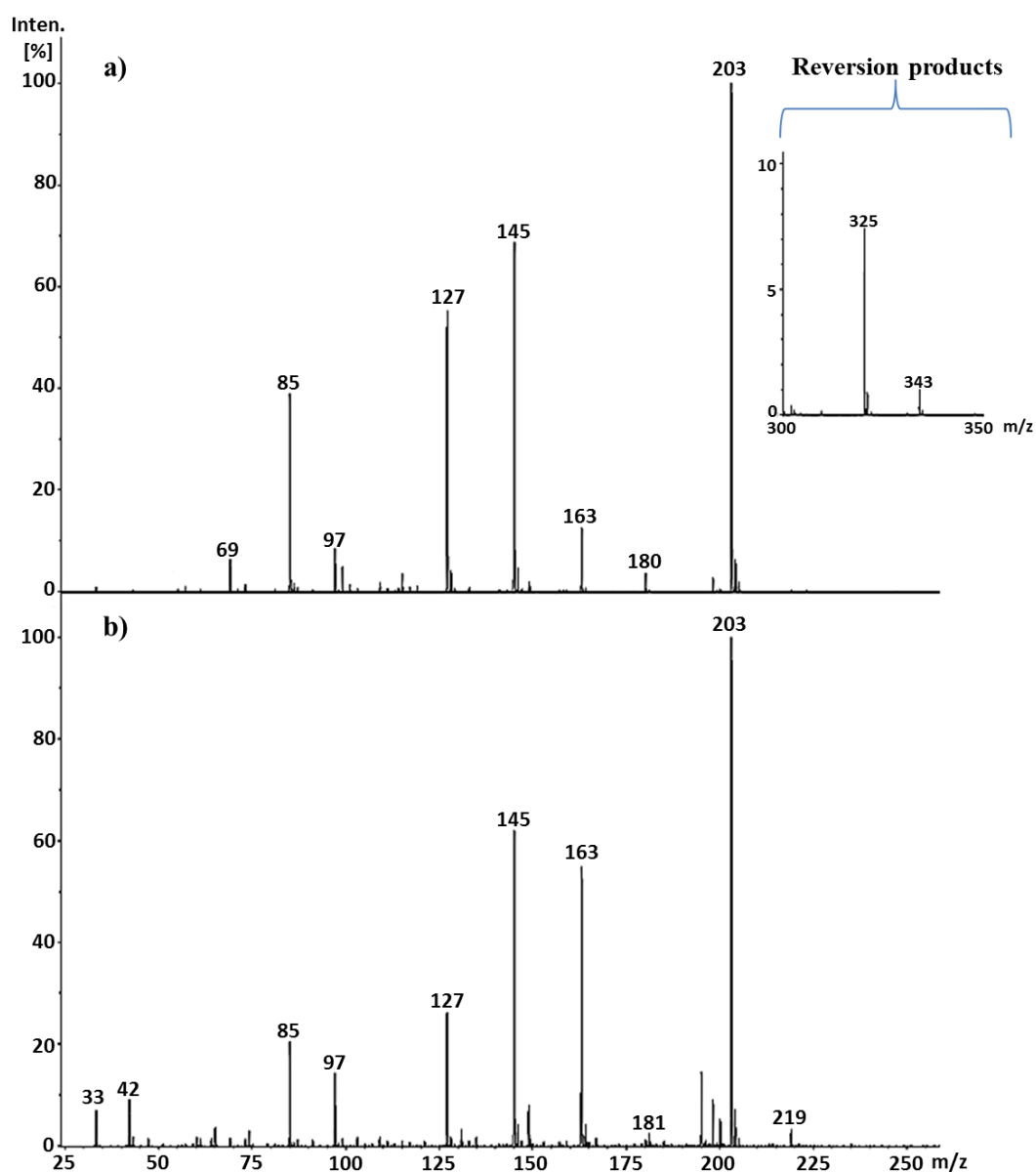


Figure 5: Comparison between the full scan mass spectra of 1×10^{-3} M solutions of D-glucose a) and D-fructose b) both in H₂O (0.1% HCOOH)/MeOH 1:1. In the inset the mass spectrum from m/z 300 to 350 showing the reversion products.

As illustrated, the ionic population observed in the gas phase in both cases is dominated by a characteristic peak at m/z 203, corresponding to the sodium

adduct ($C_6H_{12}O_6Na^+$). The metal ion Na^+ is a well-known solution contaminant, unavoidably present in the gas phase. However, from the analysis of the adduct fragmentation pattern it was found not to be the precursor of any dehydration intermediate, thus justifying its high intensity and excluding the possible interference in the present reaction mechanism study.

The ion at m/z 181, corresponding to the protonated sugar ($C_6H_{12}O_6H^+$), is characterized by an extremely low intensity, especially if compared with that of the sodium adduct. This feature could be due to its instability in the gas phase. It is reasonable to assume that the energy deriving from its formation process activates the dehydration reaction that leads to the product ions at m/z 163, 145 and 127. These ionic species in fact correspond to the consecutive losses of one, two and three water molecules from protonated D-glucose and D-fructose representing the ionic intermediates (m/z 163 and m/z 145) and product (m/z 127) of the gas-phase D-hexose dehydration process.

In the high mass range of the spectrum, the ions at m/z 343 and 325 correspond to sugar reversion products. These species are formed by the combination of a neutral D-glucose or D-fructose molecule and the corresponding monohydrate intermediate (ion at m/z 343), which in turn can dehydrate giving rise to the ion at m/z 325. The formation of these side products can prevent the efficient industrial conversion of the two hexoses to useful chemicals and their presence in the acidic reaction mixture was previously highlighted.^[56]

The mass attribution of all the ionic species described was confirmed by exact mass experiments performed with the ESI/Q-TOF mass spectrometer.

CAD experiments

In order to obtain more information on the hexose dehydration mechanisms, the starting reactant ions, the intermediates and the final product were isolated and analysed by CAD. Figure 6 shows the CAD mass spectrum of protonated D-glucose at m/z 181. The main fragmentation products arising from the parent ion dissociation effectively represent the dehydration intermediates (m/z 163 and m/z

145) and the final product (m/z 127) of the D-glucose acid catalysed decomposition.

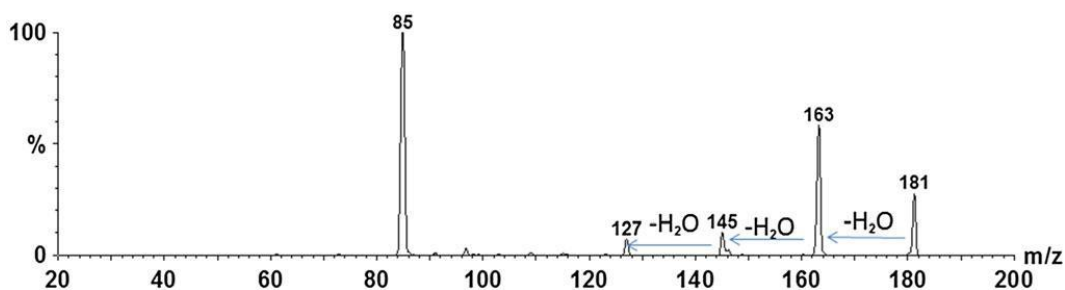


Figure 6: CAD mass spectrum of protonated D-glucose at m/z 181 recorded at 10 eV collision energy.

Also the ionic intermediates at m/z 163 and 145 were investigated by CAD experiments.

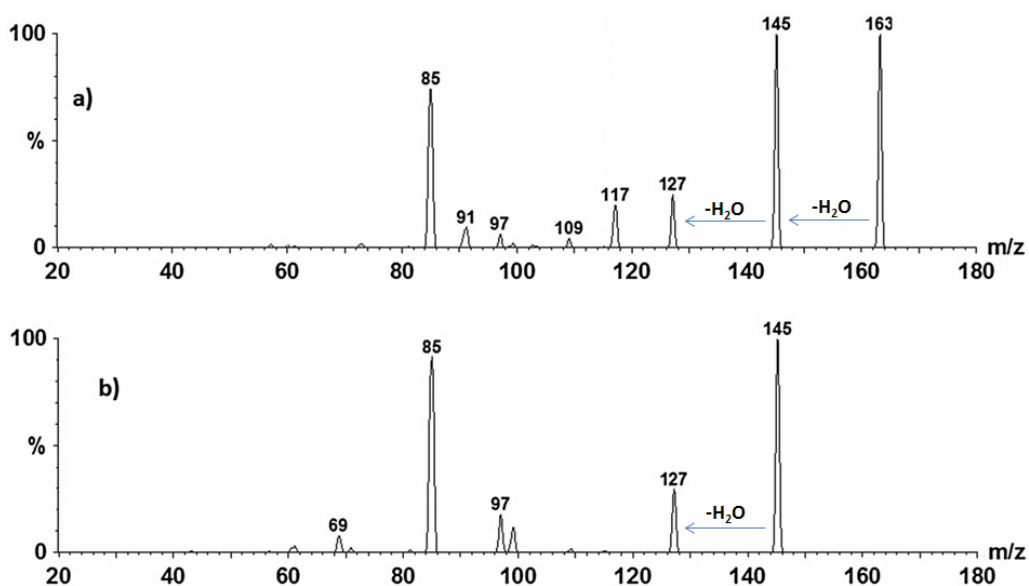


Figure 7: CAD mass spectra of the ionic intermediates at m/z 163 a) and m/z 145 b) arising from D-glucose, recorded at a collision energy of 5 and 6 eV.

As reported in Figure 7, these ionic species fragment by releasing two and one water molecules respectively giving rise to the final product ions at m/z 127. Furthermore, all displayed CAD mass spectra show an intense ionic signal at m/z

85, an ionic fragment deriving from a cross ring bond cleavage characteristic of cyclic carbohydrates.^[57]

Other important information can be obtained by the fragment ion at m/z 117 observed in the product ion mass spectrum of the intermediate at m/z 163. This ion formally corresponds to the protonated levulinic acid, one of the final products of the D-glucose dehydration reaction. To probe this attribution, the CAD mass spectrum of the ion at m/z 117 obtained from protonated D-glucose was compared to that of a commercial levulinic acid sample (Figure 8). As a result, the fragmentation patterns of the two protonated parent ions are almost superimposable and hence the formation of this product in the gas phase was also demonstrated.

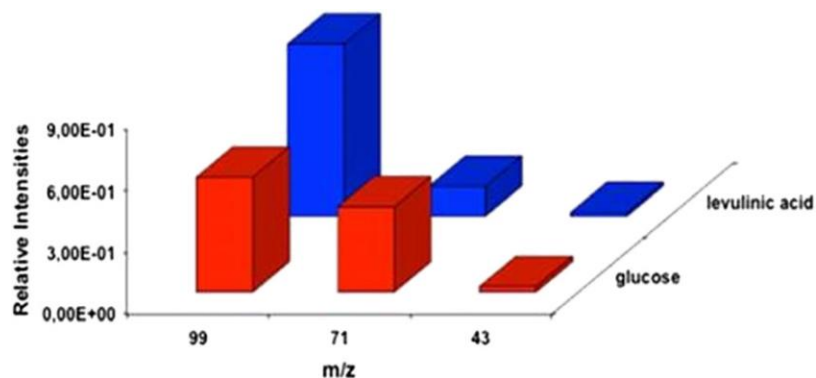


Figure 8: Comparison between the CAD mass spectra of the m/z 117 ion obtained from the m/z 163 D-glucose dehydration intermediate (red bars) and the protonated standard levulinic acid (blue bars).

In order to analyse the differences existing between the two hexose dehydration pathways, Table 2 and 3 report the relative intensities of the fragments arising from protonated D-fructose and D-glucose dehydration intermediate ions at m/z 163 and 145, respectively. CAD mass spectra were recorded at a laboratory collision energy of 15 eV using the same ESI mass spectrometric conditions.

Fragmentation patterns of D-fructose and D-glucose ionic intermediates at m/z 163 are similar, but not completely superimposable. The main differences concern

the relative abundances of the fragment at m/z 145 obtained from the dehydration channel and other minor fragments such as the ion at m/z 103, 101 and 69.

Table 2: CAD mass spectra of the ion at m/z 163 derived from protonated D-fructose and D-glucose. Each reported value was obtained as average of three different analyses with standard deviations of the fragment ion intensities around $\pm 10\%$.

Parent ion (m/z) 163	D-fructose (relative intensity)	D-glucose (relative intensity)
145	22.9	32.0
127	25.3	20.6
117	0.5	2.3
115	4.8	6.8
109	1.4	1.1
103	1.5	4.5
101	6.0	2.5
99	3.2	3.4
97	3.2	3.2
91	0.9	2.1
85	18.9	16.8
73	3.0	3.1
71	1.0	–
69	3.0	1.6
61	1.4	–
57	1.9	–
55	1.1	–

Also the CAD mass spectra of the doubly dehydrated intermediates at m/z 145 highlight slight differences between the two monosaccharides.

Fragmentation channels leading to the ions at m/z 115, 109 and 73 are observed only for D-fructose, whereas a different intensity of the main products at m/z 127 emerges from the reported data.

Table 3: CAD mass spectra of the ion at m/z 145 derived from protonated D-fructose and D-glucose. Each reported value was obtained as average of three different analyses with standard deviations of the fragment ion intensities around $\pm 10\%$.

Parent ion (m/z) 145	D-fructose (relative intensity)	D-glucose (relative intensity)
127	32.5	44.8
115	2.5	–
109	1.4	–
99	4.6	6.0
97	3.5	3.2
85	49.8	41.8
73	1.9	–
69	3.8	4.2

In order to verify the identity of the ion at m/z 127 arising from the dehydration of protonated D-fructose and D-glucose its CAD mass spectrum was compared with that of commercial 5-HMF using the same experimental conditions.

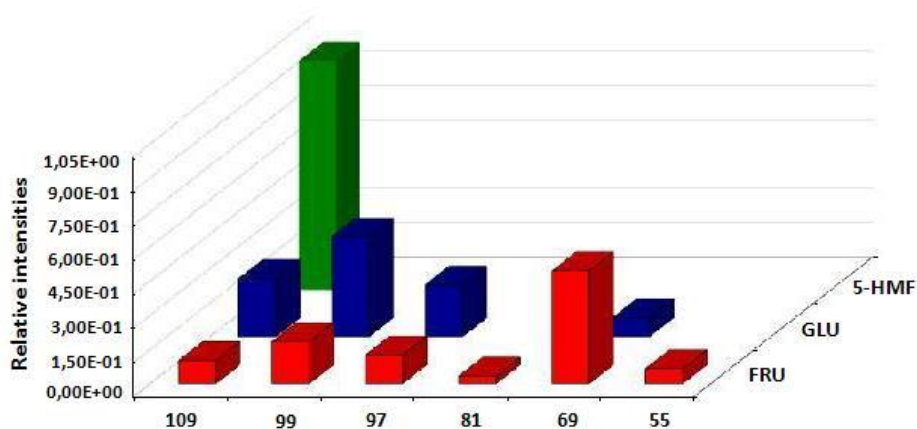


Figure 9: CAD mass spectra of the ions at m/z 127 obtained from the protonation of D-fructose (red bars), D-glucose (blue bars) and standard 5-HMF (green bars) and recorded at collision energy of 15 eV.

Figure 9 shows the comparison between the fragmentation patterns of the ions at m/z 127 obtained from protonation of commercial 5-HMF and the ions at m/z 127 arising from the dehydration of protonated D-fructose and D-glucose, respectively.

The main fragmentation channel of protonated 5-HMF (blue bars) is represented by the ion at m/z 109 corresponding to the loss of a water molecule. Conversely, the CAD mass spectrum of the ion at m/z 127 generated from protonated D-glucose shows other significant fragment ions, as those arising from the loss of CO (ion at m/z 99) and H_2CO (ion at m/z 97). These species are absent in the CAD mass spectrum of standard 5-HMF. In the case of the m/z 127 ions obtained from protonated D-fructose the fragmentation pattern is dominated by the ion at m/z 69 and shows minor fragments at m/z 97 and m/z 99. The intense fragmentation leading to the ion at m/z 69 is peculiar of D-fructose m/z 127 product ion, whereas the relative intensities of the fragment ions at m/z 99 and 97 seem to be comparable to the corresponding fragmentation observed for D-glucose.

These relevant differences demonstrate that in the gas phase protonated 5-HMF does not represent the unique ionic product at m/z 127 obtainable from D-glucose and D-fructose dehydration. It can be hypothesized that different isomers or protomers of 5-HMF are formed.

To probe the possible formation of different 5-HMF protomers, the CAD fragmentation pattern of the ions at m/z 127 obtained from protonation of commercial 5-HMF under chemical ionization (CI) conditions has been analysed. For this purpose, different protonating agents were selected to gradually increase the exothermicity of the protonation process (Figure 10).

Under the soft protonating conditions of the H_3O^+ ions obtained from H_2O/CI (Figure 10 blue bars), the CAD mass spectrum of protonated 5-HMF is comparable with the spectrum recorded under ESI conditions. Gradually increasing the proton transfer exothermicity by using CH_5^+ ions from CH_4/CI (Figure 10 yellow bars) and H_3^+ from H_2/CI (Figure 10 light blue bars) a new fragment ion at m/z 97 is observed. Interestingly, the daughter ions at m/z 99 and m/z 69, observed for the species at m/z 127 obtained under ESI conditions from

the hexose dehydration, are always absent in the CAD spectra of the corresponding species generated under CI conditions from commercial 5-HMF.

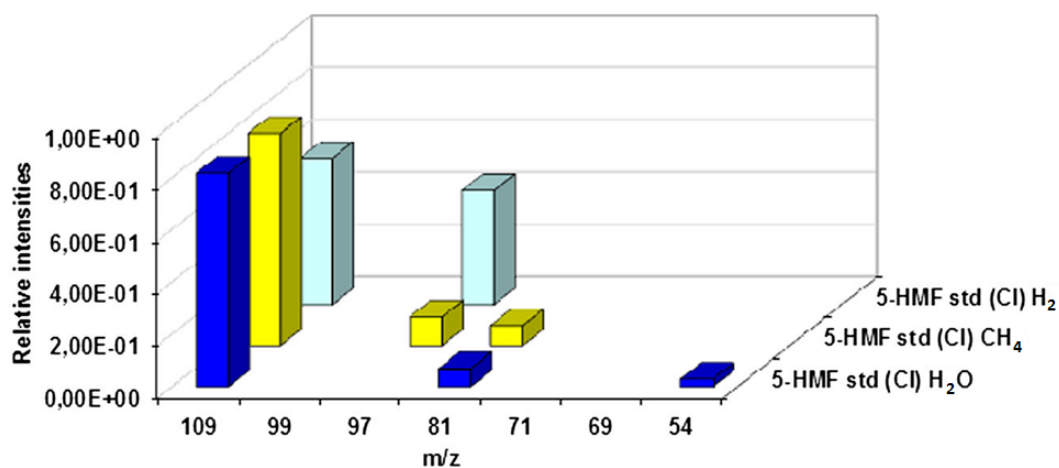


Figure 10: CAD mass spectra of protonated 5-HMF generated from different chemical ionization gases (H_2O ; CH_4 ; H_2O).

Energy-resolved CAD experiments

Triple quadrupole energy-resolved CAD spectra of D-glucose and D-fructose dehydration intermediates allow the relative water loss dissociation energies to be measured.

The measurement of the threshold energy associated to the first water loss was prevented by the low intensity of the protonated ions at m/z 181.

Figure 11 displays the energy-resolved CAD mass spectra of the ions at m/z 163 deriving from protonated D-fructose (panel a) and D-glucose (panel b) recorded at collision energies ranging from 0 to 5 eV (centre-of-mass collision energy).

Focusing on the onset of the cross section curves, the loss of the second water molecule leading to the ion at m/z 145 arises at collision energies close to the nominal centre of mass energy of 0 eV. The dehydration of D-fructose is slightly favoured respect to D-glucose as evidenced by the higher collision cross section measured.

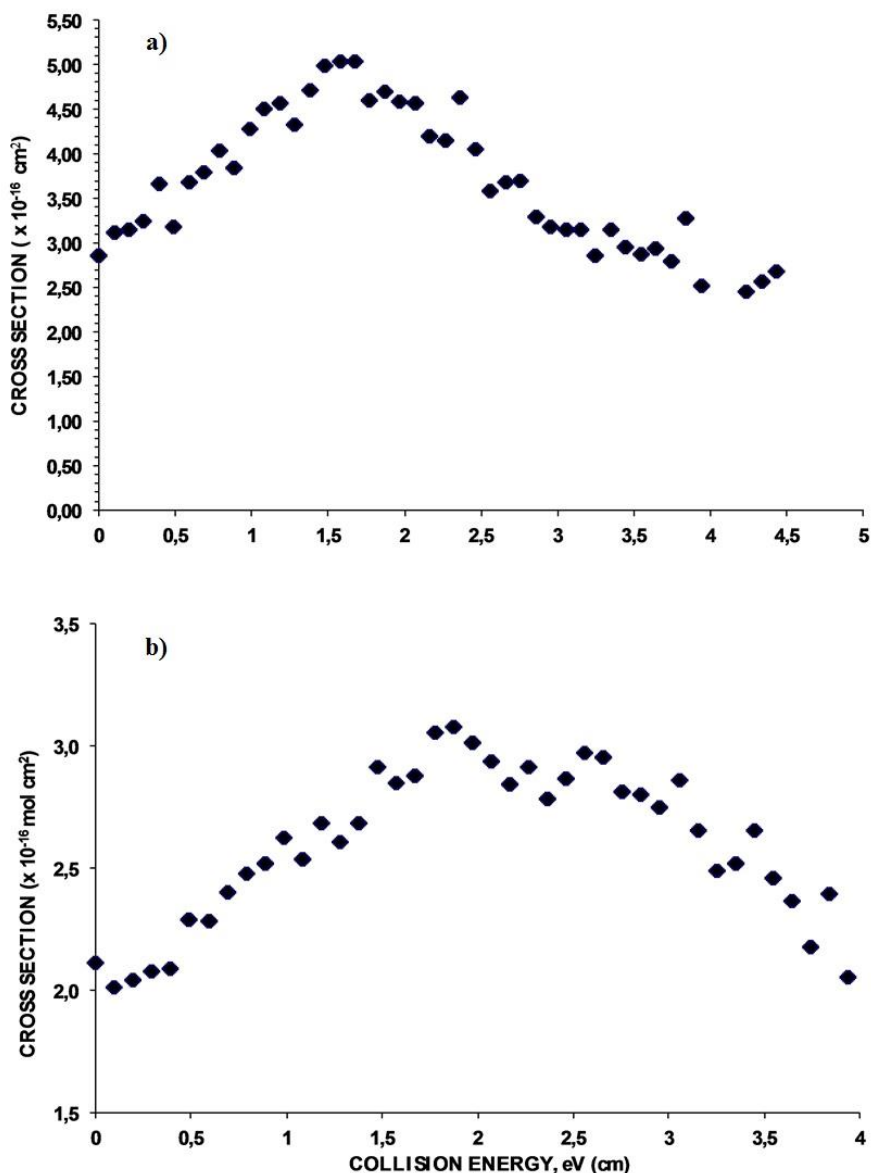


Figure 11: Energy-resolved CAD mass spectra of the ions at m/z 163 obtained from protonated D-fructose a) and protonated D-glucose b). The reported collision cross sections concern only the dehydration reaction leading to the ion at m/z 145.

The energetics of the third water loss from protonated D-fructose and D-glucose was also investigated by the energy-resolved CAD mass spectra of the ions at m/z 145 leading to the product ions at m/z 127 (Figure 12). The third water loss from D-fructose (panel a) and D-glucose (panel b) is also characterized by a threshold energy around 0 eV with the dehydration of D-fructose slightly

favoured respect to that of D-glucose as again evidenced by the higher collision cross section measured.

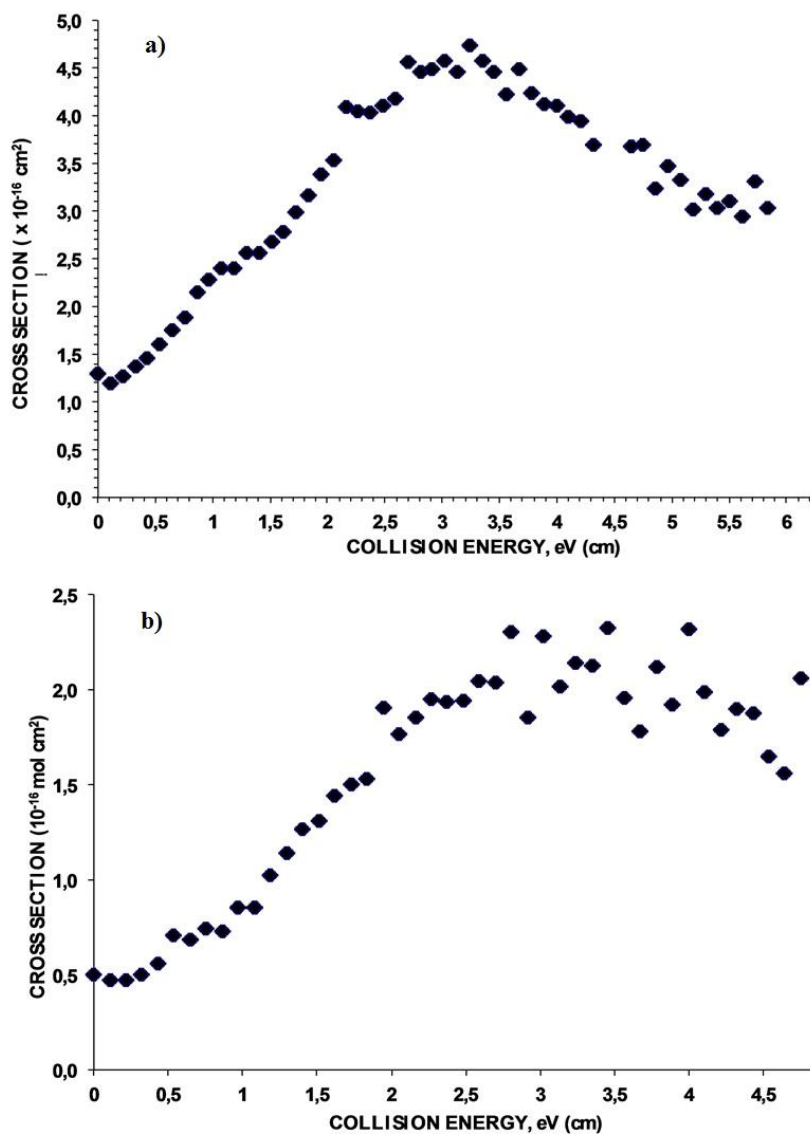
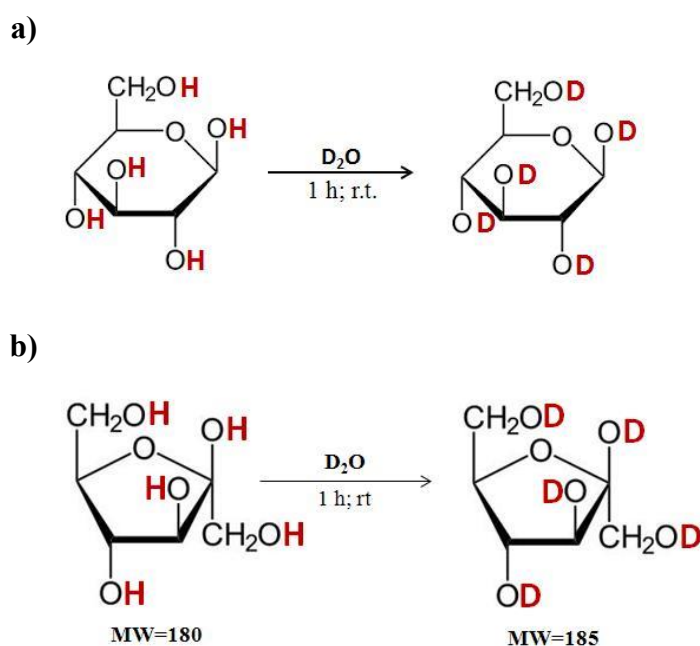


Figure 12: Energy-resolved CAD mass spectra of the ions at m/z 145 obtained from protonated D-fructose a) and protonated D-glucose b). The reported collision cross sections concern only the dehydration reaction leading to the ion at m/z 127.

H/D exchange experiments

Isotopic labelling experiments allow one to obtain additional evidence on the gas phase D-glucose and D-fructose dehydration mechanism.

When the two sugars are dissolved in D₂O at room temperature, the replacement of all the hydrogen atoms of the OH groups with deuterium occurs in several minutes, obtaining the d₅-hexose. (Scheme 10, panels a and b). The deuterated ESI parent ion shifts from m/z 181 to m/z 187



Scheme 10: *D-glucose a) and D-fructose b) H/D exchange reactions.*

This procedure permits to distinguish if the water loss involves the acidic hydrogen atoms bound to the oxygen atoms or the non-acidic hydrogen atoms bound to the carbon-ring.

The product ion mass spectrum of the ion at m/z 187 reports the loss of a D₂O molecule as the main fragmentation channel (Figure 13; panel a) and the same result emerges from the CAD mass spectrum of the ion at m/z 167 where the D₂O loss leads to the fragment ion at m/z 147 (Figure 13; panel b).

On the contrary, the third dehydration step from the ionic intermediate at m/z 147 involves simultaneously the loss of a D₂O and a HDO neutral counterparts

giving rise to the isomeric final products at m/z 127 and 128 (Figure 13; panel c). A superimposable behaviour was observed for both sugars.

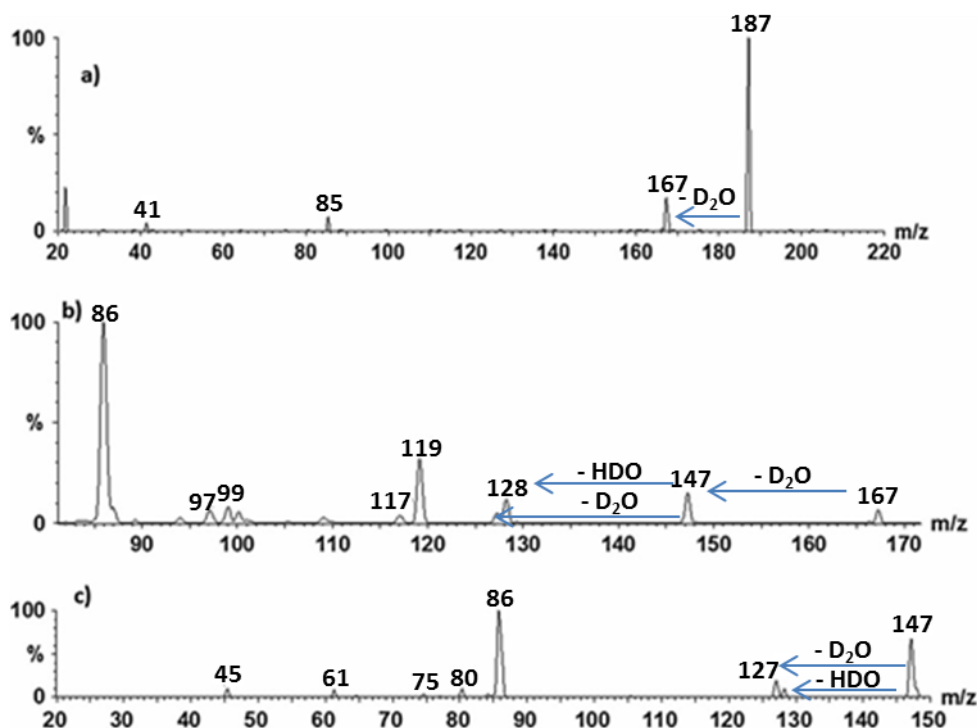


Figure 13: CAD mass spectra of the deuterated ions at m/z 187 a), m/z 167 b), m/z 147 c).

3-O-methyl-D-glucose experiments

In order to validate a feasible D-glucose dehydration mechanism leading to 5-HMF as the main product, the role of an electron-withdrawing group bound at O3 position was investigated. To this end, the ESI mass spectrum of 3-O-methyl-D-glucose was recorded.

As seen before for protonated D-glucose, also in the full-scan spectrum of 3-O-methyl-D-glucose the intensity of the protonated ion at m/z 195 is very low.

Despite the presence of a methyl group at O3 position, the first fragmentation step consists predominantly in a water loss, giving rise to the ion at m/z 177 (Figure 14). On the contrary, the loss of the CH_3OH neutral counterpart from the parent ion at m/z 195 represents a negligible fragmentation channel.

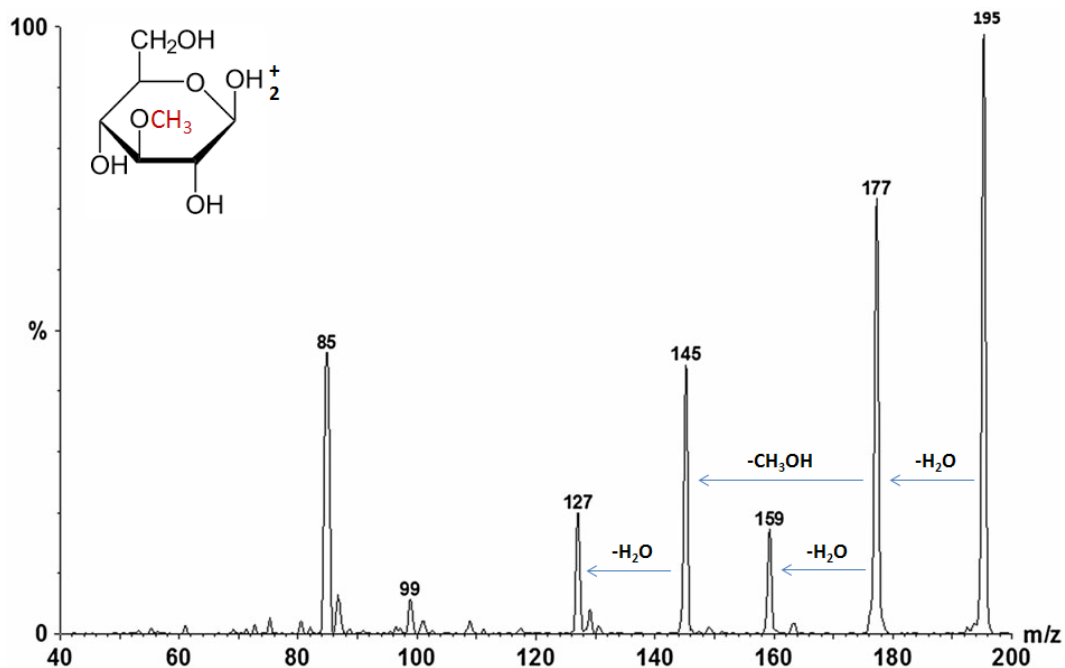


Figure 14: Product ion mass spectrum of the ion at m/z 195, corresponding to protonated 3-O-methyl-D-glucose.

The main fragmentation pathway of the ion at m/z 177 leads to the ionic intermediate at m/z 145 resulting from the loss of methanol, while the ionic species at m/z 159, resulting from the water loss, represents a secondary fragment. Finally, as observed for D-glucose, the loss of the last water molecule gives rise to the ion at m/z 127, also in this case the final product of the dehydration reaction.

The CAD mass spectrum of the ion at m/z 127 was compared to the mass spectra of protonated standard 5-HMF and the ion at m/z 127 arising from the protonated D-glucose dehydration (Figure 15).

As reported in Figure 15, the CAD mass spectrum of the m/z 127 dehydration final product derived from protonated 3-O-methyl-D-glucose (green bars) is more similar to the standard 5-HMF fragmentation pattern (blue bars) than the CAD mass spectrum of the same ion derived from protonated D-glucose (red bars).

As in the case of D-glucose, H/D solution exchange experiments have been performed for 3-O-methyl-D-glucose and the recorded CAD mass spectra show the loss of D₂O, CH₃OD and finally HDO/D₂O as main fragmentation channels.

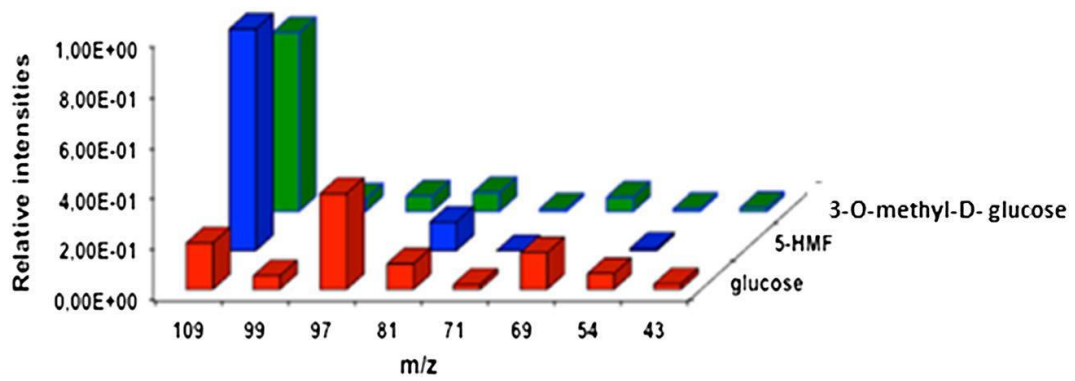


Figure 15: Comparison between the CAD mass spectra of the ion at m/z 127 derived from protonated 3-O-methyl-glucose (green bars), standard 5-HMF (blue bars) and D-glucose (red bars).

2.2 D-fructose base-assisted dehydration

Figure 16 shows the ESI mass spectrum of a D-fructose solution prepared by replacing formic acid with NH_4Cl .

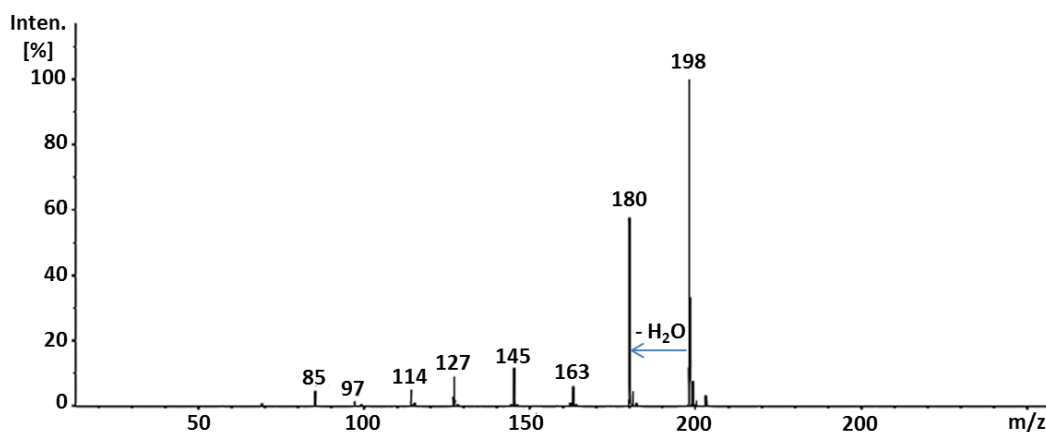


Figure 16: ESI mass scan of a 1×10^{-3} M solution of D-fructose in H_2O (0.1% NH_4Cl)/MeOH 1:1 (V/V).

The ionic population observed under these conditions drastically differs from that observed by using formic acid as a protonating agent. The spectrum is dominated by a peak at m/z 198, corresponding to the ammonium D-fructose adduct ($\text{C}_6\text{H}_{12}\text{O}_6\text{NH}_4^+$), and its dehydrated counterpart at m/z 180. The high NH_4^+ affinity of D-fructose causes a decrease of the intensity of contaminant metal adduct ($\text{C}_6\text{H}_{12}\text{O}_6\text{Na}^+$) reported above for 0.1% HCOOH solutions (Section 2.1, Figure 5, panel a).

Interestingly, ions corresponding to the intermediates (m/z 163 and 145) and product (m/z 127) of the D-fructose dehydration are still present, which points to the possible involvement of the base NH_3 in the activation of the dehydration process. This hypothesis is reinforced by the absence of protonated D-fructose at m/z 181. Indeed, it is reasonable to assume that the low-intensity peak at m/z 181 present in the spectrum corresponds to the ^{13}C -isotope of the ionic species at m/z 180, as confirmed by analysing the 180/181 ratio.

Tandem CAD experiments

After verifying that the ion at m/z 198 represents the precursor of the dehydration product at m/z 180 (Figure 17), the decomposition reaction of the ammonium adduct was followed step-by-step starting from the species at m/z 180 and isolating in turn the resulting ionic intermediates. This is possible by performing a series of *tandem CAD* experiments in an ion trap mass spectrometer.

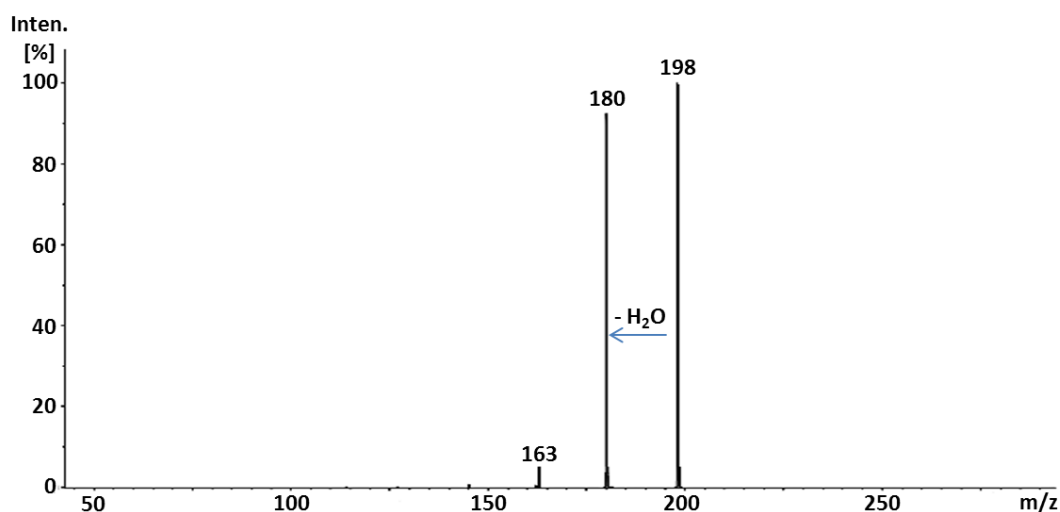


Figure 17: CAD mass spectrum of the ion at m/z 198 recorded at 10 eV collision energy.

The panel a of Figure 18 shows the CAD mass spectrum of the ion at m/z 180 recorded at 10 eV collision energy. Two main fragmentation channels are evidenced. One starts from the loss of the NH_3 neutral counterpart, leading to the ion at m/z 163 that decomposes by releasing in sequence two water molecules (Figure 18; panel b). The opposite occurs with the other one, where first two water molecules and eventually the base are released (Figure 18; panel c). In both cases the final decomposition product is the ion at m/z 127 that should formally correspond to the protonated 5-HMF.

The structure of the ions at m/z 127 alternatively formed by the two different reaction channels was investigated by means of CAD and the resulting mass spectra were compared to that obtained from protonated standard 5-HMF (Figure 19).

As previously observed (Section 2.1), protonated standard 5-HMF mainly decomposes releasing a water molecule, forming a daughter ion at m/z 109 (Figure 19; panel a).

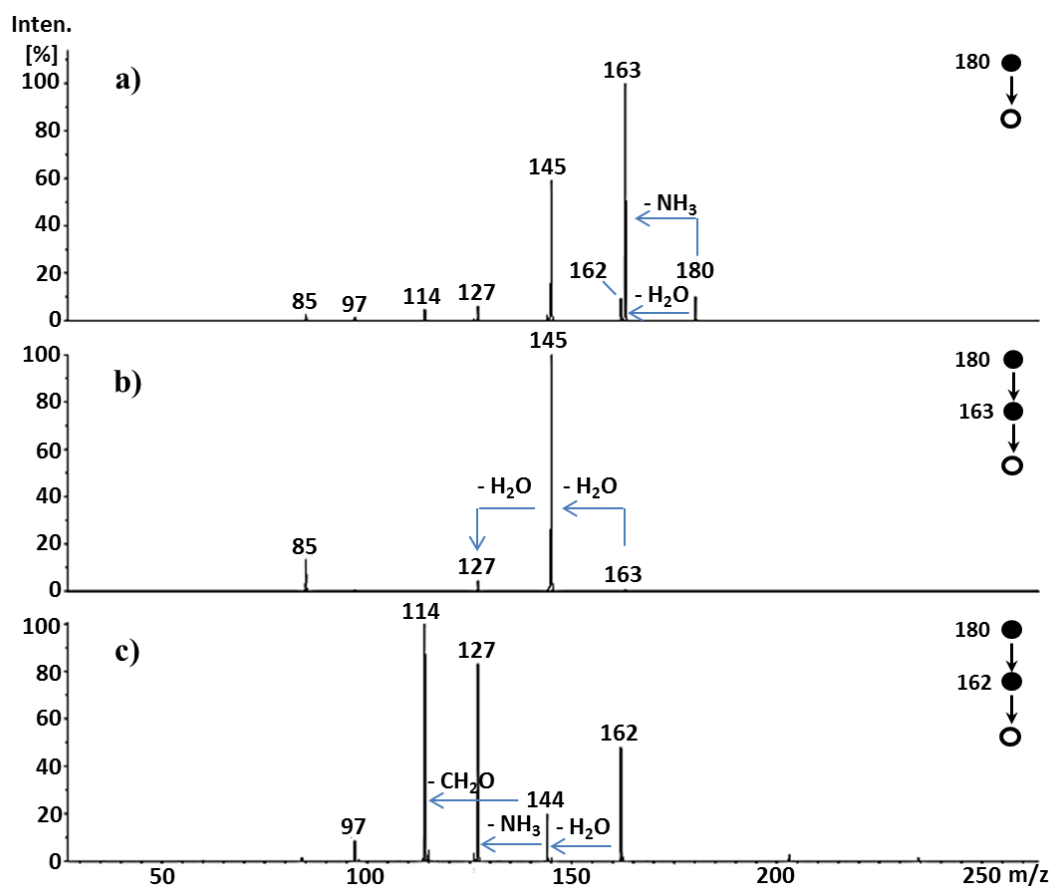


Figure 18: a) CAD mass spectrum of the ion at m/z 180; b) Tandem CAD mass spectrum of the daughter ion at m/z 163 obtained as product of the NH_3 loss from the ionic species at m/z 180; c) Tandem CAD mass spectrum of the daughter ion at m/z 162 obtained as product of the loss of a water molecule from the ionic species at m/z 180. In order to allow the mass spectrum comparison, all CAD experiments were performed by applying a 10 eV collision energy.

When the NH_3 base loss occurs from the first dehydrated intermediate at m/z 180, the $[\text{C}_6\text{H}_6\text{O}_3]\text{H}^+$ ionic population at m/z 127 thus arisen shows a fragmentation pattern completely different from that obtained from protonated standard 5-HMF (Figure 19, panel b). Conversely, when the NH_3 base loss takes place as the last reaction event, the ions at m/z 127 decompose by releasing a water molecule. The CAD mass spectrum thus obtained (Figure 19; panel c) is

perfectly superimposable to that of protonated 5-HMF, highlighting the key role played by the base in the dehydration process.

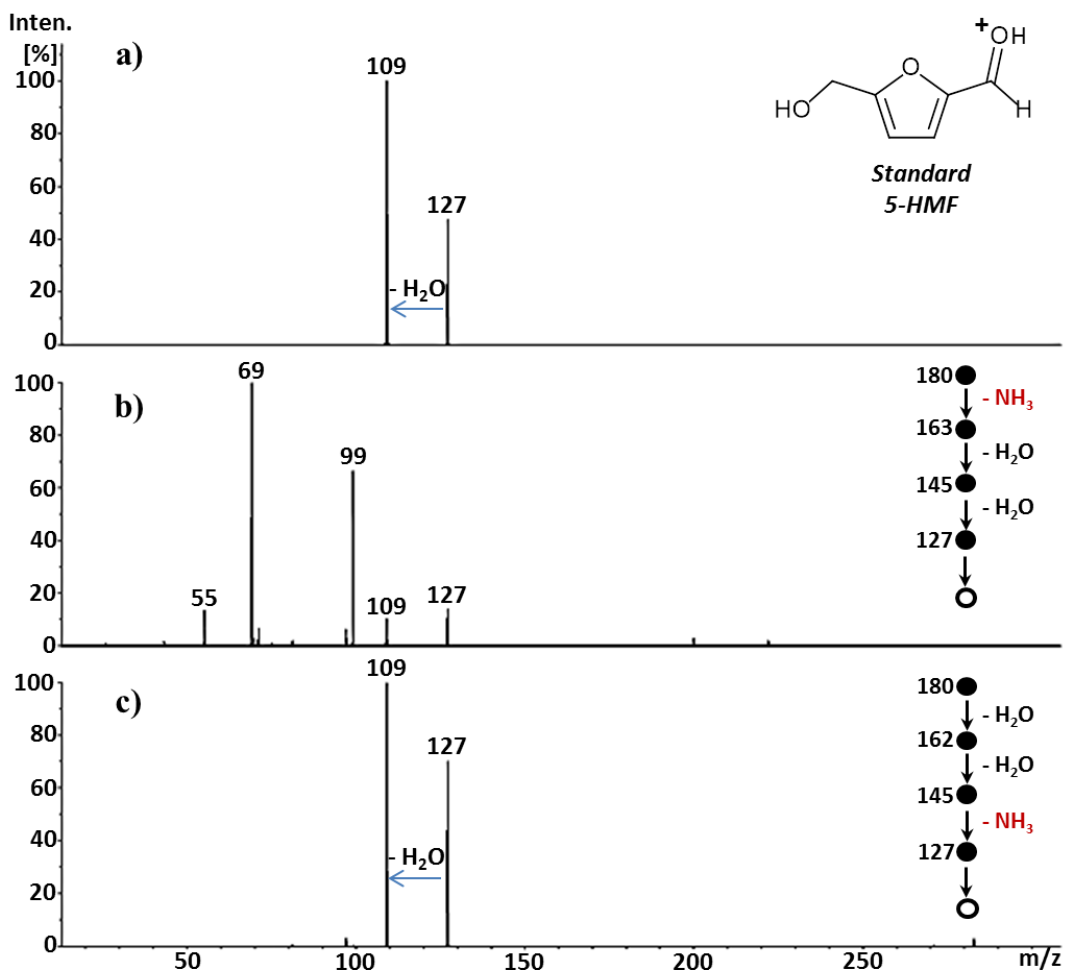


Figure 19: CAD mass spectra of a) protonated standard 5-HMF, b) ions at m/z 127 obtained after a premature base loss and c) ions at m/z 127 arising when the base loss occurs as the last reaction event. In order to allow the mass spectrum comparison, all CAD experiments were performed by applying a 10 eV collision energy.

An alternative decomposition pathway consists in the loss of a CH_2O neutral counterpart occurring after the dehydration of the intermediate at m/z 162, as reported in the panel c of Figure 18. The ionic product at m/z 114 derived from this deformylation process formally corresponds to the adduct between NH_4^+ and 2-furaldehyde (2-FA). The identity of this ionic complex was confirmed by comparing the CAD mass spectrum of the isolated ion at m/z 114 to the CAD

mass spectrum of the corresponding ionic species obtained from a solution of standard 2-FA added with NH_4Cl (Figure 20). Indeed, the strict match between the two CAD spectra confirms the attribution of the ionic species at m/z 114.

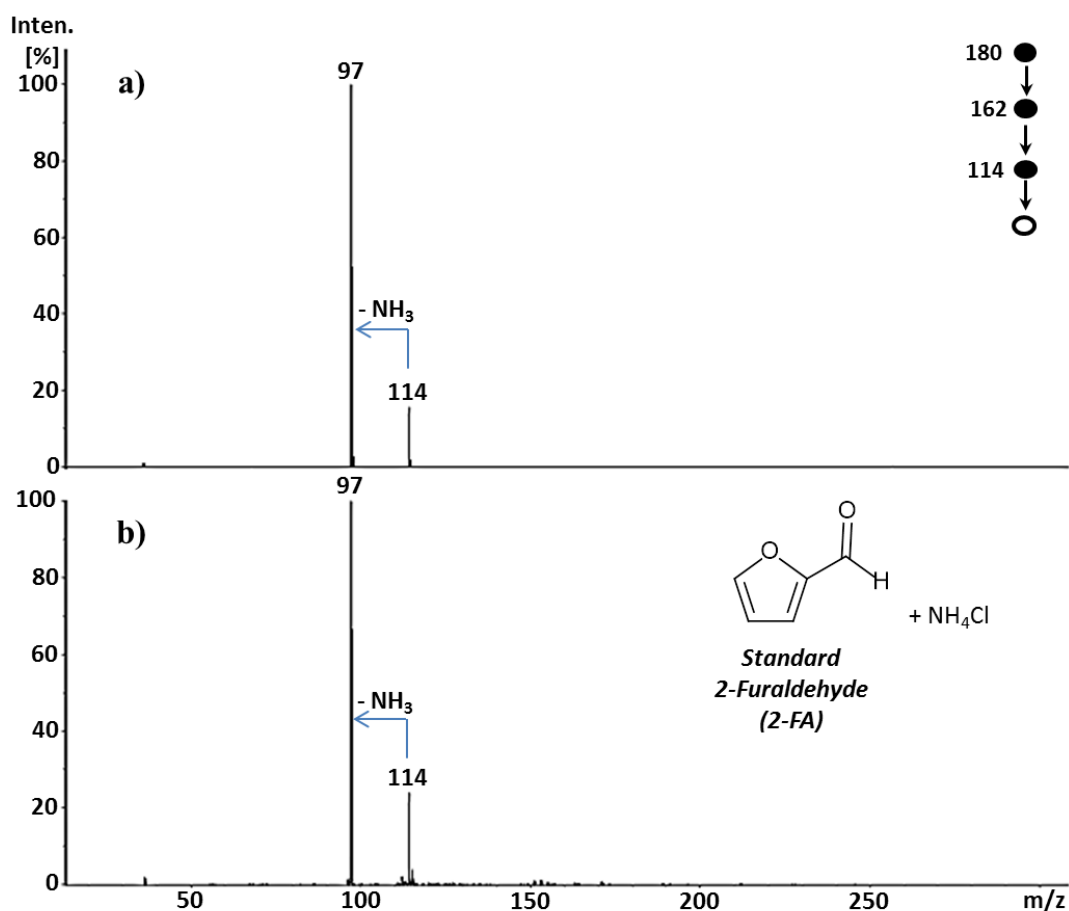


Figure 20: CAD mass spectra of a) daughter ion at m/z 114 obtained from the fragmentation of the dehydration intermediate at m/z 162, b) standard 2-FA ammonium adduct. In order to allow the mass spectrum comparison, all CAD experiments were performed by applying a 10 eV collision energy.

Isotopic labelling experiments

In order to acquire more information about the deformylation mechanism, ^{13}C -labelled D-fructose was analysed by ESI tandem mass spectrometry. As a result of the isotopic labelling on C1, the m/z ratio of the ammonium D-fructose adduct

shifts from 198 to 199. Consequently, the m/z ratio of the doubly dehydrated intermediate (the dehydration/deformylation precursor ion) shifts from 162 to 163.

As displayed in Figure 21 the loss of the CH_2O neutral counterpart does not involve the $^{13}\text{C}1$ that is still present in the 2-FA molecular skeleton. Accordingly, the deformylation reaction is probably obtained by rearrangement of the methylenhydroxyl group bound at C5.

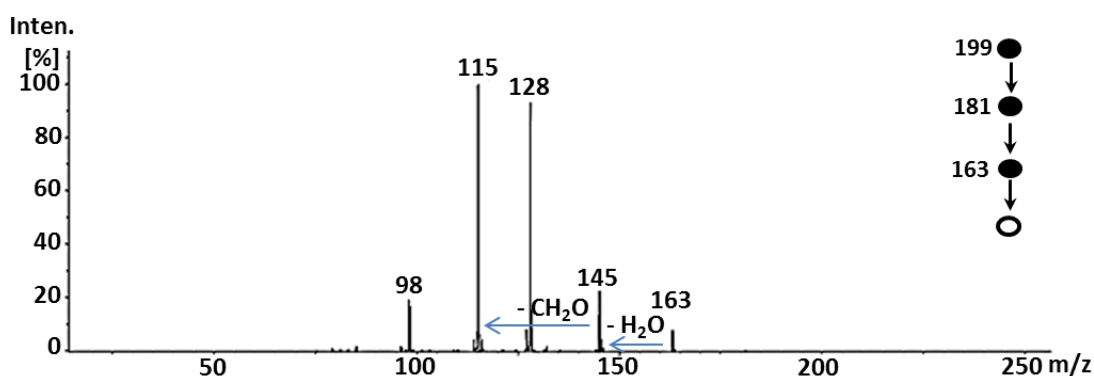


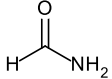
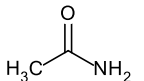
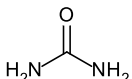
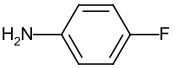
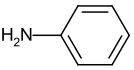
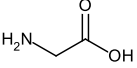
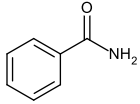
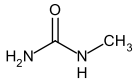
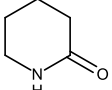
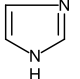
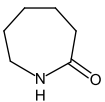
Figure 21: Tandem CAD mass spectrum of the daughter ion at m/z 163 obtained as ionic product of the two water molecule loss from the ammonium $^{13}\text{C}1$ -D-fructose adduct at m/z 199.

Base replacement experiments

The possibility to generalize the decomposition pathways experimentally found for the ammonium D-fructose adduct was evaluated by replacing NH_4^+ with the conjugate acid of a series of nitrogen-containing bases (Table 4).

Considering that an efficient formation of 5-HMF has been recently obtained in solution from fructose dehydration by developing a caprolactam hydrogen sulphate ionic liquid catalyst,^[58] a set of bases structurally related to caprolactam (12) was chosen. In particular, bases 2-4 and 8-10 show an amidic group whereas bases 5,6,8 and 10,11 are characterized by a cyclic structure. Moreover, all these compounds have proton affinity values in the range of $196.5 \text{ kcal mol}^{-1}$ (base 2) to $225.3 \text{ kcal mol}^{-1}$ (base 11).

Table 4: List of nitrogen-containing bases employed as complexation agent. The proton affinity values are available on <http://webbook.nist.gov/chemistry/>. *Ref.[59].

	Base	Chemical Structure	Molecular weight	Proton affinity (kcal mol^{-1})
1	Ammonia	NH_3	17	204
2	Formamide		45	196.5
3	Acetamide		59	206.4
4	Urea		60	208
5	p-F-aniline		111	208.1
6	Aniline		93	210.9
7	Glycine		75	211.9
8	Benzamide		121	213.2
9	Methylurea		74	213.4
10	δ -Valerolactam		99	218.6*
11	Imidazole		68	225.3
12	ϵ -Caprolactam		113	n.d.

When bases 1-4 are employed as complexation agent, the corresponding ionic adduct, schematically represented as $[\text{C}_6\text{H}_{12}\text{O}_6\text{-H-B}]^+$, follows the same decomposition routes previously observed for the ammonium complex. On the other hand, when a base from 5 to 12 is chosen to form the precursor adduct, only the first dehydration reaction occurs according to the CAD mass spectrum shown

in Figure 22. In this case, the main fragmentation channel consists in the loss of D-fructose as neutral counterpart and the protonated base as the charged product.

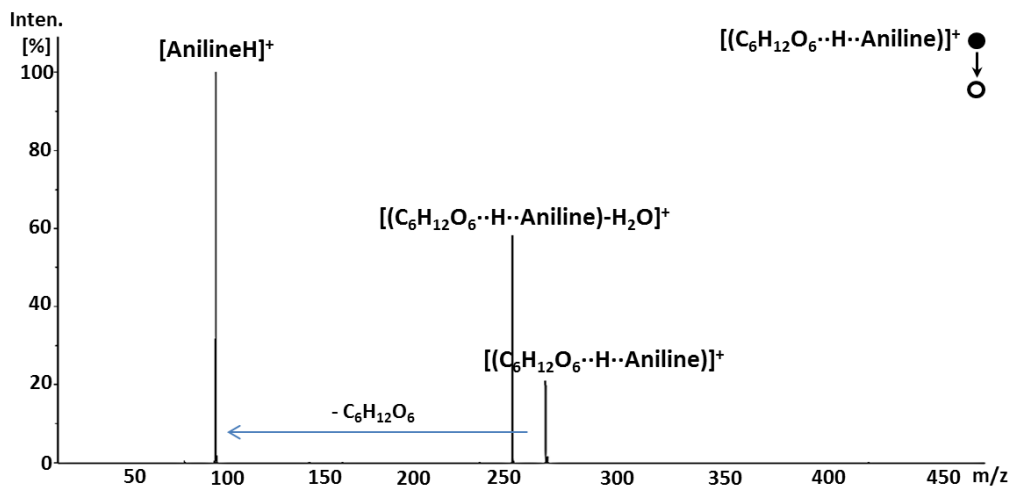


Figure 22: CAD mass spectrum of the ionic adduct $[C_6H_{12}O_6\cdot H\cdot Aniline]^+$ recorded at collision energy of 15 eV.

2.3 Pentose acid-catalysed dehydration

Figure 23 (panels a-c) displays the full scan mass spectra of D-xylose, D-ribose and D-arabinose 10^{-3} solutions.

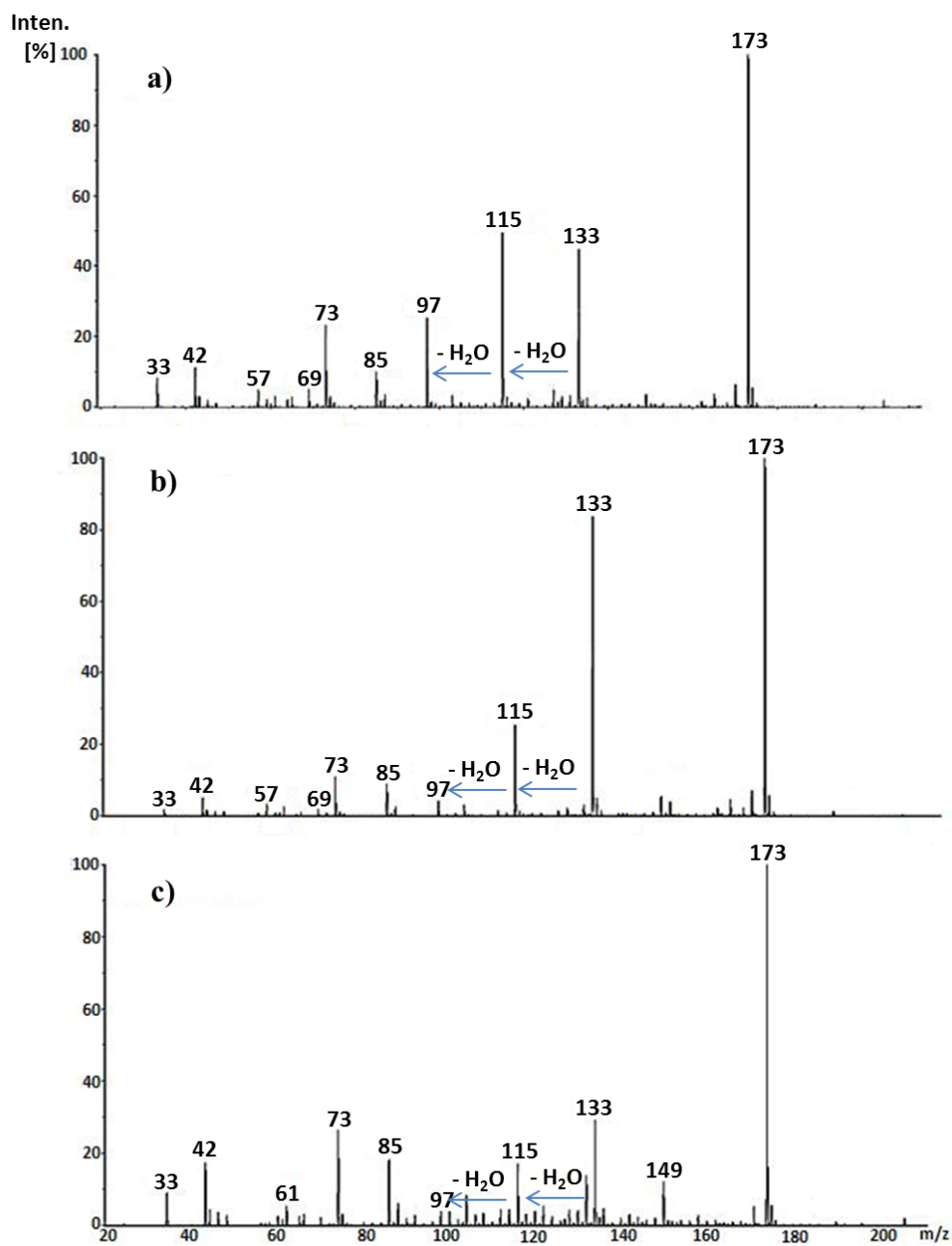


Figure 23: Positive ion ESI-MS spectra of H_2O (0.1% $HCOOH$)/ CH_3OH (1:1, V/V) solutions of D-xylose a), D-ribose b), D-arabinose c).

All spectra are characterized by several ions generally observed in monosaccharide samples and by a dominant peak at m/z 173 corresponding to the sodium-pentose adduct. Protonated pentose sugars at m/z 151 are present at lower intensities than the ions at m/z 133, m/z 115 and 97. These ionic species correspond to the intermediates and the final product of pentose dehydration reactions.

CAD experiments

Since the ion trap instrumentation allows one to perform MS^n experiments, selected precursor ions were submitted to tandem CAD in order to follow, step by step, the dehydration process.

The extremely low intensity of the ion at m/z 151 does not allow us to perform MS^n experiments that start from this ion and go to the final product. Nonetheless, its CAD mass spectrum confirms that it is the precursor of the m/z 133 intermediate, arising from the first water loss (Figure 24). The reported spectrum is a representative example for all the three monosaccharides.

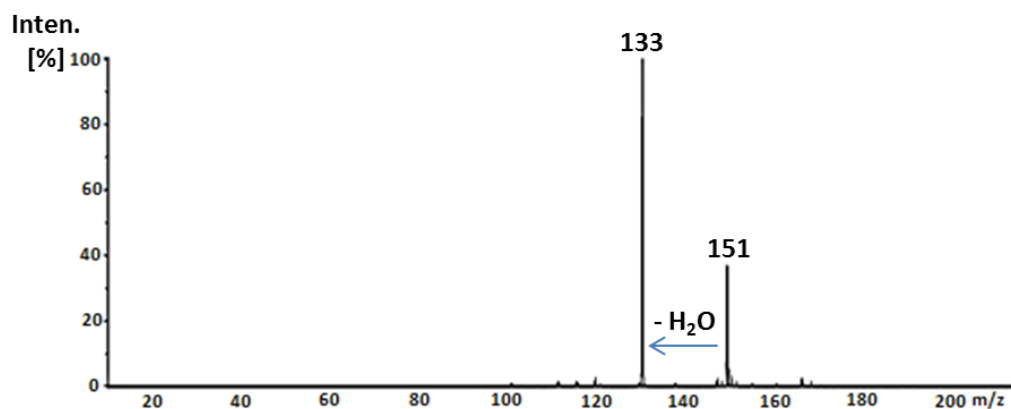


Figure 24: CAD mass spectrum of the ion at m/z 151 corresponding to the protonated pentoses.

Since the subsequent isolation of the ion at m/z 133 was prevented by its low intensity, the m/z 133 intermediate generated in the source was chosen as the MS^n precursor ion. The spectra recorded for the species at m/z 133 coming from D-

ribose are reported in Figure 25 (panels a and b), whereas the corresponding data for D-xyllose and D-arabinose are not shown since they give similar results.

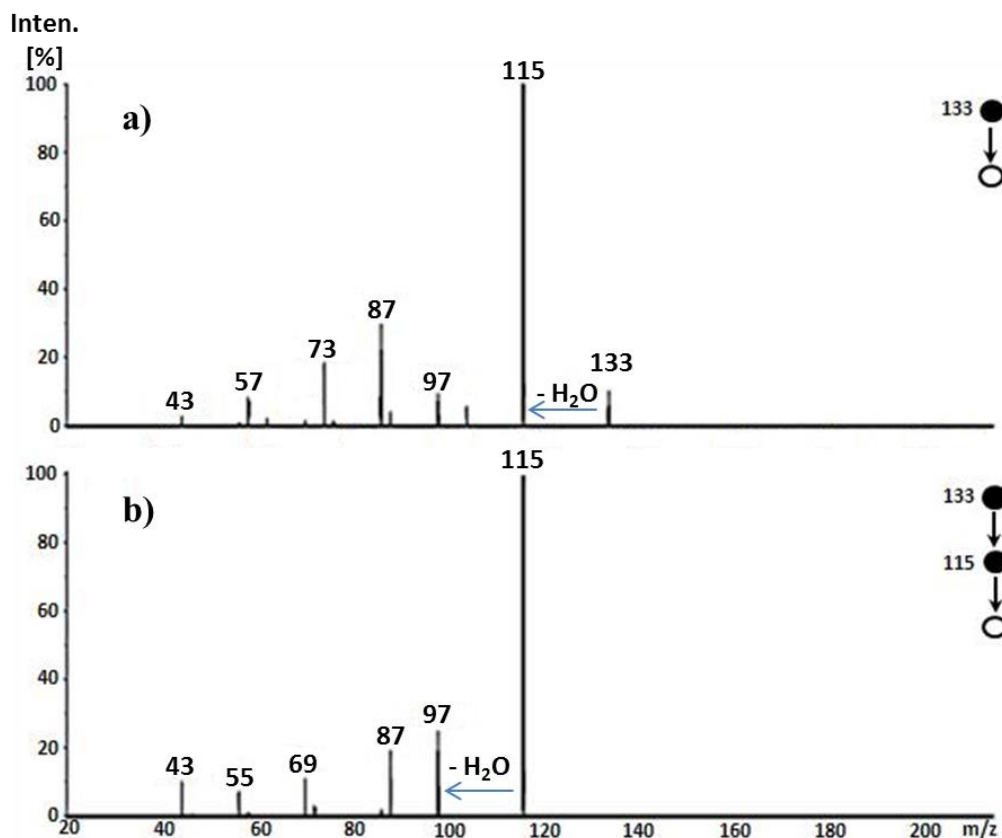


Figure 25: *D-ribose* MSⁿ spectra of the ion at m/z 133 a) and its product ion at m/z 115 b).

As shown, the first spectrum (Figure 25, panel a) is dominated by the ion at m/z 115, arising from a water loss from the parent ion at m/z 133. This confirms that the dehydration process represents the main fragmentation channel. The product ion at m/z 115, obtained from the m/z 133 intermediate, was in turn isolated. It mainly decomposes into the ion at m/z 97 (Figure 25, panel b), again arising from the loss of a water molecule. All these results show that the consecutive loss of three water molecules from the ion at m/z 151 leads to the formation of the ion at m/z 97 as the final dehydration product. Its MSⁿ CAD mass spectrum recorded from the parent ion at m/z 133 is reported in Figure 26 and results perfectly superimposable to the CAD spectrum obtained from a

standard sample of protonated 2-furaldehyde (2-FA), as also reported in a previous study undertaken in our laboratories.^[60]

Triple quadrupole CAD mass spectrometry was used to investigate the structure of the pentose dehydration intermediates and products generated in the ESI source.

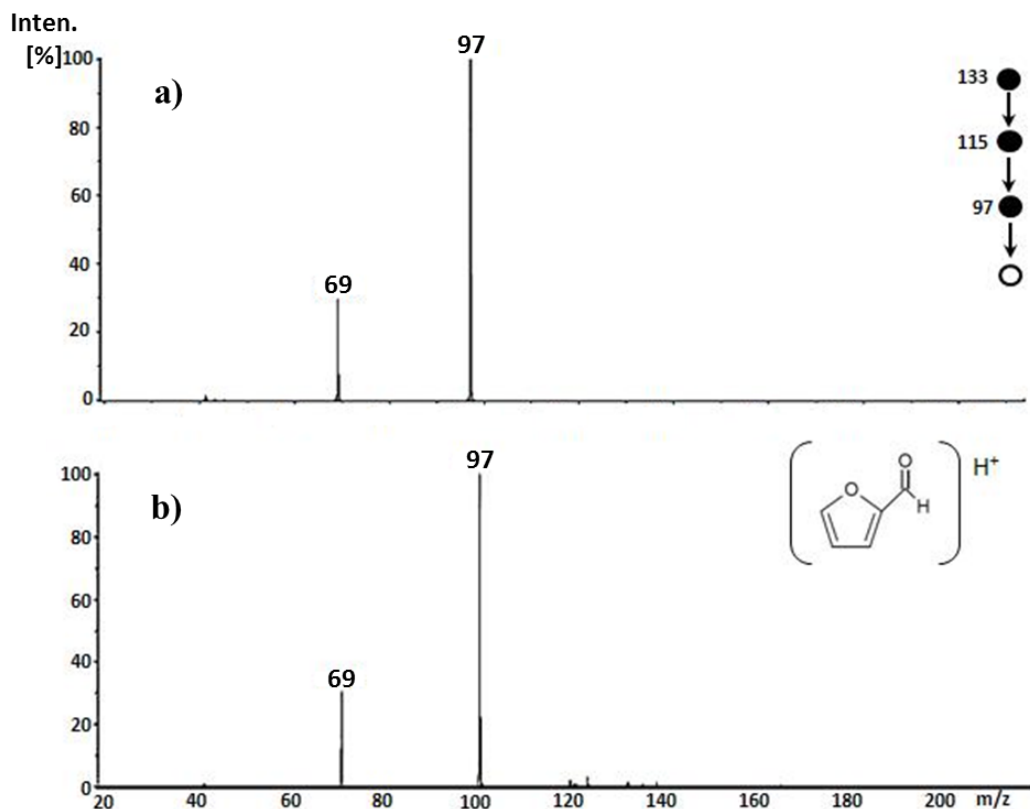


Figure 26: Comparison between the MSⁿ CAD mass spectrum of the ion at m/z 97 obtained from pentose dehydration reactions a) and the CAD mass spectrum of the protonated standard 2-furaldehyde sample b).

Tables 5, 6 and 7 show the data extrapolated from the triple quadrupole CAD spectra of the ion at m/z 133, m/z 115 and m/z 97 deriving from the decomposition of protonated D-ribose, D-arabinose and D-xylose. The product ion relative intensities were obtained from the average of three different CAD experiments at nominal collision energy of 10 eV (laboratory frame).

The pentose isomeric ions at m/z 133 and m/z 115 show the same fragmentation products, with small differences in the relative abundances of some

fragment ions. CAD mass spectra of monohydrate ions at m/z 133 mainly differ in the relative intensities of the daughter ions at m/z 73, 57 and 55 (Table 5). Conversely, the fragment ions at m/z 97, 85, 69 and 55 arising from the intermediate at m/z 115 (Table 6) show relative intensities quite similar only between D-ribose and D-arabinose.

Finally, the fragmentation patterns obtained from the ions at m/z 97 reported in Table 7 are almost superimposable. This evidence confirms the MS^n experiment results, demonstrating that the three sugars dehydrate leading to the formation of the same final compound corresponding to protonated 2-furaldehyde.

Table 5: CAD mass spectra of the ion at m/z 133 derived from protonated D-arabinose, D-ribose and D-xylose. Each reported value was obtained as average of three different analyses with standard deviations of the fragment ion intensities around $\pm 10\%$.

Parent ion (m/z) 133	D-arabinose (relative intensity)	D-ribose (relative intensity)	D-xylose (relative intensity)
115	2.9	3.4	2.5
97	2.1	4.1	3.4
87	1.6	2.1	1.3
85	6.5	8.3	8.0
73	50.8	29.5	40.0
71	1.1	4.0	1.7
69	5.3	9.3	7.6
61	5.3	4.6	4.0
59	3.7	4.6	1.6
57	11.8	15.1	26.2
55	4.8	9.5	0.8
45	2.1	1.8	1.7
43	1.6	2.8	0.8
41	0.5	0.9	0.4

Table 6: CAD mass spectra of the ion at m/z 115 derived from protonated D-arabinose, D-ribose and D-xylose. Each reported value was obtained as average of three different analyses with standard deviations of the fragment ion intensities around $\pm 10\%$.

Parent ion (m/z) 115	D-arabinose (relative intensity)	D-ribose (relative intensity)	D-xylose (relative intensity)
97	7.7	7.8	13.7
87	9.3	4.3	6.4
85	20.9	13.5	23.7
73	0.7	0.6	1.1
71	4.2	8.7	3.3
69	18.5	15.5	26.6
59	1.5	2.0	1.7
57	12.1	14.5	10.7
55	20.3	27.4	7.0
43	2.4	3.1	1.9
41	2.4	2.6	3.9

Table 7: CAD mass spectra of the ion at m/z 97 derived from protonated D-arabinose, D-ribose and D-xylose. Each reported value was obtained as average of three different analyses with standard deviations of the fragment ion intensities around $\pm 10\%$.

Parent ion (m/z) 97	D-arabinose (relative intensity)	D-ribose (relative intensity)	D-xylose (relative intensity)
71	3.2	5.3	2.1
69	51.4	50.8	52.5
55	2.2	1.6	1.2
43	5.1	4.8	3.1
41	38.1	37.5	40.1

Energy resolved CAD mass spectra (ERMS)

Triple quadrupole energy resolved CAD spectra of the ions at m/z 133 and m/z 115 allow one to measure the water loss dissociation energies of the pentose sugars to be used as relative values to compare the dehydration behaviour of the three monosaccharides. Also in this case, the very low intensity of the protonated ions at m/z 151, due to the prompt dehydration under the ESI source conditions, prevented us from recording the energy resolved CAD mass spectra. As a consequence, the first dehydration energetic barrier cannot be measured. Figure 27 reports the energy-resolved product ion mass spectra of the ions at m/z 133, arising from protonated D-ribose and D-arabinose recorded at collision energies ranging from 0 to 3.8 eV (centre-of-mass).

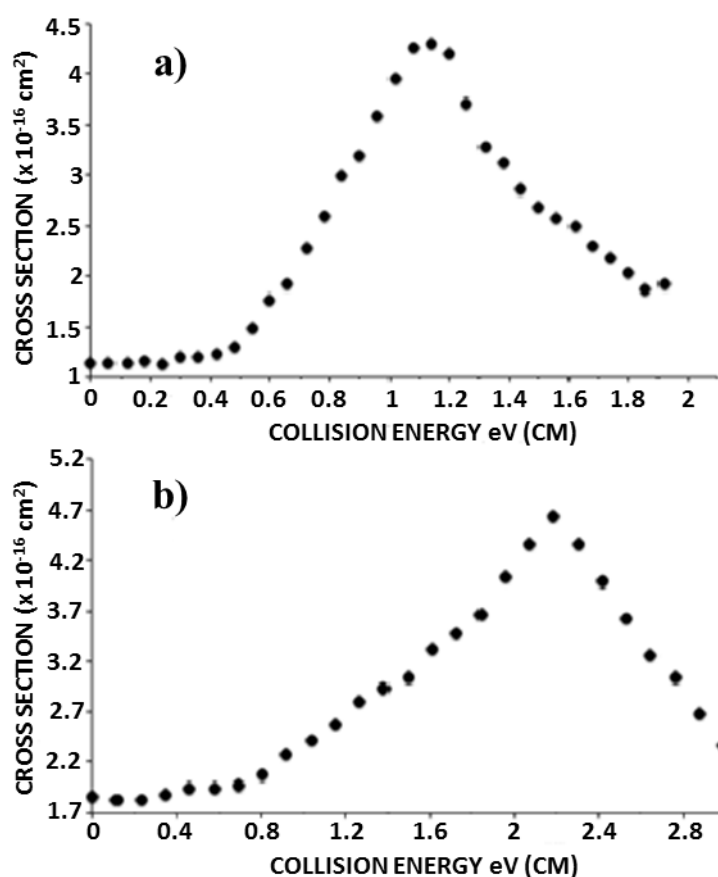


Figure 27: D-ribose a) and D-arabinose b) energy resolved CAD mass spectra of the ions at m/z 133 leading to the intermediate at m/z 115.

The dehydration reaction leading to the ion at m/z 115 is characterized by threshold energies of about 0.4 for D-ribose and 0.8 eV for D-arabinose.

Interestingly, in a previous work^[60] the same dehydration channel relevant to D-xylose was found to be characterized by a threshold energy around 0 eV, which indicates a lower dehydration barrier for the loss of the second water molecule from protonated D-xylose with respect to the other two pentoses.

The loss of the third water molecule (Figure 28) seems to be slightly easier in the case of D-arabinose, but in the range of 1.0-1.1 eV for both the sugars. These values are in agreement with the threshold energy reported for the loss of the third water molecule from D-xylose.^[60]

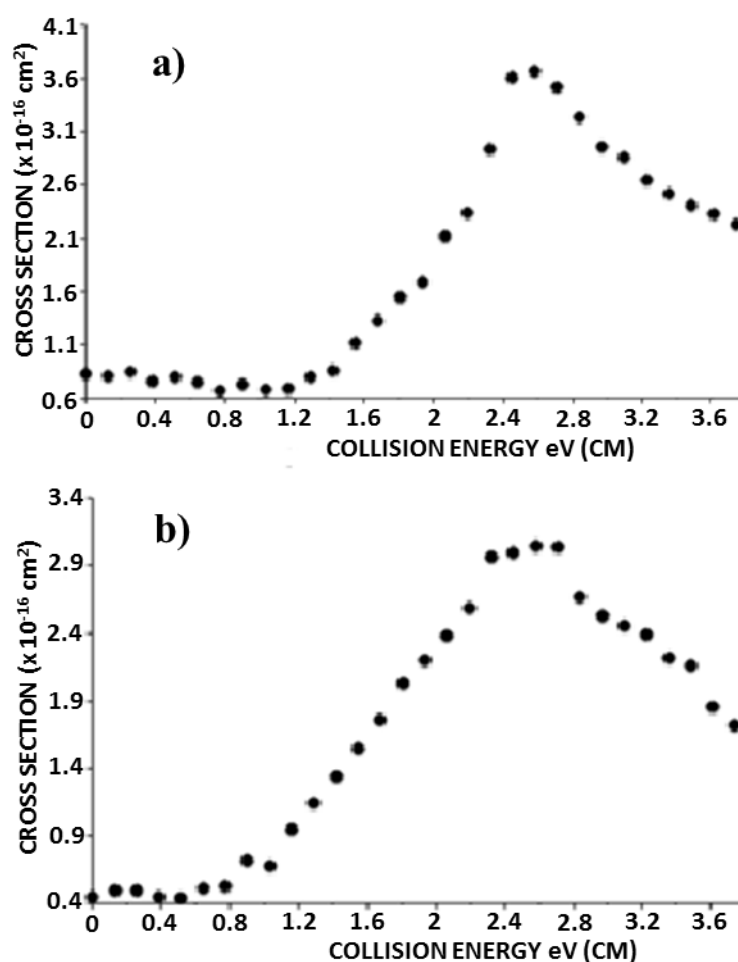


Figure 28: D-ribose a) and D-arabinose b) energy resolved CAD mass spectra of the ions at m/z 115 leading to the final dehydration product at m/z 97.

Theoretical calculations

Computational studies were performed in order to clarify the dehydration mechanisms of protonated pentoses.

The first dehydration step following protonation on C1-OH moiety of D-xylose was preliminarily investigated by means of Carlo Parrinello quantum molecular dynamics simulations, and then by M11/6-311++G(2d,2p) minimized conformations.

Both approaches have evidenced that protonated α and β -pyranose forms of the sugar easily evolve into a more stable loosely bound water cluster. As an example, protonated D-xylose optimized water cluster is more stable than both α and β -pyranose forms by about 10.0 kcal mol⁻¹. An “all equatorial” conformation characterizes the hydroxyl groups in the protonated β -D-xylopyranose minimum structure, whereas the minimization due to the “all axial” conformation leads to the water removal. Hence, the protonated species obtained from the three investigated sugars evolve to water adducts as the protonated hydroxyl group on the anomeric carbon is in the axial position. According to the experimental evidence, theoretical results confirmed the scarce stability of the protonated pentose ions at m/z 151, characterized by a weakly bound water cluster structure. Indeed, C1-OH protonated species lose the first water molecule through a barrierless process assisted by the emiacetalic oxygen lone pair, which gives to O5-C1 a partial double bond character (bond length = 1.24 Å).

The first dehydration step generates an oxonium ion **B** corresponding to the ionic intermediate at m/z 133 observed in the ESI mass spectra. Figure 29 displays the calculated geometry of D-xylose oxonium ion **B**, denoted as **Bx**, as well as those obtained for dehydrated intermediates, transition states and final product.

The reaction pathways starting from these species are summarized in the potential energy surfaces (PES) depicted in Figure 30.

After the first dehydration event, the oxonium ion **Bx** undergoes isomerization in the bicyclic ion **Cx** through the nucleophilic attack of the O4 oxygen to the C1 anomeric carbon. This process is characterized by an energy barrier of 6.9 kcal mol⁻¹ and the isomerization reaction was confirmed by CPMD simulations.

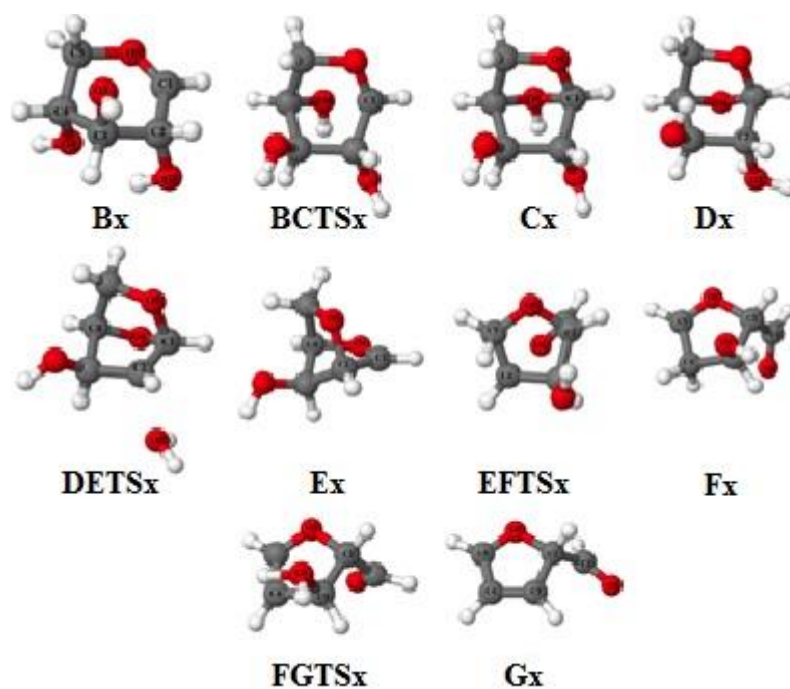


Figure 29: 3D geometry of dehydrated intermediates, transition states and final product obtained from protonated D-xylose dehydration calculated at the M11/6-311++G(2d,2p) level of theory.

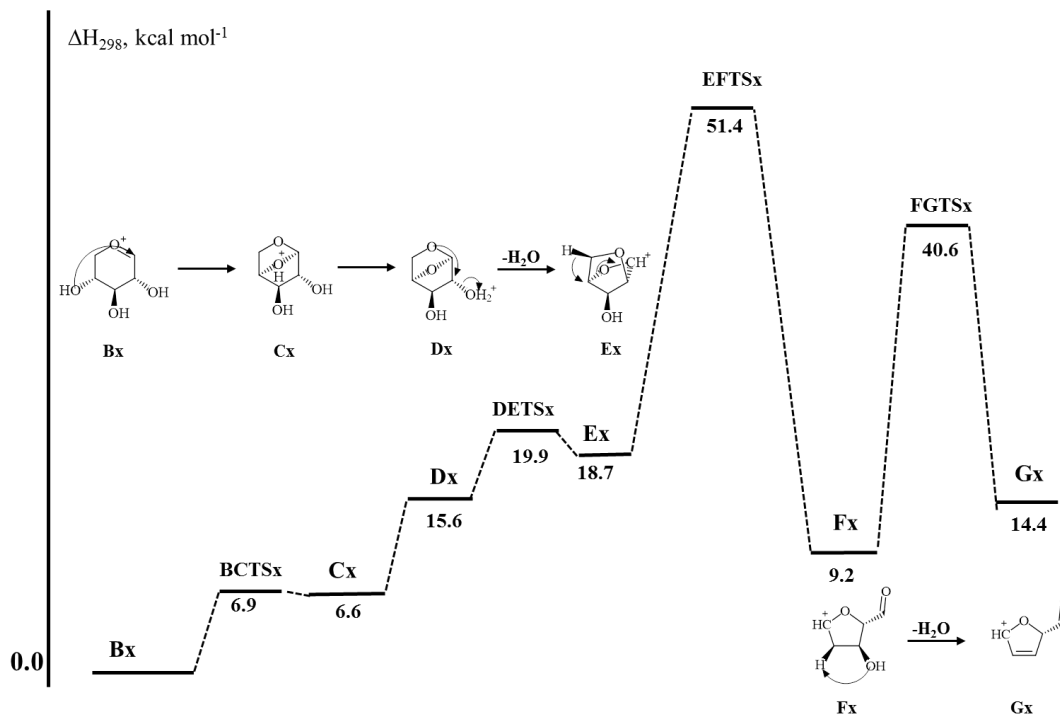


Figure 30: Potential energy surfaces and reaction pathway of the unimolecular conversion of C1-OH protonated D-xylose. The ΔH_{298} energies of minima and transition states were calculated at the CCSD(T)/cc-pVTZ//M11/6-311++G(2d,2p) level of theory.

A proton shift from O4 to O2 leads to the formation of the ion **Dx** that is 9.0 kcal mol⁻¹ less stable than **Cx**. NMR in situ spectroscopy of fructose acidic solutions^[61] has recently demonstrated the existence of neutral intermediates characterized by a bicyclic structure similar to **Cx** and **Dx**.

The emiacetalic O5 oxygen assists a ring contraction leading to the loss of the second water molecule from **C2** and the formation of the intermediate **Ex**.

The imaginary frequency inspection has indicated that transition state **DETSx** is characterized by the simultaneous C2-O2 bond breakage and O5 transposition on C2. Starting from the oxonium ion **Bx** the overall barrier relating to the loss of the second water molecule is calculated to be 19.9 kcal mol⁻¹, a lower value than that previously reported for the dehydration pathway that starts from C1-OH protonation (39.3 kcal mol⁻¹).^[38]

The calculated 19.9 kcal mol⁻¹ energy barrier does not agree with the experimental threshold energy of about 0 eV previously reported.^[60] The discrepancy between experimental and theoretically calculated barriers for the second water loss of D-xylose could be explained by assuming that the starting reactant ions at m/z 133 are characterized by the **Cx** structure. The oxonium ion **Bx**, excited by the ESI ionization process, could isomerize to the ionic species **Cx** through a process that is characterized by a barrier of only 6.9 kcal mol⁻¹. Even if this species is not trapped in a deep potential well and can back isomerize into the ion **Bx**, its possible existence in the m/z 133 ionic population cannot be excluded. The overall energy required for the second water loss starting from **Cx** is only 13.3 kcal mol⁻¹, an internal energy that can be reasonably owned by the ions transmitted in the triple quadrupole mass spectrometer at nominal collision energy of 0 eV, and moreover correctly lower than that measured for D-ribose in the ERMS spectrum.

The bicyclic ion **Ex**, corresponding to the ionic intermediate at m/z 115, evolves to the five terms carbocation **Fx** by breaking the bridged C4-O4 bond. This rearrangement is assisted by an hydride shift from C5 to C4. The lone pair of the adjacent heterocyclic oxygen atom stabilizes the carbocation **Fx** and the barrier of the entire process is estimated to be 32.7 kcal mol⁻¹.

Finally, the last water molecule is released from **Fx** as a consequence of the vicinal proton abstraction by the C3-OH group from C4 and characterized by a barrier of 31.4 kcal mol⁻¹. Hence, the overall energy required for the third dehydration from the ionic species **Ex** is 32.7 kcal mol⁻¹.

Regarding protonated D-ribose dehydration, the geometries identified for intermediates, transition states and final product (Figure 31) are similar to those calculated for D-xylose. A similar dehydration mechanism is summarized in the potential energy surface (Figure 32).

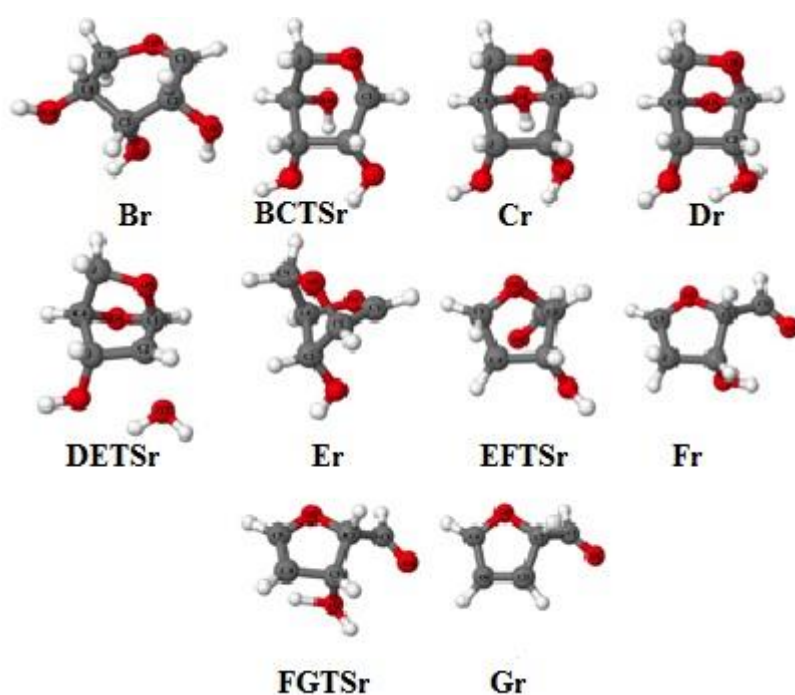


Figure 31: 3D geometry of dehydrated intermediates, transition states and final product obtained from protonated D-ribose dehydration calculated at the M11/6-311++G(2d,2p) level of theory.

According to the experimental results, the **Br** ion, as well as the intermediates and transition states, are characterized by the same connectivity of the corresponding species calculated for protonated D-xylose. As in the case of the corresponding neutral pentose sugars, the only difference between xylose and ribose concerns the orientation of OH groups.

The activation energy relating to the isomerization of the **Br** ion into the bicyclic structure **Cr**, and the subsequent proton shift leading to **Dr**, is calculated

to be only 4.6 kcal mol⁻¹. Hence, it is reasonable to suggest that the ions at *m/z* 133 isolated in the ESI mass spectra assume both the **Br** and/or **Dr** conformations. The PES profile relating to the D-ribose **Br**→**Dr** isomerization is lower in energy than that obtained for D-xylose (Figure 30), and this is probably due to the different hydroxyl group configurations. In particular, O2 and O3 were found in cis configuration in D-ribose and in trans configuration in D-xylose.

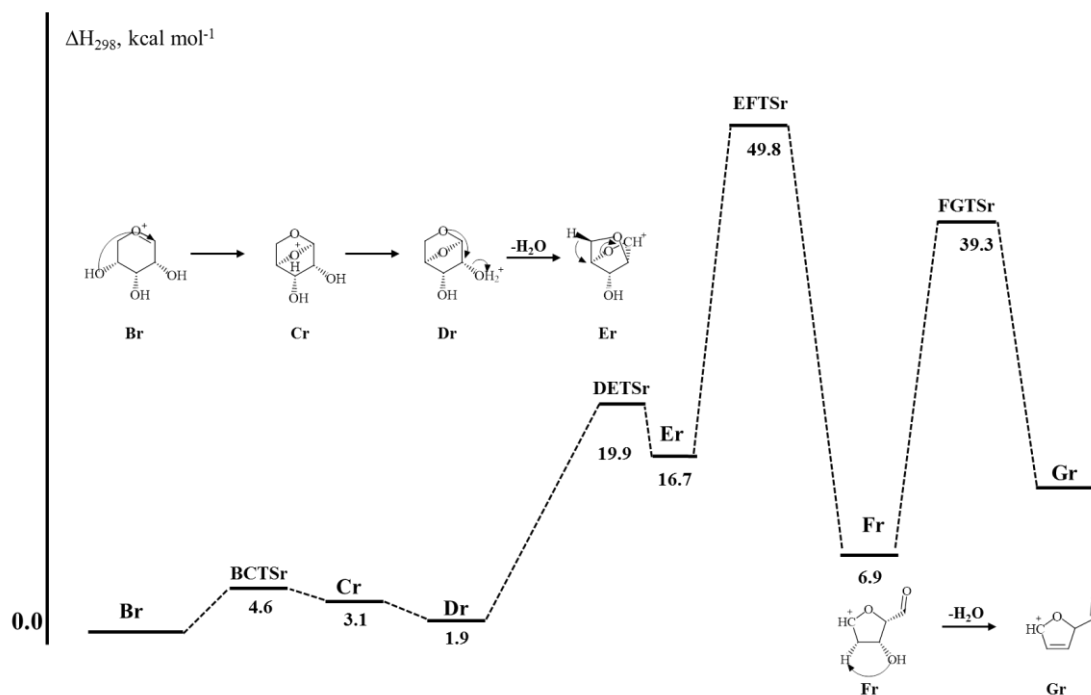


Figure 32: Potential energy surfaces and reaction pathway of the unimolecular conversion of C1-OH protonated D-ribose. The ΔH_{298} energies of minima and transition states were calculated at the CCSD(T)/cc-pVTZ//M11/6-311++G(2d,2p) level of theory.

As a consequence, the intramolecular hydrogen bond between O2 and O3 enhances the stability of **Cr**.

Dr also presents this stabilization because the shifted proton on O2 is again shared by O2 and O3. The energetic barrier of the second dehydration step from **Br** is estimated to be 19.9 kcal mol⁻¹, the same value calculated for the second water loss from **Bx**. This similar activation energy does not agree with the slightly different experimental energy threshold measured in the ERMS spectra (0.0 eV for xylose and 0.4 eV for ribose).

The ring contraction from **Er** to **Fr** occurs following the same mechanism postulated for D-xylose. A proton abstraction by O3 from C4 promotes the third water loss from the intermediate **Fr**. In this case the calculated energy profile overlaps that of D-xylose and the overall activation barrier of $33.1 \text{ kcal mol}^{-1}$ is in agreement with the similar threshold energy experimentally measured for the last dehydration of the two sugars.

Figure 33 displays the geometries of the dehydrated intermediates, transition states and final product obtained from protonated D-arabinose, whereas PES and hypothesized dehydration route are reported in Figure 34.

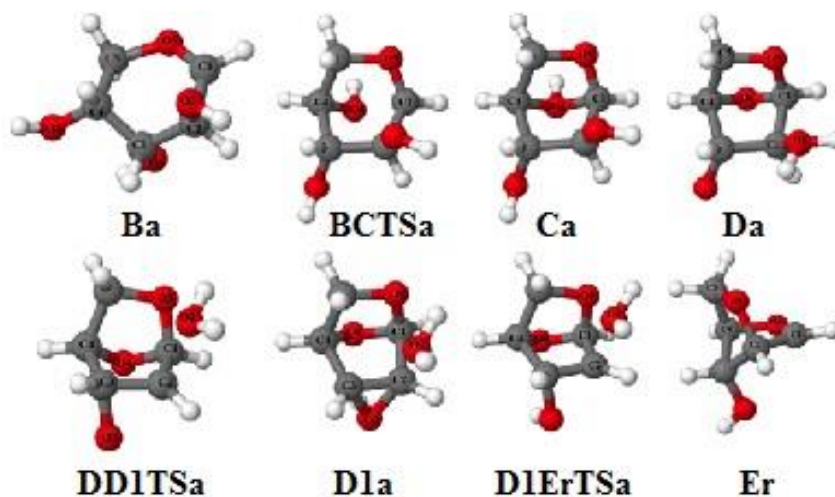


Figure 33: 3D geometry of dehydrated intermediates, transition states and final product obtained from protonated D-arabinose dehydration calculated at the M11/6-311++G(2d,2p) level of theory.

The proposed D-arabinose dehydration mechanism differs from the other two sugar pathways especially for the loss of the second water molecule. The activation energy relating to the conversion of the arabinose oxonium ion **Ba** into the **Ca** is estimated to be $8.9 \text{ kcal mol}^{-1}$.

Concerning the D-arabinose second water loss, the $32.1 \text{ kcal mol}^{-1}$ barrier is higher than the corresponding value obtained for D-xylose and D-ribose, but in agreement with the threshold energy experimentally measured. Moreover, the 0.4 eV experimental threshold energy difference between D-ribose and D-arabinose

perfectly agrees with the 12.2 kcal mol⁻¹ difference between the calculated barriers.

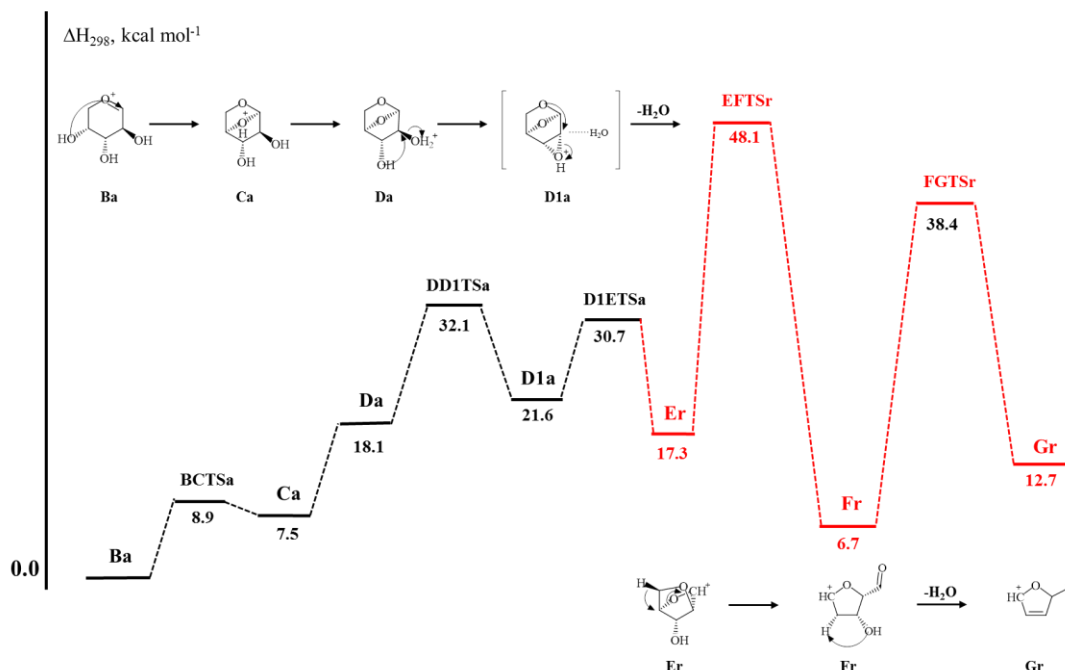


Figure 34: Potential energy surfaces and reaction pathway of the unimolecular conversion of C1-OH protonated D-arabinose. The ΔH_{298} energies of minima and transition states were calculated at the CCSD(T)/cc-pVTZ//M11/6-311++G(2d,2p) level of theory.

As reported in Figure 34, the second dehydration step occurs in a two sequence mechanism characterized by two transition states, **DD1TSa** and **D1ErTSa**. Compared to the analogue D-xylose and D-ribose transition states, **DD1TSa** and **D1ErTSa** are endowed with higher energies (32.1 and 30.7 kcal mol⁻¹) and are connected each other by the minimum **D1a**. This is characterized by an epoxy function weakly interacting with the leaving water molecule.

The subsequent O5 transposition to C2 through the transition state **D1ErTSa** allows the opening of the epoxy function and the ultimate removal of the water molecule, as indicated by the calculated imaginary frequency. After the isomerization of the **D1a** ionic species into the **Er** ionic intermediate, the mechanism follows the same pathway calculated for D-ribose.

Finally, the energy barrier relating to the D-arabinose third dehydration step is calculated to be 30.8 kcal mol⁻¹, in good agreement with the similar

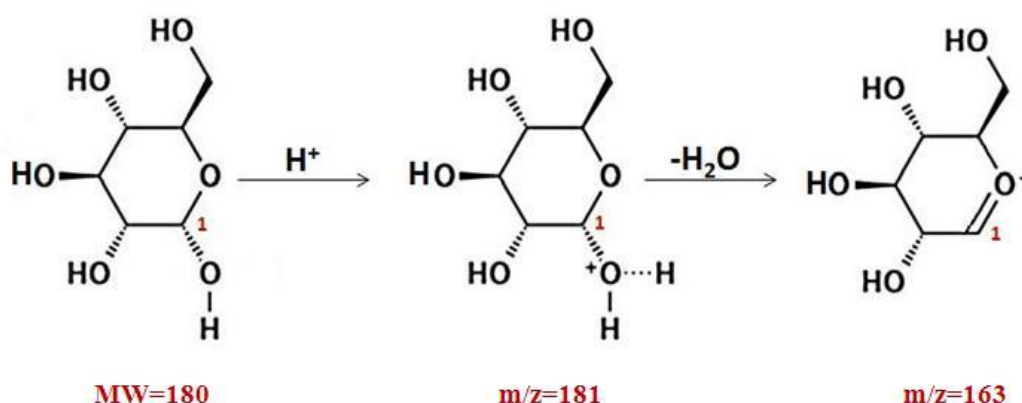
experimentally measured threshold energies of D-xylose and D-ribose (1.0 and 1.1 eV).

2.4 Discussion

All the experimental and theoretical results aiming to the elucidation of the gas-phase monosaccharide dehydration mechanisms suggest that protonation of the sugars is a necessary step to convert them to platform chemicals.

For each monosaccharide analysed, protonated parent ions (m/z 181 for D-hexoses, m/z 151 for D-pentoses) have been detected only at very low intensity. On the contrary, the dehydration intermediates and products are always observed as high-intensity peaks in the ESI mass spectra. It is reasonable to suppose that the protonation occurs at the most basic site of these monosaccharides and that the first dehydration barrier is sufficiently low to activate the dehydration process directly in the mass spectrometer source.

With regard to D-glucose, a gas-phase DFT calculations performed at B3LYP/6-311 +G(d,p) level of theory^[49] indicated the O1 as the most favourable protonation site. The m/z 181 protomer thus obtained can easily head for the first water molecule elimination leading to the ionic intermediate at m/z 163 as described in Scheme 11. Therefore, the protonation and dehydration of glucose C1-OH site result in the formation of a carbocation stabilized by the presence of the pyranosic oxygen atom. For the reported entire process the associated energetic barrier is estimated to be approximately 4 kcal mol^{-1} , an amount of excitation energy reasonable owned by the ions in the ESI ionization process.



Scheme 11: *D-glucose protonation and first water loss mechanism.*

Also in the case of D-pentoses, the protonated sugars are not observed in the ESI mass spectrum. Reasonably, these species easily lose the first water molecule, through the same hemiacetalic oxygen-assisted process observed for D-glucose. Conversely to the theoretical calculations performed by Nimlos^[38] that predicted a degradation pathway starting from D-xylose protonated at C2-OH, recent mass spectrometric experiments^[60] demonstrated that gas phase D-xylose dehydration reaction involves protonation on the OH group bound at C1 position. This evidence has been obtained by undergoing CAD experiments on C1-OH and C2-OH protonation model compounds, such as tetrahydro-2H-pyran-2-ol and tetrahydro-2H-pyran-3-ol.^[60]

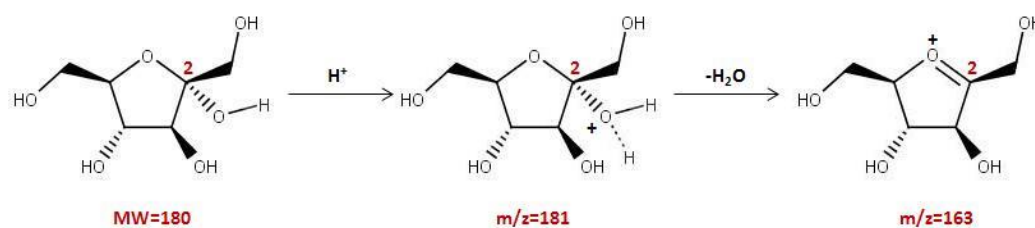
Considering the small differences in the calculated proton affinity values of D-xylose OH groups, the initial formation of other OH protonated isomers cannot be excluded. Nevertheless, the C₂₋₅-OH protonated species are all characterized by higher first dehydration energies^[38] and hence should survive to water dissociation and be observed in the mass spectra.

Concerning D-fructose protonation on the O2H most basic site, theoretical studies^[44,47,48] calculated the first water loss to be only 6.0-8.5 kcal mol⁻¹ endothermic.

Protonation at the other OH groups has been excluded since the dehydration reactions of the corresponding protonated species are characterized by calculated activation energy in the range of 25-40 kcal mol⁻¹. These energetic values are excessively high to justify the low intensity of the m/z 181 ion observed in the ESI mass spectrum.

Also in this case, the first water loss occurs in a process mediated by the furanolic oxygen lone pair (Scheme 12).

As evidenced by Scheme 11 and Scheme 12 and from the full-scan mass spectra reported in Section 2.1 (Figure 5), ions at m/163 represent the first dehydration intermediates obtained from protonated D-glucose and D-fructose conversion. The subsequent loss of an additional water molecule led to the formation of the ionic intermediate at m/z 145.



Scheme 12: *D-fructose protonation and first water loss mechanism.*

Although CAD mass spectra can provide only limited information about the minute structural details of the isolated ions, fragment at m/z 85 has resulted to be structurally diagnostic for the characterization of these dehydration intermediates. As previously reported,^[57] the presence of this fragment, corresponding to the loss of the $C_2H_4O_2$ neutral counterpart from the ionic intermediate at m/z 145, cannot be attributed to an open-chain precursor ion but is a peculiar cross ring bond cleavage of cyclic dehydrated sugars. This evidence confirms a cyclic structure for the ions at m/z 163 and 145 arisen from the mono- and double-dehydration of protonated hexose. As a consequence, the differences observed in the product ion relative abundances between the two sugars cannot be related to a different cyclic/linear connectivity, but to a different orientation of the diastereomeric vicinal hydroxyl groups.

Small differences in the daughter ion relative intensities have been reported also comparing the CAD mass spectra of the pentose ionic intermediates at m/z 133 and 115 (Table 5 and 6). Also in this case these differences can be ascribed to the orientation of the OH groups, but in general the pentose dehydration intermediates seem to be characterized by a common structure. This consideration is reinforced by the intermediate structures predicted by theoretical calculations and confirmed by the common ionic product obtained from the complete dehydration of the three sugars. In fact, the loss of the third water molecule from each ionic intermediate at m/z 115 has led to the daughter ion at m/z 97. This species is characterized by the same structure for the three sugars and corresponds to protonated 2-FA as verified by the comparison of the CAD mass spectra reported in Figure 26. According to the outcome of the decomposition reactions

performed in solution, also in the gas phase the main product of pentose dehydration reaction is the platform chemical 2-furaldehyde.

On the contrary, the gas-phase dehydration of D-glucose and D-fructose has led to the formation of a mixed ionic population at m/z 127 not entirely composed by protonated 5-HMF.

The main daughter ion at m/z 109 arising upon fragmentation of protonated standard 5-HMF is also observed in the CAD mass spectra of the m/z 127 ions obtained from protonated D-glucose and D-fructose. Nevertheless, the presence of several additional fragment ions at m/z 97, 99 and 69, could account for a parent ionic population containing a mixture of 5-HMF protomers and isomers. In particular, daughter ion at m/z 97 can be considered as a diagnostic peak to demonstrate the existence of different 5-HMF protomers. Indeed, this fragment was observed when the fragmentation of protonated standard 5-HMF has been performed under strongly exothermic chemical ionization (CI) conditions (Figure 10). Gradually increasing the proton transfer exothermicity it was possible to access to energetically less preferred 5-HMF protonation sites leading to the formation of different protonated species evidenced by the appearance of the ion at m/z 97.

Moreover, the fragmentation into the ions at m/z 69 and m/z 99, never observed under CI conditions, clearly points to the formation of isomeric $[C_6H_6O_3]H^+$ ions with a different structure than 5-HMF. This assumption seems to be in agreement with the results of a DFT study^[49] that has predicted the formation of several dehydration products from C1-OH protonated D-glucose.

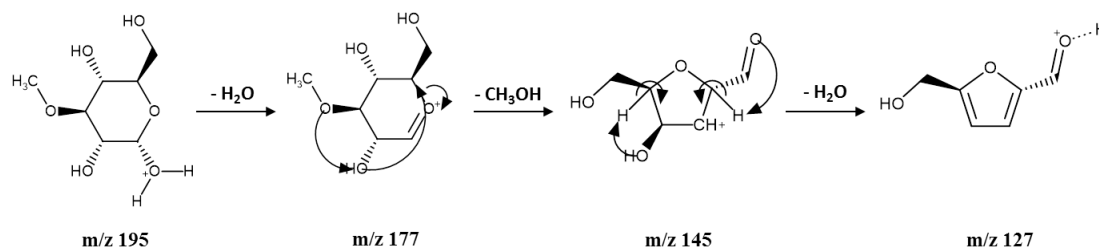
CAD mass spectra of the product ions at m/z 127 obtained from the dehydration of protonated D-glucose and D-fructose are substantially different. In particular, the CAD mass spectrum of the m/z 127 ion arising from protonated D-fructose dehydration shows an intense fragment ion at m/z 69. This evidence seems to confirm that the two sugars decompose following different dehydration routes. Hence, even if the intermediacy of D-fructose in the D-glucose conversion has been predicted by the “fructose” pathway,^[42] the differences experimentally shown in the CAD mass spectra of the intermediate and product ions indicate that

the dehydration pathway mediated by the glucose/fructose tautomerization is not the only mechanism occurring in the gas phase.

Besides, on the basis of the energetic barriers measured by ERMS experiments, the second and third dehydration steps seem to be always thermodynamically favoured in the case of D-fructose.

Experimental data discussed above allow us to corroborate the most feasible D-glucose and D-fructose dehydration mechanisms among those predicted by theoretical calculations. Furthermore, different catalytic strategies can be proposed to increase the selectivity of the D-glucose and D-fructose conversion to 5-HMF.

In the case of D-glucose, the reported reaction pathway starting from C1-OH protonation^[38] is perfectly in agreement with the results extrapolated from the gas-phase H/D exchange experiments and can be used to describe the dehydration mechanism of the 3-O-methyl-D-glucose model compound (Scheme 13). On the basis of this mechanistic hypothesis, the protonation reaction at O1H position prompts to lose the first water molecule leading to an oxocarbenium intermediate. The subsequent O2-O3 proton transfer results in the opening of the cyclic structure and the formation of a furanosic ring after the elimination of a methanol molecule. The furanosyl intermediate can subsequently release the last water molecule giving rise to the protonated 5-HMF by means of a proton transfer from the ring.



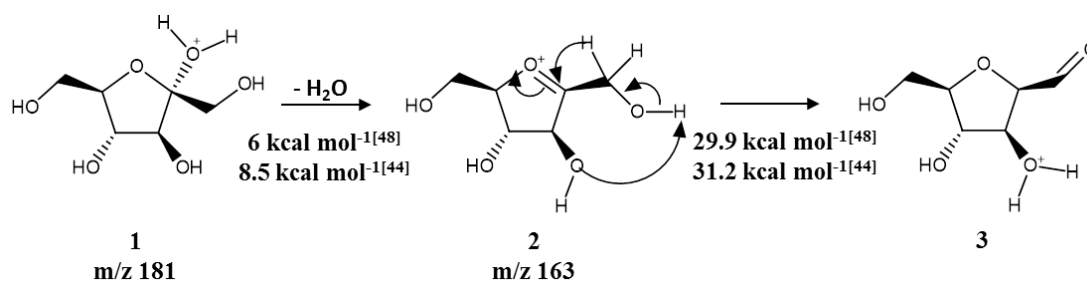
Scheme 13: Hypothesized dehydration mechanism of 3-O-methyl-D-glucose leading to protonated 5-HMF.

Since the protonated 5-HMF is not the only product ion arising from the gas-phase D-glucose dehydration, the mechanism proposed by theoretical calculations

represents one of the several possible routes for the D-glucose decomposition. On the other hand, the data reported may be useful to clarify the key role performed by an electron-withdrawing substituent eventually bound at O3 position. In fact, the results obtained by the CAD mass spectrum of the ion at m/z 127 arising from the dehydration of protonated 3-O-methyl-D-glucose suggest that the presence of the methyl group at O3-position favours a specific dehydration mechanism leading to protonated 5-HMF. This is due to the inductive effect carried out by the methyl group that increases the O3 basicity and favours the O2-O3 proton transfer. Although the O3 basicity is increased by the methyl substituent, O1 is still the most basic site and the protonation reaction occurs at this position. This hypothesis has been confirmed by the evidence that protonated 3-O-methyl-D-glucose predominantly fragments by releasing a water molecule rather than a methanol neutral counterpart (Figure 14). Indeed, the loss of CH_3OH occurs only after the first dehydration step according to the theoretical mechanism proposed.

With regard to D-fructose, the combination of experimental results and theoretical unimolecular mechanisms reported in literature^[44,48] has allowed us to validate a possible D-fructose dehydration pathway leading to $[\text{C}_6\text{H}_6\text{O}_3]\text{H}^+$ ions not corresponding to 5-HMF protonated at the aldehydic group (Scheme 14-16).

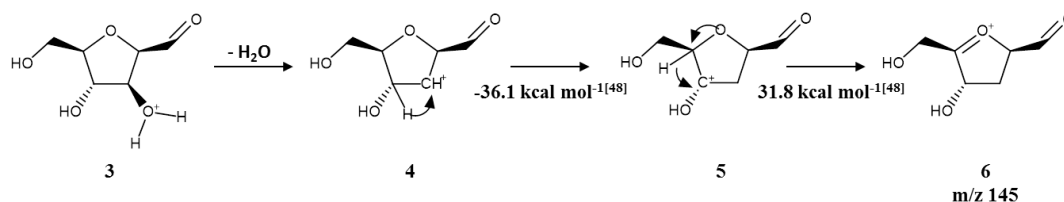
As previously reported, the protonation reaction occurs at the most basic sugar site that in the case of D-fructose corresponds to the O2H group (Scheme 14).



Scheme 14: *D-fructose gas-phase first dehydration mechanism.*

The subsequent loss of a water molecule leading to the m/z 163 intermediate (2) shows an energetic barrier of only $6.0\text{--}8.5\text{ kcal mol}^{-1}$. This intermediate can release the second water molecule after a proton transfer from the O1 to O3 and

the subsequent hydride shift from C1 to C2 leading to the species **3**. The calculated barrier for this rearrangement ranges from 29.9 to 31.2 kcal mol⁻¹ and the entire process generates an ionic structure that is prompt to lose the second water molecule (Scheme 15). According to the theoretical data,^[48] the unstable carbocation **4** can isomerize to the more stable ionic species **5**, corresponding to the ion at m/z 145, by the 1-2 hydride shift from C4 to C3. At this point, the hemiacetalic oxygen lone pair can assist the hydride shift from C5 to C4 with the subsequent formation of the ionic species **6** that is the key intermediate for the loss of the third water molecule.

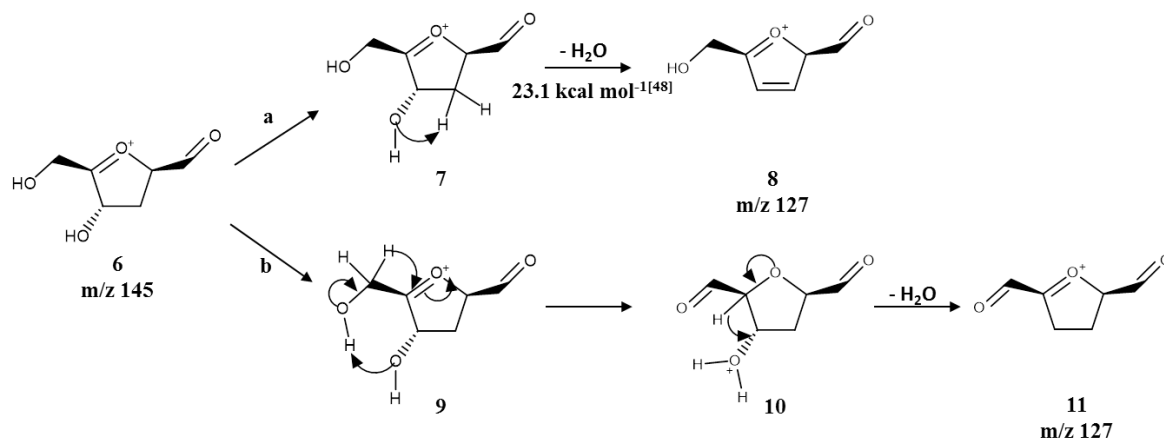


Scheme 15: *D*-fructose gas-phase second dehydration mechanism.

Species **6** can undergo a proton transfer from C3 to O4H arranging the molecule for the last dehydration step (**5**→**8**). This route leads to the ionic species **8** that corresponds to 5-HMF protonated on the ring (Scheme 16, route a). The overall activation energy for this process was calculated by Caratzoulas et al. to be 31.8 kcal mol⁻¹. It is worth of note that the calculated values for the second and third dehydration steps are similar (31.2 versus 31.8 kcal mol⁻¹), in agreement with the similar activation energy experimentally measured by the energy-resolved mass spectra.

Furthermore, it can be hypothesized that the third water loss may follow the alternative pathway **6**→**11**, mechanistically reflecting the **2**→**3** step, that gives rise to the formation of the dialdehyde **11**, a gas-phase product strictly related to 2,5-diformylfuran, a 5-HMF oxidation product reported in water-free solutions^[62] (Scheme 16, route b). The ionic species **11** represents a good candidate as precursor of the peculiar fragment ion at m/z 69 observed in the CAD mass spectrum of the ion at m/z 127. In fact, this fragment can be formed by the

breakage of the bonds between C2-C3 and C5-O as well as between C4-C5 and C2-O.



Scheme 16: *D-fructose gas-phase third dehydration mechanisms.*

The proposed dehydration mechanism reflects the results of the isotope-labelling experiments showing that the first and second water loss involves only proton bound to the OH groups, whereas the last dehydration reaction can occur in parallel by shifting an hydrogen atom from the ring or by transferring the proton between the two remaining OH groups.

Taking into account this evidence, the gas-phase selectivity of the D-fructose conversion to 5-HMF has been increased by forming an ionic adduct with the conjugate acid of a nitrogen-containing base. In particular, the ammonium ion, employed as model acid, shows the unique characteristic to simultaneously act as a protonating or a coordinating agent.

Experimental results have confirmed that when ammonium acts as a protonating agent the loss of NH_3 neutral counterpart performed by tandem CAD occurs after the first dehydration step of the ionic adduct. The subsequent loss of two water molecules leads to a m/z 127 ionic population very similar to that arising from D-fructose dehydration in acidic medium.

On the other hand, when the ammonium acts as a coordination agent and remains attached to D-fructose during the three dehydration reactions, the final ionic population at m/z 127 results to be enriched in protonated 5-HMF (Figure 19). This result seems to account for the existence of a selective and effective

base-assisted dehydration mechanism that drives the D-fructose conversion to 5-HMF. Simultaneously, the ammonium can assist also a double dehydration followed by a deformylation reaction leading to a $[2\text{-FA}\cdots\text{NH}_4]^+$ adduct. Hence, it has been highlighted a novel D-fructose conversion mechanism to 2-FA never observed in solution.

Replacing ammonia with other nitrogen bases, it has been demonstrated that the reproducibility of this selective conversion mechanism strictly depends on the proton affinity difference existing between the chosen base and the most basic site of D-fructose. In this regard, the O2 proton affinity of D-fructose has been estimated to be around $195 \text{ kcal mol}^{-1}$.^[63] Hence, comparing this value with those of the nitrogen-containing bases reported in Section 2.2 (Table 4) a significant trend has emerged. When the proton affinity difference ranges between 1.5-13 kcal mol^{-1} (bases 1-4 of Table 4) the chemical behaviour of the ionic adduct is superimposable to that obtained by employing ammonium as a coordination agent. On the contrary, when the proton affinity difference exceeds 13 kcal mol^{-1} (bases 5-12 of Table 4) the ionic adduct undergoes a single dehydration upon fragmentation.

Theoretical calculations are in progress in order to elucidate the structures of the starting reactant ion, those of the intermediates and to validate feasible reaction mechanisms.

3. L-Ascorbic acid decomposition reaction

Furan is a heterocyclic organic molecule, consisting of a five-membered aromatic ring and characterized by a low boiling point (31 °C). Chemical compounds containing such rings are also referred to as furans.

Furan products had received increasing attention since 1995 when the International Agency for Research on Cancer expressed the opinion that “*furan and its derivatives are carcinogenic in rats and mice*” and classified them as “*possible carcinogenic to humans*”.^[4]

Although the mechanism of furan’s carcinogenesis is not well-understood, several studies account for the fact that cis-2-butene-1,4-dial metabolite arising from furan microsomal oxidation is responsible for the formation of diastereomeric adducts with DNA.^[64]

In 1979 Maga^[65] first reported that furan products are present in a number of foods providing evidence that was confirmed only in 2004 by the European Food Safety Authority (EFSA)^[66] and the Food and Drug Administration (FDA).^[67] These agencies calculated the average levels of furan considering an enlarged range of food categories. Amounts over 100 µg/Kg were found especially in coffee, baby food, sauces and soups.

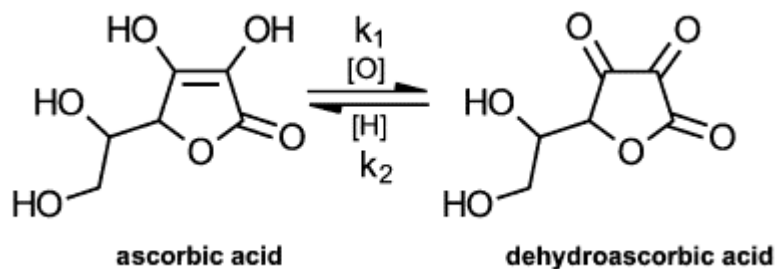
Some research groups^[68-71] have demonstrated that these dangerous compounds arise by decomposition reactions occurring upon food thermal treatment, such as extreme thermal process by which glass and metal containers are sterilised. Nevertheless, also non-thermal processing technologies such as ionizing radiation can induce furan formation.^[72]

Unsaturated lipids, reducing carbohydrates and specific amino acids are indicated as the main classes of furan precursors in thermally processed food. Among these molecules L-Ascorbic acid represents one of the major source of furan derivatives.

L-Ascorbic acid, also known as Vitamin C, is a water-soluble nutrient present in vegetables and fruits and required as part of the human diet owing to its protective role in the body. Its reducing properties are used in the pharmaceutical and food industry to protect foodstuffs against oxidation and prolong the shelf life of drugs.

L-Ascorbic acid is very effective as antioxidant because it can be quantitatively oxidized to dehydroascorbic acid in aqueous solution by different oxidizing agents (Scheme 17).

On the other hand, the exposure of Vitamin C to oxygen, metals, humidity and light can produce the degradation of this sensitive molecule.



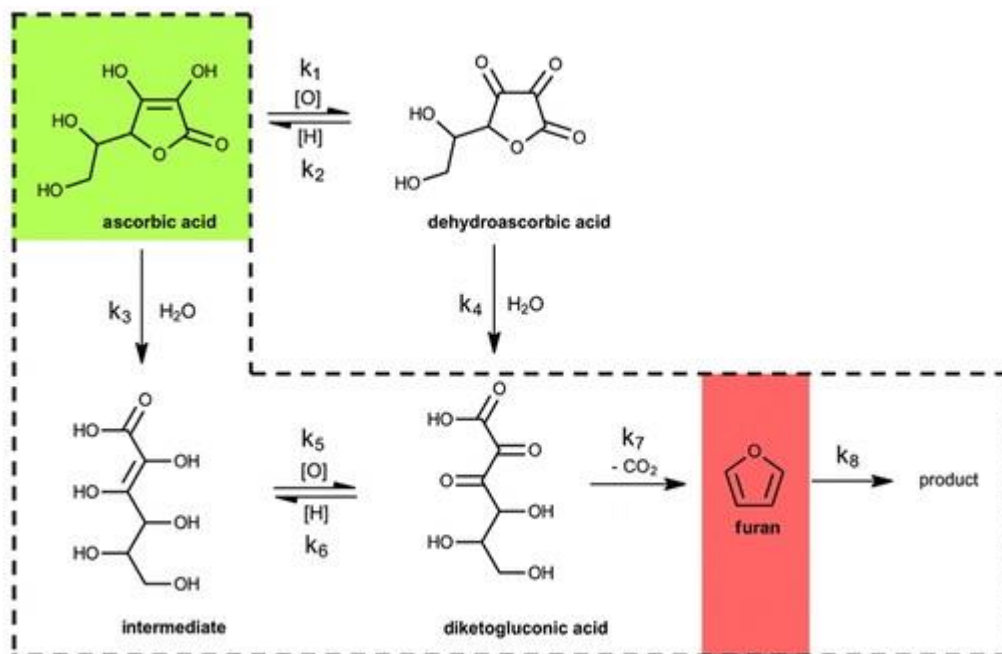
Scheme 17: L-Ascorbic acid oxidation to dehydroascorbic acid.

The identification of L-Ascorbic acid degradation products and the knowledge of the mechanisms through which these products are formed can be useful to determine optimal storage and processing conditions for foodstuffs containing vitamin C as preservative.

Considering the genotoxic potential of the furan products, the elucidation of the pathways by which furan and furan derivatives are produced is a promising approach for optimizing strategies aiming to control their formation. Indeed, the safeguard of the public health can be ensured only keeping the level of the furan products under the critical threshold.

As in the case of the monosaccharide decomposition reactions reported in this thesis, controversial mechanistic hypotheses have been predicted by theoretical studies concerning L-Ascorbic acid decomposition reaction. In this regard, Hirst et al.^[73] first reported the formation of furfural (2-furaldehyde) from Vitamin C in strong acidic media, whereas Mogol et al.^[74] investigated the effect of oxidizing and reducing agents on the formation of furan from L-Ascorbic acid degradation as a function of heating at elevated temperatures (>100 °C). According to this study, degradation of L-Ascorbic acid has been classified into two types of reactions (non-oxidative and oxidative) and the main difference is represented by

the formation of dehydroascorbic acid in the first reaction step due to the alternative presence of anaerobic or aerobic conditions (Scheme 18).



Scheme 18: Non-oxidative and oxidative decomposition pathways of L-Ascorbic acid proposed by Mogol et al. Ref. [74].

Also the non-oxidative degradation mechanism proposed by Kurata^[75] has suggested furfural as the main carbonyl product obtained in solution. This work highlighted that the dehydration reaction of 3-deoxy-L-pentosone (3-D-P) intermediate to 2-furaldehyde is accelerated by acid catalyst.

Anyway, it should be noted that most of the theoretical mechanisms consider the bimolecular reaction between protonated L-Ascorbic acid and one or more surrounding water molecules. On the contrary, the peculiar conditions of the gas-phase studies allow one to consider only intramolecular processes leading to charged intermediates in which solvent molecules are never involved. For this reason, on the basis of our experimental data collected by means of the mass spectrometric techniques, a new decomposition pathway has been suggested. Contrary to the monosaccharide sugars previously investigated, no information about the structure and ion energetics of protonated L-Ascorbic acid is available in literature. Hence, the first step of the investigation was the measurement of L-

Ascorbic acid proton affinity (PA) and gas-phase basicity (GB). Subsequently, starting from the gaseous reactant ions, the reaction intermediates and products were structurally characterized and the conversion energetic barriers measured. The whole picture emerging from the experimental and theoretical results allowed us to draw a gas-phase Vitamin C decomposition reaction mechanism.

3.1 Protonated L-Ascorbic acid structure and ion energetics

Proton affinity (PA) and Gas Phase Basicity (GB) are two thermochemical parameters defined as the negative of the standard enthalpy and standard Gibbs free energy for the protonation reaction (1), respectively :



The most common mass spectrometric approaches used to determine proton affinities are the *equilibrium method*^[76,77] and *bracketing method*.^[78,79]

Owing to the L-Ascorbic acid low vapour pressure and its pronounced tendency to decompose at high temperature, the use of the above-mentioned approaches was prevented. An advisable alternative to obtain this thermochemical information is represented by the Cooks's kinetic method.^[80]

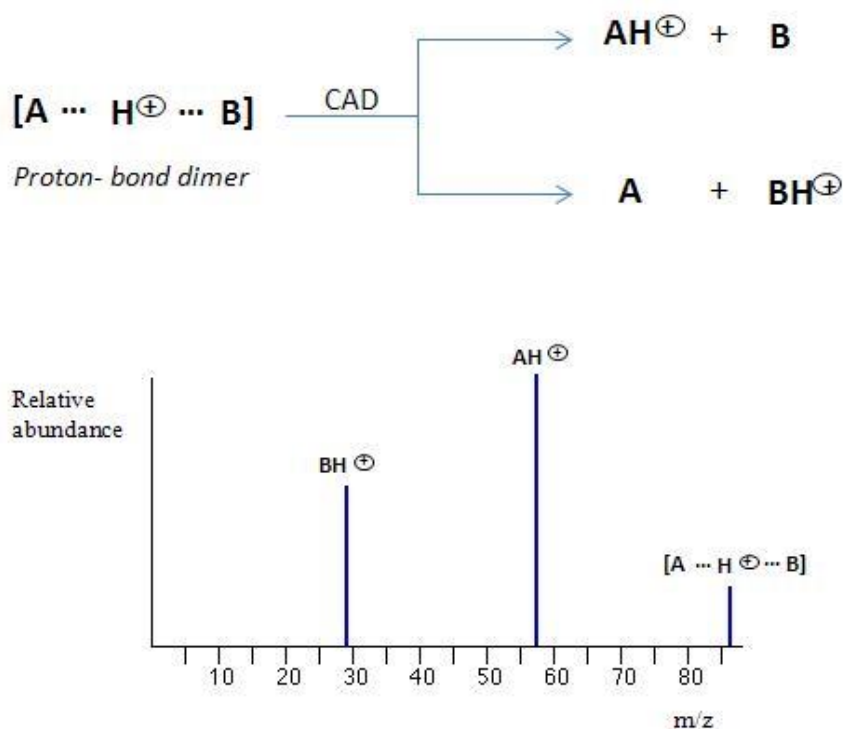


Figure 35: Characteristic fragmentation pathway and CAD mass spectrum of the proton-bond dimer ions.

This approach consists in generating a proton-bond dimer between the molecule of interest (A) and a reference base (B). Upon collisionally activated dissociation (CAD) the dimers can subsequently fragment into the protonated reference base or competitively to protonated molecule A (Figure 35).

The ratio of the two product ion abundances allows one to estimate the relative affinity of both molecules to the H⁺ ion.

Thus, the selection of a set of suitable reference bases is a critical step for the application of the method. First of all, the bases should have self-consistent thermochemical values and in order to neglect entropic factors they should be structurally similar to the analyte A. In the case of polydentate molecules, such as L-Ascorbic acid, the protonation entropy differences existing between the analyte and any selected reference base are significant, making necessary to apply the “*extended*” kinetic method developed by Fenseleau and Wesdemiotis.^[81,82]

On the basis of this approach, the PA of L-Ascorbic acid (PA_A) can be calculated using the Equation 1, where [AH⁺]/[B_iH⁺] represents the ratio of the product ion intensities observed from collisionally activated dissociation of the proton-bond dimers, PA_{B_i} is the PA of each reference base used in the determination of PA_A, PA_{avg} is the average PA of the set of reference bases and Δ(ΔS) is the difference in protonation entropy between L-Ascorbic acid (AA) and the bases.

$$\ln \left(\frac{[AH^+]}{[B_iH^+]} \right) = - \frac{PA_{B_i} - PA_{avg}}{RT_{eff}} + \left(\frac{PA_A - PA_{avg}}{RT_{eff}} - \frac{\Delta(\Delta S)}{R} \right) \quad (1)$$

The GB parameter can be derived from the PA_A by using the Gibbs-Helmoltz equation (Equation 2).

$$GB = PA_A - T\Delta S_p \quad (2)$$

To obtain the PA_A value from Equation 1 two plots were constructed. In the first diagram (Figure 36) the natural log of the experimentally determined

$[AH^+]/[BH^+]$ ratio is plotted versus $PA_{Bi}-PA_{avg}$ (where $PA_{avg}= 867.2 \text{ kJ mol}^{-1}$). Each value of $\ln[AH^+]/[BH^+]$ is obtained from averaging three different set of data recorded in the same experimental conditions.

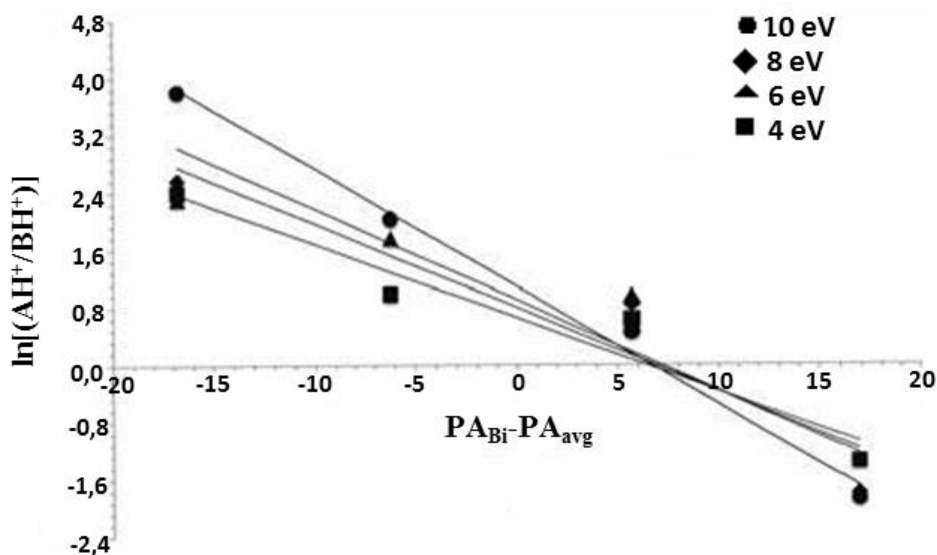


Figure 36: Plot of the $\ln([AH^+]/[BH^+])$ versus $PA_{Bi}-PA_{avg}$, taken at four different collision energies (4, 6, 8 and 10 eV).

The reference bases used for the PA_A measurement were opportunely chosen on the basis of their structures; in fact, they are all associated with the L-Ascorbic acid by the presence of a common carbonyl group. Besides, their thermochemical parameters are well-known in literature^[83] and listed in Table 8.

Table 8: Thermochemical properties of the reference bases used. a) Data taken from Ref. [83].

Reference base	Gb ^a (kJ mol ⁻¹)	Pa ^a (kJ mol ⁻¹)	ΔS_p (kJ mol ⁻¹ K ⁻¹)
Acetylacetone	836.8	873.5	123.1
Acetophenone	829.3	861.1	106.7
Methylbenzoate	819.5	850.5	104.0
Hydroxyacetophenone	851.9	883.7	106.7

Neglecting the entropic effects and applying directly the “simple” Cooks’s kinetic method, it is possible to obtain an apparent PA_A value of about 874.2 kJ mol^{-1} from the x -intercept $PA_{Bi}-PA_{avg}=7$.

The standard regression analysis allowed to define the best-fit lines to the data of the first plot (Figure 36), having slopes (m) corresponding to $1/RT_{eff}$ and y -intercepts equal to $[(PA_A-PA_{avg})/RT_{eff}-\Delta(\Delta S)/R]$.

Table 9 displays the slope m and y -intercept values obtained. Standard deviations were calculated from the square root of the variance.

Table 9: Values obtained from the standard regression analysis

Collision energies (eV)	m ($1/RT_{eff}$)	y -intercept
4.0	0.0763 ± 0.01	0.4048 ± 0.06
6.0	0.1167 ± 0.002	0.7935 ± 0.09
8.0	0.1268 ± 0.02	0.8994 ± 0.05
10.0	0.1645 ± 0.05	1.0845 ± 0.2

On the basis of these data a second diagram can be constructed plotting the m values against the y -intercept. (Figure 37).

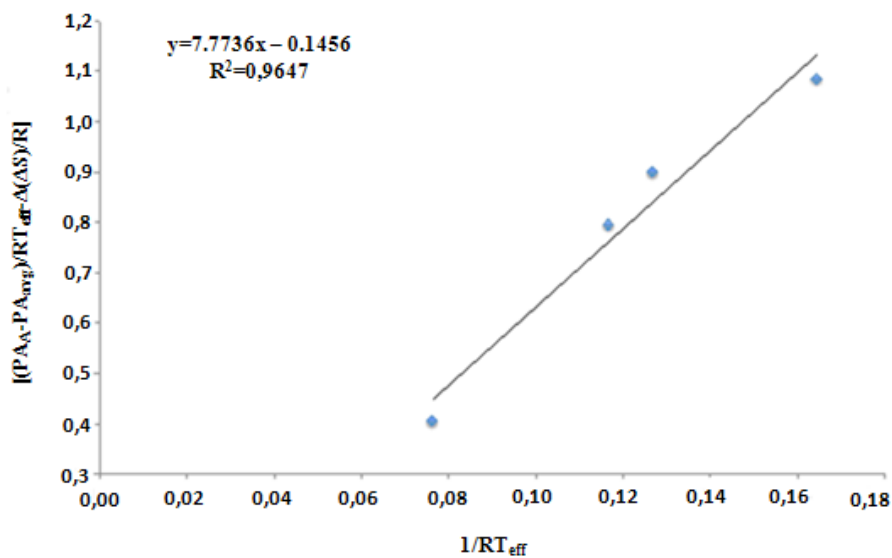


Figure 37: Plot of m values ($1/RT_{eff}$) versus the y -intercepts $[(PA_A-PA_{avg})/RT_{eff}-\Delta(\Delta S)/R]$.

A best-fit line having slope m of 7.7736 corresponding to $PA_A - PA_{avg}$ can be obtained from the second plot. Hence, the PA of AA can be extrapolate and estimated to be $875.0 \text{ kJ mol}^{-1}$. An uncertainty of $\pm 12 \text{ kJ mol}^{-1}$ is attributed to the measured value taking into account the error in the average PA of the reference bases chosen ($\pm 7 \text{ kJ mol}^{-1}$) and the uncertainties in the data obtained from the first diagram.

The y-intercept of the second diagram of Figure 37 corresponds to $\Delta(\Delta S)/R$ and considering a ΔS_{avg} value of $110.1 \text{ J mol}^{-1} \text{ K}^{-1}$ for the reference bases, a ΔS value for the protonation of AA can be calculated to be $108.9 \pm 2 \text{ J mol}^{-1} \text{ K}^{-1}$. Thus, a GB of $842.5 \pm 12 \text{ kJ mol}^{-1}$ can be estimated at 298 K.

Finally, a standard enthalpy of formation of $-509.6 \pm 12 \text{ kJ mol}^{-1}$ for protonated AA was obtained from the measured PA value of AA and its heat of formation, ΔH° , reported by Wilhoit ($-1164.6 \text{ kJ mol}^{-1}$).^[84]

Quantum mechanical calculations

A systematic quantum mechanical (QM) study at the B3LYP/6-31 +G(d,p) level of theory was carried out in order to support the mass spectrometric measurements and highlight the structures of $[C_6H_8O_6]H^+$ ions experimentally investigated.

The first step of this study consisted in evaluating the potential energy surface of neutral L-AA ($C_6H_8O_6$) and led to the identification of several low energy conformers of the considered species. This number of structures is certainly due to the structural flexibility of the molecule and the possibility to form different intramolecular H-bonds. Each conformer was generated and, consequently named, as a result of the rotation around the C4-C5 bond forming an angle O1-C4-C5-O5 of 60° , 180° and 300° , respectively. Starting from these three rotamers, the subsequent rotation around the C5-C6 bond formed an O5-C5-C6-O6 angle of 60° , 180° and 300° , leading to the optimization of nine different conformers displayed in Figure 38.

These rotamers are characterized by several H-bonds. In particular, all the rotamers show two H-bonds on the lactone ring (O2-H1 and O3-H2) and two H-

bonds on the chain and between the chain and the ring; only AA_60_180 forms one H-bond on the chain.

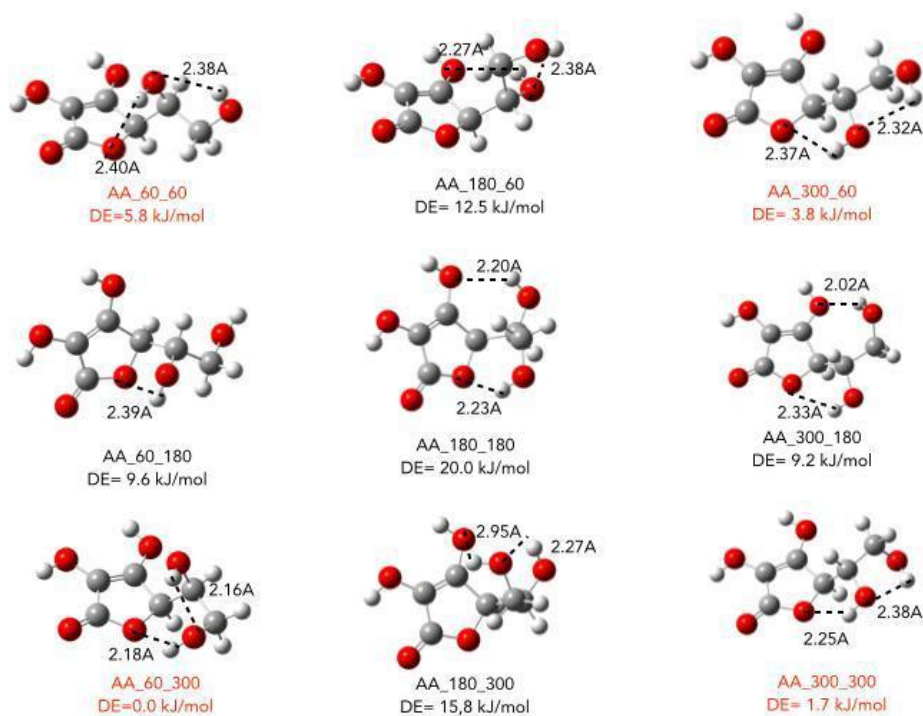


Figure 38: Geometries of the optimized conformers of L-AA and their energy difference from the lowest energy structure.

The formation of each intramolecular H-bond involves an energy gain of about 12.5 kJ mol^{-1} influencing the relative stability of neutral AA.

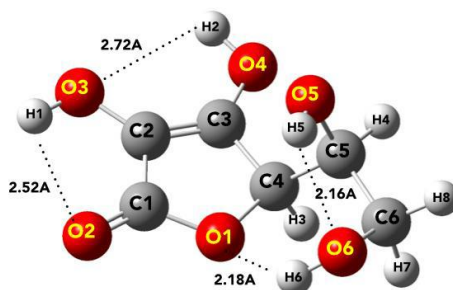


Figure 39: Geometry of the AA_60_300 lowest energy conformer.

The evaluation of the energetic contents for each rotamers identifies the conformer AA_60_300 as the most stable structure (Figure 39). This result is in agreement with previous theoretical^[85] and experimental studies.^[86,87]

Besides, the O1, C4, C5, C6, O6 and H6 atoms of AA_60_300 form a six-membered ring structure with chair conformation that is absent in the other eight conformers and accounts for its higher stability. All optimized geometrical parameters are reported in Table 10.

Table 10: Geometrical parameters of AA_60_300 conformer.

Bond	Å	Dihedral angles	Degree	Angles	Degree
O1-C1	1.379	O1-C4-C5-O5	-68.157	O1-C4-C5	110.163
C1-C2	1.458	O1-C4-C5-C6	55.909	C4-C5-C6	111.916
C2-C3	1.344	C4-C5-C6-O6	-79.013	C5-C6-O6	111.261
C3-C4	1.5	C4-C5-O5-H5	94.74	C6-O6-H6	108.477
C4-O1	1.452	C5-C6-O6-H6	65.989	O6-H6-O1	126.716
C1-O2	1.212	C6-O6-H6-O1	-38.132	H6-O1-C4	102.716
C2-O3	1.358	O6-H6-O1-C4	21.228	O1-C4-C3	103.835
C3-O4	1.346	O1-C4-C3-O4	-178.829	C4-C3-C2	109.469
C5-O5	1.413	O1-C4-C3-C2	1.745	C3-C2-C1	108.748
C6-O6	1.425	C4-C3-C2-O3	179.233	C2-C1-O1	108.376
C4-C5	1.544	C4-C3-C2-C1	-0.632	–	–
C5-C6	1.54	C4-C3-O4-H2	-175.624	–	–
O3-H1	0.971	C3-C2-C1-O2	179.504	–	–
O4-H2	0.969	C3-C2-C1-O1	-0.812	–	–
O5-H5	0.972	C3-C2-O3-H1	-178.718	–	–
O6-H6	0.97	O4-C3-C2-O3	-0.101	–	–
C4-H3	1.098	O3-C2-C1-O2	-0.368	–	–
C5-H5	1.098	–	–	–	–
C6-H6	1.093	–	–	–	–
C6-H7	1.099	–	–	–	–

The second step of this QM investigation was the elucidation of the protonated structures. Since the L-AA shows six basic sites corresponding to the six oxygen atoms, it was necessary to evaluate the GB and PA for each oxygen atom of the most stable neutral conformer, obtaining six protomers named accordingly to the protonated oxygen atom (AA_60_300_cat1; AA_60_300_cat2; AA_60_300_cat3; AA_60_300_cat4; AA_60_300_cat5; AA_60_300_cat6). Among these, four protomers are characterized by a stable structure, whereas all the optimization procedures to obtain the lowest energy geometries for cat3 and cat5 led to the isomerization into cat2 and cat6, respectively.

Figure 40 reports the optimized geometries and the relative energies of the four optimized protomers, whereas in Table 11 the bond lengths of the neutral AA_60_300 versus the protonated species are listed.

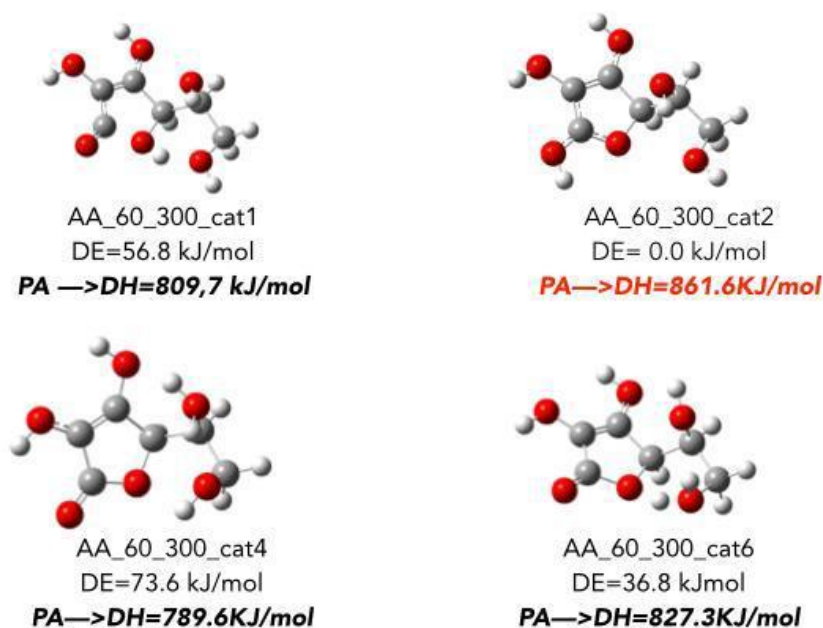


Figure 40: Optimized geometries and relative energies of the AA protomers.

Analysing the energetic parameters shown in Figure 40, it is clear that the most stable conformer is AA_60_300_cat2 and consequently the L-AA is preferentially protonated at the carbonyl oxygen.

Table 11: Bond lengths (Å) of neutral and protonated AA_60_300.

Bond	AA_60_300	cat1	cat2	cat4	cat6
O1-C1	1.379	1.579	1.312	1.392	1.432
C1-C2	1.458	1.429	1.409	1.477	1.454
C2-C3	1.344	1.359	1.373	1.342	1.349
C3-C4	1.500	1.498	1.498	1.506	1.500
C4-O1	1.452	1.477	1.467	1.438	1.460
C1-O2	1.212	1.180	1.301	1.199	1.196
C2-O3	1.358	1.352	1.347	1.338	1.346
C3-O4	1.346	1.321	1.313	1.365	1.339

In this regard, Figure 41 displays the optimized structure of this species, highlighting the intramolecular H-bonds, whereas Table 12 lists its geometrical parameters.

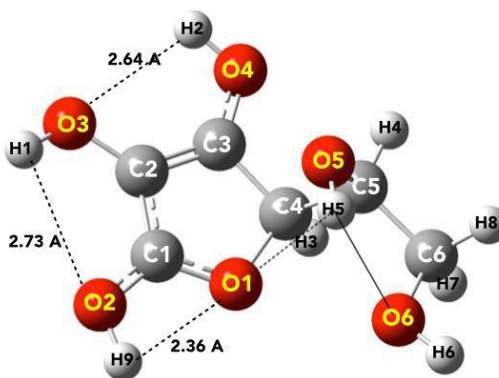


Figure 41: Optimized geometry of the lowest energy protonated conformer, AA_60_300_cat2.

AA_60_300_cat2 shows a strong electron delocalization on the lactone ring and on the neighbouring oxygen atoms (O2, O3 and O4) that can be justified by the shortening of O1-C1, C1-C2, C2-O3 and C3-O4 bonds and from the simultaneous elongation of C1-O2, C2-C3 and C4-O1 bonds respect to neutral AA_60_300. Thus, the electronic stabilization is due to the protonation at O2 and

the consequent formation of a 5-alkyl-substituted 1,2,3-trihydrocyclopentadiene structure of AA involving a cyclic diene π -electron system. Besides, the greater stability of AA_60_300_cat2 (Figure 41) can also be attributed to the presence of three hydrogen bonds (O1-H9, O2-H1 and O3-H2). In this context, comparing the geometries of all protomers (AA_60_300_cat1, AA_60_300_cat2, AA_60_300_cat4 and AA_60_300_cat6), only the conformer AA_60_300_cat2 shows a cage-like structure formed by a five atom ring (O1-C4-C5-C6-O6) with a hydrogen bond (O6-H5, 2.13 Å) as a bridge.

Table 12: Geometrical parameters of AA_60_300_cat2.

Bond	Å	Dihedral angles	Degree	Angles	Degree
O1-C1	1.312	O1-C4-C5-O5	-58.148	O1-C4-C5	110.571
C1-C2	1.409	O1-C4-C5-C6	67.74	C4-C5-C6	113.817
C2-C3	1.373	C4-C5-C6-O6	-76.777	C5-C6-O6	106.75
C3-C4	1.498	C4-C5-O5-H5	100.456	C6-O6-H6	110.191
C4-O1	1.467	C5-C6-O6-H6	-162.623	O6-H6-O1	–
C1-O2	1.301	C6-O6-H6-O1	–	H6-O1-C4	–
C2-O3	1.347	O6-H6-O1-C4	–	O1-C4-C3	102.526
C3-O4	1.313	O1-C4-C3-O4	-178.766	C4-C3-C2	110.058
C5-O5	1.404	O1-C4-C3-C2	3.047	C3-C2-C1	104.764
C6-O6	1.425	C4-C3-C2-O3	179.319	C2-C1-O1	108.376
C4-C5	1.556	C4-C3-C2-C1	-1.71	–	–
C5-C6	1.533	C4-C3-O4-H2	-176.426	–	–
O3-H1	0.969	C3-C2-C1-O2	179.702	–	–
O4-H2	0.974	C3-C2-C1-O1	-0.508	–	–
O5-H5	0.972	C3-C2-O3-H1	-178.718	–	–
O6-H6	0.966	O4-C3-C2-O3	-0.366	–	–
C4-H3	1.094	O3-C2-C1-O2	-1.409	–	–
C5-H5	1.098	–	–	–	–
C6-H6	1.096	–	–	–	–
C6-H7	1.098	–	–	–	–
O2-H9	0.976	–	–	–	–

AA_60_300_cat4 and cat6 are less stable than AA_60_300_cat2 by 73.6 and 36.8 kJ mol⁻¹ respectively and retain a furan six-membered ring structure resembling that of the neutral species. Finally, O1 protonation (AA_60_300_cat1) implicate the ring opening leading to an isomer less stable by 56.8 kJ mol⁻¹.

Table 13 reports the computed PA values of all AA_60_300 protomers. Comparing them, the carbonyl oxygen always results the preferentially protonated atom and the corresponding structure (AA_60_300_cat2) is characterized by a PA value of 861.6 kJ mol⁻¹ and a GB of 833.9 kJ mol⁻¹. The inclusion of the Grimme's dispersion has not changed the PA value that is in good agreement with the experimental result.

Table 13: *Computed PA and GB of protonated AA_60_300.*

	PA (kJ mol ⁻¹)	GB (kJ mol ⁻¹)
AA_60_300_cat1	809.7	780.8
AA_60_300_cat2	861.6	833.9
AA_60_300_cat4	789.6	757.4
AA_60_300_cat6	827.3	795.1

3.2 Protonated L-Ascorbic acid decomposition

Figure 42 shows the full-scan mass spectrum recorded from a solution of L-Ascorbic acid dissolved in a mixture of water and methanol.

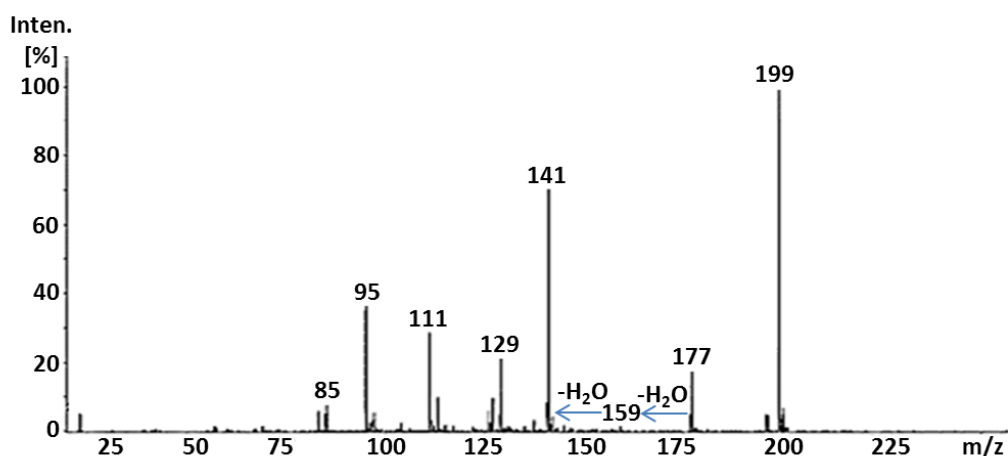


Figure 42: ESI mass scan of a 1×10^{-3} M solution of L-Ascorbic acid in H_2O MeOH 1:1 (V/V).

The ionic species at m/z 199 predictably corresponds to the sodium L-Ascorbic acid adduct, $C_6H_8O_6Na^+$, whereas the protonated form of Vitamin C is detected at m/z 177.

As in the case of the monosaccharides investigated in the previous Chapter, the source potentials applied for the ion generation and their transfer into the instrument analyser can activate the dehydration of the protonated ionic population. Indeed, the mass spectrum shows two peaks at m/z 159 and m/z 141 corresponding to the ionic intermediates obtained from the loss of one and two water molecules from the ionic species at m/z 177. In particular, the ion at m/z 159 has a lower intensity compared to that of the second intermediate at m/z 141.

As evidenced by the analysis of its fragmentation pattern, the sodium adduct at m/z 199 was found not to be the precursor of any other ion, whereas the protonated species at m/z 177 effectively represents the starting reactant ion of the L-Ascorbic acid decomposition process.

CAD experiments

The CAD mass spectrum of the ions at m/z 177 (Figure 43) demonstrates that the dehydration of protonated L-Ascorbic acid occurs in two consecutive steps leading to the ionic species at m/z 159 and 141, respectively.

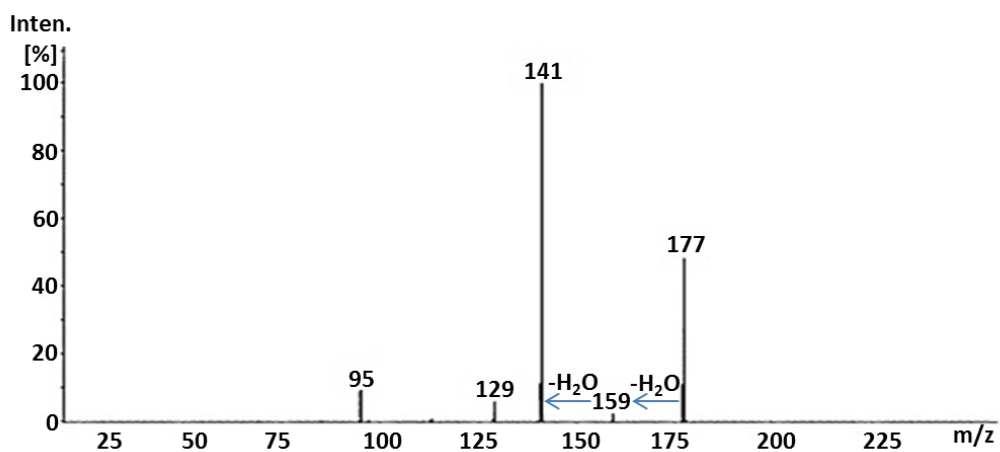


Figure 43: CAD mass spectrum of the ion at m/z 177.

Moreover, the ionic peak at m/z 95 may formally correspond to the final product of the L-Ascorbic acid decomposition reaction. This hypothesis has been confirmed by the CAD mass spectrum of the ionic intermediate at m/z 141 reported in Figure 44.

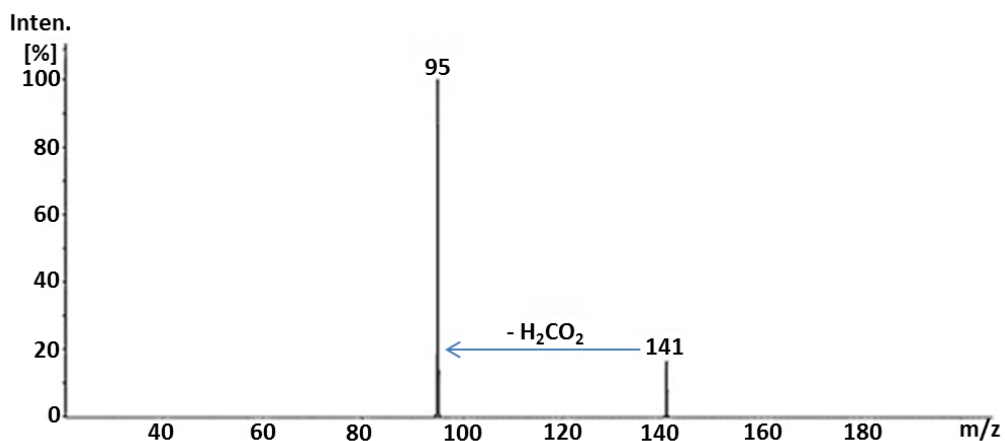


Figure 44: CAD mass spectrum of the ion at m/z 141 obtained from protonated L-Ascorbic acid.

Indeed, the fragmentation of this ionic species produces a single daughter ion at m/z 95 following the loss of a formic acid molecule as a neutral counterpart.

Energy resolved CAD experiments

Energy resolved CAD experiments have allowed us to measure the relative water loss dissociation energies.

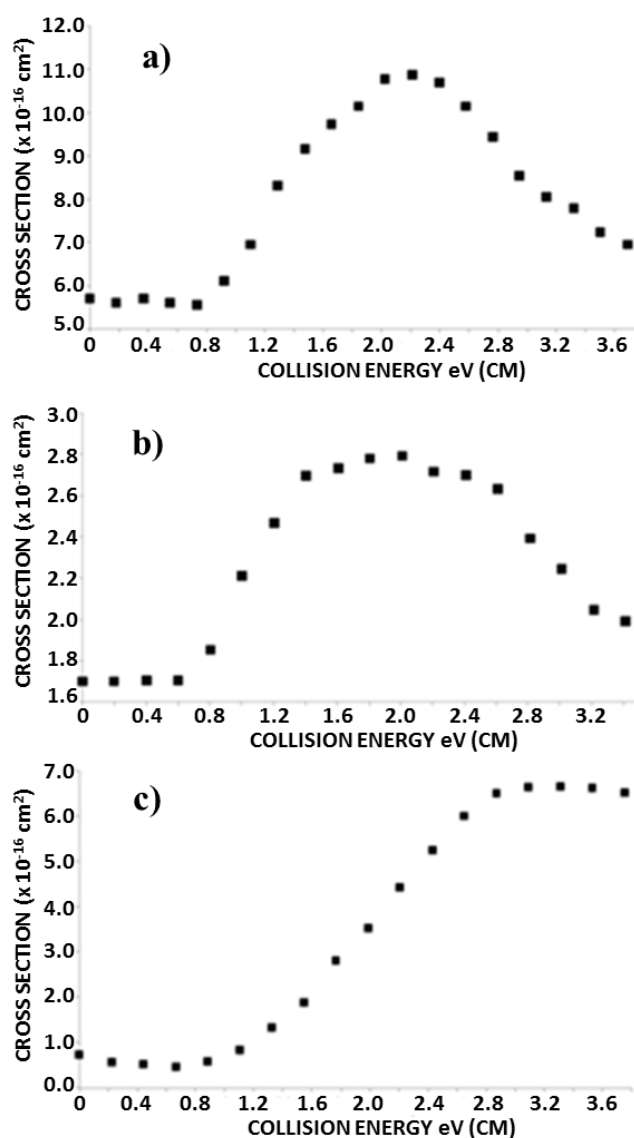


Figure 45: Energy-resolved CAD mass spectra of the ions a) at m/z 177 leading to the ion at m/z 159; b) at m/z 159 leading to the ion at m/z 141; c) at m/z 141 leading to the ion at m/z 95.

Figure 45 (panel a) shows the ER-mass spectrum of the ions at m/z 177 recorded at collision energies ranging from 0 to 5 eV (centre-of-mass collision energy). Focusing on the onset of the cross section curves, the loss of the first water molecule leading to the ion at m/z 159 arises at collision energies close to the nominal centre of mass energy of 0.8 eV.

The threshold energy relating to the second water loss was also measured and the energy-resolved CAD mass spectrum of the ions at m/z 159 is displayed in Figure 45, panel b. The second water loss is activated at a collision energy around 0.6 eV, a lower value if compared to the first water loss.

Finally, panel c of Figure 45 displays the ER-mass spectrum of the ion at m/z 141 leading to the ionic species at m/z 95. As evidenced by the analysis of the cross section curve onset, the loss of a formic acid molecule as a neutral counterpart occurs at collision energies close to the nominal centre of mass energy of 1.2 eV

Isotopic labelling experiments

In order to acquire more information about the reaction mechanism leading to the ionic species at m/z 95, a tandem CAD analysis has been realized by using L-¹³C-Ascorbic acid. As a result of the isotopic labelling on the C2 carbon, the m/z ratio of protonated L-Ascorbic acid shifts from 177 to 178. Consequently the m/z ratio of the two dehydration intermediates shift from 159 to 160 and from 141 to 142, respectively.

Interestingly, following step-by-step the decomposition of labelled L-¹³C - Ascorbic acid by tandem CAD experiments it is possible to observe that the final loss of the formic acid molecule obtained from the ionic species at m/z 142 involves the ¹³C carbon atom (Figure 46), an important result that must be considered in order to validate a possible L-Ascorbic acid decomposition mechanism.

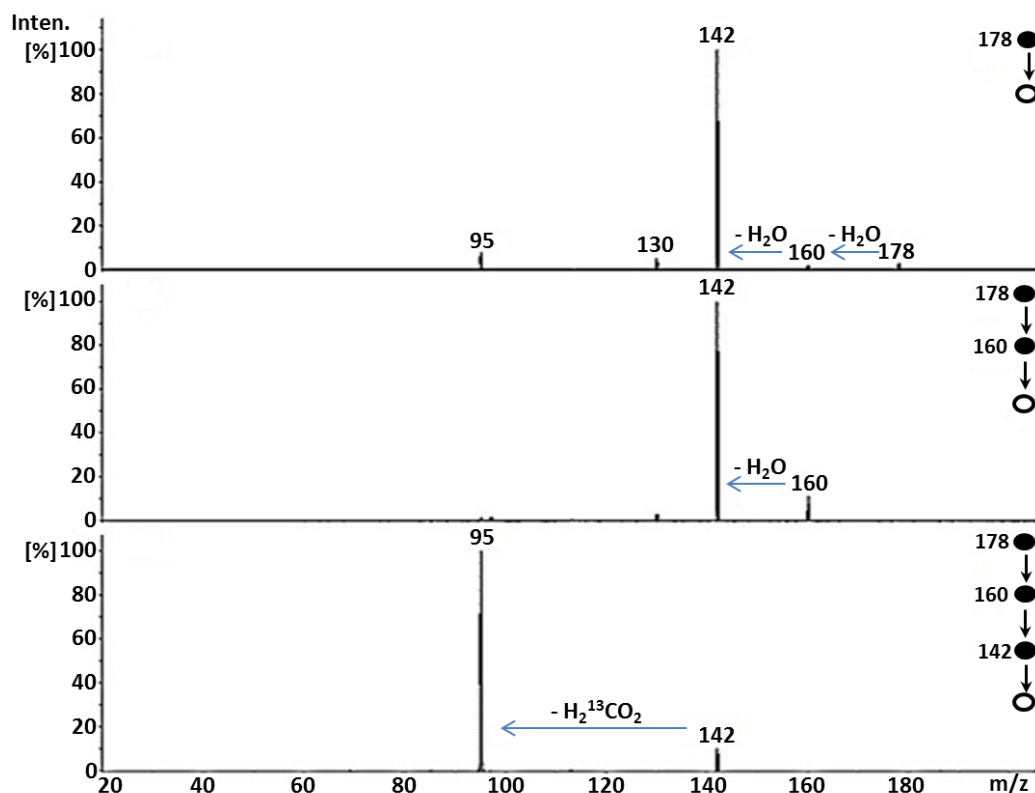


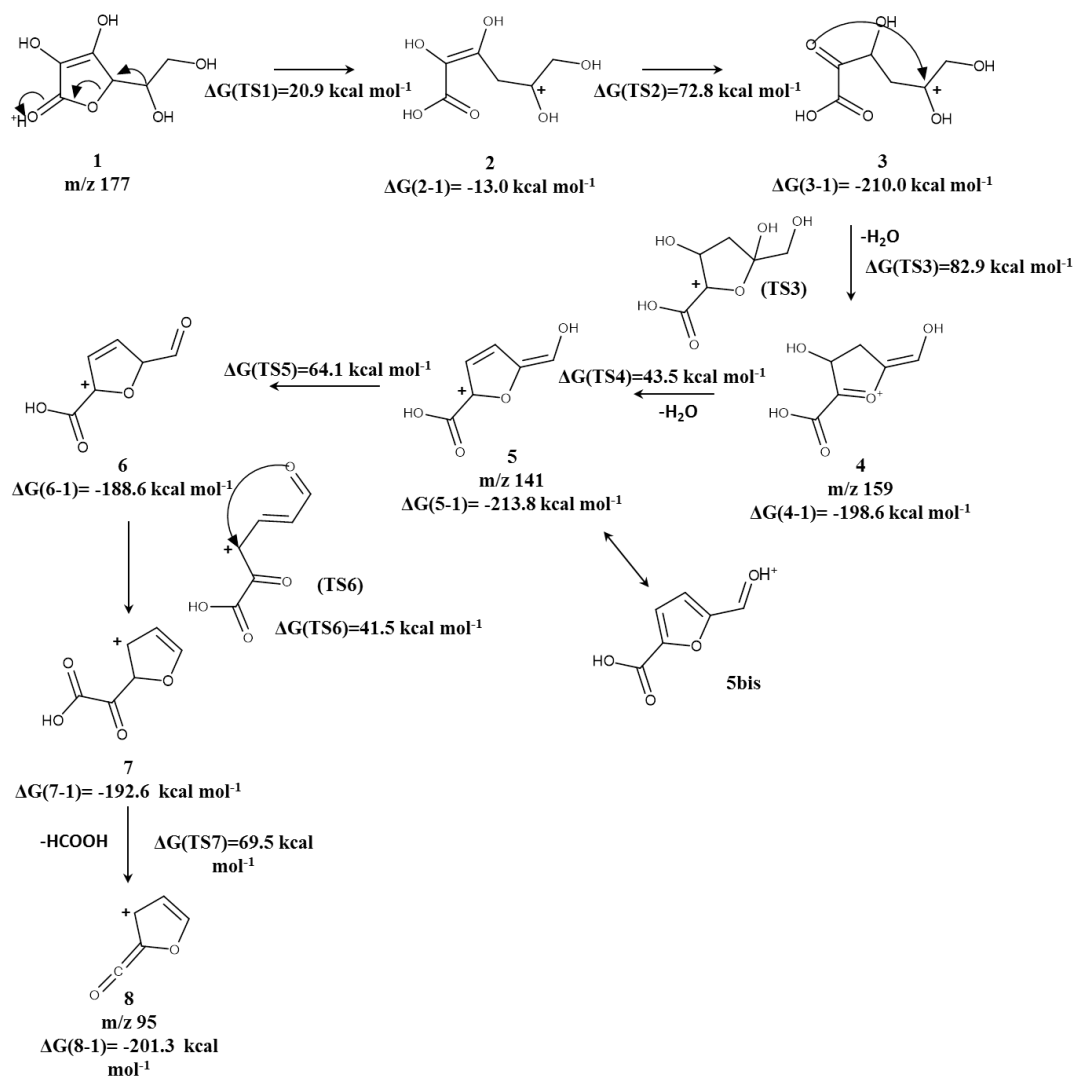
Figure 46: Tandem CAD mass spectra of a) protonated L - ^{13}C -Ascorbic acid at m/z 178; b) daughter ion at m/z 160 obtained as ionic product of the first water loss from the ion at m/z 178; c) daughter ion at m/z 142 obtained as ionic product of the second water loss from the ion at m/z 160 isolated in turn from the starting reactant ion at m/z 178.

Quantum mechanical calculations

Quantum mechanical calculations have allowed us to depict a reaction pathway which is satisfactorily consistent with the experimental results.

According to the hypothesized mechanism reported in Scheme 19 and the potential energy surfaces displayed in Figure 47, species **1** corresponding to the L -Ascorbic acid protonated at O2 (protomer AA60_300_cat2) undergoes a ring opening following an hydride shift from C6 to C5. This process leads to the formation of ion **2** and is characterized by an energetic barrier of $20.9 \text{ kcal mol}^{-1}$ ($\Delta G^\circ_{(\text{TS1})}$). The species **2** is $13.0 \text{ kcal mol}^{-1}$ more stable than the starting reactant **1** and isomerizes to the ion **3** overcoming a barrier of $72.8 \text{ kcal mol}^{-1}$ ($\Delta G^\circ_{(\text{TS2})}$) with an energetic gain of $197.0 \text{ kcal mol}^{-1}$. Ion **3** undergoes a cyclization through the

nucleophilic attack of the O2 oxygen to the C5 carbon. This process leads to the transition state **TS₃** which is prone to release the first water molecule forming the ion **4**. This ionic species formally corresponds to the ionic intermediate at m/z 159 and its formation from protonated L-AA dehydration is characterized by an energetic barrier of 59.8 kcal mol⁻¹.



Scheme 19: Hypothesized decomposition mechanism of L-Ascorbic acid computed at the B3LYP/6-31 + G(d,p) level of theory.

Ion **4** releases the second water molecule following a proton transfer from C4 to O3H in a process that is characterized by an energetic barrier of 43.5 kcal mol⁻¹ ($\Delta G^\circ_{(\text{TS4})}$). The ion **5** is 15.2 kcal mol⁻¹ more stable than the precursor species **4**

and corresponds to the second dehydration intermediate at m/z 141. Ion **5** represents a resonant structure of the protonated 5-formyl-2-furoic acid (**5bis**) and it can tautomerize into **6** by overcoming an energetic barrier of $64.1 \text{ kcal mol}^{-1}$ ($\Delta G^\circ_{(\text{TS5})}$). The species **6** rearranges forming an open structure (**TS6**) and the subsequent nucleophilic attack of the O6 oxygen to the C3 carbon produces ion **7**. An energetic barrier of $41.5 \text{ kcal mol}^{-1}$ ($\Delta G^\circ_{(\text{TS6})}$) separates **6** from **7**, but the rearrangement **6**→**7** has an energetic gain of $4.0 \text{ kcal mol}^{-1}$. Finally, the ion **7** easily evolves to the species **8** by releasing a formic acid molecule in a $8.7 \text{ kcal mol}^{-1}$ exoergonic process characterized by an energetic barrier of $69.5 \text{ kcal mol}^{-1}$. The loss of formic acid from the ion at m/z 141 is characterized by a barrier of $90.7 \text{ kcal mol}^{-1}$.

As a consequence, the hypothesized mechanism of the entire decomposition reaction results exoergonic by $-201.3 \text{ kcal mol}^{-1}$.

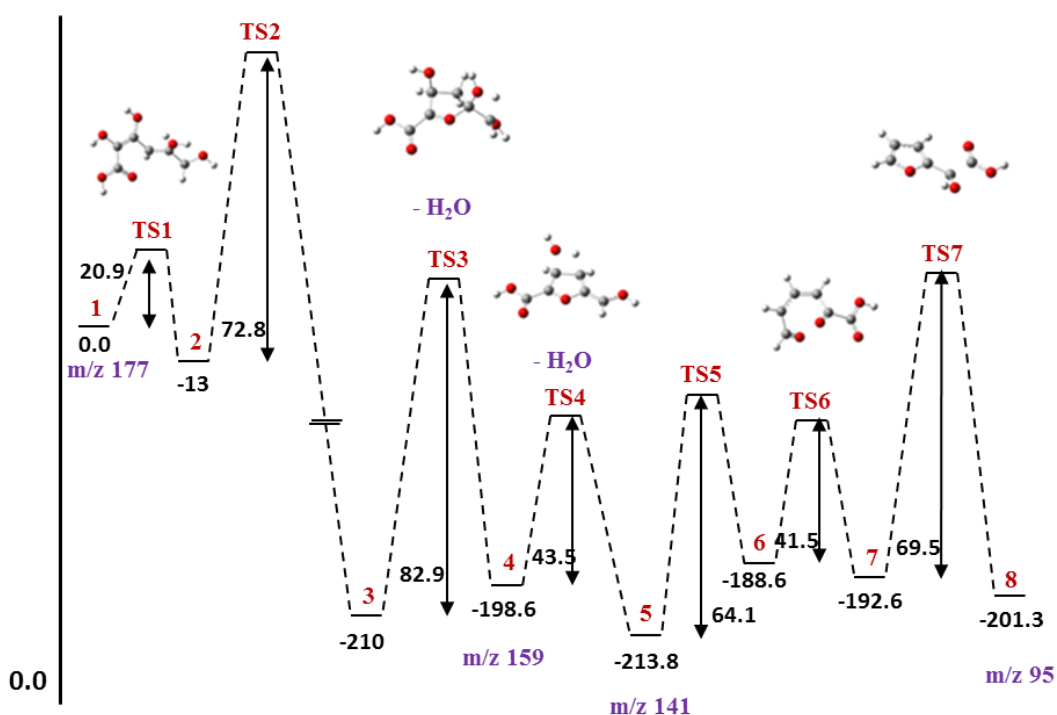


Figure 47: Geometries of the minima localized on the AA60_300_cat2 potential energy surface, optimized at the B3LYP/6-31 + G(d,p) level of theory.

3.3 Discussion

The knowledge of the proton affinity and gas-phase basicity values of a molecule in the gas phase is considered an ideal tool to detect its intrinsic molecular properties in the absence of the solvent.

These thermochemical parameters have been experimentally obtained in this work for L-Ascorbic acid and they are well comparable with the same values reported for polyfunctional molecules containing a carbonyl group as the basic site. As recently reviewed by Bouchoux,^[88] the proton affinity of unsaturated lactones is around 840 kJ mol^{-1} and the effect of intramolecular hydrogen bonds may enhance this value up to $40\text{-}50 \text{ kJ mol}^{-1}$.

In this regard, the joint application of the Cook's kinetic method and quantum mechanical calculations has allowed us to highlight the structure of gaseous protonated L-Ascorbic acid, identifying the oxygen atom (O2) of the carbonyl moiety as the most basic site and the AA_60_300_cat2 conformer as the most stable species. Indeed, the presence of other protomers under the experimental conditions has been reasonably excluded on the basis of energetic considerations.

The experimental PA value of $875.0 \pm 12 \text{ kJ mol}^{-1}$ results to be in agreement with the value of $861.6 \text{ kJ mol}^{-1}$ computed at the B3LYP/6-31 + G(d,p) level of theory. Besides, a $\Delta_p S$ value of $108.9 \pm 2 \text{ J mol}^{-1}\text{K}^{-1}$ and a GB of $842.5 \pm 12 \text{ kJ mol}^{-1}$ at 298 K were also experimentally obtained by using the same approach. The measurement of these fundamental parameters and the characterization of protonated AA structure represent the first step towards the elucidation of AA degradation mechanism to furan compounds in the gas phase.

Similarly to the dehydration of the sugars discussed in Chapter 2, the protonation of L-Ascorbic acid is a process that activates the decomposition reaction converting it to furan derivatives. This hypothesis is confirmed by the presence in the ESI mass spectrum of acidic solution of L-Ascorbic acid of the protonated ions at m/z 177 together with the ionic intermediates at m/z 159 and 141 arising from the loss of one and two water molecules respectively and a final product at m/z 95.

Contrary to what was observed in the case of the sugars, protonated L-Ascorbic acid at m/z 177 is stable and can be detected at sufficiently high intensity,

allowing us the characterization of the starting reactant ions by means of CAD experiments. This evidence can be explained by a higher energetic barrier of the first dehydration of L-Ascorbic acid compared to that calculated for the first dehydration of the previously investigated protonated sugars. By analysing the theoretical data, protonated L-Ascorbic acid loses the first water molecule following a series of unimolecular rearrangements overcoming an energetic barrier of 59.8 kcal mol⁻¹. As a consequence, the water loss occurs through an open-chain intermediate resulting from an hydride shift and a subsequent isomerization. On the contrary, the first dehydration of protonated sugars reported in Chapter 2 is always assisted by the emiacetalic oxygen atom leading to a carbocationic intermediate in a process that is only 4-8 kcal mol⁻¹ endothermic.

Since protonated L-Ascorbic acid at m/z 177 can survive to the source conditions, it has been submitted to energy resolved CAD experiments in order to measure the relative dissociation energies. According to the experimental results, the first water loss leading to the ionic species at m/z 159 occurs with an energetic barrier higher than that relating to the second dehydration process forming the ion at m/z 141 (0.8 eV versus 0.6 eV). This evidence has been confirmed by the theoretical calculations predicting an energetic barrier of 59.8 kcal mol⁻¹ for the first water loss and 43.5 kcal mol⁻¹ for the second dehydration reaction. This trend reflects the relative ionic abundances observed in the ESI mass spectrum where the ionic species at m/z 159 is detected at very low intensity whereas the intermediate at m/z 141 shows a higher ion signal.

The ionic intermediate at m/z 141 decomposes by releasing a formic acid molecule leading to the final product at m/z 95. The highest energetic barrier of 1.2 eV among those experimentally measured is associated to this last decomposition event, in excellent agreement with the barrier theoretically predicted.

Theoretical calculations have suggested that the final loss of a formic acid molecule may occur from the ionic species at m/z 141 following a tautomerization process and a subsequent rearrangement through an open structure transition state (TS6). This mechanism is in good agreement with the results of the isotopic labelling experiments performed on the L-¹³C-Ascorbic acid. According to the

experimental and theoretical data, the release of a formic acid molecule as a neutral counterpart involves the ^{13}C carbon and occurs through a proton shift from C2 to the labelled carbon. The species at m/z 95 thus obtained results to be $201.3 \text{ kcal mol}^{-1}$ more stable than the starting reactant ion at m/z 177 and shows a structure strictly related to furfural.

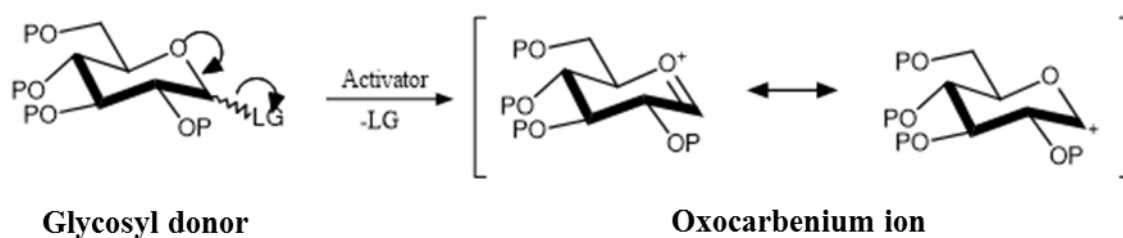
This ion represents the final product of AA decomposition reaction, but it has already been detected in the gas phase by Eberlin et al.^[89] According to this study, the ionic species at m/z 95 is the stable product of a carbonylation reaction between gaseous halocarbonyl cations and furan.

4. Glycosylation reaction

Chemical glycosylation is a coupling reaction that involves two sugar substrates forming a new *O*-linkage, known as “*glycosidic*” bond.

In a typical glycosylation one building block, named glycosyl *donor*, is a mono- or oligo-saccharide equipped with a suitable leaving group (LG) at the anomeric position, whereas the other building block, termed glycosyl *acceptor*, is a mono- or oligo-saccharide having an unprotected hydroxyl group acting as a nucleophile. Generally, all other functional groups on both glycosyl donor and acceptor counterparts are masked with temporary protecting groups (P) in order to increase the chemoselectivity of the reaction.

Schemes 20 and 21 show the general mechanism of the chemical glycosylation.



Scheme 20: 1 step: *Activation of the glycosyl donor.*

The first step consists in the interaction between an *activator* (or *promoter*) and the glycosyl donor resulting in the dissociation of the leaving group and the formation of a carbocationic intermediate.

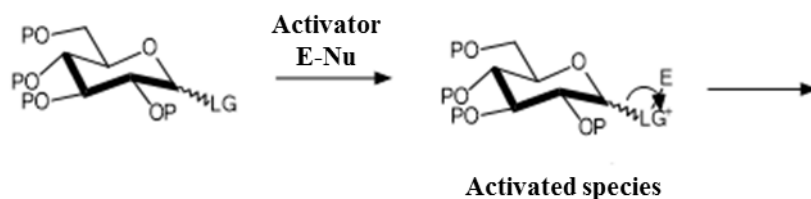
The simplest leaving group is the $-OH$ group, naturally found in the monosaccharides, and requires acid catalysis to be activated in order to promote the loss of a water molecule from the anomeric position. This specific process is known as *Fischer glycosylation*.

More effective leaving groups, such as halides, thioethers or imidates, are commonly used in the glycosyl donors employed for the synthesis of glycosides. Moreover, the leaving group needs to be activated by the use of a specific promoter, as reported in Table 14.

After the formation of the carbocationic intermediate, the glycosyl acceptor can perform a nucleophilic attack from the top or from the bottom face of the ring

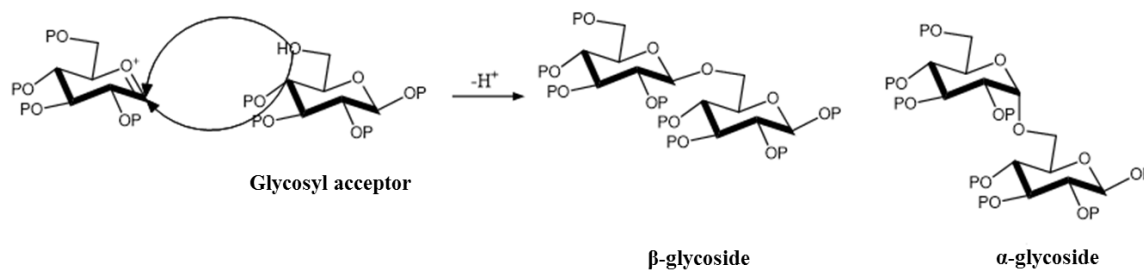
resulting in the formation of a new stereogenic centre and therefore a mixture of two compounds, (*1,2 cis*) α - and (*1,2 trans*) β -glycosides (Scheme 21).

Table 14: Typical glycosyl donors and respective activators.



	Leaving group	Activator (E-Nu)
Hydroxyl	-OH	H ⁺
Halides	-Br; -Cl; -I; -F	Silver salts
Thioethers	-SPh; -STol	N-iodosuccinimide/triflic acid
Imidates		H ⁺

The entire process can be ascribed to a nucleophilic substitution reaction, following an S_N1-like mechanism where the formation of the oxocarbenium ion intermediate represents the rate-determining step (slow step) and the generation of the final products corresponds to the fast step of the reaction. Nevertheless, examples of S_N2-like mechanism are also reported in literature.^[90-92]



Scheme 21: II step: Nucleophilic attack performed by the glycosyl acceptor.

Both α - and β -glycosidic residues are equally found in a variety of natural molecules according to their biological role and the therapeutic potential as lead compounds for drug and vaccine discovery. Therefore, the study of carbohydrate-containing chemicals is considerably challenging due to the low availability of pure sample from natural sources. As a consequence, the only approach to provide chirally pure material consists in resorting to chemical or enzymatic synthesis that allow one to obtain either α - and β -glycosides with well-defined stereochemistry. This represents the main reason why chemical *O*-glycosylation is still considered a wide-open field of study in modern synthetic chemistry.

Over the years, it has become clear that the reactivity of the glycosyl donor is directly correlated to the nature of the protecting groups. The concept of *armed* and *disarmed* glycosyl donors was theorized by Bertram-Fraser Reid^[93] referring to the increased reactivity of benzylated (*armed*) over benzoylated (*disarmed*) glycosyl donors. This phenomenon, first observed in 1982,^[94] originates from the greater electron-withdrawing capability of ester blocking groups over other ether protecting groups. Later, Bols et al.^[95] have extended this notion to *superarmed* glycosyl donor by realising that hydroxylic functional groups of carbohydrates are less electron-withdrawing toward the anomeric centre when they are in axial configuration than in equatorial. Hence, glycosyl donor conformers with more axial function groups are generally more reactive toward the chemical glycosylation. Figure 48 shows examples of disarmed, armed and superarmed donors, respectively.

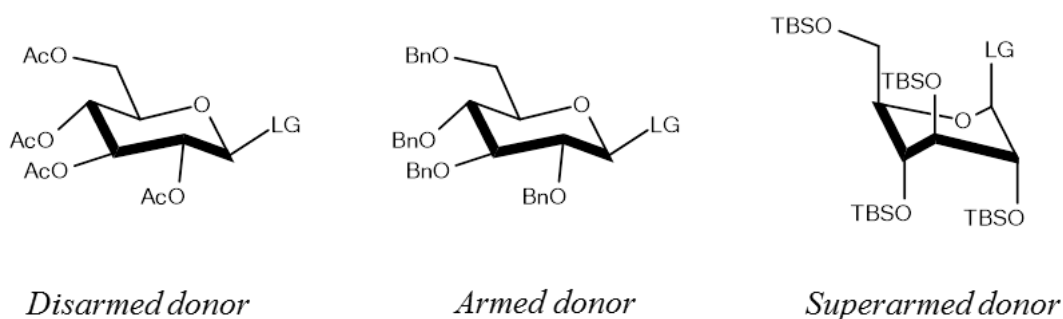
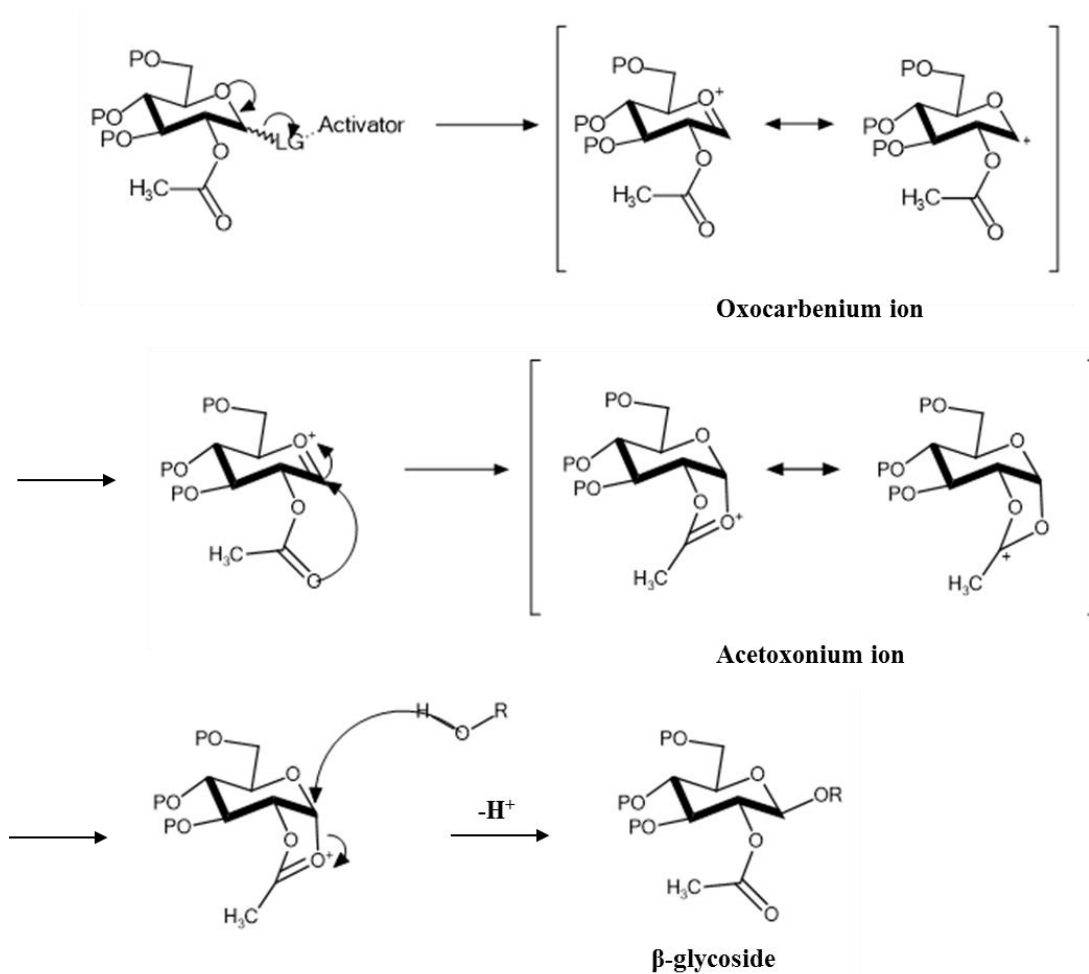


Figure 48: A series of glycosyl donor types. Ac: Acetyl group; Bn: Benzyl group; TBS: tert-butyldimethyl silyl group.

Further achievements in this field concern the possibility to control the stereochemical outcome of the glycosylation reaction that is strictly correlated to the nature of the protecting groups, especially that bound at the neighbouring C2-position.

The employment of a C2-participating group, typically equipped with a carboxylic moiety, predominantly results in the formation of a β -glycoside (Scheme 22).

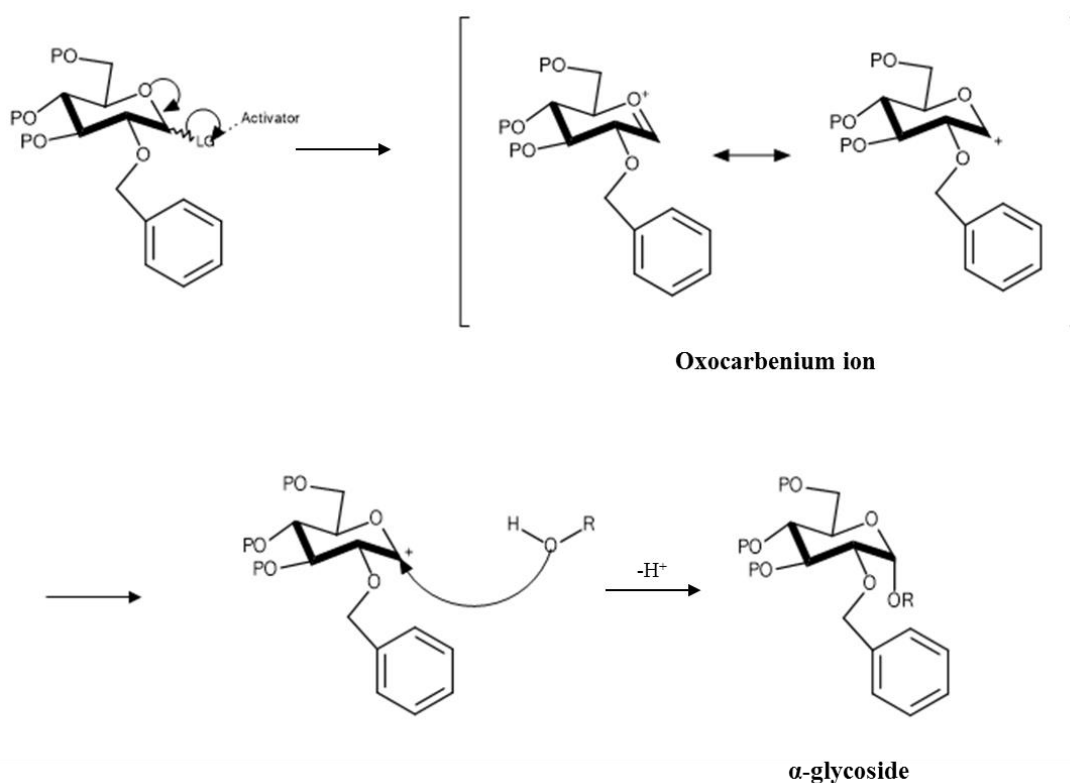


Scheme 22: Neighbouring group participation mechanism (ester protecting group at C2).

As previously reported, the first step of glycosylation allows for the dissociation of the leaving group and the generation of the carbocationic intermediate, known as the oxocarbenium ion. In the presence of an acetyl protecting group bound at C2-position, the oxocarbenium ion can evolve to an

apparently more stable acetoxonium ion^[96] that blocks the attack from the bottom face of the ring predominantly leading to the formation of the β -glycoside.

Alternatively, the absence of a C2-carboxylic participating group, as in the case of benzylic blocking group (Scheme 23), allows for either attack from the bottom or top face of the ring, but the formation of an α -glycoside usually predominates since this product is favoured by the “*anomeric effect*”.



Scheme 23: Glycosylation mechanism in the case of ether protecting group at C2.

This phenomenon, first observed by Edward,^[97] is crucial for defining the stereochemistry of processes taking place at the anomeric centre of sugars and consists in a double stabilizing effect. First of all, the axial orientation of C1–OR minimizes the repulsive interactions between the lone-pair electrons of the anomeric substituent (O-1) and those of the ring oxygen (O-5). Secondly, an axial substituent is stabilized through the hyperconjugation due to the periplanar orientation existing between the anti-bonding orbital of C-1 and the non-bonding orbital of O-5. This stabilization effect is absent in the case of β -anomers where

the two above-mentioned orbitals placed in different planes are unable to interact (Figure 49).

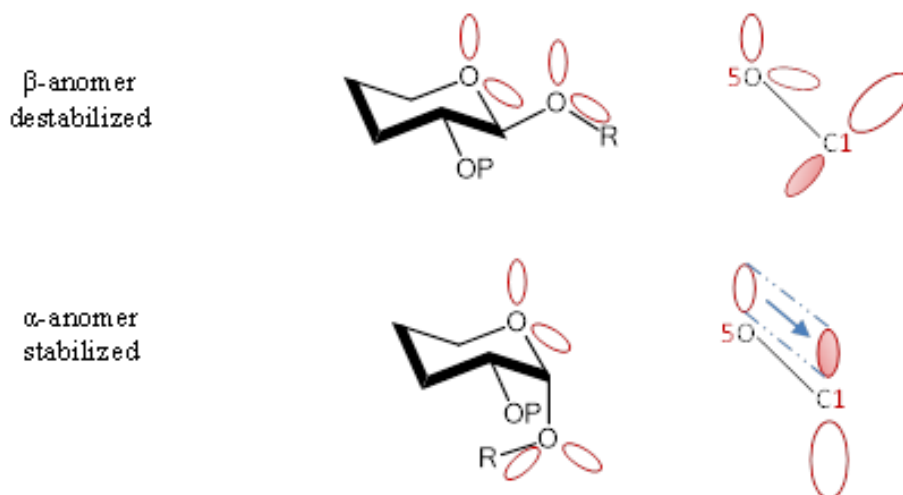


Figure 49: The “anomeric effect”, β -anomer versus α -anomer.

Despite the two hypothesized pathways, a complete stereoselectivity control is difficult to achieve. Although one of the two anomeric products is thermodynamically favourable, small amounts of the other one are often obtained. For this reason the structural characterization of the carbocationic intermediate (*oxocarbenium* ion or *acetoxonium* ion) is crucial to confirm the postulated reaction mechanisms.

As extensively discussed in the Introduction, the short life-time and low concentration of the reaction intermediates may hinder their isolation and identification in solution by means of X-ray crystallography, Nuclear Magnetic Resonance (NMR) and IR spectroscopy techniques. Hence, considering the ionic nature of the transient carbocationic species under investigation, the “gas-phase” approach can represent a valid alternative.

The combination of sophisticated gas-phase methods and quantum mechanical calculations has provided several strategies to study the structures of carbohydrates in *vacuo*.

In particular, ion mobility mass spectrometry (IM-MS) and action spectroscopy are two innovative structure-sensitive gas-phase approaches that can be efficiently

used to face the difficulties encountered in glycan characterization. Generally, the structures of saccharides are harder to investigate than other biomolecular compounds (peptides and oligonucleotides) owing to their complex regio- and stereochemistry. The information achievable by using conventional mass spectrometric methods is often limited to carbohydrate composition and connectivity. Indeed, most sugars show the same elemental composition and they cannot be distinguished according to their m/z ratio. As a consequence, isomers only differing in the orientation of chemical substituents at the stereogenic centres need to be chemically derivatised prior to be analysed.

Ion mobility spectrometry (IMS), first introduced by Cohen and Karasek^[98] in 1970 with the original name of plasma chromatography, is an analytical technique able to highlight the gas-phase conformation of ionic species. In particular, IMS measures the time that ions propelled by a weak electric field need to traverse a cell through a counter-flowing neutral gas, such as argon, helium or nitrogen. As a result, compact ions undergoing fewer collisions with the neutral gas cross the cell faster than the ions having an extended structure.

This method coupled with mass spectrometry (IM-MS) allows one to distinguish ions on the basis of their mass-to-charge ratio and subsequently to separate species sharing the same m/z , but different shapes through the measurement of their drift time.

Recently, the effectiveness of the IM-MS approach has been probed to successfully separate connectivity and configurational isomers of carbohydrates,^[99] demonstrating high resolution power and sensitivity to small structural differences.

Another approach to structurally characterize carbohydrates consists in the employment of laser spectroscopy.

Gas-phase infrared spectroscopic methods couple tandem mass spectrometry and IR optical spectroscopy in order to investigate specific vibrational modes of a mass-to-charge selected ion without the occurrence of interferences due to the solution environment.^[100-102] In this regard, action spectroscopy is particularly advantageous because structural details unavailable from more conventional MS/MS methodologies can be obtained from an IR-spectrum. Simultaneously,

biological molecules can be vaporized, ionized and manipulated by using a variety of effective gas-phase approaches (*electrospray ionization-ESI*, *matrix-assisted laser desorption ionization-MALDI*), as alternatives to the conventional laser desorption.^[103]

The main experimental methods for the investigation of molecular vibration modes in the gas phase are the *messenger* technique and the *infrared multiple photon dissociation* (IR-MPD) technique, both based on the dissociation of charged clusters or molecules induced by wavelength-selective absorption of IR radiation. This phenomenon allows the reconstruction of a “*surrogate*” IR spectrum from a series of mass spectra recorded by monitoring the fragmentation yield as a function of different wavelength radiations emitted from a tunable laser.

The main problem of this strategy is the low energy associated to a single IR photon, much lower than the threshold dissociation energy commonly reported for most molecules. Therefore, an IR-photo dissociation spectrum can be recorded employing two different approaches, by the generation of weakly bound clusters having bond energies not exceeding a few tens of kJ mol^{-1} (*messenger* technique) or by using a laser source sufficiently powerful to emit multiple photons (from ten to hundreds) all absorbed by a single ion (*IR-MPD* technique).

The messenger spectroscopy, introduced in the 1980s by Y. T. Lee and co-workers,^[104] can be eventually applied to the gas-phase study of biomolecules. The main limitation of this technique lies in the fact that the supersonic expansion, needed to achieve ions tagged with a small molecule or rare gas atom, does not allow for a gently transfer of biological molecules to the gas phase. In fact, the analytes undergoing this process are typically ionized by electron impact or by a corona discharge that can damage biomolecules characterized by a fragile structure. For this reason, IR-MPD technique has predominantly been used to study the vibrational excitations of biomolecular ions.^[100,102]

This method allows for the dissociation of covalent bonds within molecules that can be routinely detected in a tandem mass spectrometer. However, the requirement of multiple IR photons to activate the dissociation leads to highly excited species, increasing the number of populated quantum states. The resulting

broadening and shifts in the position of absorption bands can hinder the interpretation of the vibrational spectra.

Figure 50 displays the IR-MPD spectra of two monosaccharide epimers derivatised with a $C_2H_4NH_2$ and a $C_5H_{10}NH_2$ linker, respectively.

Despite the structural differences existing between the two molecules, both spectra share a broad absorption band in the range of $1000-1150\text{ cm}^{-1}$ and another low-intensity absorption band around 1490 cm^{-1} . Hence, the general appearance of the two spectra is very similar, reflecting the limited resolution achievable by using IR-MPD methods.^[105] As a result, the two monosaccharide derivatives are indistinguishable by their IR signatures preventing the acquisition of clear information about the structural details of the species under study.

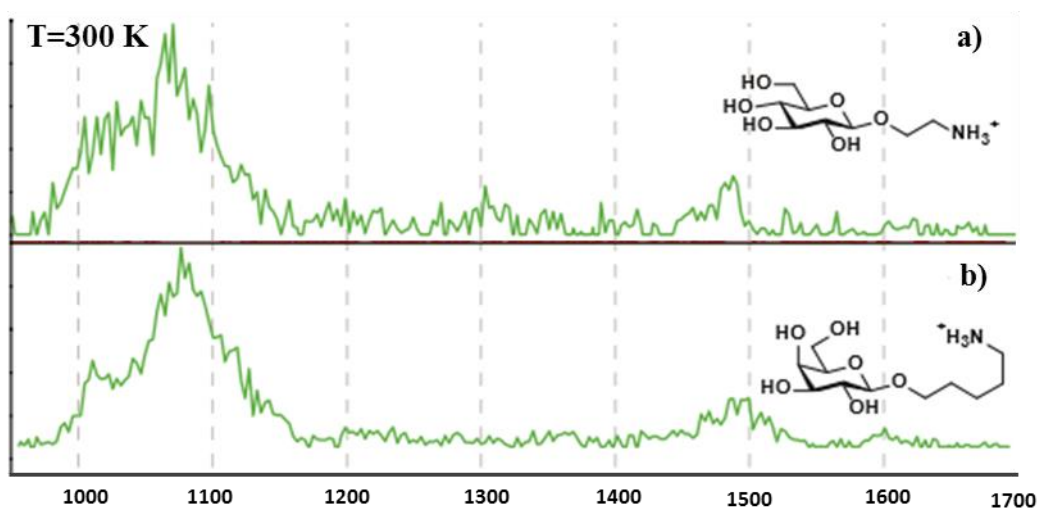


Figure 50: IR spectrum of a positively charged β -glucose derivative a). IR spectrum of a positively charged β -galactose derivative b). Both spectra were recorded in the fingerprint region at room temperature using the IR-MPD technique (data taken and adapted by Ref. [106]).

An effective strategy to overcome the scarce applicability of the IRMPD technique consists in reducing the energetic contents of the molecules implementing a cooling down process. This approach allows one to reduce the number of freedom degrees and simultaneously the number of conformations the molecules can assume at room temperature. As a consequence, the spectral congestion is markedly reduced and the sharp absorption lines obtained promote the unambiguous assignment of the spectral bands.

In this regard, cryogenic multipole ion traps have paved the way to the gas-phase investigation of molecular ions at sub-Kelvin temperatures.

According to the Gerlich's studies,^[107] ion temperatures around 6 Kelvin can be reached by coupling an rf ion trap to the head of a closed-cycle He refrigerator. The cold trap is usually placed between the two quadrupoles of a tandem mass spectrometer and the ions stored are cooled down by the pulse of Helium gas. Various action spectroscopy schemes have been designed combining cold ion traps with tunable UV/vis and IR lasers.^[108]

An alternative approach to study "cold" molecular structures in the gas phase is represented by the employment of superfluid helium droplets as a sort of nanocryostats.^[109-112] According to this method, the ions of interest, embedded inside nano droplets consisting of 10^3 - 10^{10} atoms of superfluid helium, are allowed to achieve an equilibrium temperature of ~ 0.37 Kelvin that drastically reduces their internal energy.

Subsequently, the embedded species can be interrogated by an infrared radiation and the absorption of resonant laser photons leads to the ejection of the ions from the helium droplets. Monitoring the ejection yield as a function of the wave-length of the emitted radiation allows one to obtain well-resolved infrared spectra of ultra-cold molecules.

Such an apparatus has been developed at the Fritz Haber Institute of Berlin by G. Von Helden et al.^[113-115] and it has been recently used to study the charge-induced unzipping of proteins and to structurally characterize a series of isomeric oligosaccharide ions.^[116,117] In both studies the vibrational fingerprint obtained for these cooled biomolecular ions exhibits well-resolved absorption bands that are diagnostic for minute structural variations.

In order to exemplify the unequivocal effectiveness of this method, Figure 51 reports the IR spectra of positively charged β -glucose (panel a) and β -galactose (panel b) derivatives acquired at 0.37 Kelvin by using the helium droplet approach.

The comparison of these two spectra with those recorded for the same molecules by using IR-MPD technique (Figure 50) shows that IR spectra with many well-resolved absorption bands can be obtained only by cooling down the

ions at sub-Kelvin temperature. In this case (Figure 51) the two monosaccharides can unambiguously be distinguished by their distinct absorption patterns in the spectral range between the wavenumbers of 950 cm^{-1} and 1700 cm^{-1} . In sum, the unprecedented resolving power of the cold-ion spectroscopy provides a spectral fingerprint that is unique for each monosaccharide.

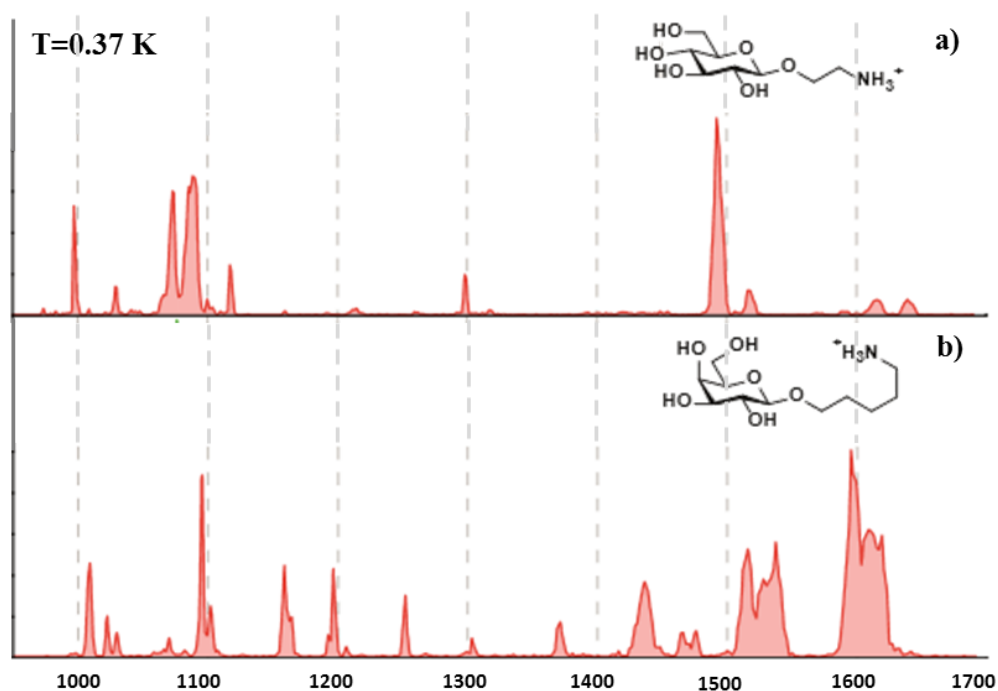


Figure 51: IR spectrum of a positively charged β -glucose derivative a). IR spectrum of a positively charged β -galactose derivative b). Both spectra were recorded in the fingerprint region at 0.37 Kelvin by using the helium droplet approach (data taken and adapted by Ref. [106]).

These excellent results have also been obtained when glycans only differ in the stereochemistry at single carbon atoms, highlighting the potential of helium droplet approach to circumvent the impediments encountered over the years in saccharide analysis.^[117] Additionally, classic and quantum mechanical calculations can contribute to assign a precise structural conformation to the carbohydrates under study through the generation of corresponding theoretical infrared spectra.

Taking into account the unequivocal advantages of the ion mobility mass spectrometry and ultra-cold spectroscopy techniques, both methods were applied

to structurally characterize the carbocationic intermediate arising along the chemical glycosylation pathway. Owing to its transient nature the oxocarbenium ion has never been isolated before and considering the key role played for the positive outcome of the reaction, the investigation of its structural details represents an extraordinary challenge.

In particular, the conversion of the oxocarbenium ion into the acetoxonium form when the C2 is masked with a carbonyl-equipped protecting group is a crucial step to control the glycosylation stereoselectivity and the final yield of the entire reaction. For this reason, the experimental confirmation of the oxocarbenium ion structure may contribute to elucidate reaction mechanisms that to best of our knowledge are only theoretically hypothesized.

4.1 Structural characterization of the oxocarbenium ion intermediate

A set of four glycosyl donors derivatised with different protecting groups displayed in Figure 52 were analysed in this work.

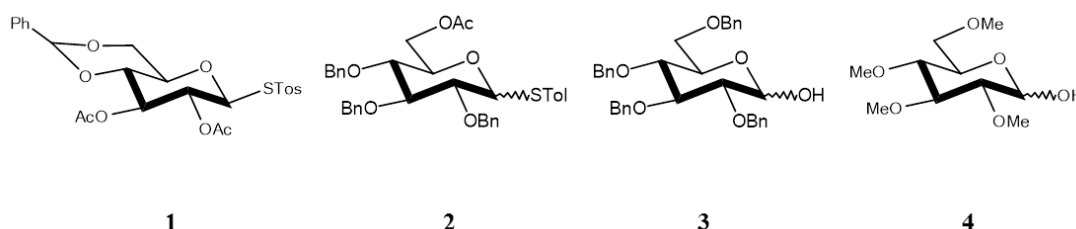


Figure 52: Glycosyl donors 1) 4-Methylphenyl 2,3-di-O-acetyl-4,6-O-benzylidene-1-thio-β-D-glucopyranoside; 2) 4-Methylphenyl 6-O-acetyl-2,3,4-tri-O-benzyl-1-thio-D-glucopyranoside; 3) 2,3,4,6-Tetra-O-benzyl-D-glucopyranose; 4) 2,3,4,6-Tetra-O-methyl-D-glucopyranose.

Carbohydrate **1** is a model of glycosyl donors equipped with a C2-carboxylic participating group owing to the presence of an acetyl group bound at C2 position. Conversely, glycoside **2** shows a C2-benzylic non-participating group and an acetyl blocking group at C6 position. This specific compound was chosen in order to verify the occurrence of a nucleophilic attack between the carbonylic oxygen of the acetyl group and the C1 anomeric carbon.

Glycoside **3** is characterized by an ether protecting group bound at C6 position in place of the acetyl group present in glycoside **2**. Finally, glycoside **4** was employed as a non-aromatic reference standard.

The possibility to effectively generate the carbocationic intermediate of interest in the gas phase was evaluated by choosing samples equipped with different leaving groups, the 4-methylphenyl thioether group for glycosides **1** and **2** and the most common hydroxyl group for glycosides **3** and **4**.

Figure 53 shows the full-scan mass spectrum obtained from a solution of glycoside **1**. The ionic population is dominated by two characteristic peaks at m/z 481 and 939, corresponding to the $[(\mathbf{1})\text{Na}]^+$ and $[(\mathbf{1})_2\text{Na}]^+$ sodium adducts, respectively. The analysis of their fragmentation patterns has revealed that they are not the precursor of any other ion, but all efforts aimed to reduce the sodium concentration in solution have been proved to be useless.

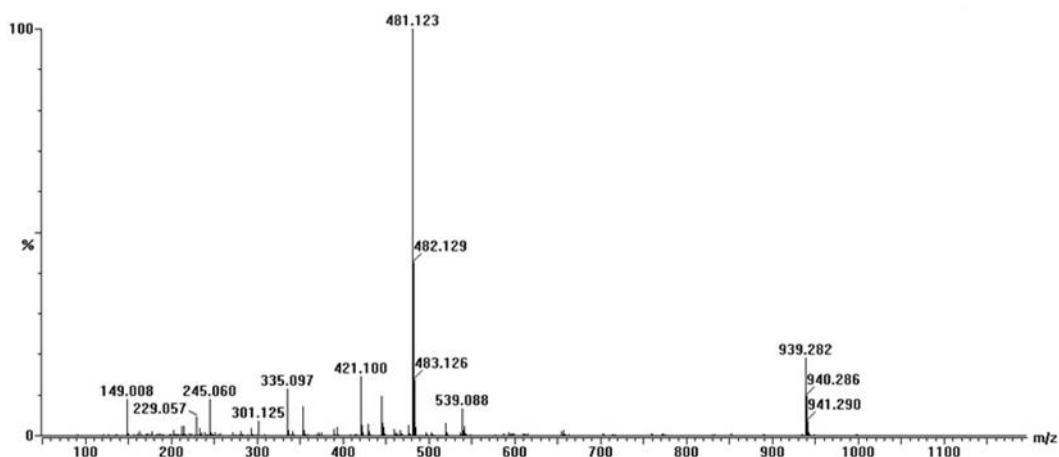


Figure 53: nano-ESI mass scan of a 1×10^{-3} M solution of sample **1** in H_2O (0.1% $HCOOH$)/ $MeOH$ 1:1 (V/V).

As reported for the monosaccharides discussed in Chapter 2 ion at m/z 459, corresponding to the protonated glycoside **1**, is present at very low intensity. It is reasonable to suppose that also in this case the energy excess deriving from the protonation may activate the reaction leading to the ion at m/z 335 that corresponds to the carbocationic species of interest.

An almost superimposable behaviour has been observed from the analysis of glycoside **2**.

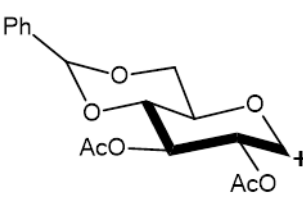
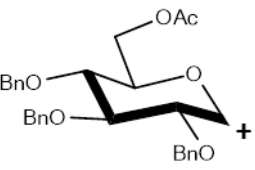
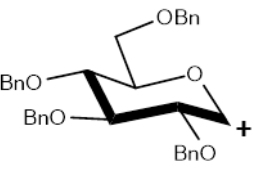
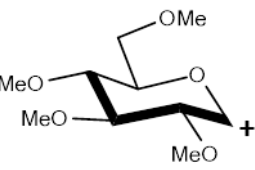
Conversely, the nano-ESI mass spectra of the glycosides **3** and **4** have highlighted a progressive decrease in the intensity of the corresponding carbocations, thus proving that the hydroxyl is a worse leaving group than the thioether one for the gas-phase oxonium ion generation.

After isolating the oxonium ion, its collisional cross section (CCS) was measured. Table 15 reports the CCS experimentally calculated for each carbocation derived from the glycosides **1**, **2** and **3**, respectively. The CCS measurement of the oxonium ion arising from glycoside **4** has been hindered by an excessively low intensity under the source conditions.

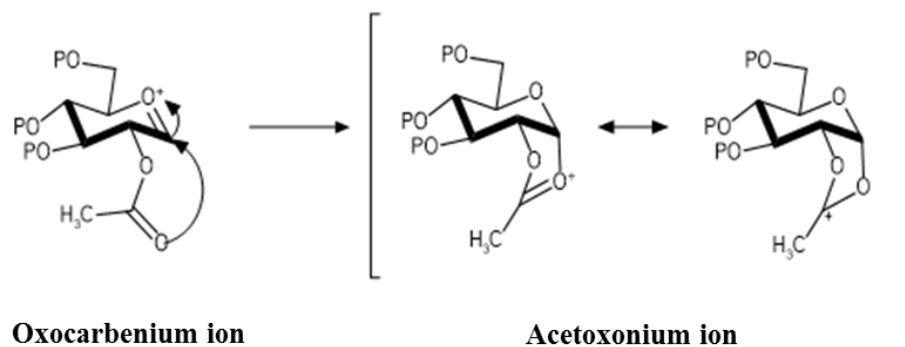
As expected, the lowest collisional cross section value corresponds to the oxonium ion obtained from glycoside **1** having the most compact structure. On the other hand, the carbocationic species arising from glycoside **3** is characterized by

the highest CCS among the other samples owing to the steric hindrance of four benzylic blocking groups.

Table 15: Collisional cross section measurements of the carbocationic species arising from each glycosidic sample.

Glycoside	Oxocarbenium ion	CCS (Å ²)
1		108.9
2		145.76
3		156.55
4		—

Considering the effectiveness of ion mobility instrumentation in successfully separating connectivity and configurational isomeric carbohydrates, the possibility to discriminate between the oxocarbenium and the acetoxonium structures has been probed. Indeed, in the presence of an acetyl protecting group bound at C2-position, as in the case of glycoside **1**, the oxocarbenium ion thus obtained can evolve to an acetoxonium ion through the nucleophilic attack performed by the carbonylic oxygen of the acetyl group to the anomeric carbon C1 (Scheme 24).



Scheme 24: Representation of the oxocarbenium-acetoxonium ion conversion.

Owing to the minute structural differences existing between these isomeric ions, it wasn't possible to distinguish the two conformers on the basis of their arrival time distributions (ATD). As reported in Figure 54, a single drift peak was derived after the ions at m/z 335 have traversed the ion mobility cell.

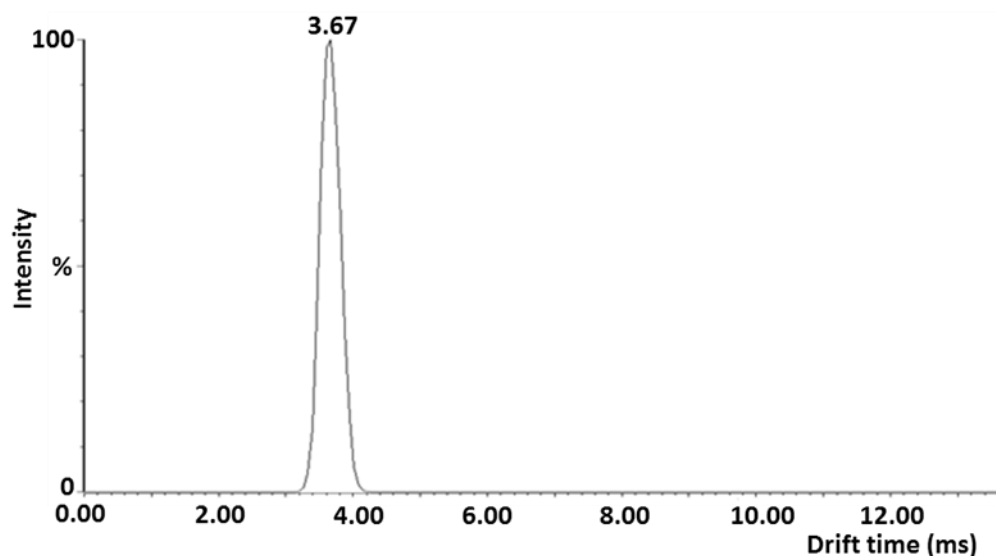


Figure 54: Arrival time distribution of the carbocation at m/z 335 obtained from glycoside **1**.

This experimental evidence has also been confirmed by theoretical results that calculated the same CCS value for both the oxocarbenium and the acetoxonium structures.

Since the ion-mobility technique does not seem to have a resolution power sufficiently high to achieve this specific conformer discrimination, the glycoside **1** has been analysed by means of Ultra-cold helium droplet spectroscopy.

Figure 55 displays the IR spectrum of the oxonium ion at m/z 335 arising from glycoside **1**.

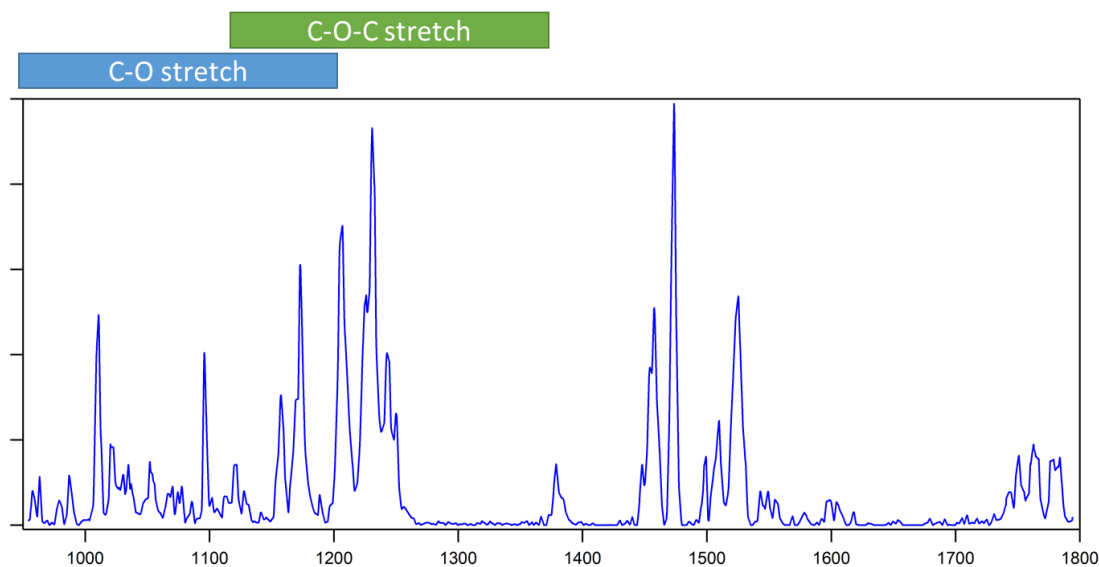


Figure 55: IR spectrum of the carbocation obtained from glycoside **1** recorded in the wavenumber range between 950 cm^{-1} and 1800 cm^{-1} at 0.37 Kelvin by using the experimental setup described in Section 7.6.

The first part of the IR spectrum represents the spectral portion where vibrational modes of C-O and C-O-C stretch are predominantly observed. As a consequence, this region is characterized by a series of extremely congested absorption bands, covering the wavelength range between 950 cm^{-1} and 1250 cm^{-1} .

Conversely, the second part of the spectrum is not affected by congestion showing distinctive sharp features, such as the narrow band around 1475 cm^{-1} and two quite well-resolved peaks at 1460 and 1525 cm^{-1} . Finally, the spectral region between 1700 and 1800 cm^{-1} shows some broad and low intensity bands.

Quantum mechanical calculations have been performed in order to obtain the corresponding theoretical IR spectrum. Owing to the fact that the phenyl group of glycoside **1** can assume an equatorial or an axial position both isomers should be

considered in the calculations, but the equatorial isomer was excluded by calculating the theoretical CCS values. In fact, the theoretical CCS value of 110 Å calculated for the axial isomer is in good agreement with the experimental CCS value of 108 Å whereas is not consistent with the theoretical CCS value of 115 Å obtained for the equatorial isomer.

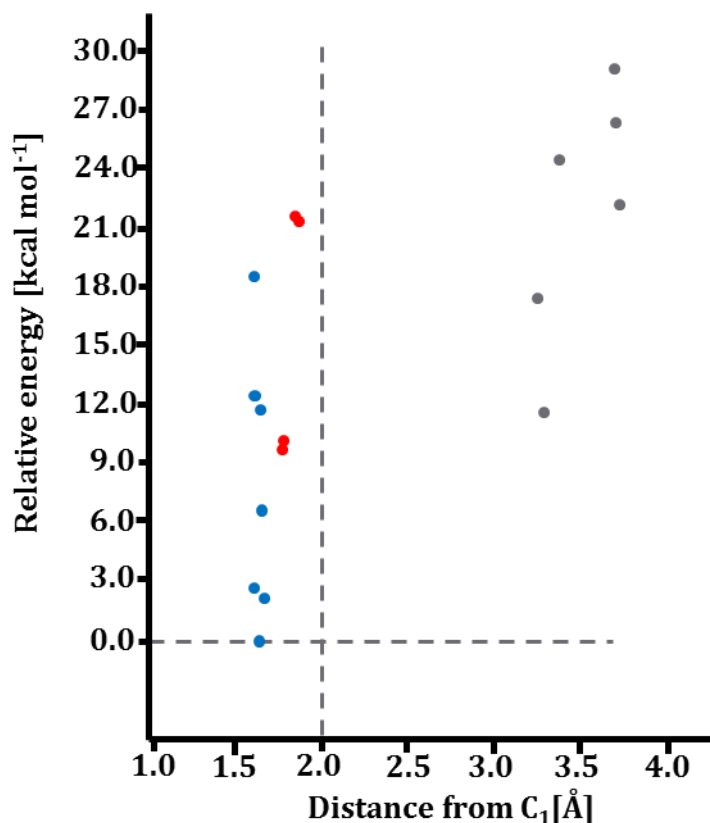


Figure 56: Relative energy distribution as a function of the distance from C₁ [Å] of open-chain conformers (grey dots), O₃-C₁ closed conformers (red dots) and O₂-C₁ closed conformers (blue dots).

Molecular dynamics approach has been used to find low energy conformers as possible structure candidates. In particular, the energetic content of the oxocarbenium structure versus the acetoxonium structure has been calculated. Concerning the carbocationic species arising from glycoside **1** and having an additional acetyl protecting group bound at C₃ position, it was evaluated the stability of closed conformers obtained from both the nucleophilic O₂-C₁ and O₃-C₁ attacks.

The diagram displayed in Figure 56 reports the relative energy of all geometries having an energetic content below 30 kcal mol^{-1} (y-axis) as a function of the distance from C1 (x-axis).

From the analysis of the geometry distribution it is possible to highlight that the stability of the conformers strictly depends on the distance from C1. As a result, when the O2 distance from C1 shifts from 3.5 \AA to around 1.6 \AA the energetic content of the system is drastically reduced. Hence, the **O2-C1** ring conformers are generally more stable than the corresponding open-chain conformers. Conversely, the same effect is not observed for the **O3-C1** ring conformers having a relative energy comparable to that of the open-chain structures. Therefore, the **O2-C1** nucleophilic attack is thermodynamically favoured compared to the **O3-C1** nucleophilic attack.

Theoretical IR spectra have been calculated for the most stable open-chain and **O2-C1** ring conformers (Figure 57) in order to evaluate the match existing between experimental and theoretical data.

The region between 1400 and 1800 cm^{-1} of the experimental IR spectrum shows a series of well-resolved and high intensity features that could be characteristic of a specific conformation. On the contrary, the area between 1000 and 1400 cm^{-1} is less diagnostic owing to the extremely congestion of the absorption bands.

In particular, the absorption band at 1460 cm^{-1} present in the theoretical spectrum of the **O2-C1** ring conformer **4H5** and the absorption band at 1475 cm^{-1} present in the theoretical spectrum of the **O2-C1** ring conformer **E5** are both well-reproduced by the experimental spectrum. This evidence seems to account for the existence of a mixed population of conformations predominantly constituted by closed conformers. Indeed, the simultaneous presence of multiple conformations is quite common for sugars owing to the flexibility of their structures. Moreover, the chemical bond **O2-C1** of both hypothesized conformers shows a covalent character. Such a structure has never been predicted and experimentally validate until now.

Considering the promising results obtained by using the Ultra-cold spectroscopy technique, the same approach has been employed to analyse the carbocation species arising from glycosides **2**, **3** and **4**.

A good ion signal has been obtained under the source conditions for the carbocationic species arising from glycoside **2**, confirming the easy departure of the 4-methylphenyl-thioether leaving group. On the other hand, a high level of fragmentation has been reported after the oxonium ion isolation and its accumulation into the ion trap, preventing from recording the corresponding IR spectrum. This is probably due to the collisions with the buffer gas and the long trapping time.

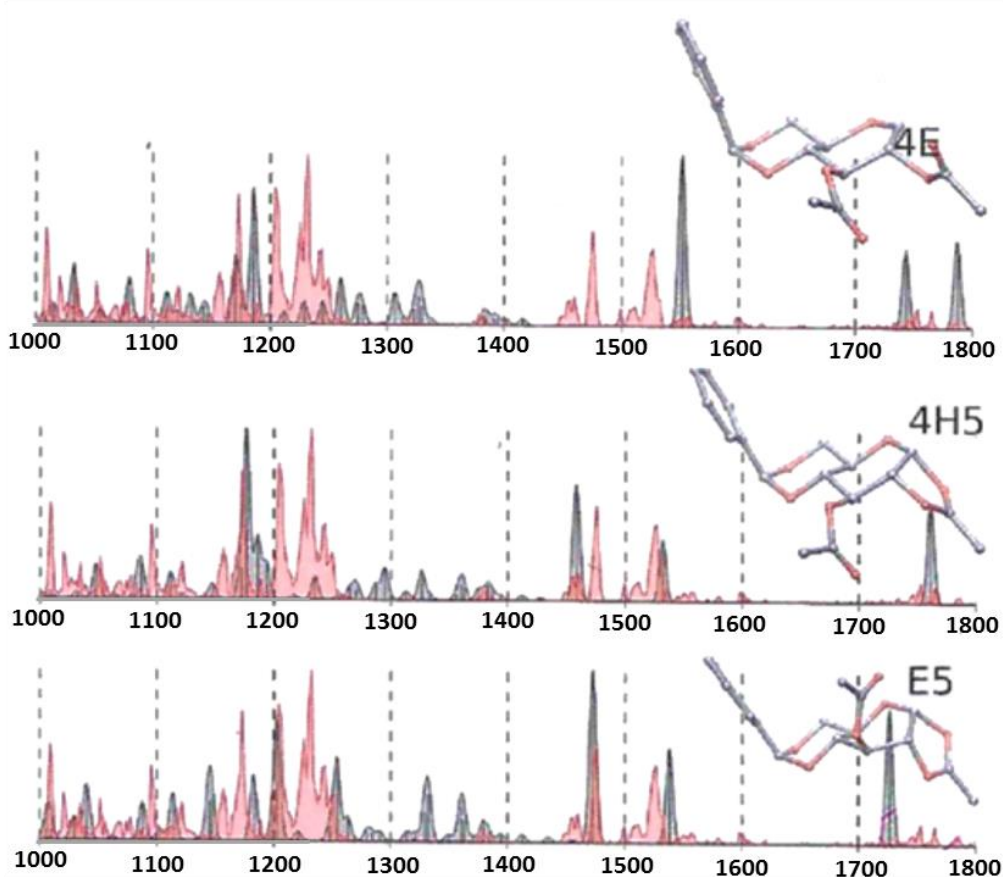


Figure 57: Comparison between the experimental IR spectrum obtained from the analysis of the carbocation at m/z 335 arising from the glycoside **1** (grey) and the theoretical IR spectra (red) calculated for the most stable open-chain conformer **4E** and the two most stable **O2-C1** closed conformers **4H5** and **E5**. Theoretical spectra were obtained by using the B3LYP functional and the def2TZVP basis set.

As expected from the ion mobility data, all attempts to acquire an IR spectrum of the oxonium ions arising from glycosides **3** and **4** are failed owing to the presence of the hydroxyl leaving group. The next step of this study will be the replacement of the hydroxyl with the 4-methylphenyl-thioether leaving group by the chemical synthesis of custom-made sugars.

5. Ion-molecule reactions

In the framework of the fundamental studies concerning the activation of inert bonds, unprecedented reactions of ions containing metals like iron and vanadium have been investigated. Iron and vanadium are two of the most common and diffuse transition metals in the Earth's crust. They play a major role in biology as active centres of some enzymes. In particular, iron represents the metal ion at the active site of important redox enzymes dealing with cellular respiration and oxidation/reduction processes in plants and animals. On the other hand, vanadium is predominantly present in the bromoperoxidase of ocean algae.^[118]

Among the low-valent iron species, ferrocene ($\eta^5\text{-C}_5\text{H}_5$)₂Fe(II) is the prototypical metallocene,^[119] a type of organometallic chemical compound consisting of two cyclopentadienyl rings bound on opposite sides to a central metal atom (Figure 58).

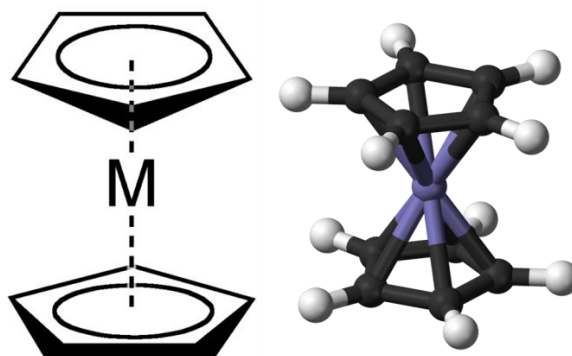


Figure 58: Schematic representation (on the left) and ball-and-stick model (on the right) of a metallocene molecule. The purple ball in the middle represents the metal cation.

Owing to the characteristic position of the metal ion, these organometallic species are also known as sandwich compounds.^[120] The excellent redox properties of ferrocene have paved the way to the use of this compound in several application fields. As an example, ferrocene has proved useful in the design of biosensors, dye-sensitized solar cells and drugs.^[121] In particular, the oxidized charged form ($\eta^5\text{-C}_5\text{H}_5$)₂Fe⁺ obtained from ferrocenium salt exhibits cytotoxic properties,^[122] showing a promising activity as antitumor agent.

On the other hand, vanadium is predominantly employed as steel additive in metallurgical industry, whereas vanadium oxides are known to be catalysts of important non-metallurgical processes, such as the production of sulphuric acid and the reduction of nitrogen oxides.^[123] Finally, a novel application of vanadium hydroxide $\text{H}_2\text{V}_3\text{O}_8$ concerns its use as nanowires in Li-ion batteries.^[124]

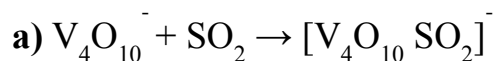
Considering the significant potential of ferrocene and vanadium hydroxydes, the intrinsic features of these compounds and the elementary reactions involved in the described processes have been extensively investigated in the gas phase at molecular level.

In order to highlight the characteristics of the ligated iron, both $(\eta^5\text{-C}_5\text{H}_5)_2\text{Fe}^+$ and $(\eta^5\text{-C}_5\text{H}_5)\text{Fe}^+$ ions have been the subjects of a number of studies. In particular, the reactions of $(\eta^5\text{-C}_5\text{H}_5)\text{Fe}^+$ with nucleophile ligands containing halogen atoms, such as substituted pyridines PyX and methyl halides CH_3X ($\text{X}=\text{F}, \text{Cl}, \text{Br}$), lead to the loss of HX molecules giving rise to species that preserve the $(\text{C}_5\text{H}_4)\text{Fe}$ kernel.^[125] Generally, the features of the products arising from the reactions of $(\eta^5\text{-C}_5\text{H}_5)\text{Fe}^+$ demonstrate that the coordination of the iron with the carbon ring is always preserved. This evidence is not influenced by the coordination site of the added nucleophile. To the best of our knowledge the unique example of iron extrusion is given by the reaction of ferrocene and ozone leading to hematite (Fe_2O_3). This process has been studied by using the so called low-temperature matrix-isolation/FT-IR technique^[126] consisting in the deposition of the reactant species onto a cooled CsI window subsequently analysed by infrared irradiation.

On the other hand, examples of C-C bond formation are reported to be catalysed by iron or bare Fe^+ and Fe_n^+ cations in alkyl halides solution reactions^[127] or in hydrocarbon reactions in the gas phase.^[128]

Passing to vanadium compounds, the ion-molecule reactions (IMR) of several homonuclear^[129] and heteronuclear^[130] vanadium oxide cations with hydrocarbons have been studied in order to gain information on reaction paths, cluster size and ligand effects. In this regard, several studies are available on singly-charged vanadium anions. For instance, a number of vanadium oxide monoanions have proved to be reactive with hydrocarbons, water and SO_2 .^[131] In particular, it has been demonstrated that the vanadium-oxide kernel of the $\text{V}_4\text{O}_{10}^-$ anion can

effectively incorporated SO_2 ^[131e] leading to a $[\text{V}_4\text{O}_{10},\text{SO}_2]^-$ complex showing a square pyramidal structure (Figure 59), whereas neutral vanadium oxides only give association intermediates or oxidation and reduction products by the reaction with SO_2 .^[132]



b)

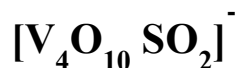
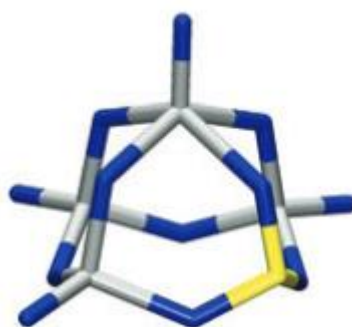
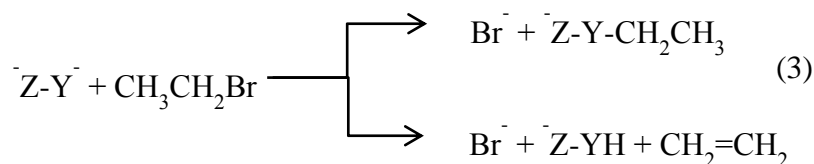
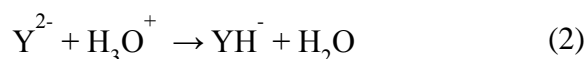


Figure 59: Scheme of the reaction of $\text{V}_4\text{O}_{10}^-$ with SO_2 a); Structure of the inclusion complex $[\text{V}_4\text{O}_{10}\text{SO}_2]^-$ assigned by means of IRMPD experiments and theoretical calculations b).

Conversely, the reactivity of multiply-charged vanadium cluster ions has not completely unravelled, still representing a field of study only partially explored. These species were first detected in a Penning trap and then analysed as oxides by electrospray-ionization mass spectrometry.^[133] In this regard, positive doubly-charged species, VO^{2+} , VOH^{2+} and VOH_2^{2+} , have been reported to be thermochemically stable and further stabilized by water solvation.^[133e] Additionally, various doubly-charged polyoxovanadate and hydroxide anions have been produced in the gas phase by electrospray of aqueous solutions of metavanadate.^[134]

The known reactions of dianions are proton-transfer and substitution/elimination (2-3), where the dianion is entirely included in the final product. In contrast, dications undergo the so-called “*bond-forming reactions*” where the simultaneous breakage and formation of chemical bonds give rise to two singly-charged species and/or a new doubly-charged ion.^[135]



Proton-transfer and substitution/elimination reactions of dianions have been described in the gas phase^[136] but no evidence of bond-forming reactions have been reported for these species.

Mass spectrometric techniques and quantum chemical calculations have allowed us to study the gas phase reactions of ferrocene and doubly-charged vanadium (V) anions with dichloromethane and SO₂, respectively.

Ferrocene reaction led to the formation of ferrous chloride and protonated benzenium ion, representing an interesting example of gas-phase iron extrusion process. On the other hand, singly-charged products that do not contain the reactant have arisen from the vanadium reactions, highlighting a bond-forming reaction performed by doubly-charged anions in the gas phase.

5.1 Iron promoted C-C bond formation

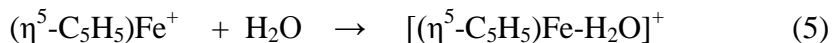
Millimolar solutions of ferrocene dissolved in a mixture of acetonitrile and water were injected into a linear ion-trap mass spectrometer and analysed.

The positively-charged ions detected in the gas phase are the molecular cation $(\eta^5\text{-C}_5\text{H}_5)_2\text{Fe}^+$ ($m/z=186$), $(\eta^5\text{-C}_5\text{H}_5)\text{Fe}^+$ ($m/z=121$) and Fe^+ ($m/z=56$). All the reported m/z ratios refer to the most abundant ^{56}Fe isotope among the four iron isotopic species. Under these experimental conditions, the ionic adducts $[(\eta^5\text{-C}_5\text{H}_5)\text{Fe-CH}_3\text{CN}]^+$ ($m/z=162$) and $[(\eta^5\text{-C}_5\text{H}_5)\text{Fe-H}_2\text{O}]^+$ ($m/z=139$) are also observed owing to the use of both acetonitrile and water as solvents.

Each ion characterized by the C_5H_5 moiety has been mass-selected and reacted with CH_2Cl_2 that was separately admitted into the reaction cell of the modified ion-trap mass spectrometer (for further details see Section 7.3). All the analysed species are found to be unreactive, apart from $(\eta^5\text{-C}_5\text{H}_5)\text{Fe}^+$ that yields an abundant ion formally corresponding to C_6H_7^+ (m/z 79) and plausibly formed by the following reaction:



The kinetic profile of the reaction (4) demonstrates that it is fast and efficient, but the analysis of the reaction is complicated by the concomitant formation of the $[(\eta^5\text{-C}_5\text{H}_5)\text{Fe-H}_2\text{O}]^+$ adduct due to the presence of background water (5). Hence, an accurate calibration procedure has been performed to subtract the background water contribution and prevent the precursor ion loss.



Except for the formation of the water adduct, the reaction of $(\eta^5\text{-C}_5\text{H}_5)\text{Fe}^+$ with CH_2Cl_2 gives only one ionic product C_6H_7^+ . Figure 60 reports the kinetic plot relating to the formation of C_6H_7^+ occurring with a rate constant of $k=7,1\cdot 10^{-10}$ ($\pm 30\%$) $\text{cm}^3 \text{s}^{-1} \text{molecule}^{-1}$ and an efficiency $k/k_{\text{coll}}=63\%$ (k_{coll} = collision rate).

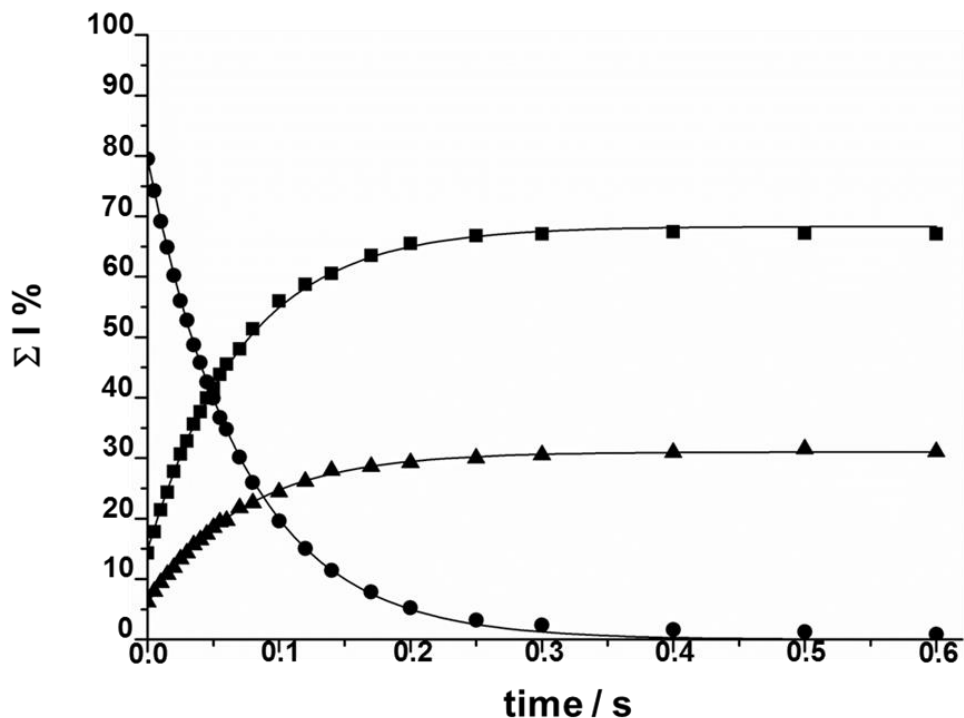


Figure 60: Kinetic plot and best-fit lines of the reaction of thermal $(\eta^5\text{-C}_5\text{H}_5)\text{Fe}^+$ ions with CH_2Cl_2 . Pressure of $\text{CH}_2\text{Cl}_2=4,9\cdot 10^{-7}$ Torr, \bullet $(\eta^5\text{-C}_5\text{H}_5)\text{Fe}^+$ ($R^2=0,9996$) \blacksquare C_6H_7^+ ($R^2=0,9990$), \blacktriangle $[(\eta^5\text{-C}_5\text{H}_5)\text{Fe-H}_2\text{O}]^+$ ($R^2=0,9991$).

The reaction intermediate $[(\eta^5\text{-C}_5\text{H}_5)\text{Fe-CH}_2\text{Cl}_2]^+$ at m/z 205 can be detected only under high-pressure conditions. Accordingly, by ionization of a mixture of ferrocene and CH_2Cl_2 in a ZabSpec mass spectrometer, $[(\eta^5\text{-C}_5\text{H}_5)\text{Fe-CH}_2\text{Cl}_2]^+$ has been observed and stabilized. Its structural characterization has been achieved by recording high-energy (8 kV) collisionally activated dissociation (CAD) mass spectra of the isolated isotopomers $[(\eta^5\text{-C}_5\text{H}_5)\text{Fe-CH}_2^{35}\text{Cl}_2]^+$ at m/z 205 and $[(\eta^5\text{-C}_5\text{H}_5)\text{Fe-CH}_2^{35}\text{Cl}^{37}\text{Cl}]^+$ at m/z 207 (Figure 61).

The formation of an intense daughter ion at m/z 79 formally corresponding to C_6H_7^+ points to the intermediacy of the ionic species $[(\eta^5\text{-C}_5\text{H}_5)\text{Fe-CH}_2\text{Cl}_2]^+$ in the C-C bond formation. On the other hand, the FeCl^+ ions (m/z 91 or 91-93) confirm that the iron transfer to chlorine is mediated by the intermediate $[(\eta^5\text{-C}_5\text{H}_5)\text{Fe-CH}_2\text{Cl}_2]^+$. Finally the minor fragments formally corresponding to $\text{Fe-CH}_2\text{Cl}_2^+$ (m/z 140 or 142) account for the iron transfer from $(\eta^5\text{-C}_5\text{H}_5)\text{Fe}^+$ to CH_2Cl_2 .

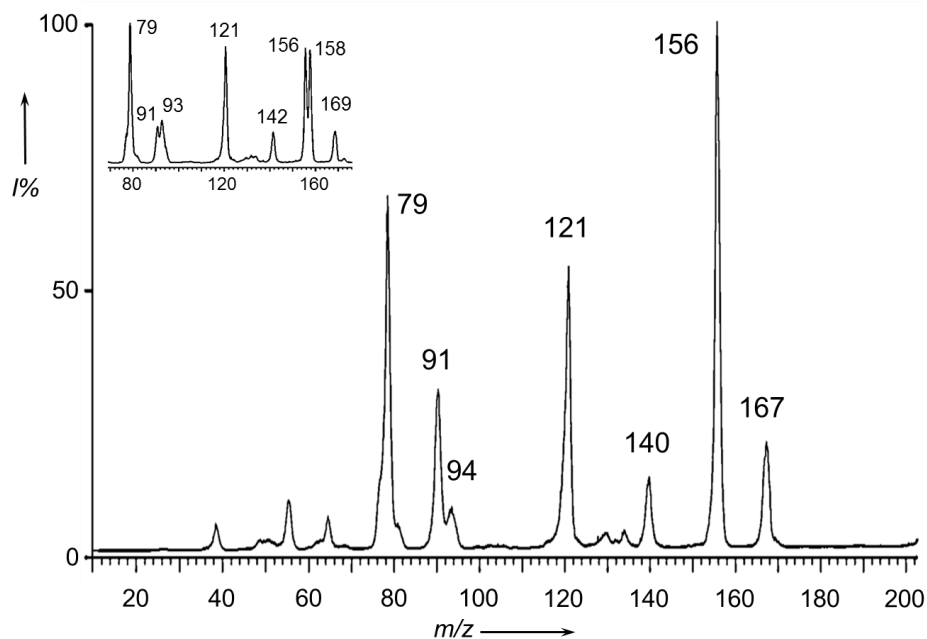
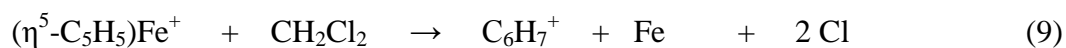
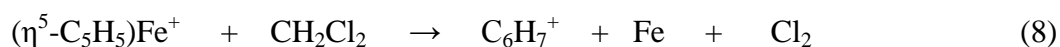
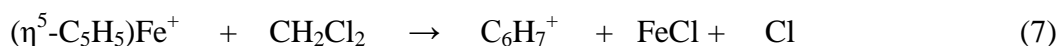
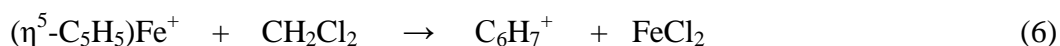


Figure 61: CAD mass spectrum of $[(\eta^5\text{-C}_5\text{H}_5)\text{Fe-CH}_2^{35}\text{Cl}_2]^+$ ions at m/z 205 with a partial spectrum of $[(\eta^5\text{-C}_5\text{H}_5)\text{Fe-CH}_2^{35}\text{Cl}^{37}\text{Cl}]^+$ at m/z 207 in the inset.

Other abundant ionic fragments containing the $\text{C}_5\text{H}_5\text{Fe}$ kernel are the ions at m/z 156 and 121, corresponding to $(\eta^5\text{-C}_5\text{H}_5)\text{Fe-Cl}^+$ and $(\eta^5\text{-C}_5\text{H}_5)\text{Fe}^+$ or its dissociation product at m/z 167, corresponding to $[(\text{C}_2\text{H}_3)\text{Fe-CH}_2\text{Cl}_2]^+$. Minor peaks at m/z 38, 49, 56, 65, 94 are related to consecutive dissociations of the $\text{C}_5\text{H}_5\text{Fe}$, C_5H_5 and CH_2Cl_2 moieties.

None structural information about the neutral products of the reaction can be obtained by the conventional mass spectrometric approach used. Hence, the possible reactions leading to the C_6H_7^+ ionic species are reported below (6-9).



For this purpose, N_fR (Neutral Fragment Reionization) experiments have been carried out in order to investigate the nature of the neutral species arising from the carbon-carbon coupling reaction. This technique allows one to analyse the neutral counterparts of the charged fragments produced from the dissociation of the $[(\eta^5\text{-C}_5\text{H}_5)\text{Fe-CH}_2\text{Cl}_2]^+$ intermediate.^[137] In particular, all neutral species are separated from the charged fragments and then reionized. The N_fR spectra of isolated isotopomers $[(\eta^5\text{-C}_5\text{H}_5)\text{Fe-CH}_2^{35}\text{Cl}_2]^+$ and $[(\eta^5\text{-C}_5\text{H}_5)\text{Fe-CH}_2^{35}\text{Cl}^{37}\text{Cl}]^+$ are reported in Figure 62.

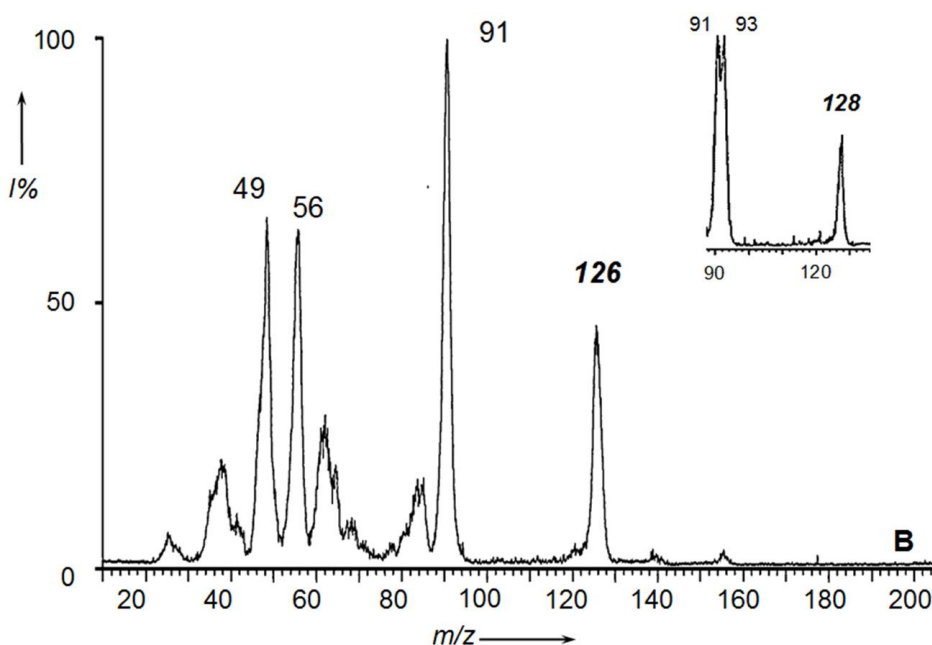


Figure 62: N_fR spectrum of $[(\eta^5\text{-C}_5\text{H}_5)\text{Fe-CH}_2^{35}\text{Cl}_2]^+$ with the partial N_fR spectrum of $[(\eta^5\text{-C}_5\text{H}_5)\text{Fe-CH}_2^{35}\text{Cl}^{37}\text{Cl}]^+$ in the inset.

Both spectra show intense peaks at m/z 126 and 128 that are absent in the CAD spectra of the ionic intermediate and correspond to the $\text{Fe}^{35}\text{Cl}_2^+$ and $\text{Fe}^{35}\text{Cl}^{37}\text{Cl}^+$, respectively. These ionic species can only be obtained by reionization of FeCl_2 , the neutral counterpart of the C_6H_7^+ ions obtained from the dissociation of the $[(\eta^5\text{-C}_5\text{H}_5)\text{Fe-CH}_2\text{Cl}_2]^+$ intermediate. According to this result, reaction (6) can be assigned to the process leading to the C_6H_7^+ ions. The other ions observed in the N_fR spectrum, such as the ionic species at m/z 91, do not account for the reaction

(7) leading to FeCl and Cl as neutral counterparts. Indeed, the ionic fragment FeCl^+ may arise from the dissociation of FeCl_2 as a consequence of the re-ionization process. Similarly, reactions (8) and (9) can be excluded because no signal at m/z 70 corresponding to Cl_2^+ were observed in the N_iR spectrum. Finally, low-resolved peaks in the m/z range between 35 and 50 were obtained from consecutive dissociations of fragments at higher m/z values.

In order to structurally characterize the ionic product at m/z 79 arising from reaction (6), a series of CAD experiments have been performed.

The ions at m/z 79 may correspond to the bicyclic form of protonated fulvene $[(\eta^5\text{-C}_5\text{H}_5)\text{-CH}_2]^+$ or to protonated benzene C_6H_7^+ . These two isomeric ions have been distinguished by comparing the CAD mass spectrum of the ion at m/z 79 obtained from the reaction (6) with the CAD mass spectrum of standard benzenium ion. Protonated benzene has been obtained under chemical ionization (CI) conditions by using CH_4 as a protonating agent.^[138]

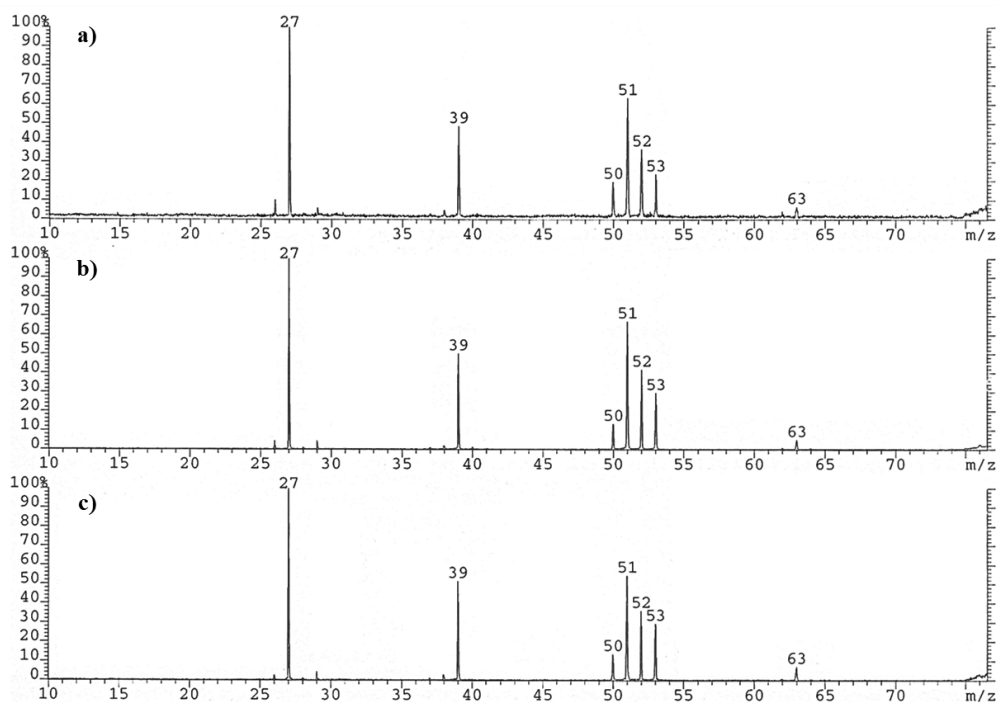


Figure 63: CAD mass spectra obtained from standard protonated benzene a); product ions at m/z 79 arisen from the reaction (6) b); fragment ions at m/z 79 arisen from the dissociation of the ionic intermediate $[(\eta^5\text{-C}_5\text{H}_5)\text{Fe-CH}_2^{35}\text{Cl}_2]^+$ c).

The CAD mass spectra of the ions at m/z 79 are reported in Figure 63 (panel a and b) and result to be superimposable, highlighting that the product ion at m/z 79 arising from the reaction (6) effectively corresponds to protonated benzene.

An additional confirmation of this hypothesis can be obtained by recording the MS^3 CAD spectrum of the fragment ion at m/z 79 arising from the dissociation of the ionic intermediate $[(\eta^5\text{-C}_5\text{H}_5)\text{Fe-CH}_2^{35}\text{Cl}_2]^+$ at m/z 205 (Figure 63; panel c). Also in this case, the CAD mass spectrum is superimposable to that obtained from protonated standard benzene.

According to the experimental results, theoretical calculations have identified a potential energy surface for the reaction (6). The energy profile and the geometries of the corresponding minima and saddle points are illustrated in Figure 64 and 65, respectively.

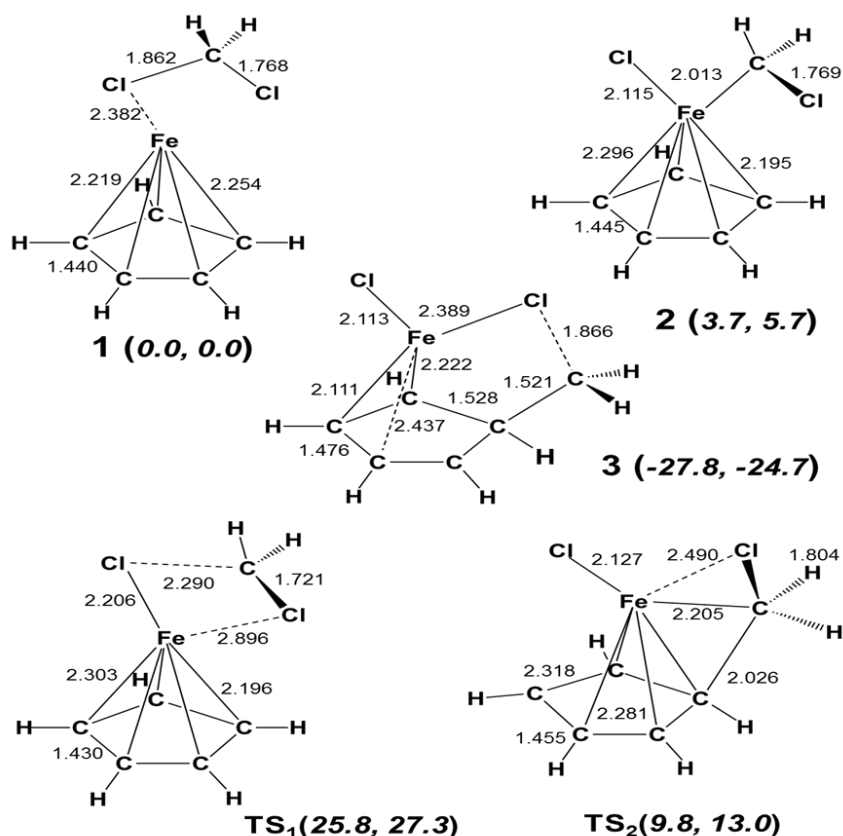


Figure 64: Structures of the minima and saddle points reported on the $[(\eta^5\text{-C}_5\text{H}_5)\text{Fe-CH}_2\text{Cl}_2]^+$ potential energy surface. Bond length in angstroms and angles in degrees. Energy values relating to **1** (ΔH° , ΔG°) in kcal mol⁻¹.

As displayed in Figure 65, the barrierless interaction of the iron atom of the $[(\eta^5\text{-C}_5\text{H}_5)\text{Fe}]^+$ precursor ion with a chlorine atom of CH_2Cl_2 leads to the first adduct **1** $[(\eta^5\text{-C}_5\text{H}_5)\text{Fe}\cdots\text{Cl}-\text{CH}_2\text{Cl}]^+$. The positive charge of the ionic species **1** is predominantly placed on the CH_2Cl_2 moiety ($0.72 e^-$) showing a long Fe-Cl bond. The **1**→**2** isomerization occurs through the transition state **TS1** by overcoming a barrier of 25.8 ($\Delta G^\circ=27.3$) kcal mol⁻¹. This process allows the activation of the first C-Cl bond and the insertion of the iron atom.

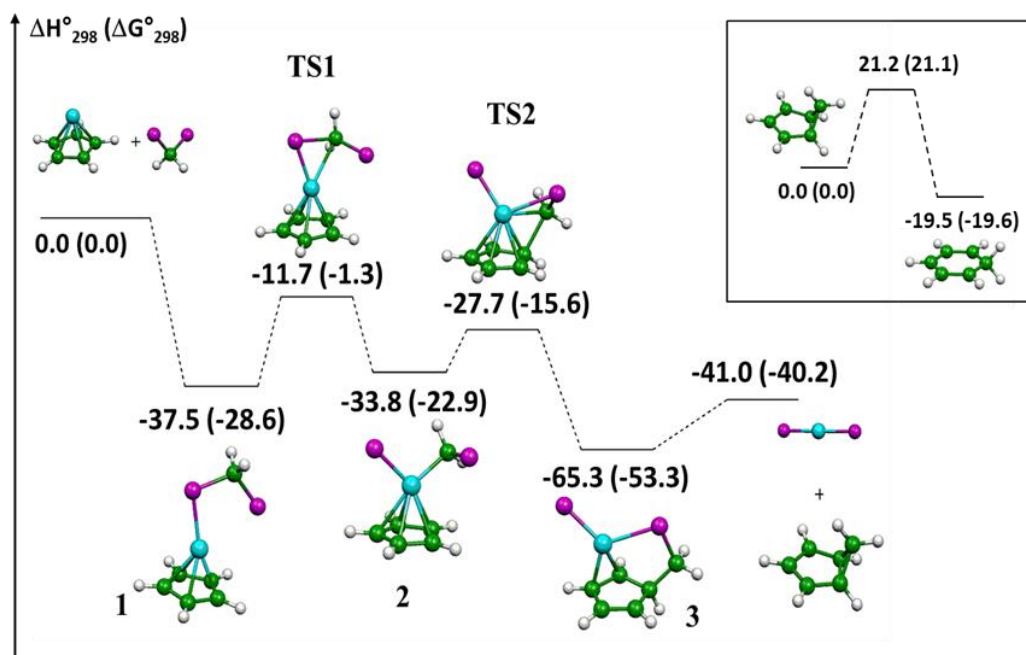


Figure 65: Schematic energy diagram of the $[(\eta^5\text{-C}_5\text{H}_5)\text{Fe}-\text{CH}_2\text{Cl}_2]^+$ potential energy surface. $\Delta H^\circ(\Delta G^\circ)$ values in kcal mol⁻¹. The inset shows the likely rearrangement of protonated fulvene to the benzenium ion.

In the $[(\eta^5\text{-C}_5\text{H}_5)\text{Fe}(\text{Cl})\cdots\text{CH}_2\text{Cl}]^+$ ion **2** structure, the chlorine atom interacting with Fe is no longer bound to the CH_2Cl group, whereas a new Fe-C bond is formed leading to a three-coordinated iron atom. The ionic species **2** is separated from the adduct **3** by a barrier of only 6.1 ($\Delta G^\circ=7.3$) kcal mol⁻¹ (**TS2**). The ion **3** still displays a weak residual interaction between the iron atom and the $\eta^5\text{-C}_5\text{H}_5$, but in this step the CH_2 moiety is carried from the iron to the carbon ring and the new C-C bond is formed. As a result, the Fe- CH_2 interaction is replaced by an elongated Fe-Cl bond. Hence, the ion **3** dissociates into FeCl_2 and $[(\eta^5\text{-$

$\text{C}_5\text{H}_5\text{CH}_2]^+$, the bicyclic form of protonated fulvene. Owing to the exothermicity of the whole process the $[(\eta^5\text{-C}_5\text{H}_5)\text{-CH}_2]^+$ ion can isomerize to the more stable benzenium ion.^[139]

5.2 SO₂ promoted V-O activation

Doubly-charged vanadium (V) hydroxoanions $\text{H}_2\text{V}_2\text{O}_7^{2-}$ and $\text{HNaV}_4\text{O}_{12}^{2-}$ were obtained in the gas phase by ESI ionization of aqueous NaVO_3 solutions and their reactivity towards sulphur dioxide was investigated by ion-molecule reactions (IMR).

To this end, $\text{H}_2\text{V}_2\text{O}_7^{2-}$ and $\text{HNaV}_4\text{O}_{12}^{2-}$ have been mass-selected and reacted with SO_2 , separately flown into the reaction cell of the modified ion-trap mass spectrometer.

Two reaction channels have been found for the $\text{H}_2\text{V}_2\text{O}_7^{2-}$ anion; the major channel (10) leads to singly-charged H_2VO_4^- and VO_3SO_2^- product ions whereas the minor channel (11) produces HV_2O_6^- and HOSO_2^- .

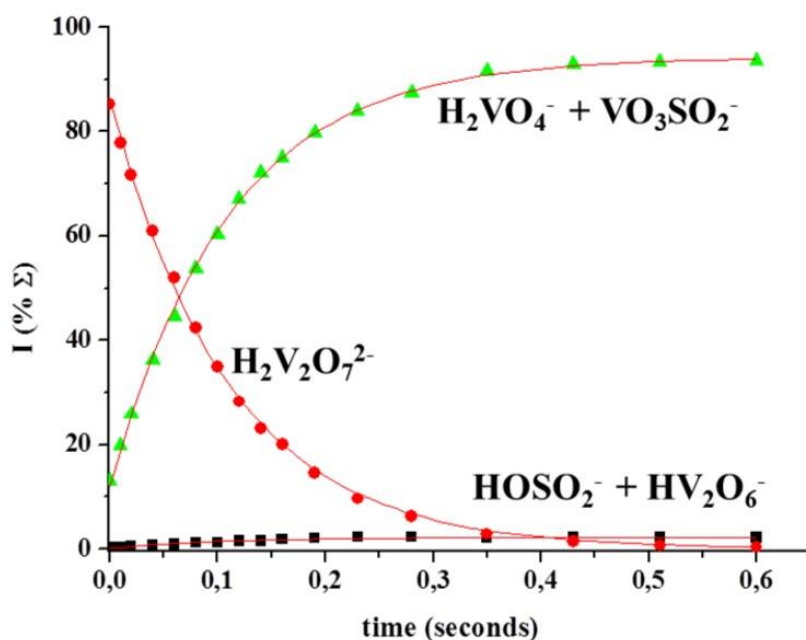
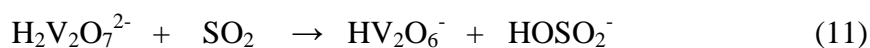


Figure 66: Kinetic plot and best fit lines of the reactions of thermal $\text{H}_2\text{V}_2\text{O}_7^{2-}$ ions with SO_2 , $P \text{SO}_2 = 2.7 \cdot 10^{-7}$ Torr, $R^2 (\text{H}_2\text{V}_2\text{O}_7^{2-}) = 0.9992$, $R^2 (\text{H}_2\text{VO}_4^- + \text{VO}_3\text{SO}_2^-) = 0.9992$, $R^2 (\text{HOSO}_2^- + \text{HV}_2\text{O}_6^-) = 0.9630$.

The kinetic profile of the $\text{H}_2\text{V}_2\text{O}_7^{2-}$ ions is characterized by an overall rate constant $k_{(\text{ov})} = 1.21 \cdot 10^{-9}$ ($\pm 30\%$) $\text{cm}^3 \text{s}^{-1} \text{molecule}^{-1}$ at 298 K, an efficiency $k_{(\text{ov})}/k_{\text{coll}}$ (k_{coll} = collision rate) = 93 %, $k_{10}/k_{11} = 42/1$ (Figure 66).

It is remarkable to observe that the reactant ion formally reported as $\text{H}_2\text{V}_2\text{O}_7^{2-}$ may include the isomeric $[\text{V}_2\text{O}_6\text{-H}_2\text{O}]^{2-}$ complex and the pirovanadate form, abundantly present in the sprayed solution. The ligated ion is the product of a gas-phase reaction between $\text{V}_2\text{O}_6^{2-}$ and H_2O .

In order to effectively prove the formation of the ionic $[\text{V}_2\text{O}_6\text{-H}_2\text{O}]^{2-}$ adduct, ions at m/z 99 corresponding to $\text{V}_2\text{O}_6^{2-}$ have been isolated and reacted with H_2O , as shown in Figure 67.

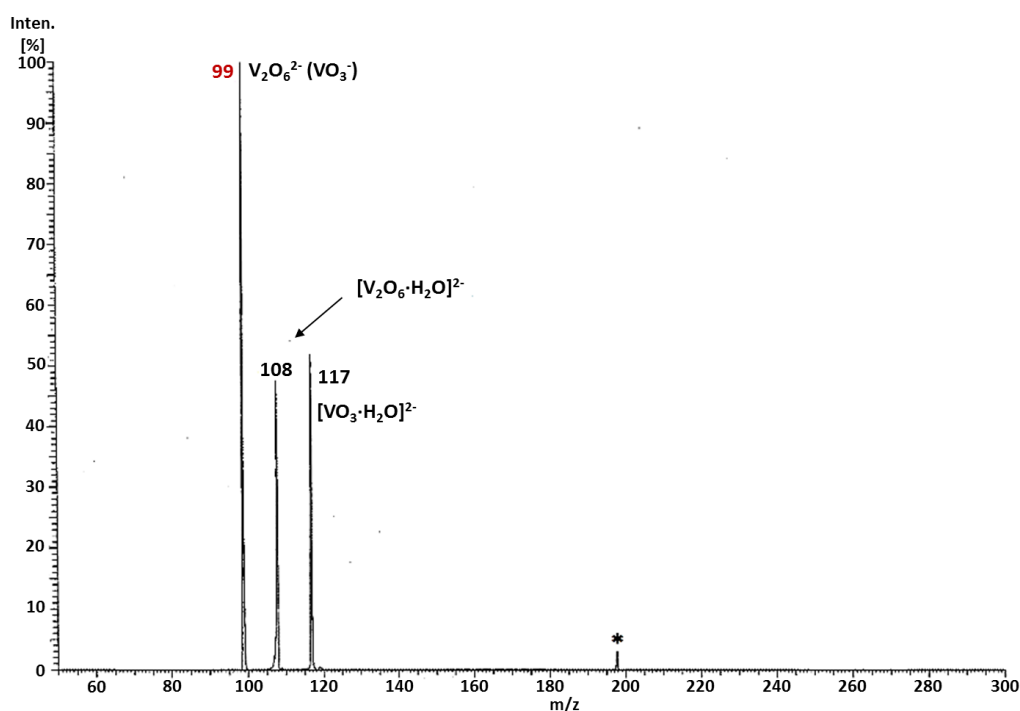


Figure 67: ITMS spectrum of the reaction of isolated $\text{V}_2\text{O}_6^{2-}$ ions (m/z 99) with H_2O . $P \text{H}_2\text{O} = 4.8 \cdot 10^{-6}$ Torr. Isobaric VO_3^- ions are also present. Observed products: $[\text{V}_2\text{O}_6\text{-H}_2\text{O}]^{2-}$ at m/z 108 and $[\text{VO}_3\text{-H}_2\text{O}]^-$ at m/z 117. The small signal * corresponds to V_2O_6^- (m/z 198) from the electron detachment of $\text{V}_2\text{O}_6^{2-}$.

Although the isobaric VO_3^- ions have been mass-selected together with the $\text{V}_2\text{O}_6^{2-}$ dianion, the obtained ionic product at m/z 108 confirms the formation of the $[\text{V}_2\text{O}_6\text{-H}_2\text{O}]^{2-}$ complex.

On the other hand, when SO_2 is admitted into the cell of the ion trap a $\text{H}_2\text{O}/\text{SO}_2$ mixture is formed and the abundance of the $[\text{V}_2\text{O}_6\text{-H}_2\text{O}]^{2-}$ adduct at m/z 108 significantly decreases due to the fastest reaction of $\text{V}_2\text{O}_6^{2-}$ with SO_2 leading to the $[\text{V}_2\text{O}_6\text{-SO}_2]^{2-}$ ionic complex (Figure 68). Hence, in the presence of sulphur dioxide, the ion $[\text{V}_2\text{O}_6\text{-SO}_2]^{2-}$ at m/z 131 represents the reaction sink.

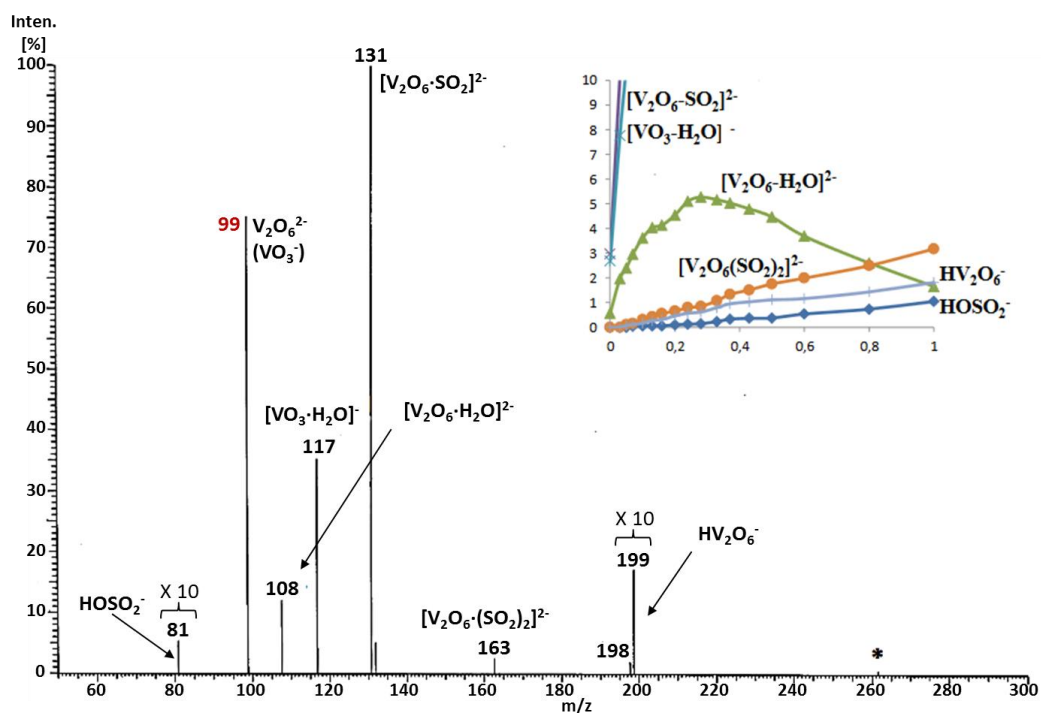


Figure 68: ITMS spectrum of the reaction of isolated $\text{V}_2\text{O}_6^{2-}$ ions (m/z 99) with $\text{H}_2\text{O}/\text{SO}_2 \approx 45/1$. $P_{\text{H}_2\text{O}} = 4.3 \cdot 10^{-6}$ Torr. The small ion * at m/z 262 comes from the reaction of V_2O_6^- (m/z 198) with SO_2 . Magnified kinetic profile at short reaction times is reported in the inset. The $\text{V}_2\text{O}_6^{2-}$, $[\text{V}_2\text{O}_6\text{-SO}_2]^{2-}$ and $[\text{VO}_3\text{-H}_2\text{O}]^-$ ions are out of scale, V_2O_6^- is not plotted.

Conversely, the $[\text{VO}_3\text{-H}_2\text{O}]^-$ ionic adduct at m/z 117 produced from the VO_3^- ionic species is still abundant in the spectrum owing to the large amount of water (Figure 68).

The minor product at m/z 163 corresponds to the doubly-charged ion $[\text{V}_2\text{O}_6\text{-(SO}_2)_2]^{2-}$ obtained from the consecutive reaction of $[\text{V}_2\text{O}_6\text{-SO}_2]^{2-}$ with SO_2 observed at longer reaction times. This peak has been assigned by the characteristic sulphur isotopic pattern and by the CAD dissociation into $[\text{V}_2\text{O}_6\text{-}$

$\text{SO}_2]^{2-}$ (m/z 131) arising from the loss of the SO_2 neutral counterpart, as displayed in Figure 69 (panel a and b).

Low signals are detected at m/z 199 (HV_2O_6^-) and m/z 81 (HOSO_2^-). Therefore, a signature of the reaction of $[\text{V}_2\text{O}_6\text{-H}_2\text{O}]^{2-}$ with SO_2 is given by the kinetic profile of the $\text{V}_2\text{O}_6^{2-}$ decay showing, at the shortest times, low abundances of $[\text{V}_2\text{O}_6\text{-H}_2\text{O}]^{2-}$ together with the reaction products HV_2O_6^- and HOSO_2^- .

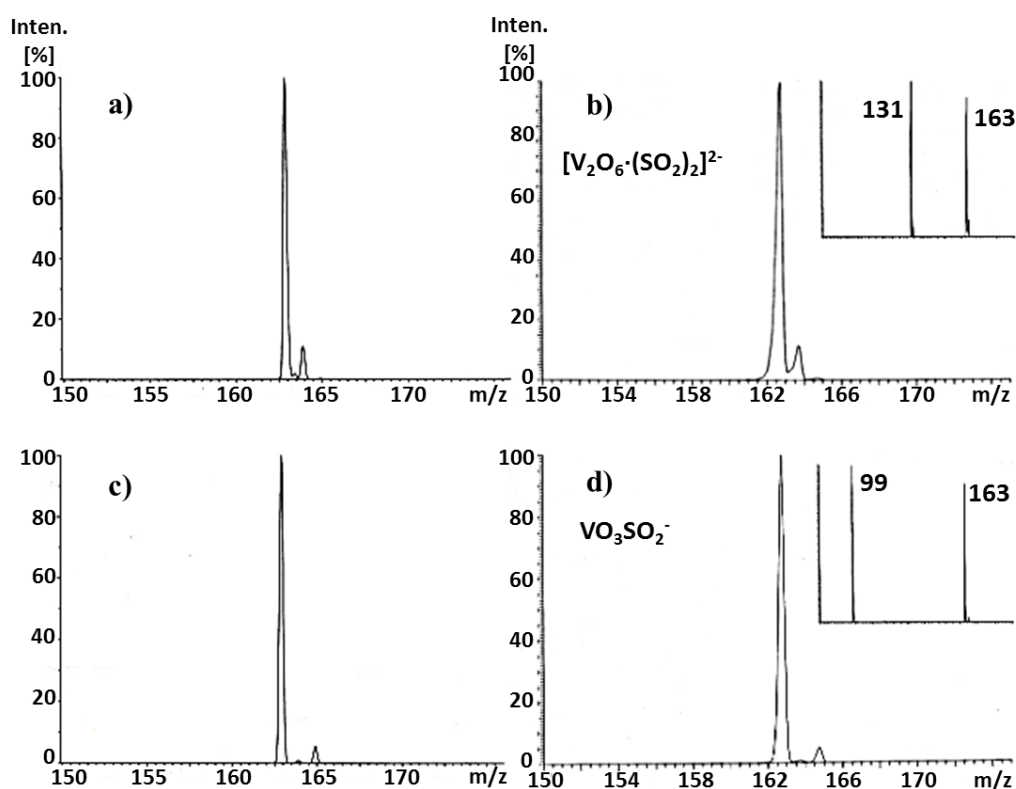


Figure 69: Isotopic patterns and CAD spectra of the isobaric peaks at m/z 163; a) Expected isotopic pattern for the doubly-charged $[\text{V}_2\text{O}_6\text{-(SO}_2)_2]^{2-}$ ion (m/z 163); b) Experimental isotopic pattern of the ion at m/z 163 formed by reaction of $\text{V}_2\text{O}_6^{2-}$ with SO_2 . In the inset the CAD spectrum showing the $[\text{V}_2\text{O}_6\text{-SO}_2]^{2-}$ fragment (m/z 131); c) Expected isotopic pattern for the singly-charged VO_3SO_2^- ion (m/z 163); d) Experimental isotopic pattern of the ion at m/z 163 formed by the reaction of $\text{H}_2\text{V}_2\text{O}_7^{2-}$ with SO_2 . In the inset the CAD spectrum showing the VO_3^- fragment (m/z 99).

Considering the above results, the k_{10}/k_{11} value previously measured cannot be considered indicative of the rate constant of the reaction (11).

Concerning the $\text{HNaV}_4\text{O}_{12}^{2-}$ species, this alkali-containing anion reacts with SO_2 leading to the $\text{NaV}_4\text{O}_{11}^-$ and HOSO_2^- ionic products (12).



Figure 70 shows the kinetic profile of the reaction (12) that is characterized by a rate constant k of $1,05 \cdot 10^{-9}$ ($\pm 50\%$) $\text{cm}^3 \text{s}^{-1} \text{molecule}^{-1}$ at 298 K and efficiency k_{12}/k_{coll} of 90%. Hence, the reaction (12) is extremely fast and efficient.

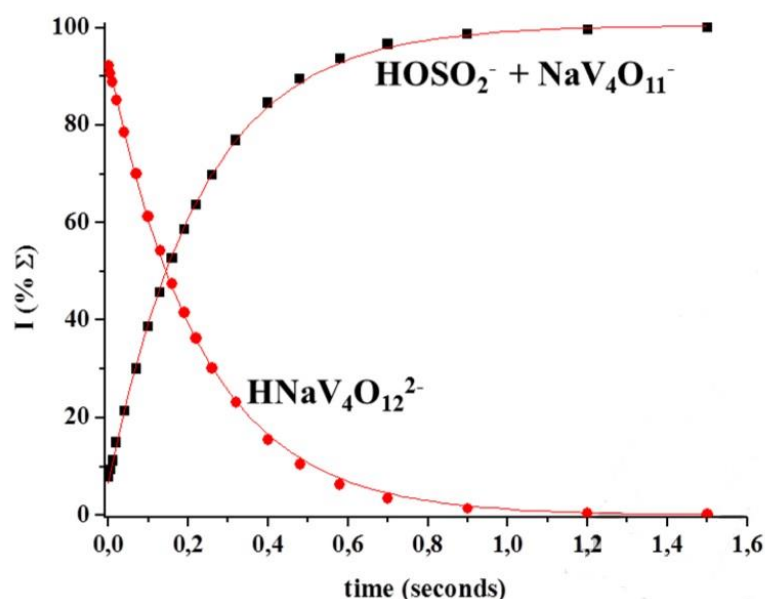


Figure 70: Kinetic plot and best fit lines of the reactions of thermal $\text{HNaV}_4\text{O}_{12}^{2-}$ ions with SO_2 , $P_{\text{SO}_2} = 1.4 \cdot 10^{-7} \text{ Torr}$, $R^2 (\text{HNaV}_4\text{O}_{12}^{2-}) = 0.9995$, $R^2 (\text{HOSO}_2^- + \text{NaV}_4\text{O}_{11}^-) = 0.9995$.

According to the experimental results, quantum mechanical calculations have been employed to validate a feasible reaction mechanism.

Two stable isomers of the pirovanadate anion $\text{H}_2\text{V}_2\text{O}_7^{2-}$ have been identified, $\mathbf{1}^{2-}$ and $\mathbf{2}^{2-}$ (Figure 71) that can easily interconvert each other. The main difference existing between the two forms consists in the orientation of the OH groups that are placed on the two vanadium atoms in $\mathbf{1}^{2-}$ and on the same vanadium atom in $\mathbf{2}^{2-}$.

Following the reaction with SO_2 , the V-O-V bridge is weakened and the ionic intermediate $\mathbf{3}^{2-}$ $[\text{H}_2\text{V}_2\text{O}_7\text{-SO}_2]^{2-}$ is formed. This species easily evolves to the product ions H_2VO_4^- and VO_3SO_2^- . H_2VO_4^- corresponds to vanadic acid anion whereas VO_3SO_2^- is structurally characterized by a heteronuclear four-membered

ring structure. The entire process is exothermic by 57.9 kcal mol⁻¹ and occurs below the reactant energies. Since it has been experimentally demonstrated that the H₂V₂O₇²⁻ anion is not the precursor ion of the HV₂O₆⁻ and HOSO₂⁻ products, no pathway starting from 1²⁻ and 2²⁻ and leading to these species has been found. On the contrary, theoretical calculations confirmed that the HV₂O₆⁻ and HOSO₂⁻ ions can be formed by the isomeric [V₂O₆-H₂O]²⁻ complex.

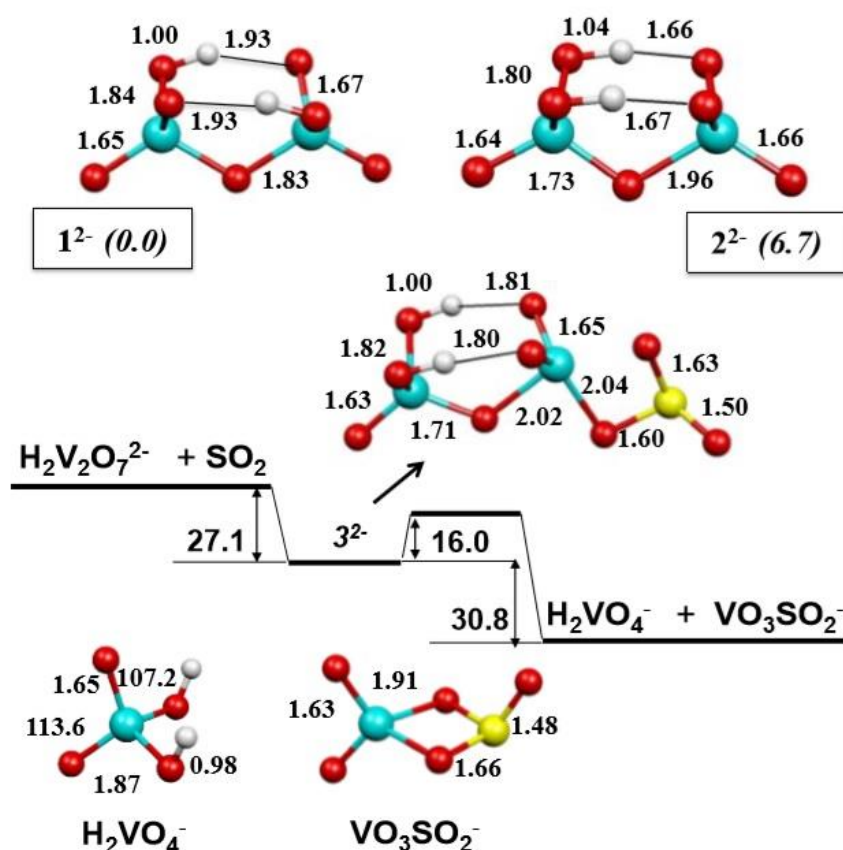


Figure 71: Geometries of the minima localized on the [H₂V₂O₇-SO₂]²⁻ potential energy surface, optimized at the BPW91 level of theory. Bond lengths in Å, angles in degrees, ΔH values in kcal mol⁻¹ computed at the BPW91 level of theory. 1²⁻ and 2²⁻ denote the H₂V₂O₇²⁻ ions, 3²⁻ the [H₂V₂O₇-SO₂]²⁻ intermediate.

Figure 72 shows the electronic structure calculations of the alkali containing anion, HNaV₄O₁₂²⁻.

As in the previous case, two stable forms quite close in energy, 4²⁻ and 5²⁻, have been identified. The main differences between 4²⁻ and 5²⁻ consist in the position of

the OH group and the interaction of the alkali metal. Moreover, 4^{2-} is characterized by two four-membered rings, whereas 5^{2-} shows only one ring. Since the HO group and the metal atom may occupy different positions, other isomers have been highlighted; however, they have not been taken into account because less stable and/or characterized by high barriers for the reaction 12.

Both the $\text{HNaV}_4\text{O}_{12}^{2-}$ ions have a structure consistent with the experimentally observed CAD fragmentation into HV_2O_6^- and NaV_2O_6^- and form two stable complexes with sulphur dioxide, (6^{2-} and 7^{2-}) with a comparable energy gain of ca. 15 kcal mol⁻¹ (Figure 73).

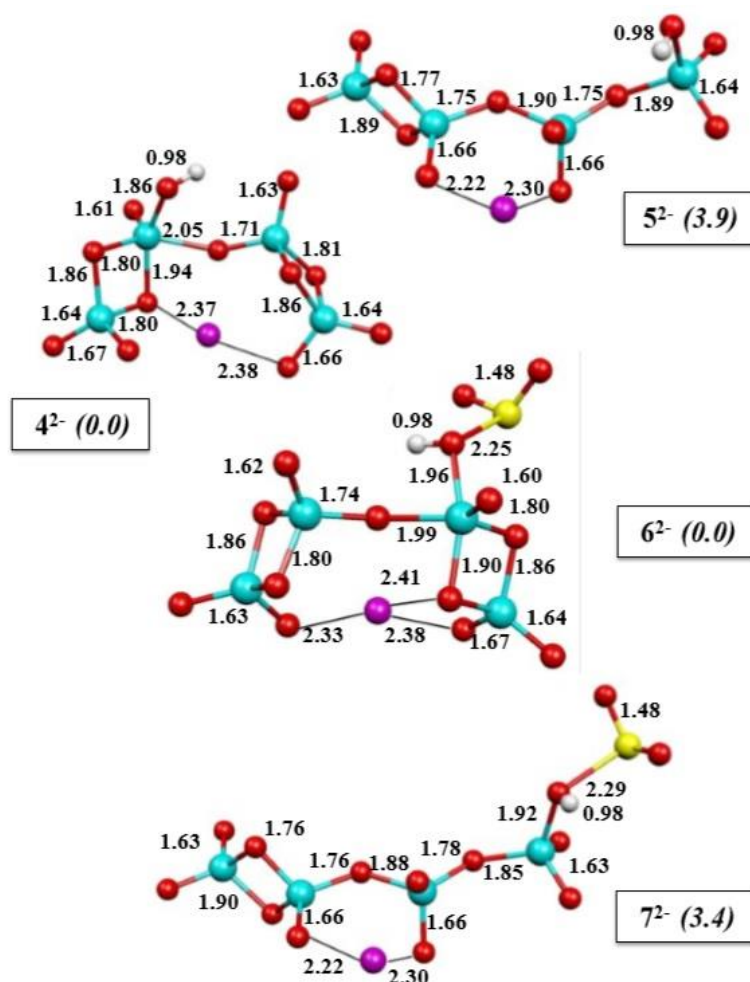


Figure 72: Geometries of the minima localized on the $[\text{HNaV}_4\text{O}_{12}\text{SO}_2]^{2-}$ potential energy surface, optimized at the BPW91 level of theory. Bond lengths in Å, ΔH values in kcal mol⁻¹ computed at the BPW91 level of theory. 4^{2-} and 5^{2-} denote the $\text{HNaV}_4\text{O}_{12}^{2-}$ ions, 6^{2-} and 7^{2-} denote the $[\text{HNaV}_4\text{O}_{12}\text{SO}_2]^{2-}$ intermediates.

After the formation of 6^{2-} and 7^{2-} , the reactions proceed along two pathways that differ for the intermediate dissociation barriers and for the structure of the products obtained (8^{2-} and 9^{2-} - Figure 73).

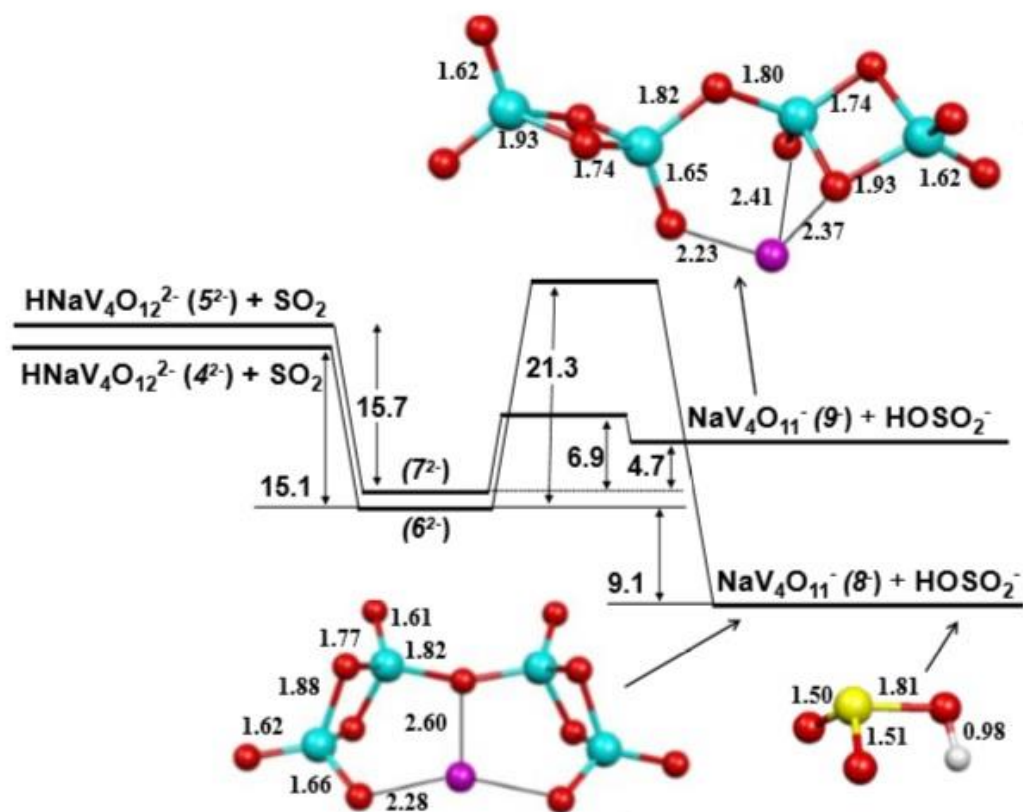


Figure 73: Schematic energy diagram of the reaction of HNaV₄O₁₂²⁻ with SO₂. Geometries of the HOSO₂⁻ and NaV₄O₁₁⁻ product ions (8 and 9) optimized at the BPW91 level of theory. Bond lengths in Å, ΔH values in kcal mol⁻¹ computed at the BPW91 level of theory.

The reaction of 4^{2-} leading to the most stable NaV₄O₁₁²⁻ ion 8^{2-} is more exothermic than that obtained from 5^{2-} ($\Delta H^\circ = -24.2$ versus -11.0 kcal mol⁻¹); on the contrary, the reaction of 5^{2-} easily occurs below the reactant energy according to the high efficiency of the process. As a consequence, it is not possible to experimentally discriminate the two routes, but they are both feasible since the most exothermic reaction of 4^{2-} requires only 6 kcal mol⁻¹ of vibrational energy excess. However, a crucial role is played by the back dissociation in the reaction of 4^{2-} that significantly depletes the intermediate 6^{2-} .

5.3 Discussion

Experimental results above reported have highlighted fast and efficient gas phase chemical reactions.

Thermal $(\eta^5\text{-C}_5\text{H}_5)\text{Fe}^+$ ions have been found to undergo an unprecedented reaction with CH_2Cl_2 giving rise to FeCl_2 and C_6H_7^+ as exclusive products. On the other hand, thermal doubly-charged vanadium hydroxoanions easily react with sulphur dioxide, behaving as effective VO_3^- and OH^- donors to SO_2 .

In the first reaction a key role is played by the iron atom that promotes the C-C coupling reaction, whereas in the second system sulphur dioxide effectively activates the V-O bonds.

Experiments performed by means of a modified ion-trap mass spectrometer allowed us to measure the kinetic constants of the investigated reactions demonstrating that all the occurring processes are fast and effective. Conversely, the employment of a ZabSpec mass spectrometer has been useful to characterize the ionic (C_6H_7^+) and neutral product (FeCl_2) and the $[(\eta^5\text{-C}_5\text{H}_5)\text{Fe-CH}_2\text{Cl}_2]^+$ ionic intermediate of the $(\eta^5\text{-C}_5\text{H}_5)\text{Fe}^+$ reaction with CH_2Cl_2 . Only by using this specific mass spectrometer it is possible to perform N_fR experiments assessing the intrinsic features of neutral species and creating the high-pressure conditions that favour the formation of ligated $[(\eta^5\text{-C}_5\text{H}_5)\text{Fe-L}]^+$ ions. It is well-known that $(\eta^5\text{-C}_5\text{H}_5)\text{Fe}^+$ ion can rapidly react with various inorganic and organic nucleophiles (L), whereas the $(\eta^5\text{-C}_5\text{H}_5)_2\text{Fe}^+$ ionic species was reported to be unreactive.^[140] In particular, the reactions of $(\eta^5\text{-C}_5\text{H}_5)\text{Fe}^+$ with L invariably lead to the ligated $[(\eta^5\text{-C}_5\text{H}_5)\text{Fe-L}]^+$ ions showing that the nucleophile is coordinated with the metal rather than the carbon ring of the reactant; this hypothesis is in agreement to the widely suggested mechanism. In the present study, the $[(\eta^5\text{-C}_5\text{H}_5)\text{Fe-CH}_2\text{Cl}_2]^+$ ionic complex easily evolves to the reaction products and it is detected only under certain conditions. Conversely, the ligated ions $[(\eta^5\text{-C}_5\text{H}_5)\text{Fe-CH}_3\text{CN}]^+$ and $[(\eta^5\text{-C}_5\text{H}_5)\text{Fe-H}_2\text{O}]^+$, always observed under the experimental conditions, have been revealed not to be the ionic intermediate of any reaction. In particular, the structural characterization of the $[(\eta^5\text{-C}_5\text{H}_5)\text{Fe-CH}_2\text{Cl}_2]^+$ ionic intermediate demonstrated its crucial role in the formation of the final products.

The data obtained from the N_fR experiments have confirmed that the neutral counterpart of the reaction corresponds to FeCl₂ (Figure 62). This result allowed us to validate the reaction (6) as the most favourable process leading to the C₆H₇⁺ product ion. The other channels from (7) to (9) have been excluded on the basis of the experimental results and on thermochemical considerations. Reaction (6) is the only exothermic process ($\Delta H = 60 \text{ kcal mol}^{-1}$), whereas reaction (7), (8) and (9) are all endothermic (46.7, 65.6 and 107.7 kcal mol⁻¹), respectively.

Finally, the structure of the ionic product C₆H₇⁺ corresponding to protonated benzene has been confirmed by both CAD mass spectra and quantum mechanical calculations predicting a thermodynamically-favoured isomerization of the bicyclic form of protonated fulvene [(η^5 -C₅H₅)-CH₂]⁺ to the more stable benzenium ion.

In particular, quantum mechanical calculations depicted a mechanism satisfactorily in line with the experimental evidence. According to the theoretical results reported in Figure 65, a stepwise sequence is required for the formation of the C-C bond and the rearrangement to FeCl₂. Although this process is believed to be entropically demanding, it occurs below the reactants energy leading to the benzenium ion. The entire reaction has proved to be fast and exoergonic ($\Delta G^\circ = -59.8 \text{ kcal mol}^{-1}$). The calculated exothermicity, $\Delta H^\circ = -60.5 \text{ kcal mol}^{-1}$, has resulted to be in good agreement with the experimentally derived value, $\Delta H^\circ = -61.8 \text{ kcal mol}^{-1}$.^[141] As a consequence, the experimental and theoretical evidence accounts for the occurrence of an iron-mediated C-C bond formation. The identity of the ligand strictly influences the nature of the bonding and the multiplicity of L-Fe⁺ cationic adducts. For instance, (C₆H₆)Fe⁺ shows three unpaired electrons, (C₅H₅N)Fe⁺ is σ bound and has five unpaired electrons, whereas (η^5 -C₅H₅)Fe⁺ has four unpaired electrons in its ground state.^[142,143] Hence, (η^5 -C₅H₅)Fe⁺ can be alternatively considered a covalently bound (η^5 -C₅H₅)-Fe(I)⁺ ion or a complex obtained from the electron transfer from Fe(I)⁺ to (η^5 -C₅H₅) and back donation to the 4s, 4p, or 3d orbitals of Fe(II)²⁺.^[142] Consequently, iron results to be three-coordinated without change of multiplicity as a result of the Lewis acid properties relating to this iron-containing ion and the spd hybridization (Figure 74).

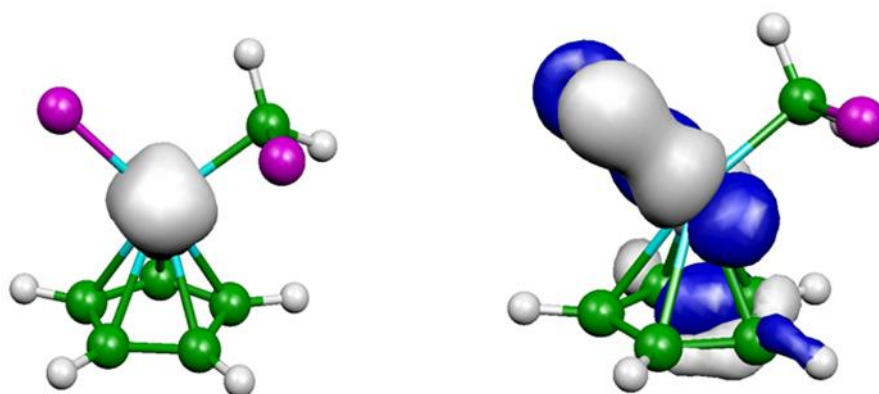


Figure 74: Spin density plot a) and doubly occupied frontier molecular orbital (MO) of the intermediate 2 b).

The interaction with the nucleophile in ion **1** is predominantly electrostatic whereas in ion **2** the three-coordinated iron represents the carrier of the CH₂ moiety from the halomethane to the (η^5 -C₅H₅) group. Both ions are more stable than the reactant species and their presence within the ionic population has been confirmed by the high-intensity fragment at *m/z* 156 (or 158) reported in Figure 61 and corresponding to the loss of the CH₂Cl radical.

The (η^5 -C₅H₅)Fe⁺ species is not reactive towards CH₄ demonstrating that the observed reaction effectively depends on the presence of the chlorine atom. Interestingly, [Pt(bipy-H)]⁺ and other cyclometalated transition-metal complexes react with CH₂Cl₂ giving PtCl₂ loss.^[144]

Passing to the doubly-charged vanadium hydroxoanions, H₂V₂O₇²⁻ and HNaV₄O₁₂²⁻ react with SO₂ leading to singly-charged products that do not contain the reactant. These processes represent a new example of bond-forming reactions performed by doubly-charged anions in the gas phase.

Also in this case mass spectrometry and quantum mechanical calculations have been combined to obtain a consistent reaction mechanism.

In particular, the experimental and theoretical results above reported demonstrate that the breakage of V-O bonds and the formation of new V-O and S-O bonds are the crucial steps of the bond-forming reactions involving the considered piro- and polyvanadate dianions. These processes occur through the action of SO₂ that

effectively favours the breakage of the stable V_2O_7 kernel of $H_2V_2O_7^{2-}$ and the terminal V-OH bond of $HNaV_4O_{12}^{2-}$. As a consequence, $H_2V_2O_7^{2-}$ acts as an effective VO_3^- donor forming $VO_3SO_2^-$, whereas $HNaV_4O_{12}^{2-}$ behaves as an effective HO- donor leading to the bisulfite ion $HOSO_2^-$, respectively.

The structural differences existing between the two reactant ions account for their different reactivity. For instance, the interaction of SO_2 with the oxygen atom is addressed by the HO groups of $H_2V_2O_7^{2-}$ involved in hydrogen bonds. Conversely, the interaction of $HNaV_4O_{12}^{2-}$ with SO_2 is promoted by the HO group and the alkali metal of the dianion that stabilize the V_4O_{11} cage.

Considering that the dissociation of $H_2V_2O_7^{2-}$ into VO_3^- shows a barrier of 36.6 kcal mol⁻¹, the formation of the product ion $VO_3SO_2^-$ is a notable process. To the best of our knowledge, the $VO_3SO_2^-$ anion has never been detected before and it has been observed for the first time in these experiments; Interestingly, its calculated structure displayed in Figure 71 resembles that of the neutral VO_3SO_2 , the main product arising from the reaction of neutral vanadium oxide clusters with sulphur dioxide.^[132a] The CAD spectrum of $VO_3SO_2^-$ does not show the SO_3^- fragment or fragments related to SO_3 loss (Figure 69, panel d), which exclude the occurrence of oxidation processes as also reported for neutral VO_3SO_2 species.^[132a]

A charge separation process is involved in the formation of singly-charged species from doubly-charged ions, causing the release of a large amount of kinetic energy from Coulomb explosion. This event leads to mass discrimination effects that however do not influence the results. Although the EA (electron affinity) of $H_2V_2O_7^-$ is calculated to be only 0.05 eV (EA of $HNaV_4O_{12}^- = 1.26$ eV), the charge separation process does not occur by electron transfer to SO_2 ((EA) = 1.10 eV),^[145] as one might suppose. The electron transfer is not even observed within the intermediate $[H_2V_2O_7-SO_2]^{2-}$, where the negative charge is predominantly placed on the $H_2V_2O_7$ moiety (net charge = 1.70 e). It has been reported^[146] that the factors influencing the stability of solvent-free dianions toward the electron detachment and the fragmentation into singly-charged ions also govern the probability of electron transfer from these species. The existence of a repulsive Coulomb barrier associated with the charge separation process may indeed

prevent exothermic fragmentation or charge transfer processes.^[146] Other factors, consisting in the spatial separation and delocalization of the excess charge, can increase the stability of medium- and large- size dianions; indeed the negative charges of $\text{H}_2\text{V}_2\text{O}_7^{2-}$ and $\text{HNaV}_4\text{O}_{12}^{2-}$ are distributed over all the oxygen atoms, as emerged from the charge analysis of this two ionic species. Accordingly, the investigated dianions undergo charge separation exclusively as a result of the chemical reaction with sulphur dioxide, whereas they are found to be stable towards the fragmentation, electron detachment and electron transfer. Besides, the permanent dipole moment of sulphur dioxide plays a crucial role in promoting the ion-neutral bonding. This is due to the ion-dipole attractive forces that, operating also at long distances, reduce the probability of electron transfer.^[135d, g]

6. Conclusions

In this thesis the uncertain reaction mechanisms of important industrial, food and synthetic processes were investigated by means of gas-phase studies.

To this end, the effectiveness of mass spectrometric techniques was probed and the experimental results were compared with the data obtained from quantum mechanical calculations. The major advantage of this approach has consisted in the possibility to obtain an environment in which solvent and counter-ion effects were completely avoided allowing the study of the intramolecular processes occurring in a gaseous medium. As a consequence, information on the intrinsic molecular properties of the ionic species involved in the reactions under investigation was achieved.

On the basis of the results presented in this work a mechanistic picture of D-hexose (glucose and fructose) and D-pentose (xylose, arabinose and ribose) acid-catalysed dehydration was outlined.

In particular, the ionic gaseous precursors of the considered reactions were identified by means of CAD experiments that were performed with electrospray ionization triple quadrupole (ESI/TQ) and ion trap (ESI/IT) mass spectrometry. The same techniques were also employed to structurally characterize the ionic intermediates and products of the decomposition reactions.

Dehydration energetic barriers were measured by means of energy resolved (ER) CAD experiments and additional mechanistic evidence was obtained by using model molecules and isotopic labelling experiments.

The D-glucose dehydration picture arising from the experimental observations resulted to be compatible with the theoretical mechanism proposed in literature for the C1-OH protonation.^[38] According to this pathway, a key role was shown to be played by the group bound at the C3 position. In fact, an increased selectivity toward the formation of protonated 5-HMF was observed when an electron-withdrawing group was bound at the C3 carbon of D-glucose.

Furthermore, the first dehydration intermediate obtained from protonated D-glucose was identified as a possible precursor of protonated levulinic acid through an alternative formation route other than the generally accepted pathway involving the double hydration of 5-HMF. In this regard, further studies are in

progress in our laboratories to investigate the mechanism of this interesting LA formation pathway.

Subsequently, a possible D-fructose dehydration route was hypothesized on the basis of the experimental results and following the theoretical unimolecular mechanisms reported in literature.^[44,48] According to the experimental and theoretical evidence protonated D-glucose and D-fructose do not follow superimposable dehydration pathways, but the dehydration of D-fructose is always slightly favoured respect to that of D-glucose. Anyway, the decomposition of protonated D-fructose showed a scarce selectivity towards the formation of protonated 5-HMF.

In order to promote the use of gas-phase studies for planning strategies that increase the reaction selectivity, a possible base-assisted decomposition process was proposed for the conversion of D-fructose to 5-HMF and 2-FA. Theoretical calculations are in progress in order to elucidate the structures of the starting reactant ion and those of the intermediates and to validate a feasible reaction mechanism.

The previously reported experimental study^[60] on protonated D-xylose was extended to the gas-phase dehydration of D-ribose and D-arabinose. According to the experimental and theoretical results a new mechanistic hypothesis on the pentose sugar dehydration was proposed. These routes follow a common reaction pathway leading to protonated 2-furaldehyde as final product. Interestingly, mass spectrometric experiments demonstrated that in the gas phase the dehydration reaction of D-pentoses involves protonation on the OH group bound at C1 position, conversely to the previously reported theoretical evidence.^[38]

The approach combining mass spectrometry and quantum mechanical calculations was also employed to investigate the gas-phase decomposition of L-Ascorbic acid. To this end, the “extended” Cook’s kinetic method allowed us to determine the unknown proton affinity and gas-phase basicity of L-Ascorbic acid (AA) and to investigate the structure of gaseous protonated AA. Subsequently, the decomposition reaction of Vitamin C was studied and a mechanistic pathway was predicted. According to the hypothesized reaction mechanism the protonated L-Ascorbic acid decomposes following two consecutive dehydrations and the loss of

a formic acid molecule as the last reaction event. A final product characterized by a structure strictly related to furfural was identified.

Considering the increasing importance of mass spectrometric techniques in the investigation of structural features of charged molecules, two novel structure-sensitive gas-phase methods were proved to be effective for the structural elucidation of the never-characterized carbocationic intermediate along the glycosylation pathway. Ion Mobility mass spectrometry was used to obtain absolute values of collisional cross section, whereas the Ultracold spectroscopy allowed us to access the minute structural details of the transient intermediate under investigation. This result represents the first experimental evidence in order to confirm the glycosylation mechanism that has been supposed by theoretical studies.

Finally, the reactivity of two model systems, the iron-containing cation ($\eta^5\text{-C}_5\text{H}_5\text{)}_2\text{Fe}^+$ and doubly-charged hydroxoanions $\text{H}_2\text{V}_2\text{O}_7^{2-}$ and $\text{HNaV}_4\text{O}_{12}^{2-}$ was probed respectively towards CH_2Cl_2 and SO_2 by means of ion-molecule reactions. These experiments were performed by using a modified Ion trap that allowed us to measure the kinetic rate constants of the two processes. As a result, both reactions resulted to be fast and efficient.

In the first case, the mechanism of the concerted iron extrusion, carbon-chlorine bond activation and carbon-carbon formation showed the crucial role of iron. In this regard, N_fR (neutral fragments reionization) experiments have been carried out allowing the analysis of the species associated with charged fragments detected in the CAD spectrum of the reaction intermediate.

In the second system, the obtained results highlighted the role of sulphur dioxide in promoting unprecedented bond-forming reactions that produce singly-charged products by breaking the V_xO_y bone or a terminal V-O bond.

7. Experimental methods

7.1 Electrospray versus chemical ionization

Mass spectrometers equipped with electrospray ionization (ESI) sources were predominantly employed in this work.

Since it was introduced in the late 1980s by John B. Fenn, electrospray ionization technique has become a major tool for producing stable ions from polar and low-volatility compounds, such as macromolecules. Owing to the capability to form ionic species in the gas-phase environment without any fragmentation, it is considered a “soft” ionization method.

The possibility to extract directly from the solution intact ions characterized by a reduced content of energy is essential to obtain precursor reactants that are representative of the species in solution. Only in this way it is achieved a connection between the gas phase and the condensed phase. Also considering the nature of the molecules analysed in this thesis (carbohydrates and organic compounds) the choice of this ionization method seemed to be inevitable, but additional information on the reaction mechanisms under study can be obtained by using chemical ionization (CI) technique.

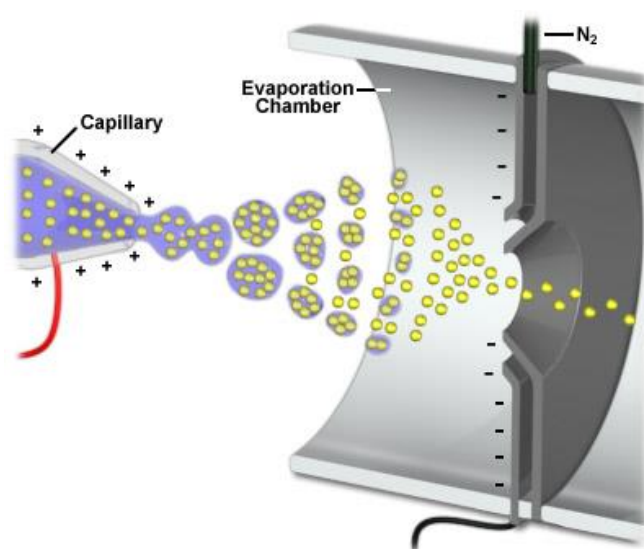


Figure 75: Schematic representation of an ESI-source.

The main differences between the two ionization processes are the following. In the electrospray ionization the analyte dissolved in a polar solvent is sprayed into a capillary where high voltage is applied with respect to a counter electrode, known as skimmer (Figure 75).

Conversely, in the chemical ionization technique the pure analyte is introduced into a low pressure ionization chamber where it interacts with a gaseous reactant previously ionized by electron impact (Figure 76).

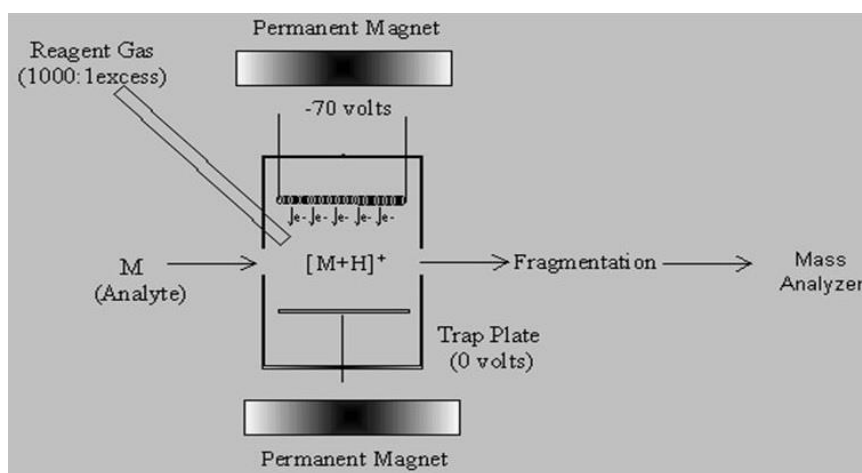
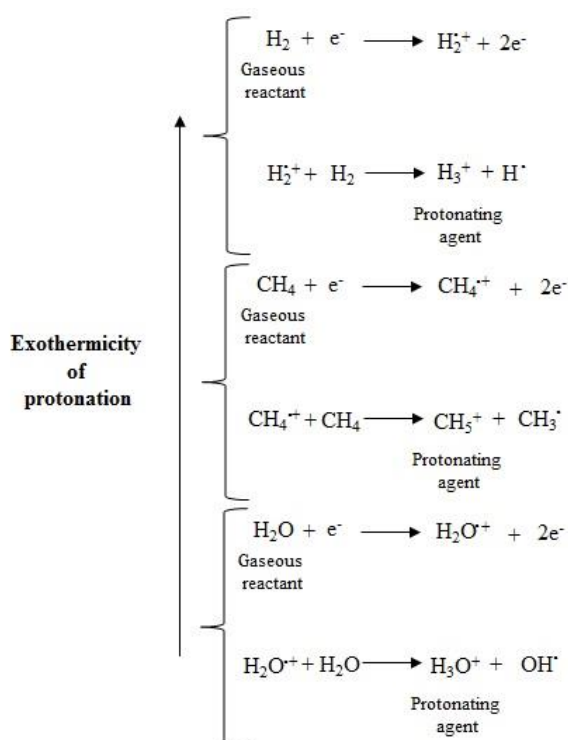


Figure 76: Schematic representation of a CI-source.

In both cases, the ionization process usually results in the formation of protonated ions (MH^+) with the only difference that by using alternative reactant gases under chemical ionization conditions (Scheme 25), different amounts of fragmentation can be observed from the same quasi-molecular ion. Hence, chemical ionization is usually more energetic if compared to electrospray ionization and this is because the amount of energy transferred to a sample molecule on protonation depends on both the proton affinity of the sample and the acidity of the reactant ion.

When the sample molecule is characterized by a single basic group the excess energy after the protonation event is dissipated through the fragmentation. On the contrary, when the molecule shows several basic groups, the energetic surplus allows one to have access to higher proton affinity basic sites, leading to a mixture of isomeric protonated ions. This second occurrence was exploited in this work to

prove the existence of different reaction channels that starting from the same reactant ion can lead to an isobaric population of several isomeric protonated products. In this way it was confirmed that the gas-phase dehydration of protonated sugars (D-glucose and D-fructose) yields not only 5-hydroxymethylfuraldehyde (5-HMF) protonated at the most basic site, but also a series of isomeric products.



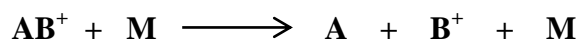
Scheme 25: Protonating agents from different neutral gaseous reactants. The exothermicity of the protonation reaction increases moving from water to hydrogen.

7.2 Collisionally activated dissociation

Collisionally Activated Dissociation (CAD) is a mass spectrometric technique commonly used to obtain qualitative information about the structure of ions analysed in the gas phase. The method is based on fragmentation processes which result in chemical bond breakage and the formation of smaller ionic fragments arising from a precursor molecular ion.

Despite the indisputable advantages of “soft” ionization techniques and their massive diffusion in modern mass spectrometry, the absence of *in-source* fragmentation events, conversely observed with “hard” ionization methods, prevents from obtaining structural information about the analyte. In this regard, if fragments are not formed in the source, they can be produced in the analyser region.

In general, an ionic species is first mass-to-charge selected and then allowed to collide with neutral molecules (helium, nitrogen, argon) causing the breaking of chemical bonds (Scheme 26).



Scheme 26: Schematic representation of the reaction occurring in CAD experiments. AB^+ is a generic ion, whereas M represents the neutral reactant gas.

Although the fundamentals of the technique are the same without regard to the type of mass spectrometer chosen, some important differences in the fragmentation process depend on the analyser employed. For instance, collisionally activated dissociation performed by means of a triple-quadrupole analyser can be considered the result of a single-collision between the precursor ion and the neutral reactant gas. On the other hand, collisionally activated dissociation obtained by using an ion trap (IT) analyser is a consequence of activating and deactivating collisions between the ionic species and the buffer gas as a function of the rf (*radiofrequency*) voltage phase that the ion experiences during the trapping cycle. Anyway, a partial or complete structural

characterization of the molecular ions can be achieved by performing CAD experiments.

In the present thesis CAD-mass spectrometry was employed to structurally characterize the reactant ions, intermediates and final products arising from the D-hexose, D-pentose and L-Ascorbic acid decomposition reactions.

For this purpose, a comparison between the CAD mass spectrum of the final product obtained from the process under examination and the CAD mass spectrum of the postulated product (standard compound) was useful to confirm or reject a specific reaction mechanism hypothesized by theoretical calculations.

7.2.1 Energy resolved mass spectrometry

Over the years, CAD experiments have also been exploited for quantitative purposes by measuring the minimum energy necessary for the dissociation of gas-phase ions, known as *critical energy* (CE). In this regard, the disappearance of the molecular ion of interest and appearance of a specific fragment ion is monitored as a function of the energy required to excite the precursor ion.

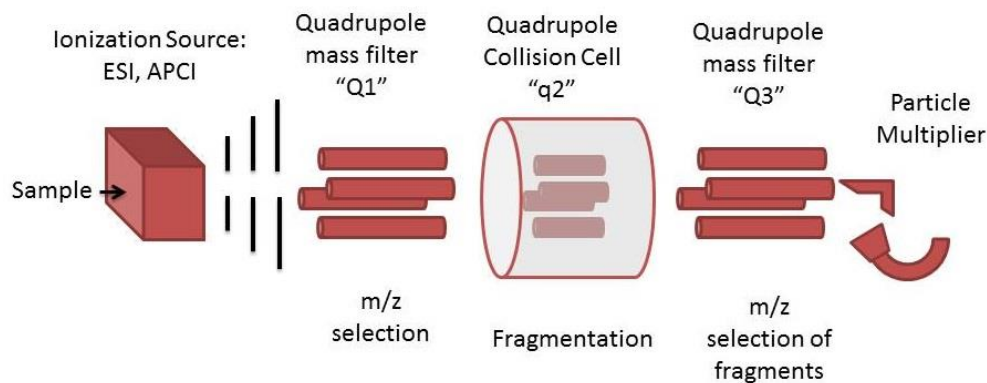


Figure 77: Schematic representation of a triple-quadrupole mass spectrometer.

This technique, named energy-resolved mass spectrometry (ERMS), has been successfully applied not only for the determination of dissociation critical energies of water clusters,^[147] metal-containing ions^[148,149] and proton-bond dimers,^[150] but also for isomer discrimination^[151] and investigation of gas-phase acidities.^[152]

The instrument of choice for the measurement of critical energies by energy-resolved collisional activation experiments is the triple-quadrupole mass spectrometer.

As shown in Figure 77, precursor ions produced by an appropriate ionization source (ESI, ect.) are mass-to-charge selected by the first quadrupole (Q1) acting as an ion filter and then accelerated through the collision cell by applying a constant or variable potential between the entrance and the exit of the second quadrupole (q2). Subsequently, the kinetic translational energy acquired by the ions during the acceleration is converted into internal energy as a consequence of the collision occurring between the ions and a target neutral gas (argon or nitrogen) previously introduced into the collision cell. Hence, the final event of this process is the breakage of chemical bonds and the formation of ionic fragments that are collected and analysed by the third quadrupole (Q3).

The present instrumentation is considered a suitable tool for the estimation of the critical energy because it allows to control the kinetic energy of the ion beam and may operate under single-collision conditions. This is a specific feature of mass spectrometers equipped with analysers that separate and select ions “in space”. Conversely, “in time” analysers, such as the ion trap (IT), operate in a dynamic mode submitting ions to continuous acceleration and deceleration events during the activation period. Thus, they are not able to recreate a single-collision activation environment that is essential to obtain ions having an uniform translational energy distribution.

As a result of each energy-resolved collisional activation experiment, a diagram reporting collision cross section (CCS) versus the centre-of-mass energy (ECM) is obtained (Figure 78). This graphic is constructed by measuring the fragmentation of the precursor ion as a function of the progressive increase of its translational energy, obtained by scanning the potential applied to the collision cell (q2) from low to high values.

As shown in Figure 78, the centre-of-mass energy represents a measure of the collision energy (x -axis) and it is calculated from the potential applied to the quadrupole collision cell and the masses of the colliding species (precursor ions and neutral gas molecules).

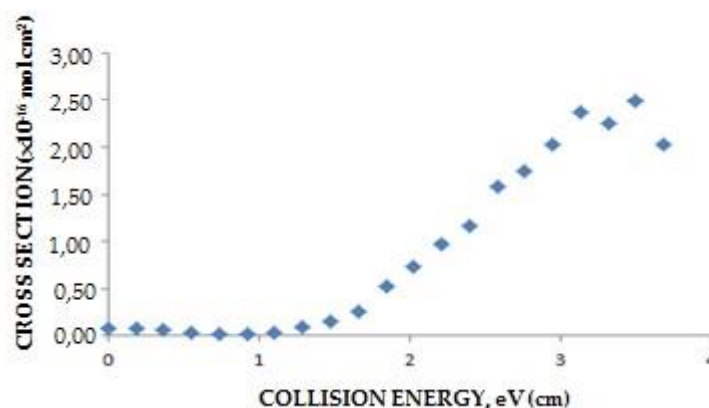


Figure 78: Typical diagram obtained by elaborating the energy-resolved collisional activation experiment data.

In this way, the comparison between different precursor masses is possible. On the other hand, the collision cross section (y-axis) is a parameter that depends on the relative intensity of a specific product ion, corrected for the number of density of the neutral gas into the collision cell and the effective gas cell length.

The onset of fragmentation obtained by linear extrapolation of the slope of the breakdown curve to the baseline provides a relative measure of the energy needed to break a specific chemical bond and hence the activation energy of that fragmentation channel.

This method was applied in our studies to measure the threshold energies associated to the dehydration reactions occurring in the gas phase for protonated D-hexoses and D-pentoses. In order to obtain absolute fragmentation threshold energy values, it is necessary to know exactly the ion-beam translational energy and this goal can be achieved only by using home-built guided ion beam instrument. On the other hand, our commercial triple quadrupole was used to measure threshold energies as relative values. In particular, a comparison based on these relative critical energies was carried out between the D-glucose and D-fructose and among the three pentoses, D-xylose, D-ribose and D-arabinose. Then, the same approach was employed to study the decomposition process of protonated L-Ascorbic acid.

The knowledge of the dissociation energy barriers relating to the dehydration reactions studied in this work represents a fundamental result in order to validate the mechanism predicted by theoretical calculations.

7.2.2 Tandem MSⁿ mass spectrometry

Tandem mass spectrometry, also known as MSⁿ, is an experimental technique that involves multiple steps of ion selection and subsequent fragmentation. Some mass spectrometers allow one to isolate a fragment ion arising from the first isolation/fragmentation cycle of the parent species and submit it in turn to CAD experiments. Supposing to repeat this process in sequence it is possible to follow step-by-step a specific fragmentation channel, progressively acquiring structural information about the precursor ion.

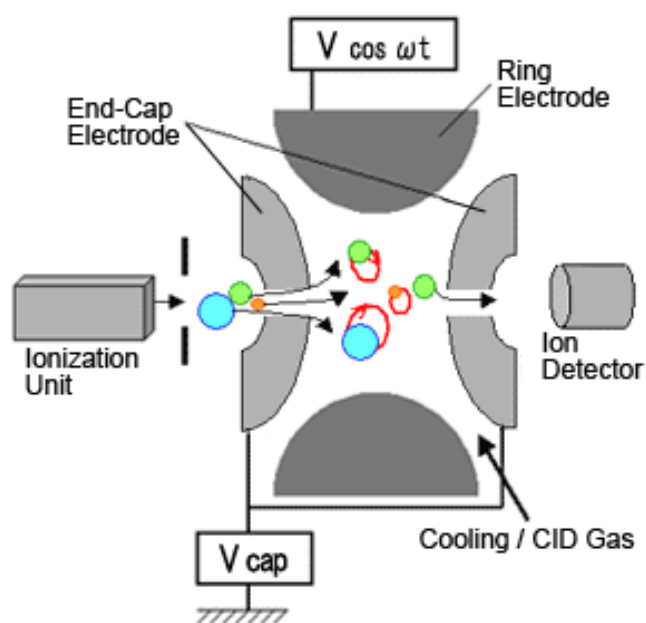


Figure 79: Schematic representation of a quadrupole ion trap mass analyser.

In this context, triple quadrupole are only able to perform a single isolation/fragmentation event and this is due to the fact that the present analyser spatially distinguishes ions. For this reason, a number of separation elements physically separated and distinct would be required to approach tandem experiments more than the MS/MS level. Thus, contrary to the energy-resolved

collisional activation experiments that need to be performed by using “in space” analysers, the preferred method to carry out a tandem MS experiment is the use of mass spectrometers equipped with analysers that temporally separate ions, such as a quadrupole ion trap.

An ion trap is a device that can accumulate ions for an extended period of time by applying an electric and/or magnetic fields (Figure 79).

Owing to its extraordinary capability to act as an ion store, quadrupole ion trap has paved the way to modern application of mass spectrometry such as the infrared multiphoton dissociation (IRMPD) technique.^[153]

By performing mass spectrometry in time, the separation is accomplished with ions trapped in the same place and the multiple separation steps occur over time. Hence, only by using trapping instruments it is possible to have access to multiple levels of analysis which are referred to MSⁿ.

In this work tandem mass spectrometry was employed to follow step-by-step the dehydration reactions under investigation.

Starting from a specific reactant ion the identity of the dehydration final products was proved in respect of the considered fragmentation channel. This approach was useful to verify the existence of a selective and effective D-fructose base-assisted decomposition mechanism.

7.3 Ion-trap kinetic experiments

Chemical kinetics represent the investigation of rates of chemical processes, including the study of different experimental conditions that may influence the speed of a reaction. As a result, information about the reaction mechanism and the structure of transition states can be gained allowing the construction of theoretical models describing the single elementary steps of the considered process.

The experimental measurement of reaction rate constants (k) is usually achieved by monitoring the concentration change of reactants and products over the time. For instance, the concentration of a reactant can be measured by using spectrophotometric techniques, but such an approach is suitable only for those analytes having chemical groups that absorb light. Moreover, reactants and products often share structural features causing band overlapping problems that are responsible for the scarce selectivity of this method.

When reactions occur between a ionic reactant and a neutral gaseous species taking at least several seconds, the rate of the process can be measured by means of mass spectrometric techniques.

Kinetic studies of ion-molecule reactions have originally been performed by using ion cyclotron resonance mass spectrometers (FT-ICR).

This instrumentation is characterized by a mass analyser that distinguish ions on the basis of their cyclotron frequency in a fixed magnetic field.^[154] In particular, the ions are stored in a Penning trap by the combination of a homogeneous axial magnetic field and an inhomogeneous quadrupole electric field. Subsequently the ionic species are isolated by using the so called “arbitrary waveform” procedure and transferred to the cell containing the neutral reactant. Here the ionic intensities of the isolated reactant ion and products are monitored as a function of the time in order to obtain a diagram where the disappearance of the reactant ion is directly related to the appearance of the products as shown in Figure 80. Owing to the excess of neutral reagent compared to the reactant ion the rate constant can be measured under pseudo-first order conditions, as verified by the logarithmic plot of the reactant ion concentration versus the time. According to the kinetic diagram, the reactant ion intensities fit the equation $c=c_0e^{-k_{\text{obs}}t}$ where c is the ion intensity at time t and k_{obs} represents the pseudo-unimolecular decay

rate constant. On the other hand, the product intensities fit the equation $c=(k_f/k_{obs})c_0(1-e^{-k_{obs}t})$ where k_f is the pseudo-unimolecular growth rate constant of a given product. As a result, the bimolecular rate constants k ($\text{cm}^3\text{s}^{-1}\text{molecule}^{-1}$) can be obtained by k_{obs} (or k_f) and the neutral reactant density.

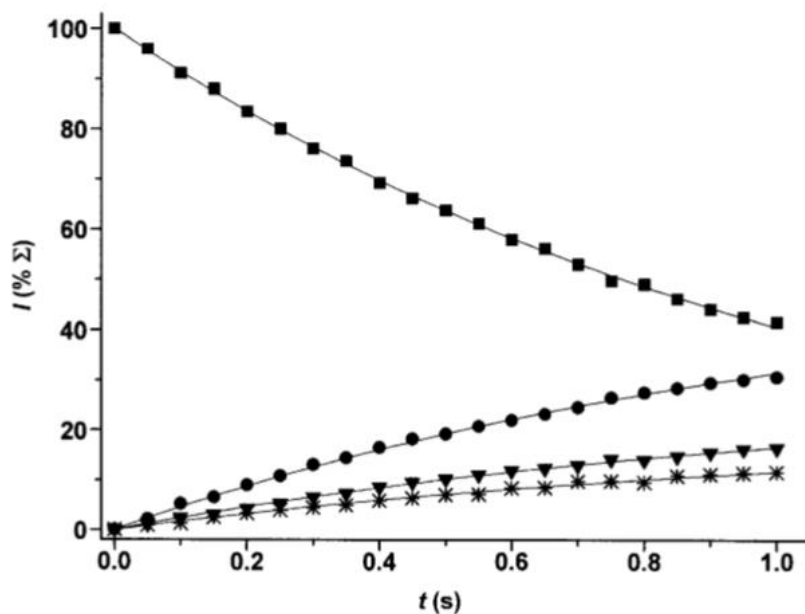


Figure 80: Kinetic diagram and best-fit lines of a model reaction obtained by plotting the ionic intensities of the reactant ion and products (y-axis) versus the time (x-axis). The measurements were performed by using an FT-ICR mass spectrometer. ■ Reactant ion; ● Product 1; ▼ Product 2; * Product 3.

In this thesis the kinetic measurements of the ion-molecule reactions described in Chapter 5 were performed by using an Ion trap mass spectrometer (IT-MS) that is considered a device for the storage of charged particles, as well as the FT-ICR.

To this end, the mass spectrometer was partially modified to allow the introduction of a reagent gas into the vacuum chamber. Hence, the rear plate of the instrument was replaced by a custom-made plate with a 6.25 mm hole equipped with a peek tube of 0.75 mm internal diameter (i.d.) (Figure 81). The peek tube enters the vacuum region and contains two deactivated fused-silica capillaries of 0.25 mm i.d., through which the neutral gases are separately introduced. The capillaries are positioned coaxially to the rear hole of the trap. The pressure of the buffer gas (helium) was measured by a Pirani APGL gauge

(Edwards), connected to a Teflon tube (4 mm i.d.) that passes through the hole of the rear plate. The tube is just in contact with the metal plate of the trap, close to the helium entrance.



Figure 81: Back side of the modified LTQ XL linear quadrupole ion-trap mass spectrometer (Thermo Fischer Scientific).

The pressure of the neutral gases flowed into the trap is kept constant by a Granville–Phillips leak valve and measured by a Granville–Phillips Series 370 Stabil Ion Vacuum Gauge (accuracy $\pm 4\%$ of reading). Owing to the position of the Pirani gauge, the effective pressure of the neutral gases can be estimated by calibrating the pressure readings through the known rate constant ion–molecule reactions performed by FT-ICR, guided ion beam (GIB), and SIFT mass spectrometers. The reactions of Pt^+ (13) and FeO^+ (14) with CH_4 reported below were used as the reference reactions^[155] and the readings are further corrected for individual response factors of the neutral reactants.^[156]



In the kinetic experiments performed by employing the above described apparatus, the reactions occur in a helium buffer gas that typically ensures pressures of the order of mTorr.^[157] This feature allows us to obtain rate constant measurements at high pressure conditions that are in good agreement with the same rate constants measured at the low FT-ICR pressures.

Another important difference between the two approaches consists in the collision conditions. The rate constants are measured under multiple-collision conditions by using the modified ion trap compared to the single-collision condition obtained with the FT-ICR. Such a difference could be responsible for a greater collisional stabilization at the high pressure of ITMS. As a result, the reaction is initiated by the same reactant ions regardless of the method employed, but possible intermediates formed with excess energy are not effectively cooled in ICR, whereas the opposite is true in ITMS.

Finally, the loss of some reactant ion can be caused by the water present in the modified apparatus. Therefore, if the reactant ion reacts with the background water an accurate calibration procedure is necessary to subtract this contribution.

7.4 Neutralization-reionization mass spectrometry

In conventional mass spectrometric techniques only charged molecules are detected. For this reason, the neutral products formed from an ion-molecule reaction typically represent the “blind” side of the reaction. However, the role of this neutral counterpart is fundamental because in most cases represents the key reactive species along the reaction pathway.

In 1966 Lavertu et al.^[158] discovered that fast ionic beams can undergo charge exchange process by colliding with a neutral target gas and forming beams of neutral molecules. This experimental evidence has paved the way to the study of neutral species by mass spectrometry.

To this end, the technique of neutralization-reionization mass spectrometry (NR-MS) has become a powerful tool to generate and identify neutral elusive species.^[159] In particular, the potential of the method was probed by the studies of McLafferty^[160] and others^[161] on polyatomic organic intermediates.

In this thesis the nature of the neutral counterpart arising from the carbon coupling reaction of $(\eta^5\text{-C}_5\text{H}_5)\text{Fe}^+$ with CH_2Cl_2 (Chapter 5) was assessed performing N_rR (neutral fragments reionization) experiments that can be considered the direct descendant of NR-mass spectrometry. A schematic representation of this technique is depicted in Figure 82.

According to this approach, the precursor ion of interest is generated in the instrument source by choosing the appropriate ion preparation methods. The ionic beam thus obtained is accelerated by applying a potential difference ranging between 4 and 8 keV. After passing the first electric sector the ionic beam reaches the magnetic sector where ions are mass-to-charge selected. The isolated ions enter a first cell where undergo dissociation induced by the collision with a target gas (such as Xe, Hg, NH₃, NO, or organic neutralization agents). As a consequence, the ions undergo a charge-exchange reaction leading to a mixed beam of ionic fragments and their neutral counterparts. The neutral and ionic molecules exit the collision cell and they are separated by charging an electrode that deflects all ionic species from the mixture. The beam obtained is constituted only by neutral molecules having the translational energy of their precursor ions. At this stage, the neutral species enter a second cell where they are reionized

through a charge exchange process upon collision with an appropriate neutral gas, such as oxygen. The reionized species are then analysed by using an additional sector or can be subjected to further structural analysis.

As a whole, the entire process occurs in two collision cells placed along the optical path, as a result of two in-time and in-space separated events. If, in the mass spectrum obtained upon reionization of the neutral species, a signal corresponding to a neutral counterpart is observed, this immediately demonstrates that the neutral fragment formed upon CAD in the first collision cell remains intact along the path to the second collision cell where it is reionized.

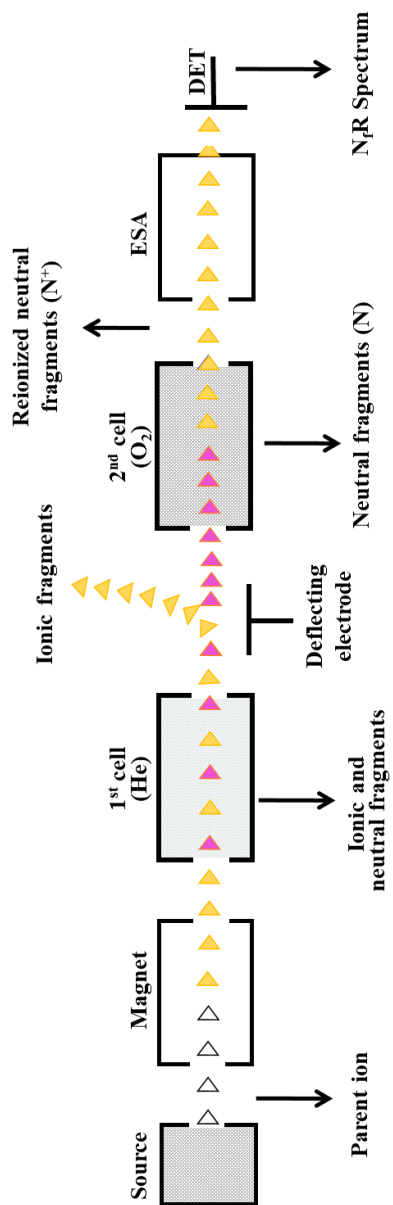


Figure 82: Schematic representation of the reaction events typically involved in a N_pR experiments performed by using a Zab Spec-*oa*-TOF mass spectrometer.

7.5 Ion-mobility mass spectrometry

Ion mobility mass spectrometry is a gas-phase analytical technique used to separate ionized molecules sharing the same mass-to-charge ratio, but different in size and shape.

The experimental apparatus employed in this work is shown in Figure 83 and it was specifically developed and commercialized by Waters Corporation to couple the main components of a mass spectrometer with a mobility cell. This setup takes advantage of ion generation and manipulation performed by using mass spectrometric methods and the possibility to separate different ionic conformers by using the ion mobility cell.

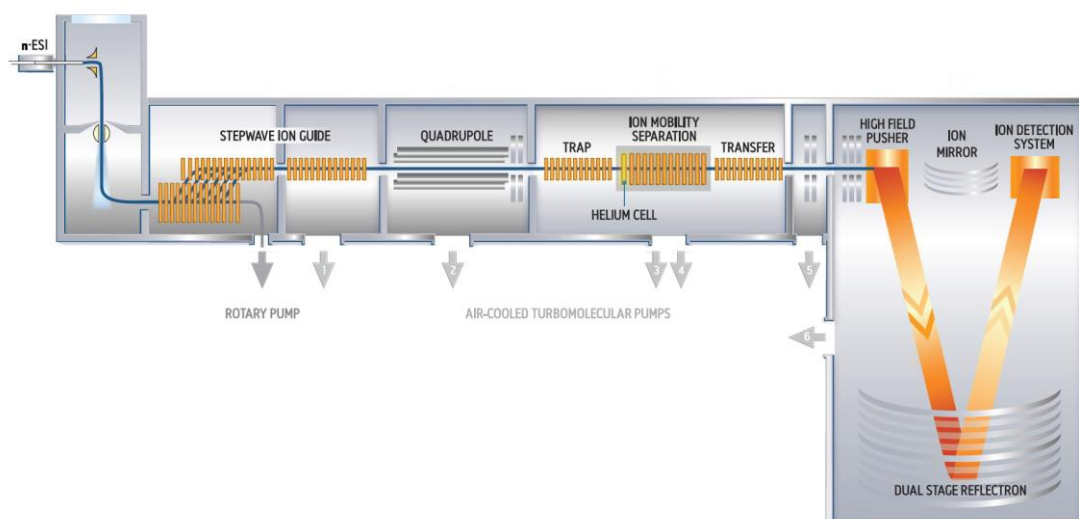


Figure 83: Scheme of the Synapt G-2S HDMS by Waters Corporation.

According to this approach, the ion beam is gently produced from an analyte solution using a nano-ESI source and collimated through a series of ion guides after covering a trajectory that resembles a flattened Z-shape. In particular, the nano-ESI represents an evolution of conventional electrospray ionization useful to reduce the analyte amount needed for the analysis. In this technique, the sample solution is pumped into a Pt/Pd coated borosilicate needle with a small opening at the tip. As a result, smaller droplets with a higher charge density can be formed

allowing for an earlier droplet disintegration and a larger portion of the analyte molecules available for the MS measurements.

After passing the stepwave ion guide, the ions are selected by a quadrupole ion filter according to their m/z . This represents the first step of separation before the ions reach the ion mobility cell where they can be distinguished on the basis of their shape and size.

The ion mobility cell is mainly constituted of a stainless steel chamber filled with a counter-flowing buffer gas, such as argon, helium or nitrogen. When a small voltage difference is applied between the entrance and exit of the chamber, the ions are propelled through the IM cell and collide with the neutral gas molecules along the path. As a consequence, ionic species characterized by compact structures undergo fewer collisions with the buffer gas and traverse the cell faster than ions showing a more extended conformation (Figure 84). Hence, the separation of molecules with the same m/z and different shape is achieved.

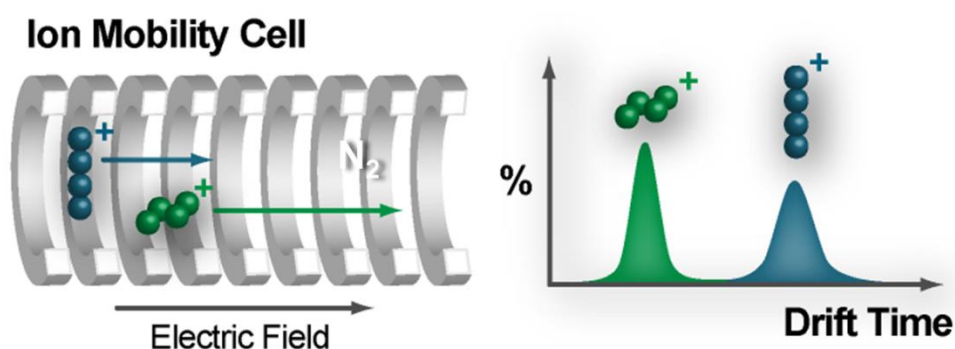


Figure 84: Schematic representation of an IM separation. The diagram on the right reports the measurement of the different times the same m/z ions need to traverse the cell as a function of their shapes.

From the measurement of the time the ions need to cross the cell (*drift time*), a collision cross section (CCS) value can be experimentally derived. CCS represents a molecular property strictly related to the shape of the ions reflecting the number of collisions between the ions and the buffer gas.

In this specific setup, the travelling wave IM (TW-IMS) cell commercially designed for this instrument was replaced by a drift tube IM (DT-IMS) cell to

obtain CCS values completely independent of instrument parameters and suitable to be stored in databases.

In the TW-IMS cell an inhomogeneous electric field is applied to the cell and the ions are propelled through the cell by a traveling voltage wave, allowing a good ion mobility separation even for short drift cells. However, the main disadvantage lies in the fact that the CCS cannot be obtained as an absolute value, but it is only estimated by calibrating the instrument using samples with known CCS, increasing the propagation of the error associated to the measurement. Additionally, the nitrogen typically used in standard Synapt instrument as drift gas cannot be easily changed. Nitrogen is usually employed to provide a better result in ion separation, but most theoretically CCS values are calculated for helium as drift gas hindering a direct comparison between the experimental and theoretical data.

On the contrary, in the DT-IMS the ions traverse the mobility cell under the influence of a homogeneous electric field (Figure 85). According to this setup, the voltage difference between the entrance and exit of the mobility cell drops linearly along the drift tube. Hence, the CCS of an ion is directly obtained by measuring the drift time as a function of the applied voltage.

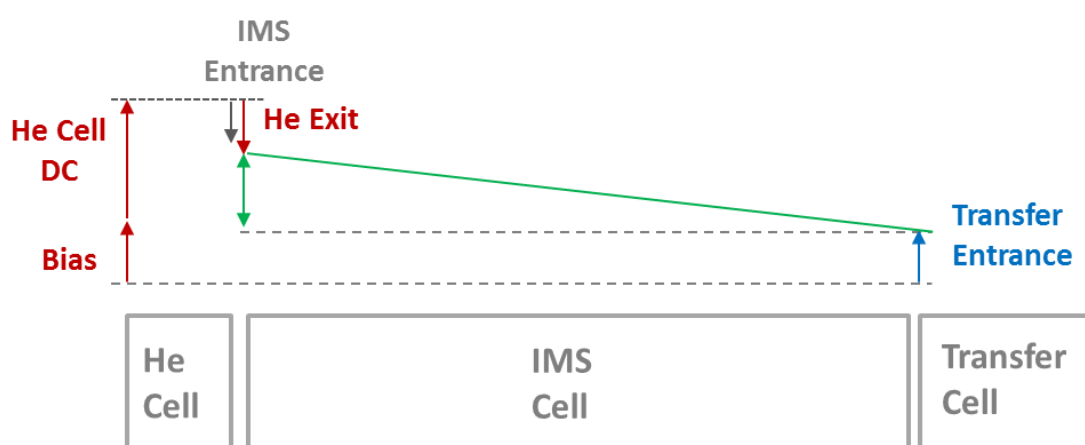


Figure 85: Schematic representation of the voltages applied at the IMS cell. As reported by the green line, the final voltage gradient linear decreases along the drift cell.

7.6 Superfluid helium nano-droplet infrared spectroscopy

Helium droplet spectroscopy is an experimental technique taking advantage of the sub-kelvin temperature cooling process combining a helium droplet source with mass spectrometry and infrared action spectroscopy. The present apparatus has been custom-made assembled at the Fritz Haber Institute of Berlin by modifying a Q-ToF Ultima (*Water Corporation*) as shown in Figure 86.

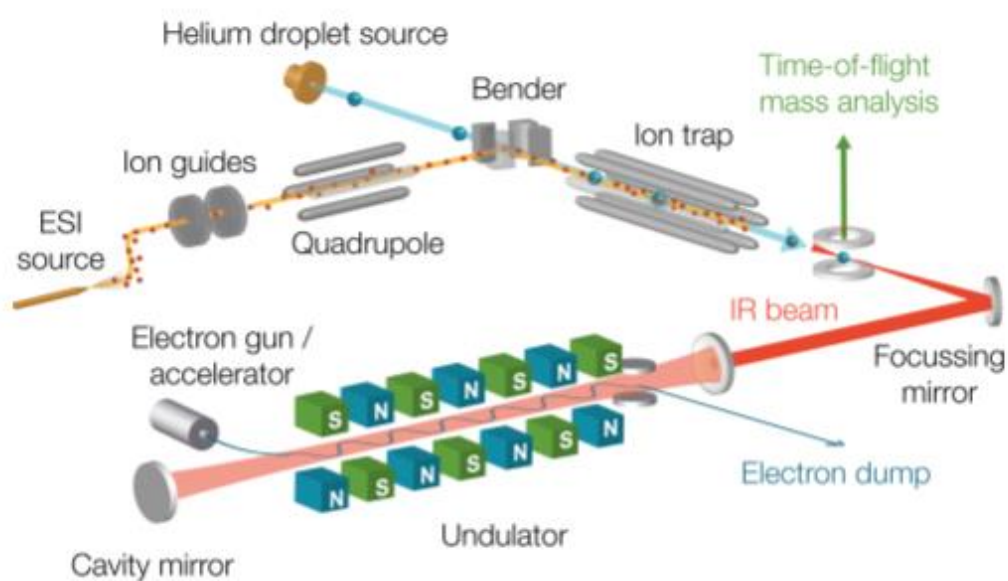


Figure 86: Schematic representation of the experimental apparatus. Ions are brought into the gas-phase, mass-to-charge selected and accumulated into the ion trap. Helium droplets can pick up the ions that are subsequently interrogated by the free-electron laser.

The generated ions are brought into the gas phase by using a nano electrospray ionization source (*Z-spray*). A Pd/Pt coated capillary is loaded with the sample and charged droplets are formed by applying a voltage of around 1 kV to the capillary tip. After the complete solvent evaporation, the ions cover a Z-shaped trajectory towards the skimmer and pass into the vacuum region. Here, the ionic stream is collimated by a series of ion guides driving the ions through two different pressure stages (from 14 mbar to 1.7 mbar).

Ionic species are then mass-to-charge selected by a quadrupole mass filter to reach an hexapole collision cell. This device, originally installed in the

commercial Q-ToF instrument, was also kept in the present apparatus with the only function to increase the ion transmission to a reflectron time-of-flight analyser that allows for the ion signal monitoring. When the source conditions and potentials are optimized, the ions can be deflected by 90° through a bender and accumulated into a linear hexapole ion trap filled with helium buffer gas. The doping region is the chamber where the ion trap is located and where the improvement in the vacuum level is fundamental to suppress the unfavourable formation of ion-water clusters inside the trap. For this reason the ion trap was placed inside a stainless steel chamber increasing the vacuum level to pressures of $\sim 10^{-8}$ mbar.

In order to achieve longitudinal confinement, the endcap electrodes at the entrance and exit of the trap are kept at a small voltage over the DC offset.

The incoming ions have a well-defined energy of ~ 34 eV and during the accumulation time the excess of kinetic energy is removed by the collisions with the helium. This process thermalizes their internal energy to the temperature of the buffer gas atoms. Furthermore, the ionic species can be cooled down to about 80 K because the trap is placed inside a copper housing refrigerated by a flow of liquid nitrogen. After several seconds, the space-charge limit (10^6 ions cm^{-3}) inside the trap is achieved and the buffer gas is removed. Typical values of the accumulation can vary from ~ 3 s up to ~ 10 s, depending on the m/z ratio of the ions and the efficiency of transmission.

The helium clusters are generated by the expansion of highly purified helium gas from high pressure and low temperature into vacuum.

Compared to all other substances, helium is known to have the lowest boiling point (4.2 K for ^4He at atmospheric pressure)^[162] as a consequence of the weak Van der Waals interactions existing between the atoms. The remarkable absence of a triple point justifies the failed attempt to produce ^4He solid and highlights the extraordinary property of remaining liquid at absolute zero temperature and ambient pressure. In particular, at the temperature of 2.17 Kelvin the isotope ^4He undergoes a unique transition phase, the so called λ transition, from the liquid state named Helium I to the superfluid state known as Helium II.^[163,164] On the

contrary, ^3He shows a superfluid behaviour only at much lower temperature ($T=2.6\text{ mK}$).^[165]

Superfluid state is characterized by a series of properties,^[166] such as the absence of viscosity, an infinite thermal conductivity and the inability to absorb light from the deep infrared to the far ultraviolet making the helium a suitable cryogenic matrix for spectroscopic studies.^[167] Besides, these features allow the superfluid helium to flow without frictions, circulating over the obstruction and through the pores of containers that hold it.

In this work, superfluid helium nanodroplets are obtained from a source consisting of a pulsed Even-Lavie valve cooled to temperature of a few kelvin by a closed-cycle helium cryostat and operating at a repetition rate of 5-20 Hz. The flux of helium droplets is controlled by the diameter of the orifice employed for the expansion process, the stagnation pressure (65-68 bars), the opening time ($\sim 19\ \mu\text{s}$) and the temperature of the pulsed nozzle. In particular the nozzle temperature can be changed in the range of 15-25 K, deeply influencing the size of the droplets (from $\sim 10^6$ to $\sim 10^4$ helium atoms) and consequently the yield of the so called *pick-up* process.^[168]

When the valve is accurately aligned, the pulsed beam traverses the ion trap and the collision occurring between a superfluid helium droplet and a ionic species can cause the entrapment of the ion inside the nano-droplet.

This phenomenon is known as pick-up process and it can be approximately described according to the physical model of the inelastic collision, in which the internal energy (E_{int}) of the guest particle (*dopant*) and the collision kinetic energy are transferred to the droplet. As a consequence, the total energy associated to the pick-up is obtained from the Equation 3 where m and v are the masses and the velocities of the dopant and the helium droplet (D), respectively.

$$E_{\text{pick-up}} = \frac{1}{2} \frac{m_{\text{dopant}} \cdot m_D}{m_{\text{dopant}} + m_D} (v_{\text{dopant}} - v_D)^2 + E_{\text{int}} \quad (3)$$

Since the velocity (20-60 m s⁻¹) and the mass of the dopant particle are both extremely lower compared to the velocity (400-500 m s⁻¹) and the mass of the droplet, Equation 3 can be simplified as follows

$$E_{\text{pick-up}} = \frac{1}{2} m_{\text{dopant}} v_D^2 + E_{\text{int}} \quad (4)$$

After the occurrence of the pick-up, the $E_{\text{pick-up}}$ is dissipated into the helium medium through the release of helium atoms from the droplet surface in a process called *evaporative cooling*. The number of helium atoms released during this thermalization phenomenon can be estimated to be around 1600 per 1 eV of the pick-up energy. As a consequence, the starting size of the droplets decreases reaching an equilibrium temperature that allow to cool down the captured ion to ~0.37 K.

Owing to the high kinetic energy (150-300 eV) associated to the helium droplets, resulting from their large mass and high velocity, only the ions embedded inside the nano-droplets can overcome the trapping potentials achieving the detection region where they are interrogated by an IR radiation.

IR photons are generated in the mid-IR wavelength regime, covering the entire fingerprint region (from 950 cm⁻¹ to 1800 cm⁻¹) by a FEL (Free-Electron-Laser). Such laser system operates according to the principle that accelerated electrons produce a synchrotron radiation. Basically, the electrons emitted by an electron gun and accelerated to velocities close to the speed of light are injected into a magnetic periodic structure named *wiggler* or *undulator* (see Figure 86). The periodic deflection of the electron beam performed by the undulator magnets leads to the emission of a monochromatic radiation at each turning point in the sinusoidal trajectory. This radiation is captured and accumulated in a laser cavity. The interaction between freshly injected electron bunches with the high pulses circulating in the cavity produces a self-amplification process creating an intensity gain on each successive pass. Because of their curved trajectory, the electrons cover a longer distance than the light beam and consequently coherent radiation is

generated only at specific wavelengths. According to the Equation 5, the wavelengths observed (λ_{obs}) depend on the undulator period (Λ_u), the relativistic energy of the electrons (γ) and the deviation of the electron path from the straight path of the light beam scaling with the magnetic field (K).

$$\lambda_{\text{obs}} = \Lambda_u \frac{1+K^2}{2\gamma^2} \quad (5)$$

From this Equation it is clear that the wavelength can be tuned by changing the magnetic field strength (K) or the relativist energy of the electrons (γ) while Λ_u is normally fixed since the undulator is constituted by an array of permanent magnets.

Infrared radiation for analysing carbohydrates embedded inside helium droplets is produced by the free-electron laser of the Fritz Haber Institute (FEL-FHI).^[169]

The trigger system setup allows the longitudinal overlapping of the IR laser beam and the pulsed flux of doped droplets in the detection region. When a resonant radiation is absorbed, the embedded ions can be ejected from the droplets as shown in Figure 87.

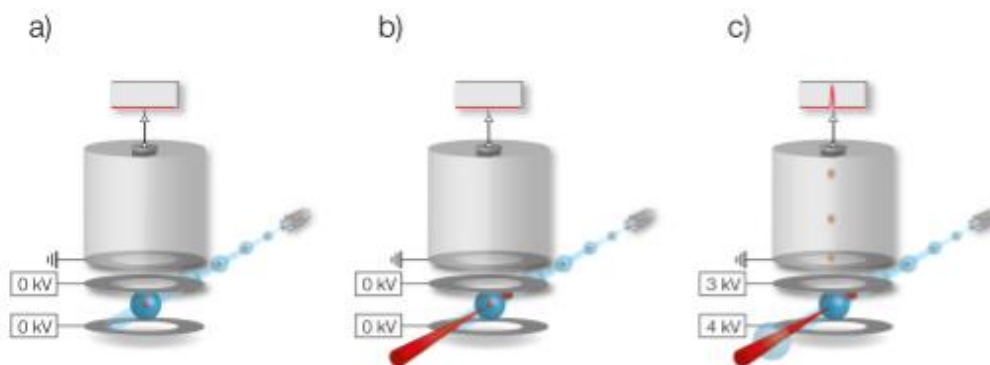


Figure 87: Schematic representation of the detection chamber. a) Doped helium droplets are placed between the extraction plates after reaching the detection chamber; b) The IR radiation overlaps the doped droplet flux; c) The potentials between the extraction plates are activated and the eventual absorption of a resonant radiation leads to the ejection of ions that are directed toward the detector.

The physical principles ruling the ejection phenomenon have not completely understood, but the process is actually object of further investigation at the FHI laboratories. Nevertheless, the occurrence of the ejection is favoured by the weakly interacting forces existing between the embedded ion and the helium droplet.

The ejected ions are deflected towards a time-of-flight analyser by applying high potentials to two extraction plates that the doped droplets reach during the overlap period. As a result, an IR spectrum can be obtained by scanning IR wavelengths in the range 950 cm^{-1} - 1800 cm^{-1} and simultaneously monitoring the ejection yield.

The orientation of a mirror can be modified during the analysis in order to change the focus of the photon flux towards the doped droplets. This tuning procedure allows one to obtain a good signal-to-noise ratio, but a photon flux excessively focused can cause the undesirable fragmentation of the embedded ions. Considering all the physical processes involved in this novel experimental approach, Figure 88 well summarizes the main differences existing between the IRMPD technique and the helium droplet method.

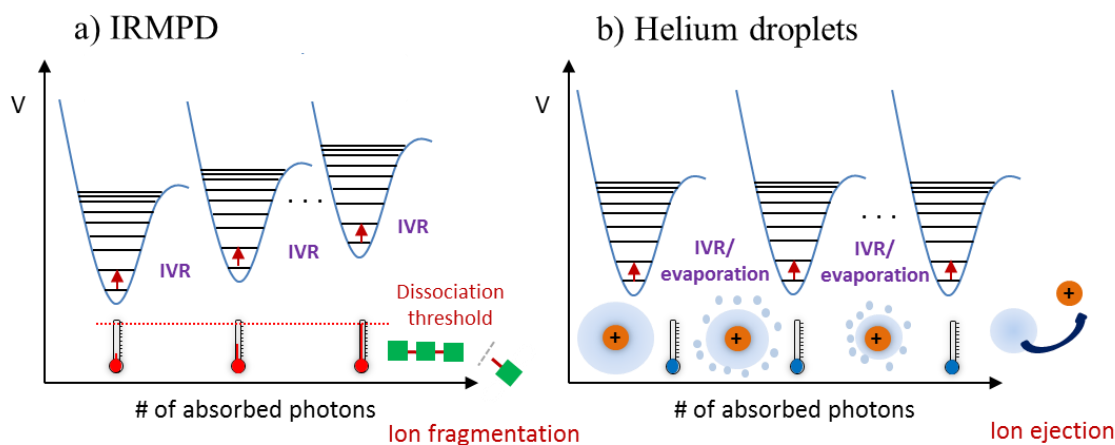


Figure 88: Schematic comparison between the fundamental principles of IRMPD and Helium droplet spectroscopy.

In the IRMPD technique the absorption of resonant photons progressively increase the internal energy of the ions. Therefore, the achievement of the

dissociation threshold finally results in the unimolecular fragmentation of the ion. On the contrary, the energy excess of a ionic species embedded in a helium droplet is dissipated into the helium medium allowing the ion to relax back into the ground state and to reach a sub-kelvin temperature. Resonant photons can be absorbed until the molecule is ejected from the droplet. As a consequence, in the IRMPD approach the dissociation yield is the property monitored as a function of the wavelength of the incident radiation, while in the case of helium droplet method it results to be the ejection yield.

7.7 Experimental details

ERMS experiments

Energy resolved CAD mass spectra were acquired by means of a TSQ 700 triple stage quadrupole mass spectrometer from Thermo Finnigan Ltd. Argon was introduced in the triple quadrupole collision cell as the target gas at pressures of about 0.1 mTorr. After the isolation, the selected ion was allowed to experience collision energies values ranging from 0 to 40 eV (laboratory frame). An upper limit of 2 eV for the kinetic energy of the reactant ion at nominal collision energy of 0 eV (laboratory frame) and an ion-beam energy spread of about 1 eV were estimated by using cut-off potentials. For comparison of different precursor masses the laboratory ion energies (E_{lab}) were transformed to centre-of-mass collision energies according to Equation 6, where m and M are the nominal masses of neutral reactant and the ionic reagent, respectively.

$$E_{\text{CM}} = E_{\text{LAB}} \frac{m}{(m+M)} \quad (6)$$

Experimental cross sections (σ_{tot}) were calculated using Equation 7, where I_{R} is the intensity of the transmitted ion beam, I_{tot} is the total intensities, n corresponds to the number density of the neutral gas ($3.5 \cdot 10^{13}$ molecule cm^{-3}) and l is the effective gas cell length (12 cm).

$$\sigma_{\text{tot}} = - \frac{\ln(I_{\text{R}}/I_{\text{T}})}{nl} \quad (7)$$

Individual product cross sections (σ_{p}) were determined from the experimental cross sections by the Equation 8, where I_{p} represents the intensity of the product ion and I_{ptot} the total product ion intensities.

$$\sigma_{\text{p}} = \sigma_{\text{tot}} \left(\frac{I_{\text{p}}}{I_{\text{ptot}}} \right) \quad (8)$$

Tandem MSⁿ experiments

Full scan and MSⁿ mass spectra were recorded by using an AmaZon SL ion trap instrument operating in the positive ion mode and equipped with an ESI source. Each spectrum is obtained by averaging 50 scans and was obtained by direct infusion of a fresh solution at a flow rate of 5 $\mu\text{L}/\text{min}$. Nitrogen was used as nebulisation and desolvation gas at 5.0 psi and 2.5 L/min, respectively. During the signal optimization procedures the potential applied on the capillary was ranged between -4000/-4500 V and the plate offset between -400/-450 V. The source temperature was kept at 200°C for all the experiments.

Mass spectrum acquisition and processing were carried out using the software Compass DataAnalysisTM version 4.0 supplied with the instrument.

Kinetic experiments

The kinetic experiments were performed on a modified LTQ XL linear ion trap mass spectrometer and alternatively equipped with an electrospray ionization (ESI) or an atmospheric pressure chemical ionization (APCI) source.

Sample compounds were dissolved in 1:1 water/acetonitrile and the obtained 10^{-3} M solutions were infused at a flow rate of 3-5 $\mu\text{L}/\text{min}$ via a syringe pump directly connected to the source. Nitrogen was used as sheath and auxiliary gas at flow rate of 15-20 and 5 arbitrary units (a. u.~ 0.37 L/min). Typical experimental ESI conditions were: source voltage 4-5 kV, capillary and vaporizer temperatures 200 °C and 80 °C, respectively. Concerning APCI source, capillary and vaporizer temperatures were set to 150 °C and 60 °C respectively and the molecules were ionized by applying a discharge current of 3-4 μA .

Neutrals were introduced into the trap by a metering valve, and their pressure was read by a Granville-Philips series 370 Stabil Ion Vacuum Gauge, after readings calibration.^[170] Ions under study were generated in the ESI or APCI source, mass-selected with an isolation window of 1 m/z and reacted with the neutral of interest (SO₂; H₂O or CH₂Cl₂) for different periods of time. Typical pressures of neutrals ranged from $0.5 \cdot 10^{-7}$ to $7.0 \cdot 10^{-7}$ Torr.

Mass spectra were acquired by using the Xcalibur 2.0.6 software and recorded for each reaction time using the full scan mode, with an injection time of 200 ms, normalized energy set to 0 eV and the activation Q value optimized to ensure stable trapping fields for all the ions. All the spectra are the average of 10 scans. Rates were measured by varying the time delay between isolation of the reactant ion and the analysis of its product ions. According to the logarithmic plot of the reactant ion concentration versus time, all rate constants k_{obs} fit the pseudo-first order conditions. When a reaction between the reactant ions and the background water present into the trap was observed, the rate constant of this reaction $k_{\text{obs(background)}}$ was measured and subtracted from the k_{obs} obtained for the reaction of interest.

Bimolecular rate constants k ($\text{cm}^{-3} \text{s}^{-1} \text{molecule}^{-1}$) were calculated by dividing the pseudo-first order rate constant by the concentration of neutral reagent in the ion-trap. The reaction efficiency, expressed as the ratio of the bimolecular rate constant k to the collision rate constant, was calculated according to the ADO theory.^[171] The bimolecular rate constants k are the average of ca. 30 independent measurements performed in different days for each precursor ion. All the rates were measured over 5-fold neutral pressure range, showing linear correlation with the neutral density. Standard deviations in the absolute rate constant were typically <10%; however, a conservative estimate of error of 30% is given, due to the uncertainties that affected the measurement of the neutral pressure.

Neutral fragment-reionization (N_fR) experiments

N_fR (*Re-ionization of Neutral Fragments*) and CAD experiments were carried out by using a modified ZAB Spec-*oa*-TOF mass spectrometer (VG Micromass) equipped with a chemical ionization (CI) source and five collision cells. Briefly, the instrument has a EBE-TOF configuration where E, B stand for electric and magnetic sectors respectively and TOF for orthogonal time-of-flight analyser. Sample compounds were directly introduced into the source through a solid probe whereas the neutral species were allowed to flow through a capillary column of deactivated silica. Typical operating conditions were: accelerating voltage 8 kV,

source temperature 400 K, repeller voltage 0 V, emission current 1 mA, nominal electron energy 50 eV, source pressure 0.05-0.08 Torr, as reported inside the source block by a Magnehelic differential pressure gauge.

Ions of interest were mass-selected by the magnetic sector and CAD mass spectra were recorded in the gas cell placed after the magnet in the second field-free region. Helium was used as the target gas in the collision cell and its pressure was chosen to provide 80% transmittance.

After recording a CAD mass spectrum, charged fragments were all removed at the exit of the cell by applying a potential of 1 keV on a pair of high voltage deflecting electrodes. As a result, a beam containing only neutrals reached the second cell where it was ionized by collision with O₂ and further analysed in the TOF sector. No signal was obtained by switching the deflector on in the absence of the re-ionizing gas. All N_fR spectra were averaged over 200 acquisitions to improve the signal-to-noise ratio.

MS³ spectra were recorded in a gas cell located in the TOF sector, by mass and energy selection of the daughter ions coming from CAD fragmentations in the second field-free region. All gases were admitted into the cells at such a pressure to achieve a beam transmittance of 80%, under near single collision conditions.

IM-MS experiments

Full scan mass spectra were recorded using a modified Synapt G2-S HDMS by Waters Corporation (Manchester, UK) operating in the positive ion mode and equipped with a nano-ESI source. The source temperature was kept at 25 °C.

Helium was introduced in the drift tube and used as drift gas. At each helium gas pressure the drift time (t_d) of an ion was measured at seven individual drift voltages (V_d) in MS/MS-Mode. The ion mobility constant (K) was calculated according to the Equation (9) where L is the drift tube length and t_0 is the time offset.

$$t_d = \frac{L^2}{K} \frac{1}{V_d} + t_0 \quad (9)$$

By plotting drift times as a function of the quotient of the voltages, time offset (t_0) was obtained from the intercept and the mobility constant K from the slope of the linear function. The constant K was employed to extrapolate the collision cross section (CCS) through the Mason-Schamp equation (10) where q is the total charge of the ion, k_B is the Boltzmann constant, N is the number density of drift gas and μ is the reduced mass (ion + drift gas molecule).

$$CCS = \frac{3q}{16N} \frac{1}{K_0} \left(\frac{2\pi}{\mu K_B T} \right)^{1/2} \quad (10)$$

K_0 represents the standard mobility constant and is derived from the calculated K value by correlating the standard temperature and pressure (T_0 ; P_0) with the drift gas temperature and pressure (T ; P) according to the Equation 11.

$$K_0 = \frac{P}{P_0} \frac{T_0}{T} K \quad (11)$$

Mass spectrum acquisition and processing were carried out using MassLynx software version 4.1 supplied with the instrument and OriginPro 9.0.

Ultra-cold spectroscopy experiments

Infrared spectra of carbohydrate ions were acquired using the experimental setup described in Section 7.6 and recorded in the wavenumber range from 950 cm^{-1} to 1800 cm^{-1} .

Using a variable focusing mirror different photon densities were applied over the wavenumber range allowing to obtain a good signal for the ion ejection. In particular, the spectral region between $950\text{-}1150 \text{ cm}^{-1}$ was scanned by using a low photon density that is sufficient to access large transition dipole modes, such as

the C-O stretching. On the other hand, high intensity focus was necessary to record the wavenumber range between 1150 and 1800 cm^{-1} .

A linear correction was performed dividing the absorption signals by the laser power as a consequence of the fact that the peak intensities are strongly influenced by the multiple-photon absorption process and the bands do not scale linearly with the laser power and the absorption cross-section. Conversely, the absorption of multiple-photon do not influence the band positions.

The shown infrared spectra represent the average of two individual scans performed in order to minimize the effect of possible fluctuations in laser power or ion intensity in the trap.

Radiation is emitted in macro and micro pulses by the FHI-FEL with a full width at half maximum of about 0.3-0.5% of the corresponding wavelength. Macro pulses have a length of up to 10 μs and contain micro pulses of 0.3 - 5 ps length, spaced by 1 ns as the total energy can reach 100 mJ.

After the acquisition of each infrared spectrum, the laser power and several wavelength points were calibrated employing a Cherny-Turner grating spectrometer.

8. Bibliography

- [1] Facing the hard truths about energy: Washington DC: U.S. *National Petroleum Council* **2007**.
- [2] Analysis of the Italian total fleet; *Statistical Yearbook* **2016**-ACI.
- [3] A. J. Ragauskas, C. K. Williams, B. H. Davison, G. Britovsek, J. Cairney, C. A. Eckert, W. J. Frederick Jr., J. P. Hallett, D. J. Leak, C. L. Liotta, J. R. Mielenz, R. Murphy, R. Templer, T. Tschaplinski, *Science* **2006**, *311*, 484-489.
- [4] A. Corma, S. Iborra, A. Velty, *Chem. Rev.* **2007**, *107*, 2411-2502.
- [5] J. Goldemberg, *Science* **2007**, *315*, 808-810.
- [6] D. R. Doods and R. A. Gross, *Science* **2007**, *318*, 1250-1251.
- [7] A. Gandini, *Polym. Chem.* **2010**, *1*, 245-251.
- [8] J. Ten Dam, U. Hanefeld, *Chem. Sus. Chem.* **2011**, *4*, 1017-1034.
- [9] J. B. Binder, J. J. Blank, A. V. Cefali, R. T. Raines, *Chem. Sus. Chem.* **2010**, *3*, 1268-1272.
- [10] F. M. A. Geilen, B. Engendahl, A. Harwardt, W. Marquardt, J. Klanlrmayer, W. Leitner, *Angew. Chem.* **2010**, *122*, 5642-5646.
- [11] J. J. Bozell, G. R. Petersen, *Green Chem.* **2010**, *12*, 539.
- [12] T. Werpy, G. Petersen, *Top Value Added Chemicals from Biomass* **2004**, Vol. *I-Results of Screening for Potential Candidates from Sugars and Synthesis Gas*; NREL/TP-510-35523; National Energy Laboratory: Golden, CO.
- [13] W. A. Bonner, M. R. Roth, *J. Am. Chem. Soc.* **1959**, *81*, 5454-5456.
- [14] Y. T. Wang, K. J. Jin, S. H. Leopold, J. Wang, H. L. Peng, M. S. Platz, J. Xue, D. L. Phillips, S. A. Glover, M. Novak, *J. Am. Chem. Soc.* **2008**, *130*, 16021-16030.

- [15] K. R. Sawyer, J. F. Cahoon, J. E. Shanoski, E. A. Glascoe, M. F. Kling, J. P. Schlegel, M. C. Zoerb, M. Hapke, J. F. Hartwig, C. E. Webster, *J. Am. Chem. Soc.* **2010**, *132*, 1848-1859.
- [16] M. Aschi, M. Attina, F. Cacace, A. Ricci, *J. Am. Chem. Soc.* **1994**, *116*, 9535.
- [17] K. B. Mathisen, E. M. Siegbahn, *Chem. Phys.* **1984**, *90*, 225-230.
- [18] P. Wentworth Jr., A. D. Wentworth, X. Zhu, I. A. Wilson, K. D. Janda, A. Eschenmoser, R. A. Lerner, *Proc. Natl. Acad. Sci. USA*, **2003**, *100* (4), 1490-1493.
- [19] F. Cacace, G. de Petris, F. Pepi, A. Troiani, *Science* **1999**, *285*, 81.
- [20] M. Yamashita, J. B. Fenn, *J. Phys. Chem.* **1988**, *20*, 4451-4459.
- [21] J. B. Fenn, M. Mann, C. K. Meng, S. F. Wong, C. M. Whitehouse, *Science* **1989**, *246*, 64-71.
- [22] a) M. N. Eberlin, *Eur. J. Mass Spectrom.* **2007**, *13*, 19-28; b) F. Coelho, M. N. Eberlin, *Angew. Chem.* **2011**, *50*, 5261-5263.
- [23] a) L. S. Santos, *Eur. J. Org. Chem.* **2008**, 235-253. b) L. S. Santos, L. Knaack, J. O. Metzger, *Int. J. Mass Spectrom.* **2005**, *246*, 84-104. c) L. S. Santos, *J. Braz. Chem. Soc.* **2011**, *22* (10), 1827-1840.
- [24] Y. Tian, J. K. Lee, *J. Org. Chem.* **2015**, *80*, 6831-6838.
- [25] F. C. C. Moura, M. H. Araujo, I. Dalmázio, T. A. Alves, L. S. Santos, M. N. Eberlin, R. Augusti, R. M. Lago, *Rapid Comm. Mass Spectrom.* **2006**, *20*, 1859-1863.
- [26] G. B. S. Miller, E. Uggerud, *Int. J. Mass Spectrom.* **2017**, *413*, 150-162.
- [27] C. Vincent, D. G. Gusev, *ACS Catalysis* **2016**, *6* (5), 3301-3309.
- [28] M. M. Cecchini, F. De Angelis, C. Iacobucci, S. Reale, M. Crucianelli, *App. Cat. A: General* **2016**, *517*, 120-128.

- [29] A. Simakov, G. B. S. Miller, A. J. C. Bunkan, M. R. Hoffmann, E. Uggerud, *Phys. Chem. Chem. Phys.* **2013**, *15* (39), 16615-16625.
- [30] L. P. E. Yunker, R. L. Stoddard, J. S. McIndoe, *J. Mass Spectrom.* **2014**, *49*, 1-8.
- [31] *International Agency for Research on Cancer* **1995**, *63*, 394-407. Lyon: IARC.
- [32] a) M. Schlangen, J. Neugebauer, M. Reiher, D. Schöder, J. P. López, M. Haryono, F. W. Heinemann, A. Grohmann, H. Schwarz, *J. Am. Chem. Soc.* **2008**, *130* (13), 4285-4295; b) D. Schöder, H. Schwarz, *Int. J. Mass Spectrom.* **2004**, *231*, 139-146; c) U. Mazurek, D. Schröder, H. Schwarz, *Angew. Chem. Int. Edit.* **2002**, *41*, 2538; d) J. Loos, D. Schröder, W. Zummack, H. Schwarz, *Int. J. Mass Spectrom.* **2002**, *217*, 169; e) U. Mazurek, H. Schwarz, *Chem. Eur. J.* **2002**, *8*, 2057; f) S. Barsch, D. Schröder, H. Schwarz, P.B. Armentrout, *J. Phys. Chem. A* **2001**, *105*, 2005; g) H. Schwarz, D. Schröder, *Pure Appl. Chem.* **2000**, *72*, 2319; h) M. Brönstrup, C. Trage, D. Schröder, H. Schwarz, *J. Am. Chem. Soc.* **2000**, *122*, 699; i) G. Hornung, S. Barsch, D. Schröder, H. Schwarz, *Organometallics* **1998**, *17*, 2271; j) S. Shaik, M. Filatov, D. Schröder, H. Schwarz, *Chem. Eur. J.* **1998**, *4*, 193; k) D. Schröder, C. Heinemann, W. Koch, H. Schwarz, *Pure Appl. Chem.* **1997**, *69*, 273; l) G. Hornung, D. Schröder, H. Schwarz, *J. Am. Chem. Soc.* **1997**, *119*, 2273.
- [33] A. Onda, T. Ochi, K. Yanagisawa, *Green Chem.* **2008**, *10*, 1033-1037.
- [34] H. Kobayashi, H. Kaiki, A. Shrotri, K. Techikawara, A. Fukuoka, *Chem. Sci.* **2016**, *7*, 692-696.
- [35] a) B. Girisuta, L. P. B. M. Jansenn, H. J. Heeres, *Chem. Eng. Res. Des.* **2006**, *84* (A5), 339-349; b) B. Girisuta, L. P. B. M. Jansenn, H. J. Heeres, *Green Chem.* **2006**, *8*, 701-709.
- [36] X. Qi, M. Watanabe, T. M. Aida, R. L. Smith Jr, *Catal. Commun.* **2008**, *9* (13), 2244-2249.

- [37] X. Qian, *Top. Catal.* **2012**, *55*, 218-226.
- [38] M. R. Nimlos, X. Qian, M. Davis, M. E. Himmel, D. K. Johnson, *J. Phys. Chem. A* **2006**, *110*, 11824-11838.
- [39] X. Qian, *J. Phys. Chem.* **2011**, *115*, 11740-11748.
- [40] M. J. Antal, W. S. L. Mok, G. N. Richards, *Carbohydr. Res.* **1990**, *199*, 91-109.
- [41] M. J. Antal Jr., T. Leesomboon, W. S. L. Mok, G. N. Richards, *Carbohydr. Res.* **1991**, *217*, 71-85.
- [42] D. W. Harris, M. S. Feather, *Adv. Carbohydr. Res.* **1973**, *28*, 161-224.
- [43] X. Qian, J. Wei, *J. Phys. Chem. B* **2012**, *116*, 10898-10904.
- [44] R. S. Assary, P. C. Redfern, J. Greeley, L. A. Curtiss, *J. Phys. Chem. B* **2011**, *115*, 4341-4349.
- [45] R. S. Assary, L. A. Curtiss, *Energy Fuels* **2012**, *26*, 1344-1352.
- [46] R. S. Assary, T. Kim, J. Greeley, L. A. Curtiss, *Phys. Chem. Chem. Phys.* **2012**, *14*, 16603-16611.
- [47] R. S. Assary, P. C. Redfern, J. R. Hammond, J. Greeley, L. A. Curtiss, *J. Phys. Chem. B* **2010**, *114*, 9002-9009.
- [48] S. Caratzoulas, D. G. Vlachos, *Carbohydr. Res.* **2011**, *346*, 664-672.
- [49] G. Yang, E. A. Pidko, E. J. M. Hensen, *J. Catal.* **2012**, *295*, 122-132.
- [50] T. Ahmad, L. Kenne, K. Olsson, O. Theander, *Carbohydr. Res.* **1995**, *276*, 309-320.
- [51] M. L. Wolfrom, R. D. Schuetz, L. F. Cavalieri, *J. Am. Chem. Soc.* **1949**, *71*, 3518-3523.
- [52] M. S. Feather, *Tetrahedron Lett.* **1970**, *11*, 4143-4145.

- [53] X. Qian, M. R. Nimlos, D. K. Johnson, M. E. Himmel, *Appl. Biochem. Biotechnol.* **2005**, *124*, 989-997.
- [54] H. Dong, M. R. Nimlos, M. E. Himmel, D. K. Johnson, *J. Phys. Chem. A* **2009**, *113*(30), 8577-8585.
- [55] X. Qian, D. K. Johnson, M. R. Nimlos; *Carbohydr. Res.* **2010**, *345*, 1945-1951.
- [56] A. Thompson, K. Anno, *J. Am. Chem. Soc.* **1954**, *76*(5), 1309-1311.
- [57] K. P. Madhusudanam, *J. Mass Spectrom.* **2006**, *41*, 1096-1104.
- [58] P. Huang, A. Gu, J. Wang, *Res. Chem. Intermed.* **2015**, *41*, 5311-5321.
- [59] G. Bouchoux, *Mass Spectrom. Rev.* **2015**, *34*, 493.
- [60] A. Ricci, S. Picolella, F. Pepi, S. Garzoli, P. Giacomello, *J. Am. Soc. Mass Spectrom.* **2013**, *24*, 1082-1089.
- [61] R. G. Akien, L. Qi, T. I. Horvath, *Chem. Comm.* **2012**, *48*, 5850-5852.
- [62] G.A. Halliday, R.J. Young Jr, V.V. Grushin, *Org. Lett.* **2003**, *5*, 2003-2005.
- [63] S. Feng, C. Bagia, G. Mpourmpakis, *J. Chem. Phys. A* **2013**, *117*, 5211-5219.
- [64] a) M. C. Byrns, D. P. Predecki, L. A. Peterson, *Chem. Res. Toxicol.* **2002**, *15*(3), 373-379; b) M. C. Byrns, C. C. Vu, L. A. Peterson, *Chem. Res. Toxicol.* **2004**, *17*(12), 1607-1613; c) M. C. Byrns, C. C. Vu, J. W. Neidigh, J.-L. Abad, R. A. Jons. L. A. Peterson, *Chem. Res. Toxicol.* **2006**, *19*(3), 414-420.
- [65] J. A. Maga, *Crit. Rev. Food Sci. Nutr.* **1979**, *11*(4), 355-400.
- [66] a) EFSA-Report of Scientific Panel on Contaminants in the Food Chain on provisional findings on furan in food, **2014**; b) EFSA-Report of the CONTAM Panel on provisional findings on furan in food, **2014**.
- [67] FDA-Exploratory data on furan in food, **2014**.

- [68] A. Limacher, J. Kerler, T. Davidek, F. Schmalzried, I. Blank, *J. Agr. Food Chem.* **2008**, *56*, 3639-3647.
- [69] A. Becalski, S. Seaman, *J. AOAC Int.* **2005**, *88*, 102-106.
- [70] J. Maerk, P. Pollien, C. Lindinger, I. Blank, T. Maerk, *J. Agr. Food Chem.* **2006**, *54*, 2789-2793.
- [71] L. C. Perez, A. Y. Varoujan, *J. Agr. Food Chem.* **2004**, *52*, 6830-6836.
- [72] X. Fan, *J. Agr. Food Chem.* **2005**, *53*, 7826-7831.
- [73] R. W. Herbert, E. L. Hirst, E. G. V. Percival, R. J. W. Reynolds, S. J. Smith, *Chem. Soc.* **1933**, 1270-1290.
- [74] B. A. Mogol, V. Gökmen, *J. Agr. Food Chem.* **2013**, *2005*, 10191-10196.
- [75] T. Kurata, Y. Sakurai, *Agric. Biol. Chem.* **1967**, *31* (2), 170-176.
- [76] D.H. Aue and M.T. Bowers, in M.T. Bowers (Ed.), *Gas Phase Ion Chemistry*, Vol. 2, Academic Press, New York, **1979**, Chap. 9.
- [77] R. W. Davidson, M. T. Bowers, T. Su, D. H. Aue, *Int. J. Mass Spectrom. and Ion Phys.* **1977**, *24* (1), 83-105.
- [78] M. Liu, M. Chen, S. Zhang, I. Yang, B. Buckley, J. K. Lee, *J. Phys. Org. Chem.* **2011**, *24*, 929-936.
- [79] A. Wiseman, L. A. Sims, R. Snead, S. Gronert, R. G. A. R. Maclagan, M. Meot-Ner, *J. Phys Chem. A* **2015**, *119*, 118-126.
- [80] a) R. G. Cooks, T. L. Kruger, *J. Am. Chem. Soc.* **1977**, *99*, 1279-1281; b) S. A. McLuckey, D. Cameron, R. G. Cooks, *J. Am. Chem. Soc.* **1981**, *103*, 1313-1317; c) R. G. Cooks, J. S. Patrick, T. Kotiaho, S. A. McLuckey, *Mass Spectrom. Rev.* **1994**, *13*, 287-339.
- [81] X. Cheng, Z. Wu, C. Fenselau, *J. Am. Chem. Soc.* **1993**, *115*, 4844-4848.
- [82] C. Wesdemiotis, *J. Mass Spectrom.* **2004**, *39*, 998-1003.

- [83] *Standard Reference Database Number 69*, Gaithersburg MD, 20899, <http://webbook.nist.gov> (Eds. P. J. Linstrom, W. G. Mallard), **2005**. Last accessed on March 2016.
- [84] D. Pramod, R. C. Wilhoit, *Thermochim. Acta* **1970**, *1*, 61-64.
- [85] a) R. A. Yadav, P. Rani, M. Kumar, R. Singh, P. Singh, N. P. Singh, *Spectrochim. Acta A* **2001**, *84*, 6-21; b) M. A. Mora, F. J. Melendez, *J. Mol. Struct.* **1998**, *454*, 175-185.
- [86] a) J. Hvoslef, *Acta Cryst. B* **1968**, *24*, 1431-1440; b) J. Hvoslef, *Acta Cryst B* **1969**, *25*, 2214-2223.
- [87] J. Hvoslef, *Acta Cryst. B* **1968**, *24*, 23-25.
- [88] G. Bouchoux, *Mass. Spectrom. Rev.* **2013**, 1-20.
- [89] L. L. da Rocha, R. Sparrapan, M. N. Eberlin, *Int. J. Mass Spectrom.* **2003**, *228*, 901-912.
- [90] R. V. Lemieux, K. B. Hendriks, R. V. Stick, K. James, *J. Am. Chem. Soc.* **1975**, *97*, 4056-4062.
- [91] N. K. Kochetkov, E. M. Klimov, N. N. Malysheva, A.V. Demchenko, *Carbohydr. Res.* **1991**, *212*, 77-91.
- [92] a) M. Huang, G. E. Garrett, N. Birlirakis, L. Bohe, D. A. Pratt, D. Crich, *Nature Chem.* **2012**, *4*, 663-667; b) M. Huang, P. Retailleau, L. Bohe, D. Crich, *J. Am. Chem. Soc.* **2012**, *134*, 14746-14749.
- [93] D. R. Mootoo, P. Konradsson, U. Udodong, B. Fraser-Reid, *J. Am. Chem. Soc.* **1988**, *110*, 5586-5584.
- [94] H. Paulsen, *Angew. Chem. Int. Ed. Engl.* **1982**, 155-173.
- [95] H. H. Jensen, L. Lyngbye, M. Bols, *Angew. Chem. Int. Ed.* **2001**, *40*, 3447-3449.

- [96] T. Nukada, A. Berces, M. Z. Zgierski, D. M. Whitfield, *J. Am. Chem. Soc.* **1998**, *120*, 13291-13295.
- [97] J. T. Edward, *Chem. Ind. (London)* **1955**, 1102-1104.
- [98] M. J. Cohen, F. W. Karasek, *J. Chrom. Sci.* **1970**, *8*, 330-337.
- [99] J. Hofmann, H. S. Hehm, P. H. Seeberger, K. Pagel, *Nature* **2015**, *526*, 241-244.
- [100] N. C. Polfer, J. Oomens, *Mass Spectrom. Rev.* **2009**, *28*, 468-494.
- [101] N. C. Polfer, *Chem. Soc. Rev.* **2011**, *40*, 2211-2221.
- [102] A. M. Rijis, J. Oomens, *Top. Curr. Chem.* **2015**, *364*, 1-42.
- [103] G. Meijer, M. S. Devries, H. E. Hunziker, H. R. Wendt, *Appl. Phys. B-Photophys. Laser Chem.* **1990**, *51* (6), 395-403.
- [104] J. M. Lisy, *J. Chem. Phys.* **2006**, *125*, 132302.
- [105] N. C. Polfer, J. J. Valle, D. T. Moore, J. Oomens, J. R. Eyler, B. Bendiak, *Anal. Chem.* **2006**, *78*, 670-679.
- [106] E. Mucha, *Master Thesis*, Freie Universität Berlin **2016**.
- [107] a) Gerlich D., *Adv. Chem. Phys.* **1992**, *82*, 1-176; b) Gerlich D., S. Horning, *Chem. Rev.* **1992**, *92*, 1509-1539.
- [108] T. R. Rizzo, O. V. Boyarkin, *Top. Curr. Chem.* **2015**, *364*, 43-98.
- [109] S. Goyal, D. L. Schutt, G. Scoles, *Phys. Rev. Lett.* **1992**, *69*, 933-936.
- [110] M. Hartmann, R. E. Miller, J. P. Toennies, A. F. Vilesov, *Science* **1996**, *272*, 1631-1634.
- [111] A. Lindinger, J. P. Toennies, A. F. Vilesov, *J. Chem. Phys.* **1999**, *110*, 1429-1436.
- [112] J. P. Toennies, A. F. Vilesov, *Angew. Chem. Int. Ed.* **2004**, *43*, 2622-2648.

- [113] F. Bierau, P. Kupser, G. Meijer, G. von Helden, *Phys. Rev. Lett.* **2010**, *105*, 133402-4
- [114] F. Filsinger, D. Ahn, G. Meijer, G. von Helden, *Phys. Chem. Chem. Phys.* **2012**, *14*, 13370-13377.
- [115] A. I. González Flórez, D.-S. Ahn, S. Gewinner, W. Schöllkopf, G. Von Helden, *Phys. Chem. Chem. Phys.* **2015**, *17* (34), 21902-21911.
- [116] A. I. González Flórez, E. Mucha, D. S. Ahn, S. Gewinner, W. Schöllkopf, K. Pagel, G. Von Helden, *Ang. Chem.* **2016**, *55*, 3295-3299.
- [117] E. Mucha, A. I. González Flórez, M. Marianski, D. A. Thomas, W. Hoffmann, W. B. Struwe, H. S. Hahm, S. Gewinner, W. Schöllkopf, P. H. Seeberger, G. Von Helden, K. Pagel, *Angew. Chem. Int. Ed.* **2017**, *56*, 1-5.
- [118] C. Leblanc, H. Vilter, J. -B. Fournier, L. Delage, P. Potin, E. Rebuffet, G. Michel, P. L. Solari, M. C. Feiters, M. Czjzek, *Coord. Chem. Rev.* **2015**, *301-302*, 134-146.
- [119] a) T. J. Kealy, P. L. Pauson, *Nature* **1951**, *168*, 1039; b) S. A. Miller, J. A. Tebboth, J. F. Tremaine, *J. Chem. Soc.* **1952**, 632.
- [120] a) P. L. Pauson, *J. Organomet. Chem.* **2001**, *637-639*, 3-6; b) A. F. Neto, A. C. Pelegriño, V. A. Darin, *Chem Inform.* **2004**, *35(43)*.
- [121] a) K. Heinze, H. Lang, *Organometallics* **2013**, *32*, 5623; b) R. Sun, L. Wang, H. Yu, Z. U. Abdin, Y. Chen, J. Huang, R. Tong, *Organometallics* **2014**, *33*, 4560; c) S. Takahashi, J.-I. Anzai, *Materials* **2013**, *6*, 5742; d) S. S. Braga, A. M. S. Silva, *Organometallics* **2013**, *32*, 5626; e) T. Daeneke, T. H. Kwon, A. B. Holmes, N. W. Duffy, U. Bach, L. Spiccia, *Nat. Chem.* **2011**, *3*, 211.
- [122] a) P. Köpf-Maier, H. Köpf, E. W. Neuse, *Angew. Chem. Int. Ed. Engl.* **1984**, *23*, 456; b) P. Köpf-Maier, H. Köpf, E. W. Neuse, *Angew. Chem.* **1984**, *96*, 446.

- [123] B. M. Weckhuysen, D. E. Keller, *Catal. Today* **2003**, 78, 25.
- [124] a) M. S. Whittingham, *Chem. Rev.* **2004**, 104, 4271; b) C. Zhang, H. Song, C. Zhang, C. Liu, Y. Liu, G. Cao, *J. Phys. Chem. C* **2015**, 119, 11391; c) X. Xu, M. Yan, X. Tian, C. Yang, M. Shi, Q. Wei, L. Xu, L. Mai, *Nano Lett.* **2015**, 15, 3879.
- [125] G. Innorta, S. Torroni, F. Basili, A. Di Fabio, *J. Organomet.Chem.* **2002**, 650, 69.
- [126] R. W. Kugel, L. F. Pinelo, B.S.Ault, *J. Phys.Chem. A* **2015**, 119, 2371.
- [127] E. Nakamura, N. Yoshikai, *J. Org.Chem.* **2010**, 75, 6061.
- [128] a) K. Eller, H. Schwarz, *Chem.Rev.* **1991**, 91, 1121; b) L. Capron, H. Mestdagh, C. Rolando, *Coord. Chem. Rev.* **1998**, 178–180, 269; c) D. K. Böhme, H. Schwarz, *Angew.Chem. Int. Ed.* **2005**, 44, 2336; *Angew.Chem.* **2005**, 117, 2388; d) M.Schlangen, H. Schwarz, *Catal. Lett.* **2012**, 142, 1265.
- [129] a) R. C. Bell, K. A. Zemski, K. P. Kerns, H. T. Deng, A. W. Castleman, Jr. *J. Phys. Chem. A* **1998**, 102, 1733; b) K. A. Zemski, D. R. Justes, A. W. Castleman, Jr. *J. Phys. Chem. A* **2001**, 105, 10237; c) S. Feyel, D. Schröder, X. Rozanska, J. Sauer, H. Schwarz, *Angew. Chem. Int. Ed. Engl.* **2006**, 45, 4677; d) S. Feyel, J. Döbler, D. Schröder, J. Sauer, H. Schwarz, *Angew. Chem. Int. Ed. Engl.* **2006**, 45, 4681; e) N. Dietl, M. Engeser, H. Schwarz, *Chem. Eur. J.* **2010**, 16, 4452; f) S. Zhou, J. Li, M. Schlangen, H. Schwarz, *Chem. Eur. J.* **2016**, 22, 7225
- [130] a) Z.-C. Wang, X. N. Wu, Y. X. Zhao, J. B. Ma, X. L. Ding, S. G. He, *Chem. Phys. Lett.* **2010**, 489, 25; b) N. Dietl, R. F. Hockendorf, M. Schlangen, M. Lerch, M. K. Beyer, H. Schwarz, *Angew. Chem. Int. Ed. Engl.* **2011**, 50, 1430; c) Z.-C. Wang, J.-W. Liu, M. Schlangen, T. Weiske, D. Schröder, J. Sauer, H. Schwarz, *Chem. Eur. J.* **2013**, 19, 11496; d) N. Dietl, T. Wende, K. Chen, L. Jiang, M. Schlangen, X. Zhang, K. R. Asmis, H. Schwarz, *J. Am. Chem. Soc.* **2013**, 135, 3711; e) Z. Y. Li, H. F. Li, Y. X. Zhao, S. G. He, *J. Am. Chem. Soc.* **2016**, 138, 9437.

- [131] a) R. C. Bell, A.W. Castleman, *J. Phys. Chem. A* **2002**, *106*, 9893; b) X.-N. Li, B. Xu, X.-L. Ding, S.-G. He, *Dalton Trans.* **2012**, *41*, 5562; c) S. Li, A. Mirabal, J. Demuth, L. Wöste, T. Siebert, *J. Am. Chem. Soc.* **2008**, *130*, 16832; d) Y.-X. Zhao, X.-N. Wu, J.-B. Ma, S.-G. He, X.-L. Ding, *J. Phys. Chem. C* **2010**, *114*, 1227; e) E. Janssens, S. M. Lang, M. Brümmer, A. Niedziela, G. Santambrogio, K. R. Asmis, J. Sauer, *Phys. Chem. Chem. Phys.* **2012**, *14*, 14344; f) A. Dinca, T. P. Davis, K. J. Fisher, D. R. Smith, G. D. Willett, *Int. J. Mass Spectrom.* **1999**, *182/183*, 73; g) Z. Yuan, Z.-Y. Li, Z.-X. Zhou, Q.-Y. Liu, S.-G. He, *J. Phys. Chem. C* **2014**, *118*, 14967.
- [132] a) E. Jakubikova, E. R. Bernstein, *J. Phys. Chem. A* **2007**, *111*, 13339; b) S.-G. He, Y. Xie, F. Dong, S. Heinbuch, E. Jakubikova, J. J. Rocca, E. R. Bernstein, *J. Phys. Chem. A* **2008**, *112*, 11067.
- [133] a) S. Krückeberg, P. Beiersdorfer, G. Dietrich, K. Lützenkirchen, L. Schweikhard, C. Walther, *Rapid Comm. Mass Spectrom.* **1997**, *11*, 455; b) Z. Parsons, C. Leavitt, T. Duong, G. S. Groenewold, G. L. Gresham, M. J. Van Stipdonk, *J. Phys. Chem. A* **2006**, *110*, 11627; c) D. Schröder, M. Engeser, H. Schwarz, J. N. Harvey, *Chem. Phys. Chem.* **2002**, *3*, 584; d) X. Zhang, H. Schwarz, *Chem. Eur. J.* **2010**, *16*, 1163.
- [134] a) D. K. Walanda, R. C. Burns, G. A. Lawrance, E. I. von Nagy-Felsobuki, *Inorg. Chem. Comm.* **1999**, *2*, 487; b) D. K. Walanda, R. C. Burns, G. A. Lawrance, E. I. von Nagy-Felsobuki, *Inorg. Chim. Acta* **2000**, *305*, 118; c) N. M. Al Hasan, G. E. Johnson, J. Laskin, *J. Am. Soc. Mass Spectrom.* **2013**, *24*, 1385.
- [135] a) Y. A. Ranasinghe, T. J. MacMahon, B. S. Freiser, *J. Am. Chem. Soc.* **1992**, *114*, 9112; b) S. Petrie, G. Javahery, J. Wang, D. K. Bohme, *J. Am. Chem. Soc.* **1992**, *114*, 9177; c) S. D. Price, M. Manning, S. R. Leone, *J. Am. Chem. Soc.* **1994**, *116*, 8673; d) J. Roithová, Z. Herman, D. Schröder, H. Schwarz, *Chem. Eur. J.* **2006**, *12*, 2465; e) J. Roithová, D. Schröder, *J. Am. Chem. Soc.* **2006**, *128*, 4208; f) J. Roithová, J. Žabka, Z. Herman, R. Thissen, D. Schröder, H. Schwarz, *J. Phys. Chem. A* **2006**, *110*, 6447; g) J.

- Roithová, D. Schröder, *Phys. Chem. Chem. Phys.* **2007**, *9*, 2341; h) J. Roithová, D. Schröder, H. Schwarz, *Chem. Eur. J.* **2009**, *15*, 9995.
- [136] a) A. Blades, M. Peschke, U. Verkerk, P. Kebarle, *J. Phys. Chem. A.* **2002**, *106*, 10037; b) A. E. Flores, S. Gronert, *J. Am. Chem. Soc.* **1999**, *121*, 2627; c) S. Gronert, *Acc. Chem. Res.* **2003**, *36*, 848.
- [137] a) C. A. Schalley, G. Hornung, D. Schröder, H. Schwarz, *Chem. Soc. Rev.* **1998**, *27*, 91; b) F. Cacace, G. de Petris, M. Rosi, A. Troiani, *Angew. Chem. Int. Ed.* **2001**, *40*, 1938; *Angew. Chem.* **2001**, *113*, 1992; c) G. de Petris, G. Angelini, O. Ursini, M. Rosi, A. Troiani, *Angew. Chem. Int. Ed.* **2012**, *51*, 1455; *Angew. Chem.* **2012**, *124*, 1484; d) G. de Petris, A. Troiani, M. Rosi, G. Angelini, O. Ursini, *ChemPlusChem* **2013**, *78*, 1065.
- [138] a) M. T. Bowers, D. D. Elleman, R. M. O' Malley, K. R. Jennings, *J. Phys. Chem.* **1970**, *74*, 2583; b) S. G. Lias, P. Ausloos, *J. Chem. Phys.* **1985**, *82*, 3613.
- [139] G. Bouchoux, M. Yanez, O. Mo, *Int. J. Mass Spectrom.* **1999**, *185/ 187*, 241.
- [140] a) R. R. Corderman, J. L. Beauchamp, *Inorg. Chem.* **1978**, *17*, 68; b) V. I. Baranov, G. Javahery, D. K. Böhme, *Chem. Phys. Lett.* **1995**, *239*, 339; c) V. I. Baranov, D. K. Böhme, *Int. J. Mass Spectrom. Ion Proc.* **1995**, *149/150*, 543; d) R. Bakhtiar, D. B. Jacobson, *J. Am. Soc. Mass Spectrom.* **1996**, *7*, 938; e) R. K. Milburn, V. I. Baranov, A. C. Hopkinson, D. K. Böhme, *J. Phys. Chem. A* **1998**, *102*, 9803; f) V. I. Baranov, D. K. Böhme, *Int. J. Mass Spectrom.* **2001**, *210/211*, 303; g) V. I. Baranov, D. K. Böhme, *Int. J. Mass Spectrom.* **2001**, *204*, 209; h) G. Innorta, S. Torroni, F. Basili, A. Di Fabio, *J. Organomet. Chem.* **2002**, *650*, 69.
- [141] a) Y. Huang, B. S. Freiser, *J. Am. Chem. Soc.* **1990**, *112*, 5085; b) NIST Chemistry WebBook, NIST Standard Reference Database Number 69, Gaithersburg MD, 20899, <http://webbook.nist.gov> (Eds. P. J. Linstrom, W. G. Mallard), **2005**; c) E. Goos, A. Burcat, B. Ruscic, Active Thermochemical Tables (ATcT) available at: <http://burcat.technion.ac.il/dir>, **2015**.

- [142] M. Sodupe, C. W. Bauschlicher, *Chem. Phys. Lett.* **1993**, 207,19.
- [143] M. Diefenbach, C. Trage, H. Schwarz, *Helv. Chim. Acta* **2003**, 86, 1008.
- [144] B. Butschke, H. Schwarz, *Int. J. Mass Spectrom.* **2011**, 306,108.
- [145] P. J. Linstrom and W.G. Mallard, Eds., NIST Chemistry WebBook, NIST Standard Reference Database Number 69, National Institute of Standards and Technology, Gaithersburg MD, 20899, <http://webbook.nist.gov>, (retrieved November 22, **2016**).
- [146] a) H.-G. Weikert, L. S. Cederbaum, F. Tarantelli, A. I. Boldyrev, *Z. Phys. D* **1991**, 18, 299; b) M.K. Scheller, R. N. Compton, L. S. Cederbaum, *Science* **1995**, 270, 1160; c) L.-S. Wang, C.-F. Ding, X.-B. Wang, J. B. Nicholas, *Phys. Rev. Lett.* **1998**, 81, 2667.
- [147] N. F. Dalleska, K. Honma, P. B. Armentrout, *J. Am. Chem. Soc.* **1993**, 115, 12125-12131.
- [148] C-X. Su, D. A. Hales, P. B. Armentrout, *Chem. Phys. Lett.* **1993**, 201, 199-204.
- [149] P. B. Armentrout, N. Adams, L. Babcock, Eds., *Advances in Gas Phase Ion Chemistry*; JAI Press: Greenwich, CT, **1992**, Vol.1, p. 83.
- [150] C. E. C. A. Hop, T. B. McMahon, G. D. Willet, *Int. J. Mass Spectrom. Ion Processes* **1990**, 101, 191-208.
- [151] J. S. Brodbelt, H. I. Kenttamaa, R. G. Cooks, *Org. Mass Spectrom. OMS* **1988**, 23, 6-9.
- [152] S. T. Graul, R. R. Squires. *J. Am. Chem. Soc.* **1990**, 112, 2517-2529.
- [153] N. C. Polfer, *Chem. Soc. Rev.* **2011**, 40, 2211-2221.
- [154] A. G. Marshall, C. L. Hendrickson, G. S. Jackson, *Mass Spectrom. Rev.* **1998**, 17 (1), 1-35.

- [155] a) D. Schröder, H. Schwarz, D. E. Clemmer, Y. Chen, P. B. Armentrout, V. Baranov, D. K. Bohme, *Int. J. Mass Spectrom. Ion Proc.* **1997**, *161*, 175; b) D. Schröder, H. Schwarz, *Can. J. Chem.* **2005**, *83*, 1936.
- [156] J. E. Bartmess, R. M. Georgiadis, *Vacuum* **1983**, *33*, 149.
- [157] S. Gronert, *Mass Spectrom. Rev.* **2005**, *24*, 100.
- [158] R. Lavertu, M. Catte, A. Pentenero, P. C. LeGoff, *R. Seances Acad. Sci., Ser. C* **1966**, *263*, 1099.
- [159] a) J. K. Terlouw, H. Schwarz, *Angew. Chem., Int. Ed. Engl.* **1987**, *26*, 805; b) J. L. Holmes, *Mass Spectrom. Rev.* **1989**, *8*, 513; c) F. W. McLafferty, *Science* **1990**, *247*, 925; d) F. W. McLafferty, *Int. J. Mass Spectrom. Ion Processes* **1992**, *118/119*, 221; e) F. Turecek, *Org. Mass. Spectrom.* **1992**, *27*, 1087.
- [160] F. W. McLafferty, P. J. Todd, D. C. McGilvery, M. A. Baldwin, *J. Am. Chem. Soc.* **1980**, *102*, 3360.
- [161] P. C. Burgers, J. L. Holmes, A. A. Mommers, J. K. Terlouw, *Chem. Phys. Lett.* **1983**, *102*, 1.
- [162] G. Schmidt, W. H. Keeson, *Physica* **1937**, *4*(10), 963-970.
- [163] P. Kapitza, *Nature* **1938**, *141*, 74.
- [164] J. F. Allen, A. D. Misener, *Nature* **1938**, *142*, 643.
- [165] T. A. Alvesalo, H. K. Collan, M. T. Loponen, O. V. Lounasmaa, M. C. Veuro, *J. Low Temp. Phys.* **1975**, *19*, 1-37.
- [166] K. K. Darrow, *Rev. Mod. Phys.* **1940**, *12*, 257-266.
- [167] X. Zhang, N. B. Brauer, G. Berden, A. M. Rijs, M. J. Drabbels, *Chem. Phys.* **2012**, *136*, 044305–044310.
- [168] a) A. Scheidemann, P. J. Toennies, J. A. Northby, *Phys. Rev. Lett.* **1990**, *64*, 1899–1902; b)

- [169] W. Schöllkopf, S. Gewinner, H. Junkes, A. Paarmann, G. v. Helden, H. Bluem, A. M. M. Todd, *Proc. SPIE- Int. Soc. Opt. Eng.* **2015**, 9512, 95121L.
- [170] G. de Petris, A. Cartoni, A. Troiani, V. Barone, P. Cimino, G. Angelini, O. Ursini, *Chem. Eur. J.* **2010**, 16, 6234.
- [171] M. T. Bowers, T. Su, *Interactions between Ions and Molecules*, Plenum Press, New York, **1975**.

List of Publications

- 1) **“Ab-initio and experimental study of pentose sugar dehydration mechanism in the gas phase”**
A. Ricci, S. Garzoli, L. Antonini, A. Troiani, C. Salvitti, P. Giacomello, R. Ragno, A. Patsilidakos, B. Di Rienzo, F. Pepi, *submitted*.
- 2) **“Vanadium hydroxide cluster ions in the gas phase: bond forming reactions of doubly-charged negative ions by SO₂-promoted V-O activation”**
A. Troiani, M. Rosi, S. Garzoli, C. Salvitti, G. de Petris, *Chemistry-A European Journal* **2017**, 23(49), 11752-11756 (DOI:10.1002/chem.201702165).
- 3) **“Synthesis and characterization of two new triads with ferrocene and C60 connected by triple bonds to the beta-positions of meso – tetraphenylporphyrin”**
F. Limosani, F. Possanza, E. Ciotta, F. Pepi, C. Salvitti, P. Tagliatesta, R. Pizzoferrato, *Journal of Porphyrins and Phthalocyanines* **2017**, 21(4-6), 364-370 (DOI: 10.1142/S1088424617500286).
- 4) **“Vitamin C: an experimental and theoretical study on the gas phase structure and ion energetics of protonated Ascorbic acid”**
A. Ricci, F. Pepi, P. Cimino, A. Troiani, S. Garzoli, C. Salvitti, B. Di Renzo, V. Barone, *Journal of Mass Spectrometry* **2016**, 51(12), 1146-1151 (DOI: 10.1002/jms.3848).
- 5) **“Characterization of naproxen-polymer conjugates for drug delivery”**
G. Forte, I. Chiarotto, I. Giannicchi, M.A. Loreto, A. Martinelli, R. Micci, F. Pepi, S. Rossi, C. Salvitti, A. Stringaro, L. Tortora, S. Vecchio Cipriotti, M. Feroci, *Journal of Biomaterials Science, Polymer Edition*, **2015**, 27(1), 69-85 (DOI:10.1080/09205063.2015.1108637).
- 6) **“Iron-Promoted C-C bond formation in the gas phase”**
A. Troiani, M. Rosi, S. Garzoli, C. Salvitti, G. de Petris, *Angewandte Chemie, International ed.*, **2015**, 54 (48), 14359-14362 (DOI:10.1002/anie.201506932).
- 7) **“A mass spectrometric study of the acid-catalysed D-fructose dehydration in the gas phase”**
F. Pepi, A. Ricci, S. Garzoli, A. Troiani, C. Salvitti, B. Di Rienzo, P. Giacomello, *Carbohydrate Research*, **2015**, 413, 145-150 (DOI:10.1016/j.carres.2015.05.013).
- 8) **“All the 2p-block elements in a molecule: experimental and theoretical studies of FBNCO and FBNCO⁺”**
A. Troiani, S. Garzoli, F. Pepi, A. Ricci, M. Rosi, C. Salvitti, G. de Petris, *Chemical Communications* **2014**, 50 (90), 13900-13903 (DOI:10.1039/C4CC05217J).

9) **“The oxidation of sulfur dioxide by single and double oxygen transfer paths”**

A. Troiani, M. Rosi, C. Salvitti, G. de Petris, *ChemPhysChem* **2014**, 15 (13), 2723-2731 (DOI:10.1002/cphc.201402306).

Acknowledgments

“Quanti di voi hanno avuto un insegnante, in qualunque grado di istruzione, che vi ha resi più entusiasti di essere al mondo, più fieri di essere al mondo, di quanto credevate possibile fino a quel momento? Alzate le mani, per favore. Adesso riabbassatele e dite il nome di questo insegnante ad un vostro vicino, e spiegategli che cosa ha fatto per voi. Ci siamo? Cosa c'è di più bello di questo?”

Kurt Vonnegut

Si conclude dopo tre anni il mio percorso di dottorato e la fine di questa esperienza porta con sé riflessioni inevitabili su quanto abbia contribuito a cambiarmi.

Fortunatamente l'inestimabile valore letterario di uno scrittore come Kurt Vonnegut viene in mio soccorso e mi offre lo spunto almeno per scrivere il capitolo conclusivo di questa avventura. Mi perdonerà, dunque, se per rispondere alla sua domanda non potrò esimermi dal fare più di un solo nome.

Ringrazio il Prof. Federico Pepi e la Prof.ssa Giulia de Petris per avermi accolto nei loro laboratori, per essere sempre stati disponibili nei miei riguardi e non essersi mai sottratti a qualsiasi occasione di confronto. Se dovessi materialmente ripagarvi di tutto questo, probabilmente il mio sarebbe un debito troppo grande da estinguere.

Ringrazio la Prof.ssa Andreina Ricci per avermi dato la possibilità di avvicinarmi ad una linea di ricerca così interessante e per essermi stata vicina quando per la prima volta ho dovuto relazionare ad un congresso.

Ringrazio la Dott.ssa Anna Troiani e la Dott.ssa Stefania Garzoli per avermi “praticamente” allevato, facendomi appassionare alla materia. Grazie per essere state sempre un punto di riferimento oltre il lavoro; se in questi anni ho avuto bisogno di un consiglio disinteressato, di una parola di supporto o di una semplice chiacchierata ho sempre saputo a quale porta bussare.

Ringrazio il Prof. Kevin Pagel perché, pur non conoscendomi, mi ha ospitato con entusiasmo nel suo laboratorio, permettendomi di vivere da berlinese per cinque intensi mesi. Grazie ai suoi ragazzi che non mi hanno mai fatto sentire esclusa in

nessuna occasione e con i quali serbo tuttora dei ricordi che porterò sempre con me.

Infine, volevo ringraziare la Prof.ssa Isabella Chiarotto e la Prof.ssa Marta Feroci perché se ho scelto di proseguire la carriera accademica è anche merito loro e perché ovunque io sia arrivata non dimenticherò mai da dove sono partita.